Exploring silicon photomultipliers for the Upgrade of the Pierre Auger Observatory

Von der Fakultät für Mathematik, Informatik und Naturwissenschaften der RWTH Aachen
University zur Erlangung des akademischen Grades eines
Doktors der Naturwissenschaften genehmigte Dissertation

vorgelegt von

Johannes Christian Schumacher, M.Sc. RWTH

aus

Düsseldorf, Bundesrepublik Deutschland

Berichter: Universitätsprofessor Dr. rer. nat. Thomas Hebbeker
Professor als Juniorprofessor Dr. rer. nat. Thomas Bretz

Tag der mündlichen Prüfung: 30.01.2019

Diese Dissertation ist auf den Internetseiten der Universitätsbibliothek verfügbar.

Abstract

Even though their existence has been known for more than a century, the nature of cosmic rays is still heavily discussed [1]. The fundamental questions refer to the origin and the acceleration mechanisms of cosmic rays specifically at the highest energies. To address these questions, it is of paramount importance to study the composition of ultra-high energy cosmic rays [2].

The Pierre Auger Observatory [3] in Argentina pursues this objective with its upgrade *Auger-Prime* [4, 5]. Within this scope, this thesis introduces silicon photomultipliers (SiPMs) to boost the performance of two detector subsystems of AugerPrime: the Surface Scintillation Detector (SSD) and the First Auger Multi-pixel photon counter camera for the Observation of Ultra-high energy cosmic air Showers (FAMOUS).

While the first chapters of this thesis deal with ultra-high energy cosmic ray (UHECR) detector projects like the Pierre Auger Observatory and its upgrade (chapter 2 & 3), the following chapter introduces intrinsic parameters of SiPMs and standard calibration routines (chapter 4). These devices and their characteristics are of fundamental importance for the work that follows.

A large-sized SiPM was used to replace a standard vacuum photomultiplier tube (PMT) in the prototype surface scintillation detector – Auger Scintillators for Composition – II (ASCII) – the predecessor of SSD. It is shown that SiPMs offer great intrinsic calibration capabilities that allow in-situ calibration of the scintillator, out-performing PMTs easily. Due to its splendid performance, the concept was adapted to SSD which is introduced afterward (chapter 5).

The idea to build a small-sized SiPM-based telescope came up in the early 2010s. The developments of the optical system were done in [6], while the work of this thesis focusses on the electronics, its calibration, and the first high-energy events. This is discussed in the last chapter (chapter 6). With its intelligent biasing and triggering system, as well as its mechanical and electrical robustness, the design of the FAMOUS telescope was duplicated and introduced in different astroparticle physics applications which will be summarized at the end of this thesis. This work concludes with a summary and a quick glance into the future.

Contents

Conventions used in this thesis

1.1. Mathematical symbols

The author will express time-dependent mathematical functions describing electrical signals with lower-case letters, that is for the voltage $v(t)$ and for the current $i(t)$. In the Laplace-domain, however, the author sticks to the typical convention that reserves capital letters $V(s)$ and $I(s)$, respectively. Laplace transforms are used in this thesis to convert sets of differential equations describing the solutions of circuit diagrams into linear algebraic equations which can be solved relatively easily. Also, Laplace transforms are used to describe the frequency response of electronic circuits and thus predict the feedback and behavior of filters, amplifiers, etc.

Appropriately, to avoid confusions between the electrical current $i(t)$ and the imaginary symbol i which is commonly used in mathematics, the latter is hence expressed with the lower case character j to interpret complex numbers, for example $z = a + j \cdot b$ where the real part of z is equal to a, and its imaginary part is b.

1.2. Diagrams

Circuit diagrams in electronics are used to express the context of a specific circuit graphically from which time- or frequency-dependent solutions of voltages and currents can be either calculated or simulated when the initial conditions are known. Special rules and guidelines apply to those diagrams, and the reader may find these in the corresponding standards, e.g. the Comité Européen de Normalisation – European Committee for Standardization (CEN), or the International Organization for Standardization (ISO). Likewise, in particle physics, Feynman diagrams are used to describe interactions between particles from which probability amplitudes are calculated. Those diagrams fix the time and space coordinates in the horizontal and vertical axes, or vice versa, in contrast to circuit diagrams which can be flipped and rotated horizontally, vertically, and wholly rearranged without distorting their meaning. In this thesis, the author makes use of circuit diagrams only. The circuit diagrams can get quite complicated, so the author tries to stick to the following convention: The vertical axis expresses the voltage level with reference to ground decreasing from top to bottom, e.g. 70 V, 5 V, GND, −5 V. The

horizontal axis is used to distinguish between input signals on the corresponding voltage nodes on the left, the circuit under investigation in the center and its output signals on the right.

1.3. Units

This thesis combines aspects of different fields of physics and engineering. These are

1. particle physics, e.g. hadronic physics in the evolution of the cosmic ray induced air shower,

2. astroparticle physics, e.g. interpretation of results of cosmic ray-specialized experiments,

3. electrics, electronics, and electrodynamics,

4. optics, and

5. mechanics.

All of those use their own set of notations, symbols, and – most importantly – units. Although natural units are most common in particle physics, i.e. $\hbar = c = 1$, the author will stick to units of the système international d'unités – International System of Units (SI), SI-derived units, and its prefixes. This means that aside from units like volts V or seconds s, the author will use $\mathrm{MeV}\,c^{-2}$ instead of just MeV for particle masses where c is the speed of light in vacuum.

1.4. Miscellaneous

To reduce the number of words, formulae, characters, symbols, etc., the author will combine decay modes like

$$K^{\pm} \to \mu^{\pm}\, \dot{\nu}_{\mu}\, \pi^0, \quad \text{or equivalently} \quad K^{\mp} \to \mu^{\mp}\, \bar{\nu}_{\mu}\, \pi^0.$$

This means that positively charged kaons K^+ decay into positively charged muons μ^+, muon-neutrinos $\nu_{\mu} \equiv \dot{\nu}_{\mu}$ and neutral pions π^0. Negatively charged kaons K^-, however, decay into negatively charged muons μ^-, anti-muon-neutrinos $\bar{\nu}_{\mu}$ and neutral pions π^0. Whenever the author combines decay modes like this the author hence discriminates neutrinos from anti-neutrinos, and in general electrical neutral particles and their anti-particles with a dot-bar combination, i.e.

$$\dot{\nu}, \quad \text{resp.} \quad \bar{\nu}, \quad \text{where} \quad \dot{\nu} \equiv \nu,$$

although this is non-standard.

Introduction

2.1. The cosmic ray energy spectrum

Figure 2.1 shows the measured all particle energy spectrum of cosmic rays above the knee, i.e. from 1 PeV to 100 EeV. The vertical axis in the left plot shows the linear energy-scaled differential flux $E \times dN/dE = dN/d\ln(E)$. Here, E is the kinetic energy in eV of the primary cosmic ray and N is the cosmic ray flux in units of $m^{-2} s^{-1} sr^{-1}$. The results of different experiments are in good agreement. The right-hand side of figure 2.1 is scaled with the third power of energy to flatten the spectrum and to make prominent features of the cosmic ray spectrum visible, e.g.
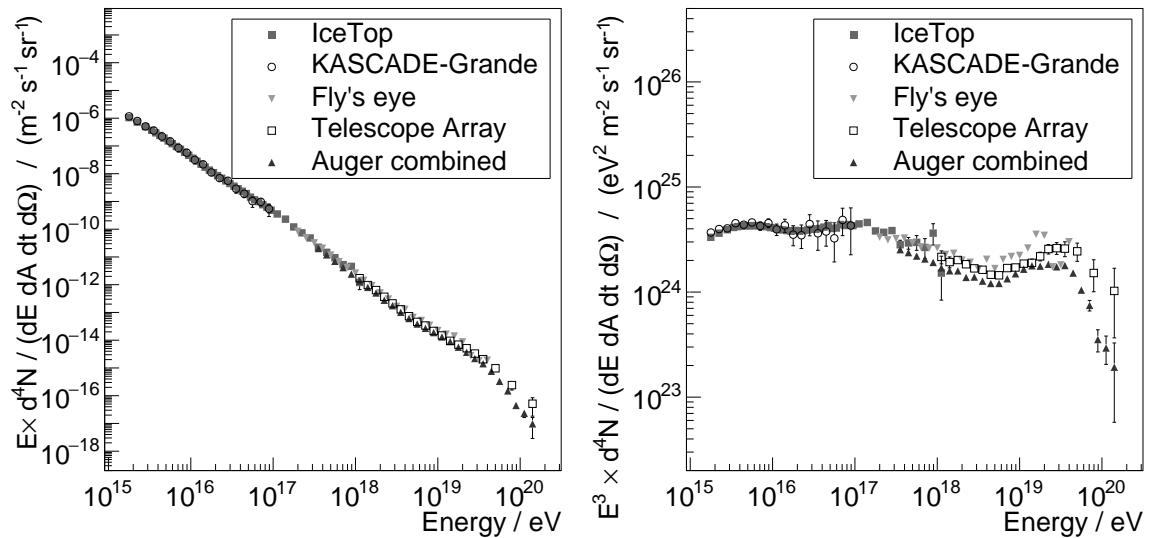

Figure 2.1.: The cosmic ray energy spectrum between 1 PeV and 100 EeV as measured by IceTop-73, KASCADE-Grande, Fly's eye, Telescope Array, and the Pierre Auger Observatory [7, 8, 9, 10, 11]. *Left:* Differential energy flux dN/dE multiplied with energy E. *Right:* Same as left but scaled with the third power of energy E^3.
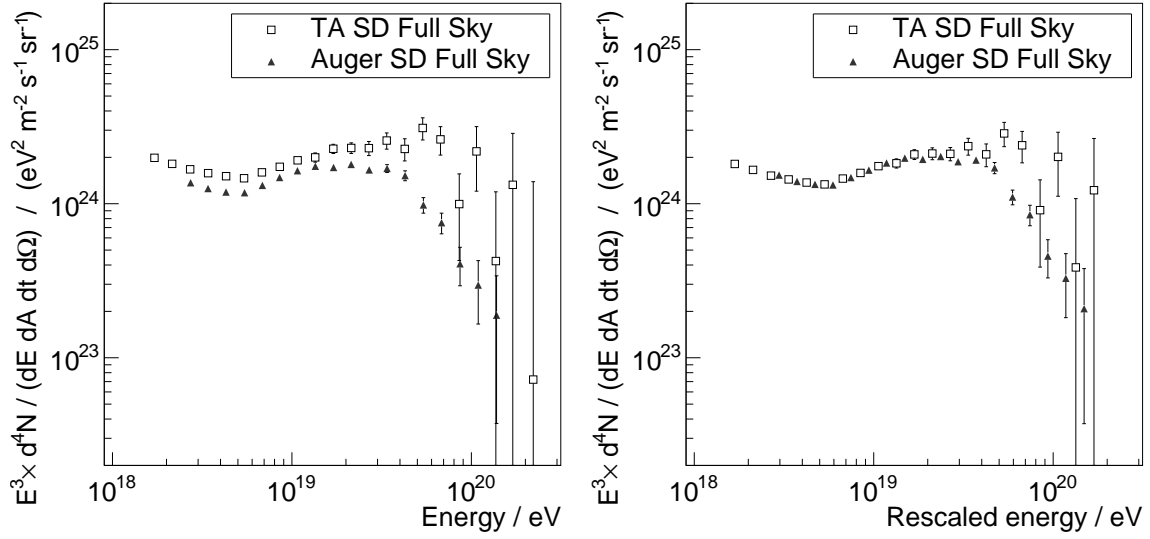
Figure 2.2.: The energy spectrum of UHECRs measured by the Telescope Array and the Pierre Auger Observatory [12]. *Left:* Unscaled energy. *Right:* Energy scaled by ±5.2 %. The data was taken from [12].

the knee at 3 PeV with a spectral index of $\gamma = -3$, the ankle at 5 EeV with $\gamma = -3.3$ and the suppression above 40 EeV as reported in [11].

All experiments whose results are shown in figure 2.1 make use of indirect detection methods. The Earth's atmosphere serves as the target, and the energy of the primary cosmic ray deposited in the atmosphere and its composition is reconstructed with several independent techniques. This method increases the effective aperture, and the use of hybrid detection techniques minimizes systematic uncertainties. An experiment, for example, with an aperture of $\pi \, \mathrm{km}^2 \, \mathrm{sr}$ will be able to measure a flux of the order of one event per second above the knee and one event per year above the ankle.

2.2. Ultra-high energy cosmic ray (UHECR) observatories

The Telescope Array and the Pierre Auger Observatory are multi-km^2 cosmic ray observatories specialized to the highest energies, i.e. UHECRs. The left-hand side of figure 2.2 shows again the differential energy spectrum $\mathrm{d}N/\mathrm{d}E$ scaled with E^3 of these two experiments. A systematic shift is observed where the Pierre Auger Observatory seems to measure a smaller flux than the Telescope Array. However, these discrepancies can be explained by a shift in energy [12]. In the right plot of figure 2.2, the energy of both experiments were scaled by ±5.2 %, respectively. This value is compatible with the systematic uncertainties on the energy scale stated by both collaborations, i.e. 13 % for the Pierre Auger Observatory and 21 % for the Telescope Array [12]. Still, while the flux up to the ankle is now in good agreement, the flux measured by the Telescope Array seems to be bigger at the highest energies, in the suppression region. As of 2017, this is not understood yet [12].
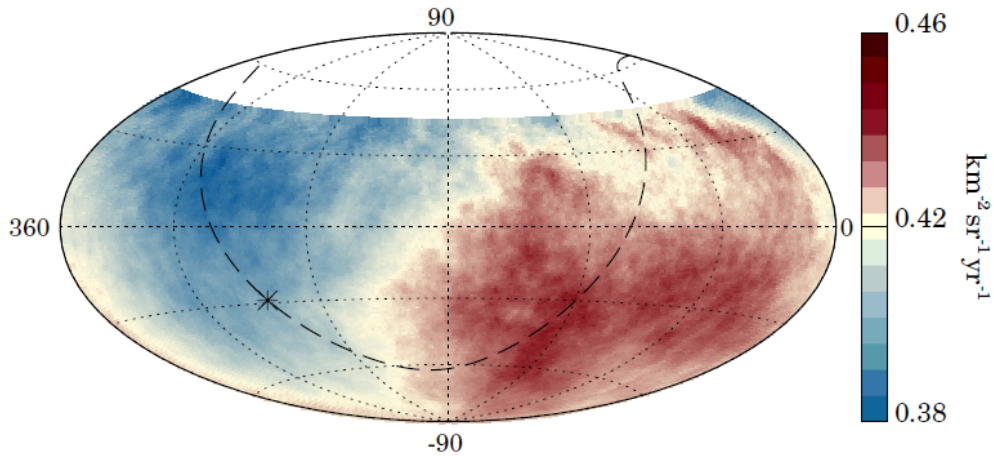
Figure 2.3.: The map of the UHECR flux in equatorial coordinates measured by the Pierre Auger Observatory with energies above 10 EeV as reported in [13] shows a significant dipolar structure. The dashed line represents the galactic plane with the galactic center indicated by the asterisk. Taken from [13].

2.3. Sources of UHECRs

In 2017 the Pierre Auger Observatory reported that an anisotropy with dipolar shape was detected with a significance of more than $5.2\,\sigma$ [13]. An abundance in the anti-galactic center indicates an extra-galactic origin of UHECRs with energies above 10 EeV, i.e. above the ankle. The arrival directions of those events are shown in the equatorial map in figure 2.3. The galactic center is indicated with an asterisk along the dashed line symbolizing the galactic plane. In anisotropy searches of Telescope Array data, evidence for a hotspot was found pointing to the northern hemisphere with $3.74\,\sigma$ level of significance and energies above 56 EeV [14].

2.4. Chemical composition of UHECRs

The outcome of point source analyses strongly depend on the primary composition of UHECRs. Charged particles in an external magnetic field get deflected due to the Lorentz force where the amount of deflection scales linearly with the charge, i.e. the charge number Z for completely ionized atoms and with the magnetic field strength B, as well as inversely with momentum p. From galactic field models, one can search for the origins of cosmic rays once their kinetics $p \cdot c$ and their charge Z are known [16]. Both, the Telescope Array [17] and the Pierre Auger Observatory [15] favor lighter chemical compositions at intermediate energies, i.e. elements between Helium and Nitrogen. Contradictions between the post-Large Hadron Collider (LHC)-tuned hadronic interaction models are reported but they all agree with a missing Iron component between $10^{18.3}$ eV and $10^{19.4}$ eV [15], see also figure 2.4. In this image, an estimator for the chemical composition is plotted against the energy of the primary particle for three different hadronic interaction models. All models show the same trend to lighter elements up to energies around the ankle, i.e. at $10^{18.5}$ eV, and a sudden change to heavier nuclei
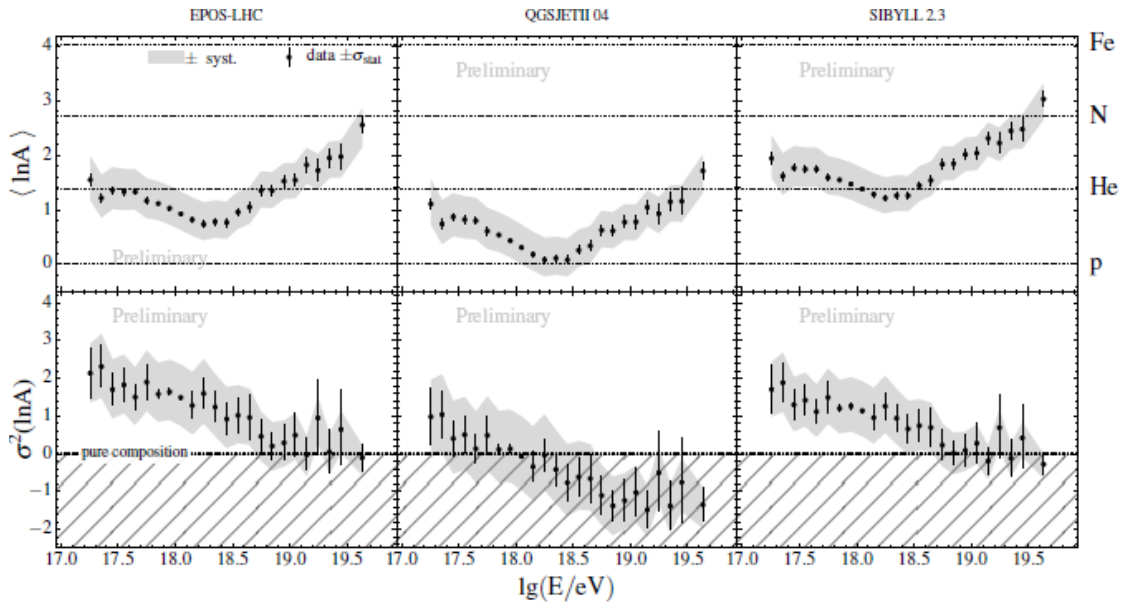
Figure 2.4.: Results from the composition studies on data from the Pierre Auger Observatory done in [15] show the mean mass number versus energy for three different hadronic interaction models. See text for details. Taken from [15].

in the region of the suppression. It is also said, however, that the models cannot find statistical combinations of fractional compositions to describe all data. Energy bins exist in figure 2.4 that are statistically compatible with a negative logarithmic mass number $A < 1$.

It would be beneficial to discriminate between heavy and light ions with respect to their mass number A on an event-by-event basis. One approach is to measure the atmospheric depth of the shower maximum $X_{\max}$ with air-fluorescence telescopes like the data obtained for figure 2.4 [15]. The other is to discriminate between the muonic and electromagnetic component of the air shower with a combination of specialized surface detectors [18].

2.5. The superposition model

In the superposition model, the cosmic ray nucleus of mass number A can be thought of A nucleons that carry on average an equal fraction of the primary energy [19]. The superposition model is a good approximation since the binding energy per nucleon is less than $10\,\mathrm{MeV}$ [20] and thus much smaller than the kinetic energy of the cosmic rays in question, which is $> \mathrm{PeV}$ per nucleon.

Therefore, the shower of an ion with a larger mass number A develops faster in the atmosphere than a lighter ion. The maximal extension of the shower in terms of traversed mass $X_{\max}$ of a heavy ion is smaller than that of a lighter ion. The number of muons detected on the ground also correlates with the mass number whereas the electromagnetic component hardly depends on the primary composition [19].

Figure 2.5 shows the muon number estimator S_μ and the depth of the shower maximum $X_{\max}$ for hydrogen and iron primaries simulated for energies of $10\,\mathrm{EeV}$ and zenith angles of $38°$. The hadronic interaction model was tuned with LHC data [21]. In this specific case, one can
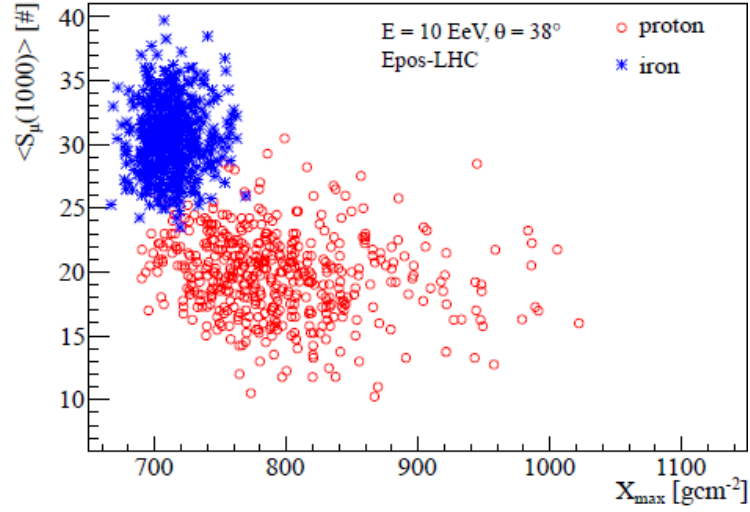
Figure 2.5.: Simulation of the muon signal estimator S_μ for a $10\,\text{m}^2$-detector and the atmospheric depth of the shower maximum X_{max} for hydrogen and iron primaries with energies of $10\,\text{EeV}$ and zenith angles of $38°$ with an LHC-tuned hadronic interaction model. Taken from [21].

see that the mean number of detected muons S_μ of an iron primary is approx. $50\,\%$ larger than that of an hydrogen primary (approx. 30 versus 20), while the depth of the shower maximum X_{max} is about $100\,\text{g}\,\text{cm}^{-2}$ smaller, i.e. approx. $700\,\text{g}\,\text{cm}^{-2}$ versus $800\,\text{g}\,\text{cm}^{-2}$. Likewise, the superposition model predicts a $50\,\%$ to $100\,\%$ larger muon number for iron than for hydrogen, calculated with the scale factor $A^{1-\alpha}$ with $\alpha = 0.8\ldots0.9$ [19] depending on the charged and total particle multiplicities. This plot does not contain measurement resolutions, e.g. on X_{max}. After introducing the merit factor, that is

$$f_{\text{MF}} = \frac{\left|\langle S_i \rangle - \langle S_j \rangle\right|}{\sqrt{\sigma(S_i)^2 + \sigma(S_j)^2}} \tag{2.1}$$

one can estimate from figure 2.5 that the merit factor f_{MF} for differentiating between proton and iron on S_μ is above 2, and slightly below 2 on X_{max}. Both observables are thus good estimators when it comes to identifying the primary composition. The disadvantage of using X_{max} as a composition-sensitive observable is that to this day only optical telescopes can measure X_{max} with a sufficient resolution. However, the air-fluorescence telescopes of the Pierre Auger Observatory suffer from a low duty cycle of approx. $15\,\%$ [5] inevitably reducing the amount of detectable ultra-high energy events. The disadvantage of the second quantity S_μ is that dedicated detectors are necessary to distinguish between the muonic and the electromagnetic shower content on the ground.

2.6. Detection principles of extensive air showers

Following the universality approach, three parameters are sufficient to characterize an extensive air shower; namely the primary energy, the atmospheric depth of shower maximum

X_{max} and the muon flux normalization N_μ [22]. The job of a hybrid observatory is to measure those quantities with, in the best case, several independent methods.

Primary cosmic rays initiate cascades of secondary particles on impact on the Earth's atmosphere. An extensive, also known as extended, air shower is born. Secondaries of the early evolution are highly relativistic and generate more secondaries. This process keeps on running until the mean energy per secondary drops below a critical value from where no additional secondary particles can be created. This point is related to the maximum extension of the air shower. The symbol X_{max} can be found in literature which is the depth of the maximum extension of the air shower related to the primary interaction point folded with the density of the atmosphere and thus given in units of g cm^{-2}.

2.6.1. Secondary particles

Secondary particles of extensive air showers either undergo inelastic scattering, annihilate or decay. For the first ultra-high energy hadronic interactions following the primary vertex, i.e. secondary nucleons that react with nuclei of the gas molecules in the atmosphere, no experimental data exists, and they need to be modeled for example in air shower simulation software like the Cosmic Ray Simulations for Kascade (CORSIKA) [23] using cross-section data extrapolated to higher energies.

Those interactions generate charged or neutral pions or kaons among others. At small momenta, neutral pions π^0 decay almost instantaneously into two photons (>98 %) because of their small mean lifetime of $\sim 10^{-16}$ s [24]. As this decay is purely electromagnetic, neutral pions initiate the *electromagnetic component* of the air shower. At higher momenta, i.e. in the early evolution of the air shower, π^0 also scatter inelastically.

Charged pions $\pi^\pm$ invoke the *muonic component* and the *terrestrial neutrino component* of the air shower. $\pi^\pm$ have a rather long lifetime of $\sim 10^{-8}$ s [24] which means that decay and nuclear interactions with molecules in the atmosphere compete. Dominant decay modes are of leptonic nature and create muons μ and neutrinos ν.

Likewise, highly energetic kaons $K^\pm$ and K^0 behave like charged pions. Having a higher mass than pions, i.e. approx. $500\,\text{MeV c}^{-2}$ versus $135\,\text{MeV c}^{-2}$ for π^0 resp. $140\,\text{MeV c}^{-2}$ for $\pi^\pm$, kaons typically decay into pions $\pi^\pm \pi^0$ (plus π^0) or $\pi^\pm \pi^\pm \pi^\mp$ (>25 %, pure hadronic decay) or into muon and muon-neutrino pairs $\mu^\pm \dot{\nu}_\mu$ (>60 %, pure leptonic decay) with optional neutral pions $\mu^\pm \dot{\nu}_\mu \pi^0$ (>3 %, semi-leptonic decay). A decay into electron, electron-neutrino and neutral pion $e^\pm \dot{\nu}_e \pi^0$ is also common (>5 %, semi-leptonic decay). Neutral kaons follow the K^0_S and K^0_L decay modes which are typically purely hadronic or semi-leptonic. Other, higher order decay modes are less common and often neglected in particle simulation software. See also [24] for a full list of decay modes and branching fractions of pions and kaons.

Muons $\mu^\pm$ are produced dominantly through the decay of charged pions and kaons as described above. $\mu^\pm$ loose energy with atomic nuclei through $e^+ e^-$-pair production and photonuclear interactions, or with atomic electrons through bremsstrahlung and ionization in the atmosphere, or decay. Highly energetic muons are minimal ionizing and happen to reach the surface of the Earth due to their long lifetime of $\sim 10^{-6}$ s [24] and constitute the *muonic component* of an air shower. The criterion for a charged, massive particle to be minimal ionizing (MIP = minimal ionizing particle) follows from the Bethe-Bloch formula for energy loss in matter and can be found at $\beta\gamma \sim 3$. For larger momenta, the energy loss increases only logarithmically. That means that muons with momenta $p_{\mu,\text{MIP}} > 300\,\text{MeV c}^{-1}$ are hardly ionizing. The expected distance traveled in the lab frame before muons with momenta $p_{\mu,\text{MIP}}$ decay is larger
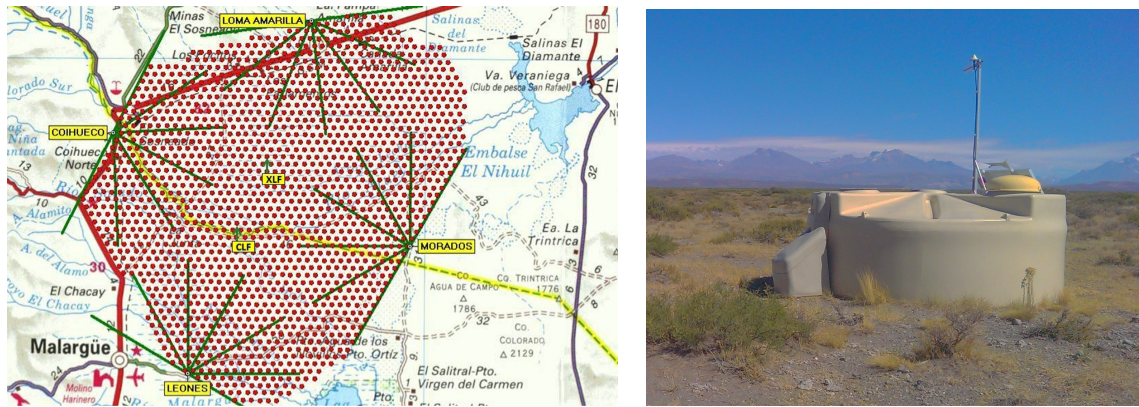
Figure 2.6.: *Left:* A map indicating the positions of the 1660 WCD tanks (red dots) and the four air-fluorescence telescope sites (green lines) near the city of Malargue, Argentina, covering an area of $3000\,\mathrm{km}^2$ of the Pierre Auger Observatory. The image is taken from [3]. *Right:* A picture of a single WCD tank instrumented by three PMTs and filled with $12\,000$ liter ultra-pure water. The picture was taken by the author.

than 2 km. The electromagnetic shower component is further fed by photons γ and positrons and electrons $e^\pm$ through muon-induced pair production and bremsstrahlung.

2.6.2. Surface particle detectors

The final state particles of these shower components, that are μ, e, γ, protons p, neutrons n, and also mesons and neutrinos ν, can be detected on the surface of the Earth with particle detectors such as scintillators (plastic scintillators, crystals), gas (drift chambers) and liquid volumes (WCDs), or even with semiconductors (High-purity germanium or silicon). Cosmic ray and gamma-ray observatories that employ these techniques are for example the Pierre Auger Observatory, the Telescope Array and the High-Altitude Water Cherenkov observatory (HAWC).

The Pierre Auger Observatory is located in the Pampa Amarilla in Western Argentina close to the natural border to Chile embodied by the Andean Mountains on an altitude between 1340 m and 1610 m – with an atmospheric bulk of $875\,\mathrm{g\,cm}^{-2}$ on average. The Surface Detector (SD) of the Pierre Auger Observatory consists of 1660 water-Cherenkov tanks spread over $3000\,\mathrm{km}^2$. The SD-stations form an isosceles triangular pattern with a nearest-neighbor distance of 1500 m and a smaller array with an equilateral separation distance of 750 m. The former, also known as SD-1500, reaches full sensitivity at energies above $10^{18.5}$ eV, the latter, SD-750, extends the threshold down to energies as low as 10^{17} eV. With an uptime close to 100 % each SD-station is running autonomously. A solar panel regularly recharges two 12 V batteries connected in series. This system is providing a power of 10 W on average for the electronics in each station. Three PMTs with a cathode diameter of 9 inch each (22.86 cm) face down into $12\,000$ liter ultra-pure water, measuring Cherenkov light emitted by charged particles in the medium [3]. The left-hand side of figure 2.6 shows a map visualizing the positions of all 1660 WCDs, while its right-hand side shows a picture of a single water-Cherenkov tank.

The Telescope Array with its 507 SD stations is using $3\,\mathrm{m}^2$ plastic scintillators, read-out by wavelength-shifting (WLS) fibers and PMTs. With a mean altitude of 1.4 km above sea level,

the SD of the Telescope Array reaches full efficiency for energies above 10^{19} eV and zenith angles smaller than $45°$. The stations are spread on a square grid with 1.2 km spacing covering an area of approx. 700 km^2 of the Utah desert, 200 km south-west of Salt Lake City, UT, USA. Every station consists of two layers of plastic scintillators. Per layer 104 WLS fibers are guided to one PMT. Both PMTs are read-out by 12 bit 50 MSa s^{-1} analog-to-digital converters (ADCs) individually. A solar system is providing power for the PMTs and electronics, letting each station work autonomously [25].

HAWC was designed for multi-TeV hadron and gamma-ray air showers. It consists of 300 WCD covering an area of 0.022 km^2. Each detector is filled with $188\,000$ liter ultra-pure water and instrumented by three 8 inch PMTs and one 10 inch PMT. The observatory is located at an altitude of 4.1 km in the Pico de Orizaba National Park in Mexico [26].

Many other observatories exist that are laid out to detect the footprint of extensive air showers on the ground. However, because of the stable and well-known spectral flux of cosmic muons, especially those of low-energetic air showers, these particles are also perfect candidates for calibration of detectors that are not designed for air shower detection, such as the Compact Muon Solenoid (CMS) at the Organisation européene pour la recherche nucléaire – Organization for Nuclear Research (CERN) [27].

2.6.3. Electromagnetic emission

Secondary particles of electromagnetic origin also initiate photons in the visible range through two independent mechanisms. The first mechanism is the production of air-fluorescence light [28]. The molecules in the Earth atmosphere are excited and emit photons in the ultraviolet (UV) range on de-excitation through electron transitions, dominantly the second positive system of diatomic nitrogen N$_2$ 2P, yet also the first negative system of ionized diatomic nitrogen N$_2^+$ 1N [29]. The photon emission follows discrete emission lines with the most probable transitions between 0-0, 0-1, 1-0, and 0-2 levels, sorted in decreasing order, corresponding to wavelengths of 337.1 nm, 357.7 nm, 315.9 nm, and 380.5 nm, respectively, which make up two thirds of the observed photon emission [30]. The radial emission is isotropically distributed, making it possible to observe the longitudinal evolution of an air shower from all directions. The light yield per MeV deposited energy is about 11 photons [28]. Due to the isotropic light production, single optical detectors only observe fractions of the light. Consequently, only air showers initiated by cosmic rays of the highest energies can be triggered efficiently.

The second mechanism is the production of air-Cherenkov photons [31]. Due to the Cherenkov effect, charged particles that move faster than the speed of light in a medium with refractive index n generate photons. The Cherenkov condition is therefore

$$\beta > n^{-1}. \tag{2.2}$$

With the definitions of the Lorentz factor γ and Energy-mass-momentum relations from special relativity, the Cherenkov condition can be written as

$$p\,m^{-1}\,c^{-1} > \left(n^2 - 1\right)^{-1/2}. \tag{2.3}$$

Cherenkov photons are emitted in a cone with an opening angle θ described by the relation $n\,\beta = \cos^{-1}(\theta)$. The faster the particles get through β and/or the opaquer the medium gets through n, the larger the angle θ becomes. In air at sea level, i.e. $n - 1 = 3 \cdot 10^{-4}$, the lower energy threshold is $p\,m^{-1}\,c^{-1} \gtrapprox 40$. For muons µ, and electrons e, and their anti-particle
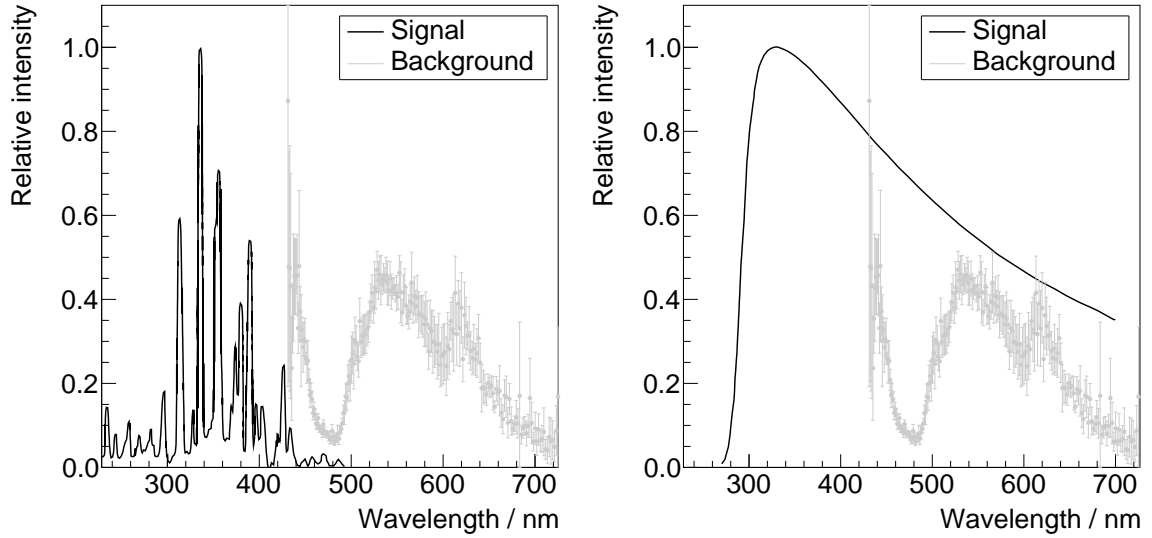
Figure 2.7.: Light emission in extensive air showers. *Left:* air-fluorescence spectrum through N_2 and N_2^+ emission, from [29]. *Right:* Cherenkov spectrum simulated for observation at 2200 m above sea level with atmospheric O_2 and O_3 absorption below 300 nm, from [32]. The spectrum of the night-sky background above 440 nm as observed from Aachen, Germany on 27th/28th June 2018, in grey.

partners this leads to momenta limits of about $4\,\text{GeV}\,c^{-1}$ and $20\,\text{MeV}\,c^{-1}$ in air, respectively. Confer with water, i.e. $n-1 = 0.33$, yielding $p\,m^{-1}\,c^{-1} \gtrsim 1$, thus $100\,\text{MeV}\,c^{-1}$ and $500\,\text{keV}\,c^{-1}$, respectively.

Cherenkov photons in air are boosted within a small solid angle $\theta < 1.4°$ which lowers the energy threshold of telescopes compared to the detection of air-fluorescence light significantly. The spectral radiation of air-Cherenkov light is continuous with $dW/d\lambda \propto \lambda^{-3}$ with a cut-off below 300 nm due to molecular absorption by dioxygen and trioxygen in the atmosphere [31], O_2 and O_3.

Figure 2.7 shows the normalized, relative spectral photon emission of the air-fluorescence and air-Cherenkov effect, the latter for an observation height of 2200 m, superimposed with an estimated night-sky spectrum for Aachen, Germany, obtained by the author of this thesis. Although strongly smeared out, the lines observed in Aachen below 440 nm and at 545 nm, as well as at 615 nm were most probably due to Hg I originating from mercury lighting, and Na I pollution from high-pressure and low-pressure sodium lamps in the atmosphere [33, p. 31 tab. 14] – so urban lighting in general [34]. The setup was not sensitive to UV light – however, through the detection of the Hg I and Na I lines, estimations can be made on the night-sky spectrum in the near UV with the help of literature. Also, this measurement indicates that telescopes can benefit from UV passing filters when they are operated near a city like Aachen for both cases: the air-fluorescence and the air-Cherenkov use case.

2.6.4. Optical telescopes

While the air-fluorescence spectrum is found in the deep to near UV light range only, photons emitted through the Cherenkov effect are also found in the visible light range, i.e. blue to red. For air-fluorescence detection, telescopes are typically equipped with UV passing filters to
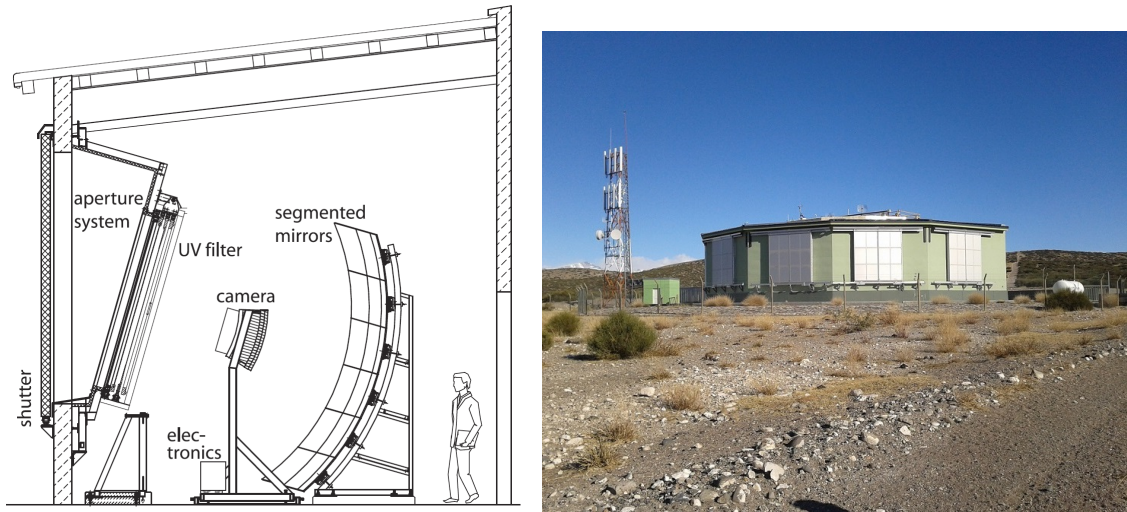
Figure 2.8.: *Left:* A sketch of a single air-fluorescence telescope of the Pierre Auger Observatory. The light enters from the left through the aperture and UV passing filter, gets reflected on the mirror, and is detected by the 440-pixel PMT camera. Taken from [3]. *Right:* A picture showing the building at one of the four FD sites which hosts six air-fluorescence telescopes. Taken by the author.

eliminate diffuse night-sky background photons in the green and red due to oxygen in rural areas, and due to mercury and sodium in urban regions, as discussed earlier.

Light emitted through the air-fluorescence or air-Cherenkov effect is typically detected collaterally [35]. Nonetheless, the design of telescopes explicitly constructed for air-fluorescence measurements differ from those for air-Cherenkov: Air-fluorescence telescopes in the Schmidt design offer apertures with a large field of view through spherical mirrors [36]. UV passing filters allow to record a significant fraction of the UV-dominated air-fluorescence light. While air-Cherenkov photons are emitted within a few degress only (see earlier discussion), the design of air-Cherenkov telescopes, e.g. Davies-Cotton or Schwarzschild-Coudé, aims for a small field of view but a high angular resolution, see for example [37]. Experiments that make use of the air-fluorescence or air-Cherenkov technique are the Pierre Auger Observatory, the Telescope Array, and the Major Atmospheric Gamma-Ray Imaging Cherenkov (MAGIC) project among many others.

The Fluorescence Detector (FD) of the Pierre Auger Observatory consists of 24 telescopes which overlook the SD-array from four different locations. Six telescopes are operated at each location. The light enters through a Schott MUG-6 UV passing filter. The light is collected at a $13\,\mathrm{m}^2$ segmented spherical mirror. A matrix of 22×20 PMTs of type Photonis XP3062 transforms the light into an electrical signal. The XP3062 is an 8-stage PMT with a peak quantum efficiency of 25 %, and 40 mm pixel size corresponding to 1.5° field-of-view per pixel. Figure 2.8 shows a sketch of a single air-fluorescence telescope of the Pierre Auger Observatory and a picture of a building hosting six telescopes in total. The event rate is approx. 12 mHz per FD site, i.e. per six telescopes [3]. In the case of a hybrid shower reconstruction – i.e. SD and FD combined – the energy resolution is about 8 % and the resolution on X_{max} better than $20\,\mathrm{g\,cm}^{-2}$. About three to 30 well-reconstructed hybrid events can be found daily per site, depending strongly on the quality and lengths of nights, i.e. summer or winter. The High

Elevation Auger Telescopes (HEAT) extension is made up by three additional air-fluorescence telescopes operated at a single FD location yet tilted by 30° upwards compared to the regular FD telescopes. In combination with the SD-750 infill array, the HEAT extension allows for air shower measurements down to 10^{17} eV. The total event rate of the HEAT extension is about 26 mHz [3]. The FD locations became operational between 2005 and 2007 – the HEAT telescopes in 2009 [3].

The Telescope Array has also adopted the air-fluorescence technique at three locations surrounding its SD array. Fourteen telescopes have been installed at the location in the north-west which originated from the High Resolution (HiRes) Fly's Eye experiment. The other two locations inhabit twelve newly designed air-fluorescence telescopes each. Like the air-fluorescence telescopes of the Pierre Auger Observatory, the new Telescope Array FD telescopes are made of spherical mirrors and PMTs in the *multi-faceted eye* design for which the HiRes Fly's Eye experiment was known for. The aperture of every telescope scales to $6.8 \, \text{m}^2$ and every camera consists of 16×16 pixels with a field of view of 1° per pixel. Two cameras are stacked on top of each other leading to a total field of view per location of $30° \times 108°$. The design is optimized for the detection of air-fluorescence light at primary energies of 10^{20} eV at a distance of 30 km [38]. The low-energy extension TALE extends the field of view up to about 60° in elevation by using ten additional tilted telescopes. This lowers the energy threshold down to 4 PeV by making use of the detection of air-Cherenkov light [39].

The two MAGIC telescopes are located on the Roque de los Muchachos, La Palma, Canary Islands, Spain at an altitude of 2.2 km. The MAGIC experiment is designed for the detection of air-Cherenkov light emitted by gamma ray-induced air showers down to 30 GeV [40]. Both telescopes feature 17 m diameter single mirror apertures. The two telescopes are physically separated by a distance of 85 m which allows for stereoscopic measurements increasing the angular and energy resolution and reducing the energy threshold in analyses. The camera holds 1039 pixels made up by PMTs with a field of view of 0.1° each. The electronic read-out system is based on the Domino Ring Sampler (DRS) in version 2 running at $2 \, \text{GSa s}^{-1}$ to $4 \, \text{GSa s}^{-1}$ [41]. In summer 2011 and 2012 the MAGIC-I camera, its trigger system, and the read-out systems of both telescopes were upgraded [40].

2.6.5. Other detection techniques

Other detection principles include the detection of electromagnetic waves of larger wavelengths than visible light, also created during the evolution of the air shower. This is for example radio in the very-high frequency (VHF) band between 30 MHz and 80 MHz [42], and microwaves of a few GHz. Prominent examples of experiment sub-systems that exploit radio and microwave detection are the Auger Engineering Radio Array (AERA) on the one hand and GIGAS and MIGAS [43, 44] on the other. Especially the VHF detection seems to be a very promising addition to the standard methods. A recent analysis on AERA data promises an energy resolution of as good as 17 % [45]. AERA is a $17 \, \text{km}^2$ sub-array employed with radio antennas in the Engineering Array of the Pierre Auger Observatory.

The Pierre Auger Observatory is currently undergoing an upgrade of its major detector systems to increase the duty cycle of its telescopes by up to 50 % and to determine the muon component with ground-based detectors [4, 5]. For this purpose new electronics [46], new detectors [47, 48], new light sensors [49], and new calibration plans [5, 50] have been worked out.

The Upgrade of the Pierre Auger Observatory

The Upgrade of the Pierre Auger Observatory, alias AugerPrime, refers to several enhancements of the Pierre Auger Observatory. It covers five major upgrade tasks:

1. a new detector subsystem – the Surface Scintillation Detector (SSD) – which will be installed in the $3000\,km^2$ array to get a hand on a second composition sensitive quantity

2. new electronics – the Upgraded Unified Board (UUB) – which allows for faster sampling, a better sampling resolution, and increased linearity through SSD

3. a new small-sized vacuum photomultiplier tube (PMT) – the small PMT (SPMT) – for an extended dynamic range of the water-Cherenkov detectors (WCDs) to sample secondary particles near the shower core without saturation

4. explicit muon detectors in the infill array – the Auger Muons and Infill for the Ground Array (AMIGA) extension – to crosscheck the performance of the SSD–WCD combination

5. and an extended duty cycle for the Fluorescence Detector (FD).

The author will go into details about the SSD system and the UUB electronics as these are critical for the work done in this thesis and briefly outline the remaining upgrade plans, i.e. SPMT, AMIGA and the duty cycle upgrade to complete this chapter. The information presented here has been shown and published in proceedings of the International Cosmic Ray Conference (ICRC) in 2015 and in 2017 and can be found here [4, 5, 46, 47, 48, 49, 50].

3.1. The Scintillator Surface Detector

To obtain a second composition-sensitive observable, i.e. the number of muons in a given air shower on ground level, the Pierre Auger collaboration chose a second detector to complement the existing Surface Detector (SD) – the SSD. These new detector elements will be installed on top of every single WCD in the field, i.e. 1660 in total. As the name suggests, SSD features

plastic scintillators to detect secondary air shower particles. The idea is to use detector simulations that are rich in detail to obtain the number of muons from both, the WCD and the SSD signal as those two systems respond differently to muons and electromagnetic air shower particles.

3.1.1. The matrix inversion method

The reconstruction of the muonic and electromagnetic fluxes F_μ and F_ϵ expressed in units of $\text{VEM} \cdot \text{m}^{-2}$, i.e. Vertical Equivalent Muons per square meter, from the measured signals in the two detectors S_1 and S_2 can be achieved by a linear superposition of the type

$$\begin{pmatrix} S_1 \\ S_2 \end{pmatrix} = \mathscr{A} \begin{pmatrix} F_\epsilon \\ F_\mu \end{pmatrix} = \begin{pmatrix} \lambda(\theta) \cdot A_1 & A_1 \\ \beta(\theta) \cdot A_2 & A_2 \end{pmatrix} \begin{pmatrix} F_\epsilon \\ F_\mu \end{pmatrix}. \tag{3.1}$$

A_1 and A_2 are the horizontal areas of the two detectors. $\lambda(\theta)$ and $\beta(\theta)$ describe the normalized electromagnetic fraction in the signal of the first and second detector, respectively. In general, they depend on the detector and shower geometry through the zenith angle θ. For two identical detector geometries placed on top of each other, the matrix elements can be obtained analytically [21]. In the case of the Upgrade of the Pierre Auger Observatory let $S_1 \equiv S_{\text{SSD}}$ be an SSD element on top and $S_2 \equiv S_{\text{WCD}}$ be the WCD tank, and correspondingly $A_1 \equiv A_{\text{SSD}}$ and $A_2 \equiv A_{\text{WCD}}$. Then parameter $\beta(\theta) = \cos(\theta) + 0.42 \sin(\theta)$ becomes unity in the case of vertical incidence, $\theta = 0°$. Parameter $\lambda(\theta)$ needs to be derived from detector simulations.

If the determinant of the matrix $\mathscr{A}$ exists, the inversion of $\mathscr{A}$ can be calculated through its adjugate and its determinant. Through the inversion of $\mathscr{A}$, the muonic and electromagnetic fluxes F_μ and F_ϵ can be obtained from the measured signals S_1 and S_2. For the muonic signal in the WCD, it follows from above that

$$S_{\text{WCD},\mu} = A_{\text{WCD}} \cdot F_\mu = \delta(\theta) \cdot S_{\text{WCD}} - \gamma(\theta) \cdot S_{\text{SSD}} \tag{3.2}$$

with the definitions

$$\delta(\theta) \equiv \frac{\lambda(\theta)}{\lambda(\theta) - \beta(\theta)} \tag{3.3}$$

and

$$\gamma(\theta) \equiv \frac{\beta(\theta)}{\lambda(\theta) - \beta(\theta)} \cdot \frac{A_{\text{WCD}}}{A_{\text{SSD}}}. \tag{3.4}$$

Simulations [2] show that the coefficients δ and γ depend only slightly on primary mass, primary energy, core distance, zenith angle, and hadronic simulation model. δ can be found between 1.4 and 1.5 and γ between 1.1 and 1.2 for stations near the shower core, i.e. for those with a radial distance smaller than 1200 m, and energies above 3 EeV [2]. S_{WCD} is expressed in units of VEM, vertical equivalent muons, and S_{SSD} in units of MIP, minimal ionizing particles.

In principle, the matrix inversion method could be applied on single stations of a given air shower event. The merit factor as defined in equation (2.1) for differentiating between proton and iron on the single station level becomes $f_{\text{MF}} < 1$ at a distance of 800 m from the shower core and energies above $10^{19.5}$ eV [2]. This follows from the single station muon number resolution of only 20 % to 30 %. After introducing a parameterization of the muon lateral distribution function (LDF) and applying the matrix inversion method afterward, statistical
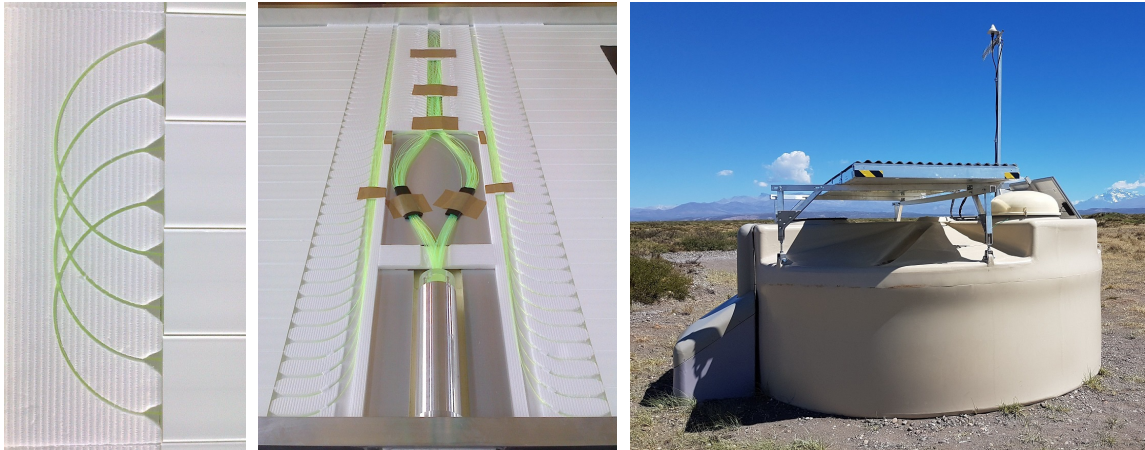
Figure 3.1.: *Left:* The guiding of the WLS fibers through the scintillator bars. *Center:* The central part of the detector with the WLS fibers being guided on the cookie shielded by the metal tube, cf. with figure 3.2. *Right:* A single SSD element installed on top of a WCD. The scintillator area measures $3.8\,\mathrm{m}^2$. 48 WLS fibers are guided through the scintillator bars to a single PMT. All pictures were taken from [4, 47].

uncertainties can be reduced significantly due to the increased amount of SD stations that are considered in the fit procedure. Usually, the LDF is evaluated at a distance of $800\,\mathrm{m}$ or $1000\,\mathrm{m}$, i.e. $S_{\mathrm{WCD},\mu}(800)$ or simply $S_\mu(800)$. The reason to choose this distance is that the resolution worsens for larger shower core distances as the signal size decreases. On the other hand, the signal close to the shower core itself is typically dominated by electromagnetic particles and choosing the estimator there will reduce the effectiveness of the matrix inversion method. Applying the LDF lets the merit factor increase to more than 1.5 for energies above $10^{19.5}$ eV making iron and proton primaries more differentiable than on the single station level. The results presented here assumed that $\delta(\theta), \gamma(\theta) = \delta, \gamma = \mathrm{const}$. The inclusion of dependencies on zenith angle θ and shower core distance leaves room for improvement [2].

3.1.2. Technical details

One SSD element is based on plastic scintillators read-out by WLS fibers which are guided to a photosensitive device. With this technique, a sufficient fraction of the light emitted by the plastic scintillator can be picked up by a single highly-dynamic photosensitive optoelectronic device, e.g. a PMT. This design drastically reduces costs compared to a system which for example reads-out all fibers individually. All SSD elements will be built in Europe, e.g. in Aachen, Germany, transported to Argentina, and set up in the array within the timespan of a few years. The pre-production started in 2016, and the production is expected to be fully efficient in 2018. Figure 3.1 shows pictures of the inner part of the detector and an SSD demonstrator deployed on top of a WCD in Argentina.

One SSD station is made of two mechanical wings. Both wings contain 24 extruded scintillator bars each, i.e. 48 bars in total. The dimensions of a single bar are $1600\,\mathrm{mm} \times 50\,\mathrm{mm} \times 10\,\mathrm{mm}$. The scintillator bars were manufactured by Fermi National Accelerator Laboratory, IL, USA. Two holes were drilled into each bar through which the WLS fibers are guided. In total there are 48 WLS fibers which are each $5.8\,\mathrm{m}$ long with $1\,\mathrm{mm}$ diameter and of type Kuraray Y11(300)M,S.
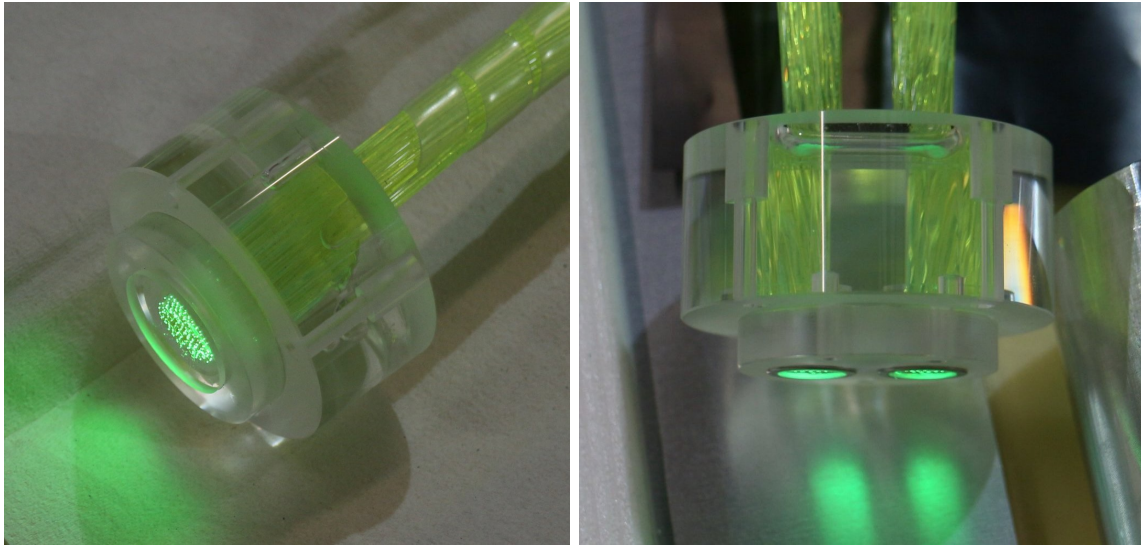
Figure 3.2.: This figure shows pictures of two variants of the so-called *cookie* that fixes all 96 fiber ends in front of the opto-electronic device. *Left:* The PMT-version of the baseline design and *right:* the SiPM-version. The fiber bundle was split in two for the latter variant to match the size of two SiPMs. Both pictures were taken from [51].

These fibers collect the ultraviolet (UV)/blue scintillation light emitted by the plastic scintillators after excitation through secondary particles of air showers and *shift* the energy of the photons down to the blue/green waveband. A fraction of the wavelength-shifted photons is trapped and travels along the fiber finally leaving the plastic scintillator. All 96 fiber ends are collected on a single point, fastened in a *cookie* that is made of acrylic glass, polymethyl methacrylate (PMMA), with optical cement. Figure 3.2 shows pictures of such *cookies*. The figure shows two variants of the *cookie*. The left picture is the baseline design and fits to the entrance window of the PMT R9420 manufactured by Hamamatsu Photonics [52]. On the right-hand side, the *cookie* splits the fiber bundle equally in two to match the limited size of two SiPMs of type S13360-6025PE [53], i.e. two times $6\,mm \times 6\,mm$. The signal of both SiPMs is planned to be summed up in the front-end electronics which will be discussed in a subsequent chapter of this thesis. The optics of the *cookie* were optimized to their respective optoelectronic device – for both cases individually. In the case of the SiPM-*cookie* whose optimization was more tricky, the simulations and laboratory measurements were published in [54]. The optoelectronic device is enclosed by an aluminum tube, shielding the device from possible detector light leaks and electromagnetic interference, and a mechanical spring holds the device in place. Depending on the detector revision, either connectors or cable feed-throughs route the signal and slow control cables out of the detector.

The left-hand side of figure 3.3 shows the non-attenuated emission spectrum of the scintillator bars and the absorption spectrum of the WLS fibers. Its right-hand side shows the emission spectrum of the WLS fibers attenuated by $3\,m$, folded with the quantum efficiency of the PMT used in the baseline design, as well as with the photon detection efficiency of the S13360-6025PE SiPM without any efficiency losses in the optical coupling. Note, that the scintillator bars are not transparent to photons below approx. $400\,nm$ which amounts to about half of all
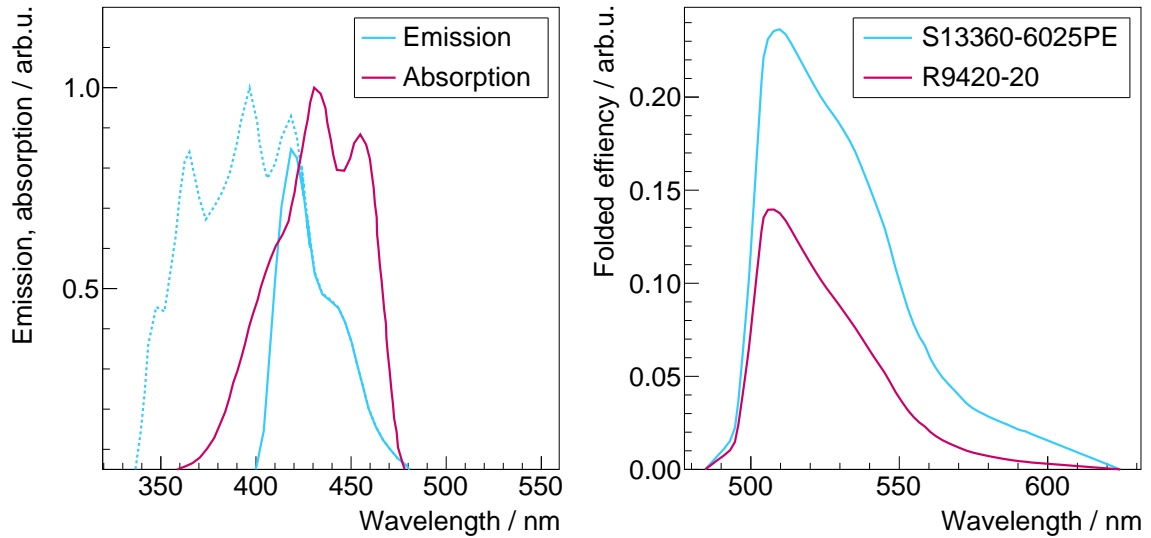
Figure 3.3.: *Left:* The pure emission spectrum of the scintillator bars (blue dashed) [55] together with the absorption spectrum of the WLS fibers (red solid) [56]. The emission spectrum is folded with the scintillator transmittance (blue solid) which leads to absorptions below 400 nm. *Right:* The wavelength shifted emission spectrum of the Kuraray Y11(200) WLS fibers attenuated by 3 m [56] folded with the spectral quantum efficiency of the Hamamatsu R9420 PMT (red solid) [52], and separately with the photon detection efficiency of the Hamamatsu S13360-6025PE SiPM (blue solid) [53].

fluorescence photons. Nevertheless, all components were chosen such that their optical spectra ideally match each other's: The emission spectrum of the scintillator bars can be picked up quite well by the wavelength-shifting fibers as a significant fraction of their absorption spectrum overlaps with the emission spectrum of the scintillator bars. The emission of the WLS fibers lies within the wavelength-dependent quantum efficiency of the R9420 PMT. However, the integrated efficiency of an SiPM, i.e. the integral over the curves in the right-hand side of figure 3.3, is about twice as large when an ideal optical coupling is considered.

The scintillator bars, WLS fibers and the optoelectronic device, i.e. the PMT in the baseline design, are sheltered by an aluminum enclosure which can be seen in the picture in figure 3.1 on the right. The aluminum shields the light-sensitive components from the environment and protects them from degrading and aging. An undulated roof optimizes heat transport and serves as a water drain.

3.2. The Upgraded Unified Board (UUB)

The electrical signal of the SSD's optoelectronic device is amplified by up to three individual channels with independent amplification gain and finally digitized individually by individual fast analog-to-digital converters (ADCs). When the signals of the stations meet the requirements of the local trigger conditions, a timestamp is generated and sent to the central data acquisition (DAQ) system. The digitized event is stored and, when a global trigger condition is met, the station waits for further data handling by the central DAQ system. Including the power
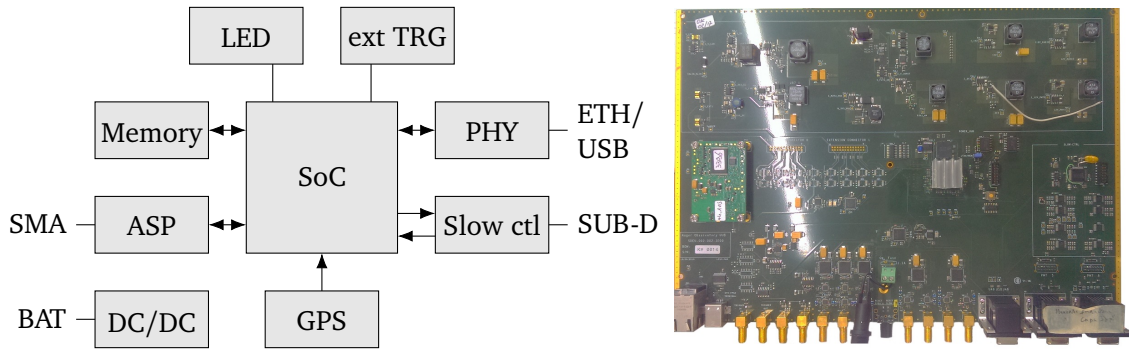
Figure 3.4.: *Left:* An oversimplified schematic sketch of the UUB as of December 2017. ASP: analog signal processing. SMA: Sub miniature A connector. BAT: battery. PHY: physical interfaces. ETH: Ethernet. TRG: Trigger. *Right:* A picture of one UUB from the pre-production batch as of March 2017, developed by the Pierre Auger collaboration [46]. The sketch on the left was depicted from the detailed schematics of the UUB that is available for members of the Pierre Auger collaboration. The picture on the right was taken by the author during an installation campaign in Argentina in March 2017.

control of the optoelectronic device, all this is done or initiated by the UUB, see figure 3.4. The UUB is an updated version of the Unified Board (UB) which is currently being installed at the 1660 WCDs, making the UB obsolete. A more practical reason, other than having more powerful electronics than before, is that the UB only featured ADCs for the three WCD PMTs. The UUB, on the other hand, can operate the new detector systems as well as the WCD PMTs.

3.2.1. Pre-amplifiers and ADCs

To gain from the new ADC's sampling rate of $120\,\mathrm{MSa\,s^{-1}}$ in contrast to the UB's $40\,\mathrm{MSa\,s^{-1}}$, the pre-amplifiers, which were initially bandwidth-limited to approx. $20\,\mathrm{MHz}$ in accord with the Nyquist-Shannon sampling theorem, needed to be replaced. Therefore, and to make the UUB inputs more universal, the WCD pre-amplifiers are bridged, and the UUB holds pre-amplifiers for every channel instead. In the design as of December 2017, the UUB features ten ADC channels – two for every WCD PMT split in high and low pre-amplifier gain, up to two for the small PMT, and two for the SSD optoelectronic device, again split in high and low pre-amplifier gain. As the SPMT is only used for high dynamic applications, e.g. events with shower cores near the station, the second SPMT channel is not in use. As of December 2017, it is discussed to use it as a third SSD channel. In the scope of this thesis, the channel is used for the third SiPM channel which will be introduced in a subsequent chapter.

The motivation behind the two-gain settings, low and high, is merely a matter of limited digital resolution and electronic noise. The high gain channel is used to increase the signal-to-noise ratio (SNR) of small signals, e.g. single particle events, like single muons. Monitoring the single muon events and expressing the muon flux in units of single muons, see section 3.1.1, allows to suppress effects in the analysis like temperature variation, aging and so on.

The pre-amplifier design is a two-stage single-ended to differential topology with anti-aliasing filters. The input is terminated with $50\,\Omega$. The first amplifier stage transforms the pseudo-differential single-ended input into a truly-differential signal and amplifies the signal with a

channel dependent gain. A differential band-pass filter follows, whose $-6\,\mathrm{dB}$ corner frequencies are about $3.3\,\mathrm{kHz}$ and $60\,\mathrm{MHz}$. An offset is added. During normal operation, the PMT signal is expected to be a pulsed direct current (DC). That means that the signal is pulsed only in one direction with reference to ground, in contrast to alternating current (AC) that is defined over an equal amount of charge transported in either direction with reference to the common potential. Therefore, an offset is implemented which shifts the baseline close to the upper dynamic range of the ADCs' $2\,\mathrm{V}$ dynamic to make use of almost the full $12\,\mathrm{bit}$. The second differential amplifier stage drives the input of the ADC and amplifies the signal differentially, thus ignoring the DC level of the offset, with a channel dependent gain.

Please note, that the UUB signal input system was still in the prototype phase and was improved continuously by the UUB front-end experts. The measurements shown in the following chapters are taken with various revisions of the UUB. The author will point out the critical changes in the specific topics if necessary. As of December 2017, the absolute amplification factors of the pre-amplifier channels are $0\,\mathrm{dB}$ for the low-gain channels of the WCD and the SPMT, $-12\,\mathrm{dB}$ for the SSD low-gain channel, and $30\,\mathrm{dB}$ for all high-gain channels. In the case of the SiPM-version, the gain was changed to $0\,\mathrm{dB}$ for the two SSD channels and the second SPMT channel because the SiPM module developed in this work already hosted pre-amplifiers.

The ADCs, type AD9628 by Analog Devices, digitize the analog voltages and are read-out by a field-programmable gate array (FPGA). The data is stored in memory. The FPGA is manufactured by Xilinx and of type Z-7020 which features a Dual-core ARM Cortex-A9 hardware-implemented central processing unit (CPU) which runs a Linux operating system. The FPGA features firmware-implemented code programmed in Verilog, i.e. everything that runs on the FPGA logic blocks, e.g. triggers, as well as software-implemented C++ code which is operated by the Linux system, e.g. calibration routines.

3.2.2. Trigger

The trigger is implemented in digital logic. The trigger logic of the old UB has been emulated in the UUB meaning that the data is artificially sampled down and filtered to $40\,\mathrm{MSa\,s^{-1}}$. The current implementation of the local trigger in the UUB includes a simple threshold trigger, a time-over-threshold trigger (ToT) and the multiplicity of positive steps (MoPS) trigger [46]. Due to increased logical power, the new FPGA allows for the adaption of new trigger topologies and coincidence triggers between the WCD and SSD. The UUB also features an external low-voltage transistor-transistor logic (LVTTL) trigger input, physically implemented with a $50\,\Omega$ terminated sub-miniature version A (SMA) connector. By using a dedicated transistor circuit, the FPGA drives a $50\,\Omega$-optimized line from which the trigger master can be tapped.

3.2.3. Slow control

A microcontroller of type Texas Instruments MSP430 supervises the UUB. It enables and disables voltages for biasing the PMTs, for the communication antenna, and for the FPGA. The microcontroller checks for power failures, monitors the electrical current and voltages of all significant power rails, and reads out the temperature sensors. During normal operation, the microcontroller communicates with the FPGA via $\mathrm{I^2C}$ – a high-speed serial bus with a clock line provided by the master and a data line which is shared by the master and the slave. The aforementioned observables, voltage, current, temperature, etc. are made available through this bus and sent to the central DAQ system by the FPGA. The microcontroller also features

a dedicated universal asynchronous receiver-transmitter (UART) bus – a simple asynchronous serial communication interface – which is connected to an FTDI FT232R Universal Serial Bus (USB) interface.

Standard HD-SUB 15 connectors link the PMT bases (12 V supply, reference command voltage, high-voltage monitor, current monitor, temperature monitor) with the UUB. The PMT bases generate the PMT high-voltage from the 12 V themselves which on the other hand is regulated according to the reference command voltage, supplied by the slow-control of the UUB.

3.2.4. PHY USB & Ethernet

The UUB also features a USB and an Ethernet interface which is routed to the CPU of the FPGA. That means that the Linux operating system can access USB and Ethernet directly. USB and Ethernet allows communications with other computers through Ethernet or with slave devices through USB, such as USB memory sticks. The SiPM module developed for SSD makes use of the USB connection instead of the slow control HD-SUB 15 connectors and is thus not supervised by the microcontroller. Its motivation will be explained in a subsequent chapter. The Linux operating system runs a web server which shows a live view of the slow-control data, locally triggered ADC traces, and so on. This interface is helpful for debugging and monitoring of the detectors on site, i.e. in the Argentinean Pampa.

3.2.5. Miscellaneous

The UUB holds many other components which are only used indirectly and can be considered as is. This includes the power supply of the UUB. Supplied by two 12 V-nominal lead-acid batteries in series, thus nominal 24 V, the UUB hosts direct-current-to-direct-current (DC/DC) switching converters which generate all the voltages needed by the UUB and the detectors connected to it. Depending on the charge of the batteries and the power load, the voltage across the batteries can easily vary between 19 V and 32 V. Under-voltage and over-voltage sets power failure conditions which prompt the microcontroller of the slow control.

Time synchronization is implemented with a global positioning system (GPS) module. The LLC I-Lotus M12M receiver features an intrinsic device accuracy of roughly 2 ns which is well below the Upgrade requirement of about 5 ns.

A light emitting diode (LED)-controller is available, too. LEDs can be connected externally and driven by the UUB. This is useful when LEDs are installed in the SD subsystems like SSD or WCD. Although the LED-controller is not calibrated, i.e. the number of photons per pulse versus digital value is not known as this depends explicitly on the LED, on temperature, and the like, photon pulses can be used to check the detector and to identify a broken PMT.

3.3. Further upgrade plans of the Pierre Auger Observatory

3.3.1. The small PMT (SPMT)

The Pierre Auger Observatory has been operational for several years now, and scientist involved with this project have learned about the advantages and flaws of its detector systems. Simulations show that 20 % of all events with energies above 10^{19} eV contain at least one saturated WCD station. This probability increases to 40 % at energies above $3 \cdot 10^{19}$ eV [2].

Although dominated by electromagnetic particles, and thus not that interesting for muon-electron separation, the particle density near the shower core is the highest. Once the number of particles is reconstructed correctly, the stations closest to the shower core dominate the LDF fit through statistics and are thus of major importance. Today, the signal of saturated stations is tried to be recovered offline. This approach, however, introduces systematics.

To solve this problem, the Pierre Auger collaboration decided to add a fourth PMT to every WCD – the SPMT. Model Hamamatsu R8619 was chosen. With 1 inch, the photocathode of this PMT is smaller than that of the three existing 9 inch-WCD PMTs. Naively one expects from the ratio of the photocathode areas of SPMT to the standard PMT, that the SPMT can measure an energy deposit in the WCD that is two orders of magnitude larger. On the other hand, single particle events can not be recorded which means that the SPMT needs to be calibrated with respect to the standard PMT [49]. The dynamic range also depends on the quantum efficiency of the PMT, that is the probability that a photon knocks an electron from the photocathode creating a measurable signal after the dynode multiplication stage. The gain of the PMT also plays a role as the dynamic range of an individual PMT is typically limited by the anode current which depends on the gain. It is expected that the dynamic range extends from about 1000 VEM in the case of the large WCD PMTs to more than 20 000 VEM for the SPMT. This means that events above $10^{19.5}$ eV could be sampled at distances down to 250 m instead of only 600 m without saturation [49].

3.3.2. Auger Muons and Infill for the Ground Array (AMIGA)

Using a scintillator detector on top of the WCDs and applying the matrix inversion method seems to be complicated and not the logical choice for determining the muon component of an air shower on the single shower level. One could, for example, deploy a large-sized detector underneath the WCDs as proposed by the Aachen Muon Detector (AMD)-group [57] to shield a significant fraction of the electromagnetic component directly. Another approach is that the detector could be buried in the ground to get rid of all electromagnetic particles. This is the idea behind the underground muon detector system of AMIGA [48].

Deployed in the infill area of the Pierre Auger Observatory, an array of 23.5 km^2, AMIGA consists of 30 m^2 underground muon detectors and accompanying standard WCDs. This combination is used to validate the matrix inversion method applied to SSD and the WCD by directly measuring the muon density of given air showers.

The underground muon detectors are buried 2.3 m deep next to the WCD. Based on plastic scintillators, these detectors are made of 64 scintillator strips with embedded wavelength shifting fibers. Initially designed for the 64 multi-anode PMT from the Hamamatsu H8804 series [3], the concept was changed in favor of a SiPM-based read-out [58].

3.3.3. Duty cycle upgrade of the Fluorescence Detector (FD)

Measurements in the laboratory have shown that the up-time of the FD telescopes could be increased by extending their operation into time intervals with high variance, i.e. brighter nights. During such periods the high voltage of the PMTs must be reduced to avoid high anode currents which accelerate aging of PMTs. Two voltage levels are foreseen, a nominal voltage which coincides with today's high voltage setting and a reduced high voltage level. Additional calibration runs will be added throughout the night to guarantee a stable operation, simplifying

offline analyses. With this implementation, the duty cycle of the FD could be increased by 50 % [2].

3.4. This work

This thesis addresses three main topics. First, an optical module was developed based on SiPMs which could replace the PMT-based module in SSD with minimal changes on the detector layout: a cookie needed to be designed holding two WLS fiber bundles instead of one and the amplification factors of the pre-amplifiers in the front-end of the UUB must be changed to unity. The SiPM module must offer a well-known dynamic range of at least 12 000 MIP in the shower front, i.e. within 100 ns, a simple calibration and a stable operation for a detector lifetime of seven years. A low power consumption of less than 500 mW was mandatory to compete with the PMT module.

The second topic is about the development of an optical telescope for the detection of extensive air showers which also featured SiPMs. The requirements to this telescope include a low-cost, small, light-weight and robust design which could easily be transported to distant places like Argentina, yet also to Mexico or even Antarctica. The telescope shall be fully efficient for primary cosmic rays with energies above 100 TeV using the air-Cherenkov detection technique. Arrangements for a telescope upgrade for efficient detection of air-fluorescence light had to be foreseen. In the scope of this work, the electronic system was developed, built, and tested, and the first air showers were recorded with a fully functional 61 pixel telescope.

Finally, characterization studies of SiPMs were carried out – with the focus on the requirements of the two detectors, which are their temperature dependence, gain stability and dynamic range. The results of these studies are described in the succeeding chapter. The developments and first results of the SSD optical module and the telescope were both pre-released in separate journal articles, [54, 59].

Silicon photomultipliers (SiPMs)

Silicon photomultipliers (SiPMs) are cell-structured, photosensitive semiconductors. A single SiPM consists of hundreds to several ten-thousands avalanche photodiodes (APDs) which are operated in Geiger-mode, confer with Geiger-mode avalanche photodiodes (G-APDs). A photon can initiate an avalanche in a G-APD with a probability depending on the photon's energy, the substrate structure of the G-APD, either p-on-n or n-on-p, and on its gain. The G-APD breaks down, responds with a standard signal while a series resistor quenches the avalanche.

The waveband of photons that can be detected with at least 5 % efficiency exceeds the human-visible light spectrum. It ranges from 280 nm to 800 nm for modern P-on-N silicon processed SiPMs [60]. All G-APDs are arranged on a quadratic grid and electronically connected in parallel. The output signal of an analog SiPM is the sum over all G-APDs – the information about the individual G-APDs that responded with a signal is not preserved. That is why the G-APDs of an SiPM are called *cells* instead of *pixels*.
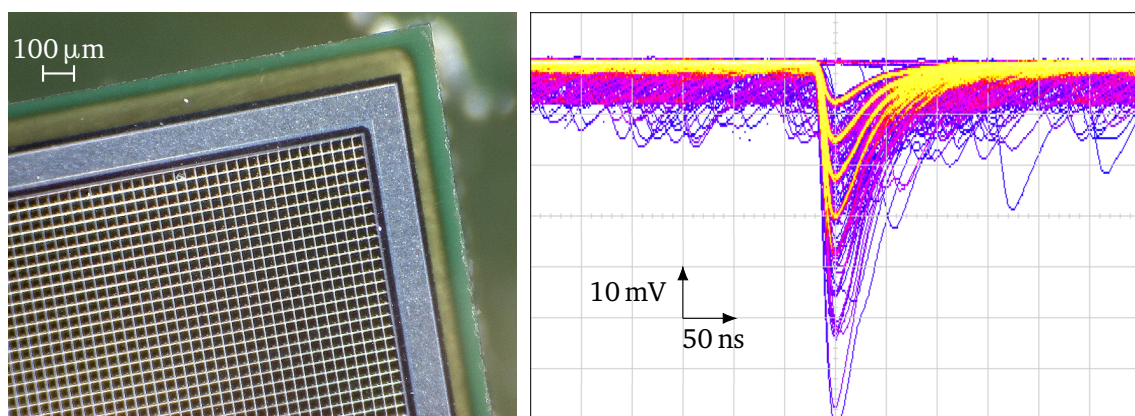

Figure 4.1.: *Left:* A microscope picture of a 6 mm × 6 mm SiPM type S13360-6050PE manufactured by Hamamatsu Photonics with a 50 μm cell pitch. *Right:* A modified, false-colored oscilloscope screenshot of an amplified S13360-6050PE which was exposed to nano-second light flashes. Both images were taken by the author.

Today's single SiPMs typically cover an area of $1\,\text{mm}^2$ up to $36\,\text{mm}^2$ [53] and the cell pitch, that is the center-to-center distance of neighboring cells in the quadratic grid, usually lies between $10\,\mu\text{m}$ and $100\,\mu\text{m}$ [61, 62]. A close-up view of a recent SiPM generation, the Hamamatsu S13360-6050PE [53], is presented on the left-hand side in figure 4.1. A fraction of all SiPM cells and its package housing is visible. Once amplified, the response of the individual SiPM cells can be made visible by connecting the signal to a data acquisition (DAQ)-system while the SiPM is exposed to a pulsed light beam. An oscilloscope screenshot taken with such a setup is shown in figure 4.1 on the right. The SiPM was flashed by a blue light emitting diode (LED), featuring a peak wavelength of $\lambda_{pk} = 390\,\text{nm}$, which was pulsed by a small, nanosecond-long electrical signal. The read-out was synchronized with the LED trigger. The screenshot overlays approx. $100\,000$ events whose abundance is color-coded, increasing from blue to yellow. The response of the SiPM is discrete as indicated by the distinctively colored curves piling up. These are the individual cell breakdowns which are called photon equivalents (pe). The number of photons that are generated by the LED, as well as the number of detected photons by the SiPM, underlie stochastic processes. A spread of several pe is visible.

The discrete response of an SiPM and its utilization allows calibrating the SiPM on the fly, whereas the passive quenching of its cells makes the SiPM optically robust. Both options open new possibilities in photon detection and are exploited in this work.

4.1. Intrinsic and non-intrinsic parameters

In this section, the intrinsic SiPM parameters and their derived quantities are introduced. These are the breakdown voltage and its associated optical and electrical properties, like gain, correlated noise, dark noise, photon detection efficiency (PDE), and dynamic range. The ideal SiPM series and cell size is chosen from the demands of the application. Characterization studies follow at the end of this chapter.

4.1.1. Breakdown voltage

SiPMs are operated with a reverse-bias. When the bias voltage v_b which is applied between cathode and anode of the SiPM exceeds the breakdown voltage $v_\text{bd} < v_\text{b}$, the SiPM enters the Geiger-mode of operation. The excess voltage over breakdown is the overvoltage

$$v_\text{ov} \equiv v_\text{b} - v_\text{bd}. \tag{4.1}$$

Although non-intrinsic, the overvoltage is an essential parameter for the operation of SiPMs. The gain, i.e. electron-hole-multiplication, PDE, and noise directly correlate with the overvoltage. It is, therefore, preferable to keep the overvoltage constant during operation. This makes the breakdown voltage v_bd a fundamental intrinsic parameter of an SiPM through its relation to the bias-dependent overvoltage and needs to be characterized thoroughly.

In [63], it was reported that an avalanche in a single SiPM cell shows two characteristic voltages. The avalanche trigger probability and the cell charge originate in two different voltages. This can be explained qualitatively by the following: While the gain increases linearly with the electric field and thus with the applied voltage, a cell breakdown will not occur until the avalanche multiplication becomes large enough to sustain an avalanche in the cell. The latter is the standard definition of the breakdown voltage. The former is usually known as the *turn-on* voltage and which is smaller than the breakdown voltage [63]. It is thus expected

that different measures like the gain-voltage or the current-voltage measurements return different results as the former is related to the *turn-on* voltage, and the latter to the photodiode breakdown voltage.

4.1.1.1. Homogeneity

The breakdown voltage value itself depends on the structural characteristics of the G-APDs and therefore varies from manufacturer to manufacturer and from series to series.

The average breakdown voltage is for example around 70 V for the Hamamatsu S10362-series, around 50 V for the Hamamatsu S13360-series and 25 V for the SensL J-series [53, 60, 62]. Within a given series, however, the breakdown voltage only varies slightly from device to device. In [64], the breakdown voltages of nearly 150 000 devices of the SensL B-series were determined. A standard deviation in the distribution of breakdown voltages of 73 mV was found which was less than 0.3 % with reference to the mean of the distribution of 24.69 V. Assuming an operation with 5 V overvoltage, it was equal to a spread of ±1.5 % with respect to the gain. Nowadays, the manufacturing process of SiPMs yields an excellent homogeneity. When necessary, SiPMs can be characterized and pre-selected – a task that was also done for this work, see chapter 5 on page 73ff.

4.1.1.2. Temperature dependence

The breakdown voltage of SiPMs is known to be temperature-dependent, see for example [65]. Near room temperature, that is about 25 °C, a polynomial of first degree suffices to describe its increase with temperature, that is

$$v_{\mathrm{bd}}(T) = v_{\mathrm{bd}}(T_0) + \frac{\mathrm{d}v_{\mathrm{bd}}}{\mathrm{d}T} \cdot (T - T_0). \tag{4.2}$$

Like the breakdown voltage itself, its temperature progression factor $\mathrm{d}v_{\mathrm{bd}}/\mathrm{d}T$ depends on the structural characteristics of the G-APDs and similar small variations in its value can be found between devices of the same family. $\mathrm{d}v_{\mathrm{bd}}/\mathrm{d}T$ typically lies between $20\,\mathrm{mV\,K^{-1}}$ in the case of the SensL J-series, and $60\,\mathrm{mV\,K^{-1}}$ for the Hamamatsu S10362 and S13360 family [53, 60, 62].

4.1.2. Gain

The gain g of the SiPM, or more strictly speaking, the mean electron-hole-multiplication of the G-APDs of a single SiPM, is defined over the average charge $\langle q \rangle$ released instantaneously by the SiPM in the event of a single cell breakdown, i.e.

$$\langle q \rangle = \langle g \rangle \cdot e = \langle C_{\mathrm{cell}} \cdot v_{\mathrm{ov}} \rangle \tag{4.3}$$

after introducing the cell capacitance C_{cell} and the elementary charge $e = 1.6 \cdot 10^{-19}\,\mathrm{C}$. $\langle q \rangle$ in this definition does not include correlated noise. The gain of an SiPM is typically in the order of 10^6 at the nominal operating voltage [53] and comparable to that of standard vacuum photomultiplier tubes (PMTs), like the aforementioned Hamamatsu R9420 [52].

4.1.3. Photon detection efficiency (PDE)

The probability for an SiPM to detect a photon is determined by its photon detection efficiency (PDE). When the SiPM is at *rest*, i.e. the SiPM is not saturated due to an intense light flux, the nominal PDE is defined over three parameters: the geometric fill factor ϵ which is the ratio of sensitive to total area of the SiPM, the quantum efficiency (QE) of a single cell, and the avalanche probability p_{av} which describes the chance for a photon to trigger a cell breakdown, thus

$$PDE = \epsilon \cdot QE \cdot p_{av}. \; [65] \tag{4.4}$$

The geometric fill factor ϵ is production intrinsic to the SiPM series and their cell sizes. Neighboring cells need to be geometrically separated to leave room for quenching resistors, electrically conducting traces, as well as electrical isolation. Therefore, SiPMs with the largest cells, e.g. a cell pitch of $100\,\mu m$, have the highest geometric fill factors, e.g. close to $80\,\%$ [62], and hence the highest PDE. Disadvantages of large cells are a limited dynamic range and large signal decay times due to their large capacitance. However, the decay time also depends on the values of the quenching resistors.

A photon can create an electron-hole pair within the G-APD with a probability determined by the photon's energy, the quantum efficiency of the G-APD and its avalanche probability. The last two parameters depend on the substrate structure of the G-APD. Electrons move from the p-region to the n-region, and holes move vice versa. The chance to create an avalanche is the highest for electrons which is why the avalanche probability peaks in the p-layer. Photons with small wavelengths, i.e. ultraviolet (UV) and blue, do not penetrate deep into the silicon. Therefore, a p-on-n structure serves best for UV and blue photons whereas an n-on-p structure maximizes the PDE for red and infra-red photons. The QE peaks around $80\,\%$ and $90\,\%$ [65]. The SiPMs that were used in this work had all been p-on-n type SiPMs, like the Hamamatsu S13360-series [53], the Hamamatsu S10943-series [66] and the SensL J-series [60], as the photo signals were expected in the UV, blue and blue-green wavebands in all applications.

4.1.4. Noise effects

Avalanche cell breakdowns induced by noise can be categorized into random and correlated events. Electron-hole pairs and hence avalanches can be triggered through thermal excitation which happens randomly, and which is the dominating noise effect on long timescales [65]. Correlated noise only occurs once an initial cell has broken down, either through the detection of a photon or preceding breakdowns initiated by random or correlated noise.

4.1.4.1. Random noise

Random noise is typically generated by thermal excitation of electron-hole pairs which happen to initiate an avalanche. This effect is called thermal noise and is usually characterized through the dark count rate, the dark current, or time-difference histograms, see next section. The dark count rate is the trigger rate measured with a threshold of $0.5\,pe$. This quantity however also includes afterpulsing when they exceed the trigger threshold.

The dark current is determined through the average electrical current drawn by the SiPM in darkness. It includes all effects of correlated noise, i.e. afterpulsing and optical crosstalk.

Thermal noise is strongly temperature dependent. The dark count rate approx. doubles every 8 K, which will be presented at the end of this chapter.

The dark noise rate also scales linearly with the bias excess above the breakdown voltage, i.e. the overvoltage. Typical values of thermal noise rates of modern SiPMs are about $20\,\mathrm{kHz\,mm^{-2}}$ to $50\,\mathrm{kHz\,mm^{-2}}$ at room temperature [67], whereas the older SiPM generations suffered from noise rates as high as $1\,\mathrm{MHz\,mm^{-2}}$ [62].

4.1.4.2. Correlated noise

In contrast to random noise, correlated noise requires a preceding cell breakdown. This can either be an avalanche triggered by a photon or any noise event.

Two effects dominate the correlated noise. One is called *afterpulsing*. Through defects in the silicon lattice, free carriers, i.e. holes and electrons, are blocked and happen to initiate an avalanche in the same cell after a short period [65]. This effect is time-correlated. As the cell needs to recover from the first cell breakdown, the effective overvoltage and hence the effective charge released by an afterpulsing event is only a fraction of the nominal charge and recovers exponentially with time. The afterpulsing probability can be minimized when silicon with fewer defects is used, i.e. purer silicon. Typical values, although strongly overvoltage-dependent, range from above 40 % for old SiPM series to less than 1 % for newer series [53, 62]. The effect of afterpulsing is studied in more detail at the end of this chapter.

The second correlated noise effect is entitled *optical crosstalk*. The term *optical* is used to differentiate from electronic crosstalk. Photons are produced in the event of recombination of electrons and holes. These photons can initiate breakdowns in neighboring cells. However, those photons need to be of a longer wavelength to pass through the silicon [65]. The chance for optical crosstalk photons to reach neighboring cells can be reduced by implementing optical trenches between neighboring cells. This process is done in newer SiPM generations, for example in the Hamamatsu S13360-series [53]. The probability for optical crosstalk can be calculated from finger spectra, which is done later in this chapter. It is found, that the crosstalk probability also increases with increasing overvoltage.

4.1.5. Operating point

There is no precise definition for the nominal overvoltage, i.e. the operating point of a given SiPM. For the early generation of SiPMs, the operating voltage could be defined at the point with the best efficiency-to-noise ratio. As the older SiPM series suffered from high noise rates and correlated noise probabilities, the nominal overvoltages were found in the range between 1 V and 3 V [62]. Nowadays, with lower noise contributions, the operating voltage could be set to the point where the PDE flattens. Thereby, if the overvoltage was not stable during operation, e.g. because of temperature variations and in the absence of a voltage-temperature adaption, confer with equation (4.2), the change in overvoltage would not affect the optical efficiency significantly. Typical values are found between 3 V and 5 V [53].

In this context, the temperature progression factor $\mathrm{d}\nu_{\mathrm{bd}}/\mathrm{d}T$ as defined in equation (4.2) in section 4.1.1.2 can be used to identify the change of the gain with temperature. However, this quantity depends on the arbitrary definition of the nominal overvoltage and will not be used here any further, i.e.

$$\frac{\mathrm{d}g}{\mathrm{d}T} \propto \frac{1}{\nu_{\mathrm{ov}}} \cdot \frac{\mathrm{d}\nu_{\mathrm{bd}}}{\mathrm{d}T}. \tag{4.5}$$

4.1.6. Recovery time

After a cell breaks down, it recharges exponentially before it finally reaches full sensitivity again. Meanwhile, the detection efficiency of the cell, as well as its gain, recover with time. This is known as the cell recovery time. The recovery of the overvoltage, for instance, can be parameterized with a single exponential function

$$v_{\mathrm{ov}}(t) = v_{\mathrm{ov}}(t_0) \cdot \left(1 - H(t - t_0) \cdot \exp\left(-\frac{t - t_0}{\tau_r} \right) \right) \tag{4.6}$$

in the presence of a single cell recovery time constant τ_r. $v_{\mathrm{ov}}(t_0)$ is the overvoltage of the cell at the time before the breakdown t_0, and $H(x)$ is the Heaviside function. This function is valid if the SiPM is read-out with a pre-amplifier that has a negligible input impedance R_{in}, i.e. $N \cdot R_{\mathrm{in}} \ll R_q$, with the number of cells N and the mean cell quenching resistance R_q. By studying the parasitic elements of a G-APD, particularly its capacitances and the limited input impedance of the front-end, it stands to reason that at least two time-constants are necessary to describe the recovery of a single cell, see also [54, 68].

4.1.7. Dynamic range

As SiPMs are structured in APDs which are operated in Geiger mode, the single cell output signal is quantized. With a non-zero cell recovery time $\tau_r > 0\,\mathrm{ns}$ and a non-zero dead time, the response of an SiPM is obviously non-linear. In the case of a single cell breakdown, the nominal fill factor of an SiPM with N cells gets reduced by $1/N$. Following the definition of the PDE from equation (4.4), this directly reduces the PDE. For many cells N, or a randomly distributed, yet small photon flux, this effect can be neglected. A small photon flux is defined as either a small number of photons over a short period, e.g. single particle events in a scintillator, or many photons distributed over a long period, e.g. night-sky background.

For a large number of photons that arrive at the SiPM in a short, yet non-zero period $\mathrm{d}t > 0\,\mathrm{ns}$, the individual cell recharge through the cell recovery time τ_r needs to be considered, too, especially when $\mathrm{d}t \lesssim \tau_r$. In applications of wide dynamic range, this effect usually must be corrected for in dedicated analysis software, as the effect depends on preceding photon pulses, i.e. historic volatility.

For more information concerning the parameterization of the dynamic range, measurements studies and algorithms which aim at correcting for the non-linear dynamics, consider [69].

4.2. Equivalent circuit diagram

Figure 4.2 shows an equivalent circuit of an SiPM in the state of $M < N$ simultaneous cell breakdowns at time $t = t_0$. Its parameterization was taken from [70, 71]. N is the number of cells, R_q the quenching resistance, C_q the parasitic quenching capacitance, C_d the cell diode capacitance, and C_g the grid capacitance, see also [68].

All values are taken to be the respective average over all cells. Electric parameters of an SiPM can be obtained through impedance versus frequency measurements of the SiPM, see for example [72], or extracted from single pe pulse shape analyses. The total complex impedance is given by
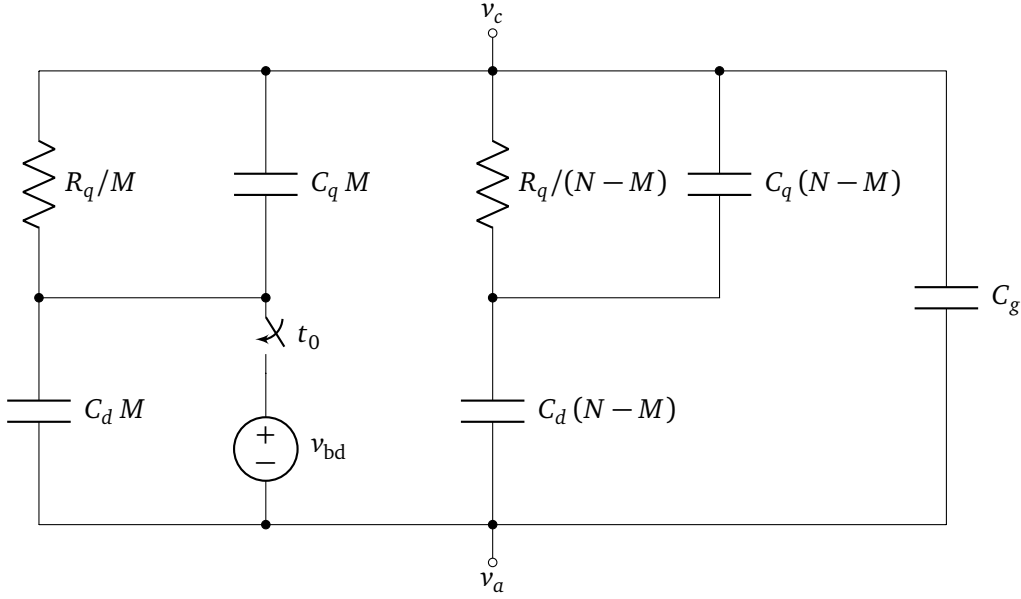
Figure 4.2.: The equivalent circuit diagram of an SiPM as parameterized in [70, 71] for M out of N simultaneously firing cells, see text for details.

$$Z(s) = \left(\left(\frac{R_q}{N} \| \frac{1}{s\,N\,C_q} \right) + \frac{1}{s\,N\,C_d} \right) \| \frac{1}{s\,C_g}, \tag{4.7}$$

when the voltage applied to the SiPM approaches the breakdown voltage $v_c - v_a \nearrow v_{\text{bd}}$ with the complex Laplace number $s = \sigma + j\,\omega$, and $\sigma, \omega > 0$, from which the absolute impedance $|Z(j\,\omega)|$ can be obtained. Typical values of the quenching resistance R_q lie in the range between hundreds of kΩ and a few MΩ. C_q and C_d are of similar size, e.g. around 100 fF where C_d naturally scales with the SiPM cell size. C_g can be found in the 10 pF range and increases with increasing SiPM package size [72].

As the SiPM behavior depends strongly on the electronic front-end, especially on its load impedance, this diagram is very useful and is referred to from succeeding chapters of this thesis. This circuit can be analyzed easily using integral transform methods from which the output voltage, e.g. for a transimpedance amplifier connected to the SiPM anode, is derived. Influences on SiPM properties like recovery time τ_r, signal decay time τ_d, and amplitude v_0 can be predicted. With this information, negative impacts on parameters like signal slew rates, bandwidth, and signal-to-noise ratio (SNR), as well as on the dynamic range can be avoided and the best read-out technique suiting the application can be identified. For calculations, the author refers to a slightly modified version of this circuit in which the switch and the constant voltage source are replaced by an infinitesimal current source $i_d(t) = M\,v_{\text{ov}} \cdot (C_q + C_d) \cdot \delta(t - t_0)$.

In the following, the author will present calculations for the special case that $v_c - v_a \equiv v_b = \text{const.}$, i.e. in the presence of an ideal bias voltage source v_b that is independent of time. Intermediate steps are left out on purpose. However, these steps are given in detail in [68].

With v_d being the voltage across $C_d\,M$, v_q that across $C_q\,M$, and i_b the current from the bias voltage source, the results become [68]

$$v_d(t) = v_b - v_{\text{ov}} \cdot \exp\left(-\frac{t - t_0}{R_q \cdot (C_q + C_d)}\right) \tag{4.8}$$

$$v_q(t) = v_{\text{ov}} \cdot \exp\left(-\frac{t - t_0}{R_q \cdot (C_q + C_d)}\right) \tag{4.9}$$

$$i_b(t) = M\, v_{\text{ov}} \cdot \left(\frac{C_d}{R_q} \cdot \exp\left(-\frac{t - t_0}{R_q \cdot (C_q + C_d)}\right) + C_q \cdot \delta(t - t_0)\right). \tag{4.10}$$

When i_b is converted into a voltage by an ideal transimpedance amplifier, yet with a limited bandwidth and a finite slew rate, the second summand of equation (4.10) turns into a regular symmetric function. This is visible in measurements with fast DAQ-systems as a fast symmetric spike which can also lead to oscillations.

It is interesting to note that above calculations predict only one real time constant τ for the cell recovery time through v_d. Only in the presence of a non-zero read-out impedance, a second time constant emerges. Incidentally, calculations become much more complicated and are omitted at this point, but can be found in [68] in great detail.

4.3. Characterization studies

In the scope of this thesis, the author performed many studies to characterize SiPMs. The author shows in detail how he extracted the intrinsic and non-intrinsic SiPM parameters for a Hamamatsu S13360-6050PE [53], a modern 6 mm × 6 mm SiPM with a 50 μm cell pitch. This type of SiPM was used in the optical modules that were developed for the Auger Scintillators for Composition – II (ASCII) surface scintillator prototypes of the Pierre Auger Observatory in 2015.

A summary of the results of other types of SiPMs follows at the end of this chapter. These are:

1. The Hamamatsu S13360-6025PE [53], a 25 μm cell pitch variant of the S13360-6050PE. It was chosen for the developments of the optical modules for the Surface Scintillation Detector (SSD) in 2016 due to its enhanced dynamic range compared to the 50 μm version.

2. The Hamamatsu S10943-3580X [66], an older SiPM generation with 100 μm cell pitch that was custom UV enhanced. It served as the baseline design of the First Auger Multi-pixel photon counter camera for the Observation of Ultra-high energy cosmic air Showers (FAMOUS) telescope [73].

3. The SensL J-series [60] that was foreseen for the follow-up instruments based on the FAMOUS [59] telescope like IceAct [74] and HAWC's Eye [75, 76].

4. The older SiPM generation from Hamamatsu Photonics, i.e. the Hamamatsu S10362-series [62], for benchmark tests and comparison studies.
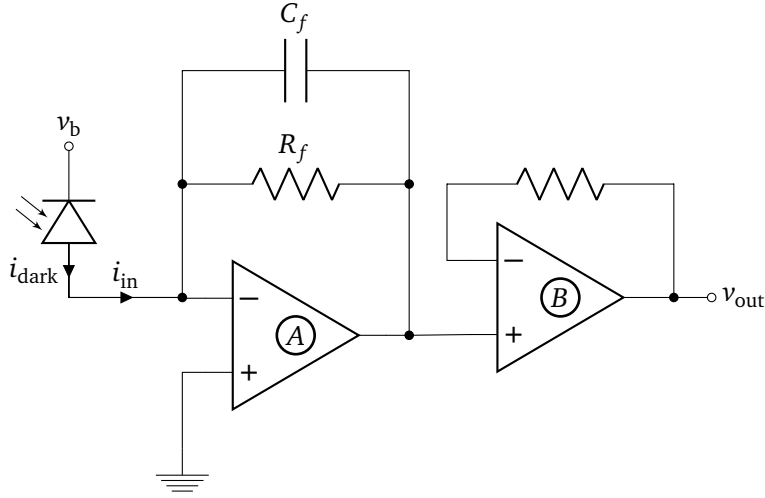
Figure 4.3.: Schematic overview of the read-out setup based on a transimpedance amplifier. A slow VFA, the STMicroelectronics TS912 [77], was used to determine the dark current of an SiPM with a large feedback resistance of $R_f = 1\,\text{M}\Omega$ and feedback capacitance of $C_f = 100\,\text{nF}$. The fast read-out made use of a fast CFA, the Texas Instruments THS3202 [78] with $R_f = 1.5\,\text{k}\Omega$ and $C_f = 1.5\,\text{pF}$.

4.3.1. Electronic setup

Two electronic circuits were developed for the characterization studies that follow this introduction. A dedicated circuit based on a slow voltage-feedback amplifier (VFA) connected as a transimpedance amplifier was used to determine the average dark current as a function of the bias voltage, see figure 4.3. The same setup was used for the determination of the single photon response of the SiPMs but implemented with a fast current-feedback amplifier (CFA). In both cases, the SiPM was placed in a dark box, operated at room temperature around 20 °C, and optionally illuminated with a pulsed UV LED, unless noted otherwise.

The slow circuit

Although the dark current is very small, with typically less than 1 μA around the nominal operating voltage, i.e. at $v_{\text{b,nom}} = v_{\text{bd}} + v_{\text{ov,nom}}$, and at room temperature, a simple electronic circuit like that shown in figure 4.3 allows to determine the dark current without the need of an expensive pico-ammeter. The SiPM is operated with a positive bias voltage from the cathode to the anode and the transimpedance amplifier is connected to the anode. This results in a negative output voltage $v_{\text{out}} < 0\,\text{V}$, as the transimpedance amplifier converts the current into a proportional voltage with

$$v_{\text{out}} = -R_f \cdot i_{\text{in}} = -R_f \cdot i_{\text{dark}} < 0\,\text{V}, \quad i_{\text{dark}} > 0\,\mu\text{A}. \tag{4.11}$$

The feedback resistance R_f determines the transimpedance gain of the amplifier. With a large resistance, e.g. several hundred kΩ, the low dark current turns into a comfortable voltage.

The STMicroelectronics TS912 VFA [77] was chosen as amplifier *A*, as defined in circuit diagram 4.3, with $R_f = 1\,\text{M}\Omega$ and $C_f = 100\,\text{nF}$. The latter reduced the −3 dB-bandwidth from effectively 500 kHz to approx. 1.5 Hz which averaged out SiPM pulses and electronic noise.

The second TS912 amplifier, denoted B in above figure, served as a voltage follower and drove the load. For an ideal amplifier, this results in $v_{out} = 1\,V$ at $i_{dark} = 1\,\mu A$. For a real amplifier, the input resistance needs to be considered. However, due to the architecture of the TS912, the input bias current of the amplifier is typ. less than 150 pA [77] which has, therefore, a negligible effect on the dark current obtained through its output voltage v_{out}. The 1 MΩ resistor was not calibrated, and thus, a systematic error of about 0.2 % to 0.3 % through the resistor tolerance needs to be foreseen on the absolute current scale. This, however, is not visualized in the plots. The output voltage v_{out} was digitized by the Rohde & Schwarz HMO1002 [79] mixed signal oscilloscope. The errors from the non-linearity of the analog-to-digital converter (ADC) were neglected. The bias voltage was provided by a self-designed voltage regulator whose output voltage was checked with a Fluke 8842A [80] precision multimeter, see next chapter.

The fast circuit

The fast circuit was very similar to the slow circuit. Instead of a slow VFA, a fast CFA was installed, the Texas Instruments THS3202 [78]. The THS3202 is a very fast amplifier with a bandwidth of up to 2 GHz at −3 dB and unity amplification. The THS3202 is very power consuming which is why its bipolar supply of nominal ±5 V was current-limited to ±20 mA. The THS3202 was connected as a transimpedance amplifier as shown in figure 4.3 with a feedback resistance of $R_f = 1.5\,k\Omega$ and a $C_f = 1.5\,pF$ feedback capacitor for stability. According to equation (4.11) the resulting pulses were expected to be negative. The amplifier was read-out with the HMO1002 oscilloscope at 50 Ω.

The screenshot that was shown at the beginning of this chapter on the right-hand side of figure 4.1 was taken with the circuit described here, although it was bandwidth limited to 20 MHz for a better single pe visibility due to electronic noise suppression.

All circuits were simulated with LTSpice [81] and checked for stability and linearity. LT-Spice, developed by Linear Technology, is an analog electronic circuit simulator based on the Simulation Program with Integrated Circuit Emphasis (SPICE) [82].

4.3.2. Determination of the breakdown voltage

To determine the breakdown voltage of a given SiPM, one must measure its signal versus the applied bias voltage. This can be done either on the direct current (DC) level by measuring the dark current, i.e. i-v curves, on the pulse level by measuring the charge or amplitude of SiPM pulses, i.e. finger spectra, or by counting active cells in the case of a digital SiPM [**JOPPE_2017**]. All measurements can be done either in the dark or illuminated with a pulsed light emitting device, e.g. an LED or a laser. For a precise measurement, the effective bias voltage needs to be corrected for possible voltage drops at resistors placed in series with the SiPM, e.g. low-pass filters or read-out resistors, as a function of the dark current, i.e. $v_{b,\mathrm{eff}} = v_b - R_{series} \cdot i$. In the setup described above, this effect accounted to a change of less than $R_{series} \cdot i_{max} = 0.4\,mV$ and was neglected.

i-v **curves**

Determining the breakdown voltage through i-v curves is a stable and simple method as no high-speed DAQ is required. The setup featuring the slow VFA was used for this purpose. The left-hand side of figure 4.4 shows the i-v curve obtained with a Hamamatsu S13360-6050PE
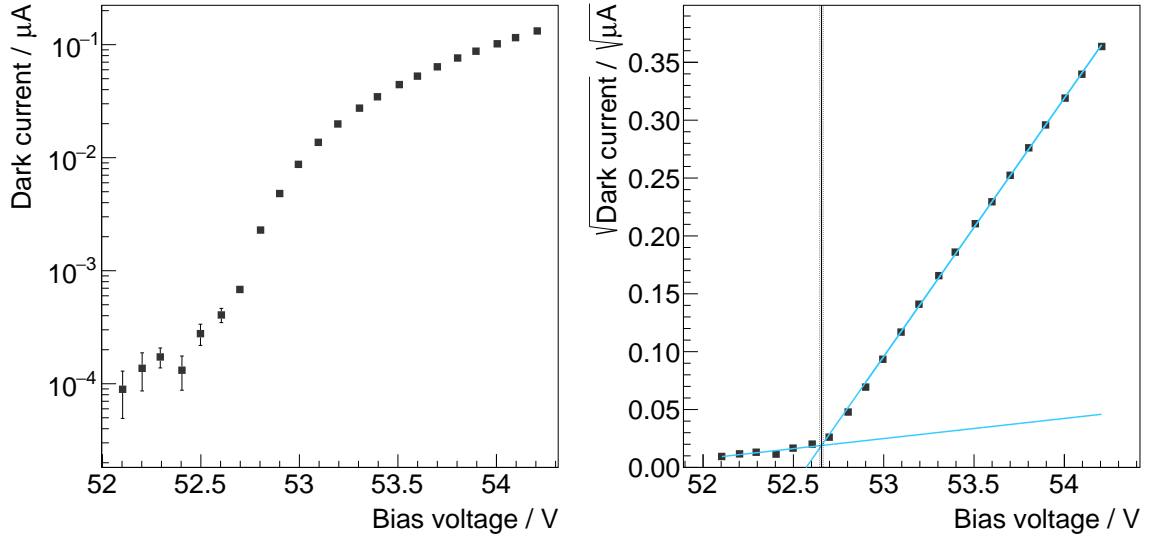
Figure 4.4.: The result of a measurement for a Hamamatsu S13360-6050PE [53] recorded with the slow circuit shows the dark current versus the bias voltage at 19.8 °C. *Left:* A logarithmic plot. *Right:* A visualization of the extraction method through the intercept in square root of the dark current as described in [67], see text for details. The vertical line and the shaded area indicate the intercept of the two linear fits and its error.

[62] SiPM. The dark current increases with bias voltage as expected. The measurement was taken at room temperature of 19.8 °C.

Algorithms for extracting the breakdown voltage from i-v curves are discussed for example in [63]. Those algorithms usually extract the breakdown voltage through determining the maximum of $d^n \log(i_{dark})/dv_b^n$ in natural powers of $n = 1, 2, 3$. Also, quadratic intersection fits are common, which will be discussed in the following.

An empirical analysis is described by the SiPM manufacturer SensL in [67]. The idea is to extract the breakdown voltage from the intersection of two linear fits to the square root of the dark current $\sqrt{i_{dark}(v_b)}$. The first function is fitted to the data points below the discrete rise of $\sqrt{i_{dark}(v_b)}$, the second function above. Applying this method yields a breakdown voltage of $v_{bd} = (52.66 \pm 0.01)\,\text{V}$. The right-hand side of figure 4.4 illustrates this extraction method.

Finger spectra

Another approach to determine the breakdown voltage is to measure the photoelectron multiplication gain of the SiPM versus bias voltage. Applying a linear fit to the gain and by choosing the intersection point where the gain becomes zero allows to extract the breakdown voltage, or more precisely, the *turn-on* voltage, as discussed earlier. The reason is that the gain $g = dg/dv_b \cdot v_{ov}$ scales linear with the overvoltage, and following the definition of the overvoltage from equation (4.1), the gain is also linear in the bias voltage v_b, so

$$g(v_b) = \frac{dg}{dv_b} \cdot (v_b - v_{bd}).$$ (4.12)

The photoelectron multiplication gain can be obtained by analyzing so-called finger spectra.
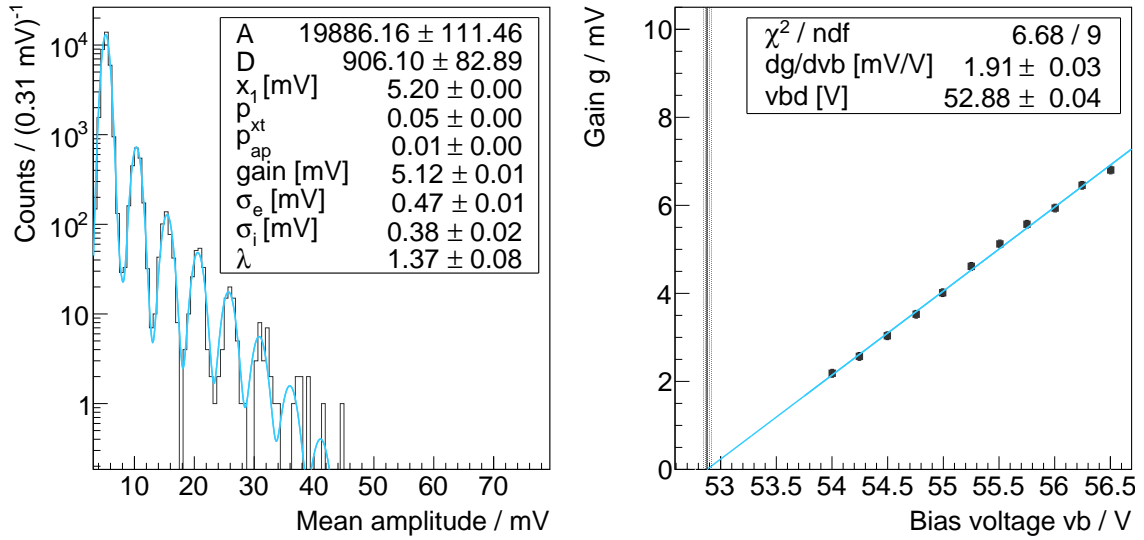
Figure 4.5.: This figure shows the result of the breakdown voltage determination using finger spectra. *Left:* A typical SiPM finger spectrum which was recorded with the Hamamatsu S13360-6050PE [53] at $(21.8 \pm 0.2)\,^{\circ}\mathrm{C}$ and $v_\mathrm{b} = (55.751 \pm 0.001)\,\mathrm{V}$. The SiPM was illuminated by a pulsed LED. The plot includes a fit whose composition is described in the text. The gain is extracted from the fit. *Right:* This plot shows the result when the gain is extracted from finger spectra of various bias voltages. The interception with a gain of $0\,\mathrm{mV}$ determines the breakdown voltage, indicated by the vertical line (fit value) and the shaded area (fit error).

A finger spectrum is a charge or amplitude histogram of an amplified SiPM. Since each cell of an SiPM creates a standardized signal, the charge and amplitude values accumulate at discrete points in these histograms.

The position of these points are related to the number of simultaneous[1] cell breakdowns, i.e. the mean charge of the n-th cell breakdown is located $q_n = (n-1) \cdot g^*$ away from the first, where g^* is the SiPM gain in units of the charge histogram. The gain g^* can be extracted from these discrete peak positions – henceforth called the photoelectron (pe) peaks. In the dark, only the optical crosstalk probability and random coincident dark noise events account for higher orders of cell breakdowns.

The left-hand side of figure 4.5 shows a typical finger spectrum of the Hamamatsu S13360-6050PE [53]. It was recorded with the fast circuit. A bias voltage of $(55.751 \pm 0.001)\,\mathrm{V}$ was applied to the cathode of the SiPM in this specific case. The setup was operated with a pulsed LED. The oscilloscope was set to record 20 traces à $500\,\mu\mathrm{s}$ with a sampling rate of $1\,\mathrm{GSa\,s^{-1}}$ for each bias voltage step.

A signal extraction procedure was implemented that scanned a recorded trace, searched for pulses, and integrated over a fixed time window for every pulse that was found. Pulses were identified with a threshold level which was defined dynamically for every trace: The baseline v_baseline and the typical baseline noise σ_baseline were extracted through the mean and the root mean square (RMS) of a trace with the SiPM turned off. The threshold was hence set to

---

[1] Simultaneous in this context means within the integration window of the charge extraction algorithm.

$v_\text{baseline} - 7.5\,\sigma_\text{baseline}$. Every time the voltage value exceeded this threshold[2] and a leading edge was found, i.e. the slope was negative, the trace was integrated with a constant time window t_gate of 25 samples, i.e. 25 ns. The lower limit of the integral window t_0 was determined by the point where the voltage exceeded the threshold minus one sample.

If the baseline within 15 samples, i.e. 15 ns, prior to t_0 was not stable, the pulse was discarded. This was determined through the RMS of the data points and compared with the typical baseline noise in σ_baseline. The feature was added to eliminate pile-up, i.e. stacked pulses.

Several other implementations were tested, for example integrating over a dynamic time window from t_0 up to the point where the trace settles below the threshold again, or just by taking the amplitude of the pulse. However, the separation power between the photoelectron peaks was the best with the procedure described above. Figure A.4 in appendix A.6 contains an instructive image on how the extraction algorithm works on a real SiPM signal trace.

Finally, the gain was extracted with a binned log-likelihood fit to the finger spectrum. The correlated spectrum function used here is based on the one introduced in [83]. The spectrum was taken from random data of an illuminated SiPM. Therefore, it included the typical SiPM dark noise spectrum and a *photon* component. The former has been implemented with an exponential distribution proportional to p_xt^n, the latter with a Poisson distribution $p_{\lambda,n}$ convoluted with the crosstalk probability density function. Constants D and A describe the differential abundance of the dark noise and photon components. n denotes the number of photon equivalents, and λ the expected value of the Poisson distribution, both given in units of pe. An infinitive number of correlated Gaussian peaks, located at positions $x_n = x_0 + n \cdot g$, gain g and widths $\sigma_n^2 = \sigma_e^2 + n\,\sigma_i^2$ smear out the single pe distribution. Here, x is the position of the data in units of the bin width, σ_e expresses the electronic noise, and $\sqrt{n}\,\sigma_i$ estimates the intrinsic variation of the G-APD charge towards the nominal value, as introduced in [83]. However, this description expects the electronic noise distribution to be white, thus purely Gaussian, and the width of the individual G-APD charge to be dominated by a single quantity. By looking at equation (4.3), this means that either the individual breakdown voltages are normally distributed, or that the individual cell capacitances are normally distributed. It stands to reason that both parameters might even be correlated. As soon as the relative width of one quantity dominates the other, the distribution follows a perfect Gaussian. As no evidence was found in data, that the single photon peaks differed from normal distributions, the author made use of correlated Gaussians in the following.

An asymmetric contribution was added by events that gained additional charge through afterpulsing. The shape parameter ρ is a function of the afterpulsing time constant and the cell recovery time, i.e. $\rho = \tau_\text{r}/\tau_\text{ap}$.

The complete spectrum function reads

$$\frac{\mathrm{d}N}{\mathrm{d}x}(x) = \sum_{n=1}^{\infty}\left(\sum_{m=0}^{n-1}\left(D\,p_{\lambda,n-m}\cdot p_{\text{xt},m}\cdot p_{\text{xt},0}^{n-m-1}\cdot b_{m,n}\right) + A\,p_{\text{xt},n}\right)\cdot f_n(x - x_n, \sigma_n), \qquad (4.13)$$

with

---

[2]In the case of a transimpedance amplifier, the output signal is negative, so, the voltage value needed to be smaller than the threshold value to *exceed* the threshold.

$$f_n(x, \sigma) = (1 - n\, p_{\text{ap}}) \cdot g(x, \sigma)$$
$$+ n\, p_{\text{ap}} \cdot \frac{\rho \cdot (-x + g)^{\rho - 1}}{2\, g^\rho} \cdot \left(\text{erf}\left(-\frac{x - \hat{g}}{\sqrt{2}\, \sigma} \right) - \text{erf}\left(-\frac{x}{\sqrt{2}\, \sigma} \right) \right)$$
$$g(x, \sigma) = \frac{1}{\sqrt{2\pi}\, \sigma} \cdot \exp\left(-\frac{x^2}{2\, \sigma^2} \right),$$

and

$$p_{\lambda, k} = \frac{\lambda^k}{k!} \cdot \exp(-\lambda)$$
$$p_{\text{xt}, k} = p_{\text{xt}}^k \cdot (1 - p_{\text{xt}}), \quad p_{\text{xt}, k < 0} = 0$$
$$x_n = x_0 + n \cdot g$$
$$\sigma_n = \sqrt{\sigma_e^2 + n \cdot \sigma_i^2}$$
$$\hat{g} \equiv g \cdot \left(1 - \exp\left(-\frac{\mathrm{d}t}{\tau_r} \right) \right).$$

Analytical derivations for the individual spectral components follow in the distinctive sections below. The binomial indices $b_{m,n}$ are tabulated in appendix A.2 on page 164 for $m = 0 \ldots 5$. Higher orders of $b_{m,n}$ can be neglected. Also, the author eliminated multiples of p_{ap}^n with $n \geq 2\,\text{pe}$. Furthermore, the convolution of the afterpulsing contribution with a Gaussian probability density function was simplified: The afterpulsing contribution contained a geometric component and two Heaviside functions. The convolution was only done on the two Heaviside functions as they introduced the main change of the spectrum, i.e. the geometric component was taken as a constant. The convolution of a Heaviside function with a Gaussian can be estimated with the error function erf, which is given in above formula. Both simplifications were justified by the small afterpulsing contribution $p_{\text{ap}} \leq 2\,\%$.

The fit for the spectrum taken at $v_b = (55.751 \pm 0.001)\,\text{V}$ is also shown on the left-hand side of figure 4.5. The spectrum describes the measured data very well. Repeating this procedure for different bias voltages and extracting the gain g^* allowed to plot the bias voltage dependence of the gain. The error on the gain was determined through fits to histograms with different bin widths, whose deviations were added quadratically.

A linear extrapolation to $g^* = 0\,\text{mV}$ was performed and the breakdown voltage was recovered, see figure 4.5. Its result was $v_{\text{bd}} = (52.86 \pm 0.04)\,\text{V}$ at $(21.8 \pm 0.2)\,°\text{C}$. The uncertainty on this value could be reduced by determining the gain for bias voltages closer to the breakdown voltage, by recording more traces whose increased number of events would have a smaller impact on the error propagation on the gain results, or by improving the signal extraction methods.

Apparently, the breakdown voltages extracted through the dark current and the finger spectra do not match, i.e. $v_{\text{bd}} = (52.66 \pm 0.01)\,\text{V}$ versus $v_{\text{bd}} = (52.88 \pm 0.04)\,\text{V}$. Both values were obtained at different temperatures with $\Delta T \approx 2\,\text{K}$ which would introduce a change of about $\Delta v_{\text{bd}} \approx 0.12\,\text{V}$. Within the uncertainty of the value obtained through the finger spectra, both values were compatible. A significant systematic deviation in the procedure as presented in [63] could not be confirmed here.
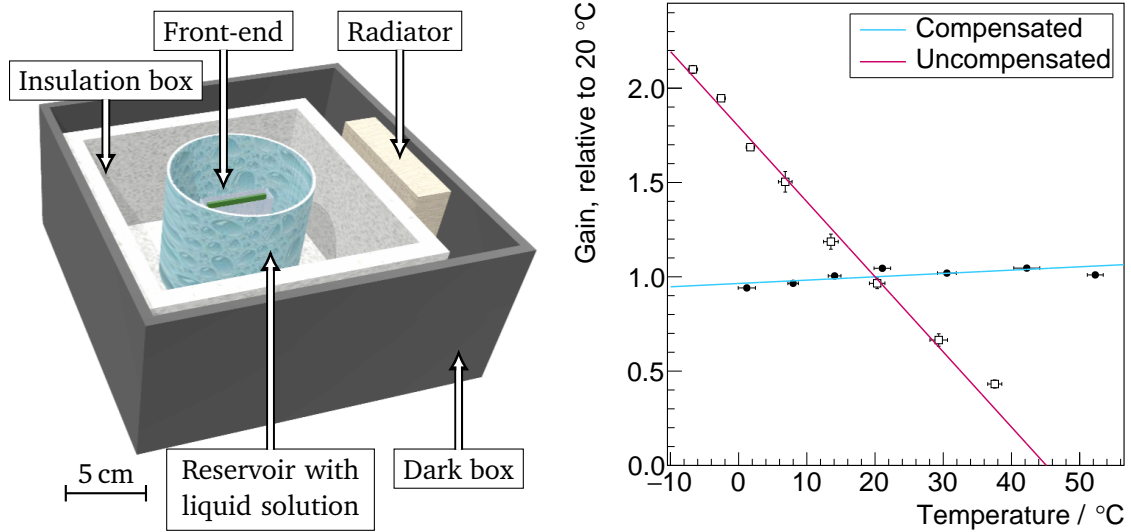
Figure 4.6.: *Left:* Sketch of the experimental setup that was used to evaluate the temperature dependence of the SiPM breakdown voltage. *Right:* Gain versus ambient temperature in the case of an uncompensated bias voltage and in the case of a linear temperature progression for a Hamamatsu S10362-33-100C SiPM.

Whatever extraction method is used, it is essential to stick to one algorithm to get a reliable and stable estimation of the breakdown voltage for different SiPM species. This is especially true when comparing the properties of SiPMs like the PDE or the thermal and correlated noise effects.

It can be concluded that both methods work very well for the extraction of breakdown voltages of SiPMs. The *i-v* method is simple and can be used to determine the breakdown voltages of many SiPMs in a short period without the need for fast DAQs. The advantage of the finger spectra method is that it can be applied to SiPMs that are already operating in an experimental setup, like a scintillator detector or an air-Cherenkov telescope.

The result obtained through the finger spectra will serve as the reference value for the characterization studies that follow. The error on its value will serve as a systematic error, when properties like crosstalk and afterpulsing are stated at the 3 V overvoltage reference on an absolute scale.

4.3.3. Gain versus temperature

As the breakdown voltage is temperature dependent, the gain will change with temperature when the bias voltage applied to the SiPM is kept constant. By combining equations (4.1)–(4.3), a linear decrease is expected while $dv_{bd}/dT > 0\,\mathrm{mV\,K^{-1}}$. To measure this effect, the author set up an experiment featuring a water reservoir with a magnesium chloride hexahydrate $MgCl_2(H_2O)_6$ additive, see figure 4.6. This magnesium salt kept the water liquid even at temperatures below 0 °C. Initially, the temperature of the water reservoir was approx. −10 °C, provided by a commercial refrigerator. The electronics was packed in a zipper storage bag and placed in the water reservoir. A radiator heated up the reservoir with a rate of approx. $10\,\mathrm{K\,h^{-1}}$. This setup was surrounded by an insulation box made of polystyrene and a dark box. The temperature was monitored by an Analog Devices AD22100 [84] analog tempera-

ture sensor, digitized by a Texas Instruments MSP430 microcontroller [85]. The SiPM, type Hamamatsu S10362-33-100C, was amplified by the front-end electronics invented in [68], and read-out by a Lecroy WaveJet 354A, 500 MHz [86] oscilloscope. A simple peak-finding and integration procedure was implemented, scanning the recorded traces and generating finger spectrum histograms, like the one introduced before. The front-end electronics featured a linear temperature progression of the bias voltage, adjustable through an analog potentiometer. At first, the potentiometer was set to a value which corresponded to approx. $0\,\mathrm{mV\,K^{-1}}$, i.e. a constant bias voltage.

On the second run, the potentiometer was set to a value close to approx. $55\,\mathrm{mV\,K^{-1}}$, as the SiPM progression factor of the S10362-33-100C was expected to be around $56\,\mathrm{mV\,K^{-1}}$ [62]. The left-hand side of figure 4.6 summarizes the experimental setup in a small sketch while the right-hand side of figure 4.6 shows the result of this measurement.

This plot proofs that the gain of an SiPM can be kept stable for a wide range of the ambient temperature if the temperature progression $\mathrm{d}v_{\mathrm{bd}}/\mathrm{d}T$, cf. with equation (4.2), is known. In the scope of the bachelor thesis in [87] the temperature dependence of the new Hamamatsu S13360-series was measured over a temperature range between $-30\,\mathrm{°C}$ and $40\,\mathrm{°C}$, a temperature span that is typical for the operation in the Argentinian Pampas. A professional climate chamber was programmed to cycle the ambient temperature, and the temperature dependence of the breakdown voltage was determined through i-v curves and independently through finger spectra. The temperature progression of the S13360-series was found to be

$$\left(\frac{\mathrm{d}v_{\mathrm{bd}}}{\mathrm{d}T}\right)_{\mathrm{S13360}} = (55.16 \pm 0.44)\,\mathrm{mV\,K^{-1}}. \ [87] \tag{4.14}$$

In [87], it was also shown that the gain could be kept stable within $0.05\,\%\,\mathrm{K^{-1}}$ with a digitally programmable front-end that was invented in the extent of this dissertation and pre-released in [54]. It will be introduced in the next chapter, see figure 5.10 on page 95.

4.3.4. Photon detection efficiency (PDE)

The PDE relative to a nominal operating point $\mathrm{PDE_{rel}}$ can be extracted from the LED data set by integrating around the LED trigger position. This analysis eliminated the bias from the efficiency of the peak finding analysis described before. An integration window of 50 ns was chosen. The charge integrals were filled into a histogram, once with the LED turned on and once with the LED turned off, see figure 4.7.

The relative PDE was extracted by estimating

$$\mathrm{PDE_{rel}}(v_b, v_{b,\mathrm{ref}}) = \frac{\lambda(v_b)}{\lambda(v_{b,\mathrm{ref}})}, \tag{4.15}$$

where

$$\lambda(v_b) = \ln\left(\frac{N_{\mathrm{tot}}}{N_{\mathrm{ped}}}\right)(v_b) - \ln\left(\frac{N_{\mathrm{tot,dark}}}{N_{\mathrm{ped,dark}}}\right)(v_b). \tag{4.16}$$

Equation (4.16) is the expected value of the Poisson distribution $P_\lambda(k=0)$ corrected for dark noise (second summand). λ is extracted from the pedestal, i.e. $k=0$, and does not include correlated noise. However, above thoughts imply that the light source is purely Poissonian.
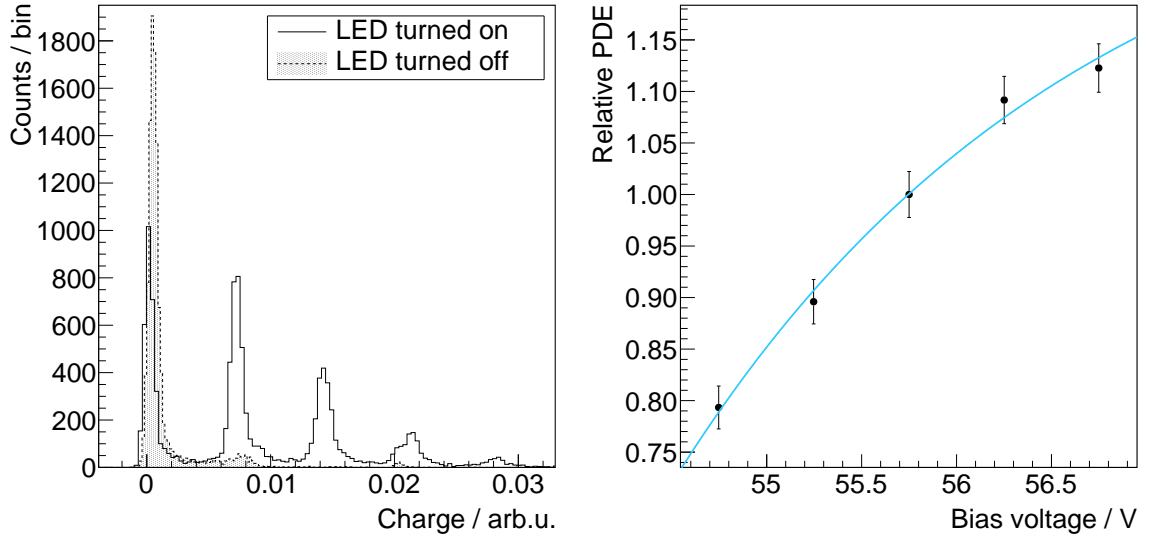
Figure 4.7.: *Left:* A finger spectrum filled with LED triggered integrals on the SiPM signal traces for the Hamamatsu S13360-6050PE [53] at a bias voltage of $(55.750 \pm 0.001)\,\mathrm{V}$ with the LED turned on (black solid) and turned off (black dotted). *Right:* Relative PDE extracted from the finger spectrum for various bias voltages v_b and an empirical fit with $v_{\mathrm{bd}} \equiv 52.75\,\mathrm{V}$ fixed.

N_{tot} and N_{ped} are the number of all events in the histogram and the number of events in the pedestal, i.e. 0 pe, respectively. $N_{\mathrm{tot,dark}}$ and $N_{\mathrm{ped,dark}}$ are the corresponding number of events obtained in the dark, i.e. with the LED turned off. The uncertainties on the number of events is simply given by their square roots, i.e. their Poisson errors. The value of the nominator in equation (4.15) is taken at a given bias voltage v_b while the reference value in the denominator is taken at the nominal operating voltage $v_{b,\mathrm{ref}} = v_{\mathrm{bd}} + v_{\mathrm{ov}}$.

The exemplary finger spectrum in the left-hand side of figure 4.7 was taken with a bias voltage of $v_b = (55.750 \pm 0.001)\,\mathrm{V}$ for the Hamamatsu S13360-6050PE at room temperature. Equation (4.15) was evaluated for five different bias voltages – at the nominal operating voltage of 55.750 V and two voltages each with a distance of approx. 500 mV above and below. In the right-hand side of figure 4.7, the PDE relative to the value at 55.750 V is plotted against the bias voltage v_b. An empirical exponential fit of the form

$$\mathrm{PDE}_{\mathrm{rel}}(v_b) = a \cdot \left(1 - \exp\left(-\frac{v_b - v_{bd}}{b}\right)\right) \qquad (4.17)$$

is added to make the reader aware of the saturating nature of the relative PDE towards high bias voltages, i.e. $v_b > v_{\mathrm{op}} \equiv 55.750\,\mathrm{V}$. As this fit describes the data very well, it can be evaluated to quantify the change of the relative PDE by a small relative change ϵ of the bias voltage around the nominal operating voltage. Mathematically, this can be expressed with

$$\Delta\mathrm{PDE}_{\mathrm{rel}}(\epsilon) = \frac{\mathrm{PDE}_{\mathrm{rel}}(v_{\mathrm{bd}} + (1+\epsilon) \cdot v_{\mathrm{ov}}) - \mathrm{PDE}_{\mathrm{rel}}(v_{\mathrm{bd}} + v_{\mathrm{ov}})}{\mathrm{PDE}_{\mathrm{rel}}(v_{\mathrm{bd}} + v_{\mathrm{ov}})}$$

$$\approx \frac{v_{\mathrm{ov}}}{b\,(\exp(v_{\mathrm{ov}}/b) - 1)} \cdot \epsilon, \qquad (4.18)$$
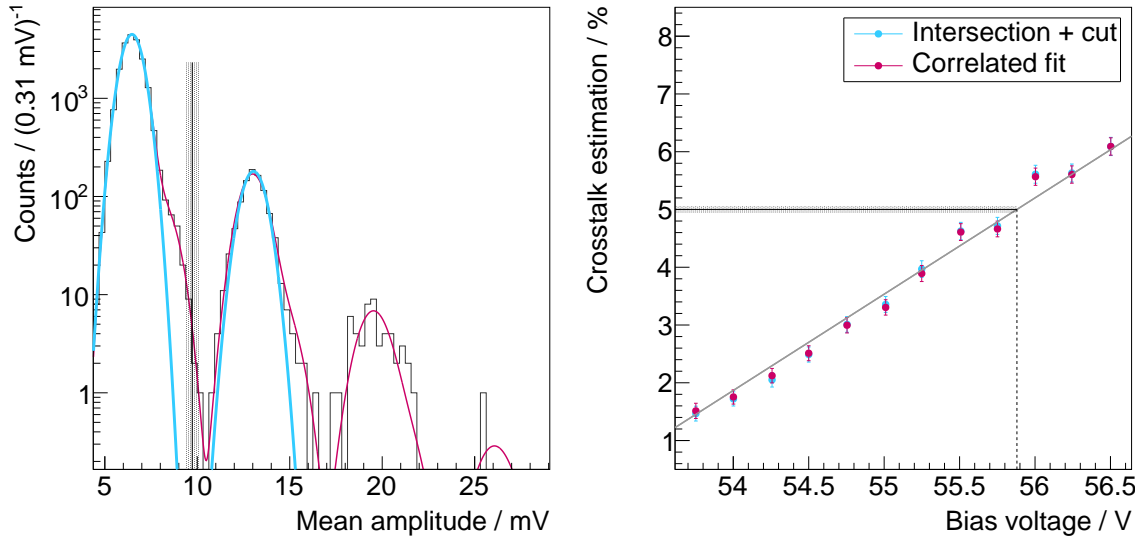
Figure 4.8.: *Left:* A finger spectrum of a Hamamatsu S13360-6050PE [53] SiPM operated at 55.749 V. The procedure of determining the crosstalk probability is visualized by the blue Gaussian fits and their intersection, the vertical line. A correlated fit is added in red, according to equation (4.13). *Right:* The bias voltage dependence of the crosstalk probability yields a p_{xt} of approx. 5 % at the nominal operating voltage of $v_{bd}(T_0)+3\,V \approx 55.88\,V$. Measurements were taken at room temperature of $T_0 = 20.1\,°C$.

or alternatively with the slope at the nominal bias voltage, i.e. the mathematical derivative of equation (4.17). For this very SiPM, a change of the overvoltage of $\epsilon = 1\,\%$ introduces a change of $\Delta PDE_{rel}(1\,\%) = (0.50 \pm 0.01)\,\%$, where the fit result and its error was taken from the right-hand side of figure 4.7 and a nominal overvoltage of $v_{ov} = 3\,V$ was assumed. The consequence is that the PDE changes by approx. 0.5 % when the gain changes by 1 % – which is why the gain of SiPMs is tried to be kept stable with better than 1 %.

4.3.5. Correlated noise

In the following, the author will not discriminate between afterpulsing events and delayed optical crosstalk events that both happen on large time scales. These contributions cannot be distinguished on a single event level – at least not with the methods the author introduces in the following. Furthermore, the author assumes that direct and external optical crosstalk events occur in coincidence with their respective initial events. That means that the author neglects the time delay between initial and correlated events of fractions of pico-seconds.

4.3.5.1. Optical crosstalk

The probability to not have any optical crosstalk events $1 - p_{xt}$ is merely the number of dark counts with exactly 1 pe, i.e. $N(1\,pe)$ divided by the number of all events N for an SiPM in the dark. To account for random coincidences, see also [88], this has to be multiplied with the Poisson probability to find a dark count in the integration gate t_g. With this definition, the optical crosstalk probability p_{xt} can be written as

$$p_{xt} \equiv 1 - \frac{N(1\,\text{pe})}{N} \cdot \exp\left(-f \cdot t_g\right) \approx \frac{N(>1\,\text{pe})}{N}, \tag{4.19}$$

where f is the dark count, resp. thermal noise rate. With a fast read-out, clipped SiPM pulses, and small t_g, the approximation holds. Here, $N(>1\,\text{pe})$ is the number of events with more than 1 pe.

The fast read-out circuit was used, and the SiPM was operated in the dark. The crosstalk probability was estimated with a correlated fit through p_{xt}, see equation (4.13), and independently with a simple cut on the single photon peaks in the histogram and by determining the ratio $N(>1\,\text{pe})/N$. Both methods are visualized on the left-hand side of figure 4.8.

The cut between the 1 pe and the 2 pe was determined by fitting Gaussians to the individual peaks and determining their intersection. This is indicated by the blue curves and the vertical line. Its uncertainty, propagated from the error of the fits, is visualized by the shaded area. All events on the right side of this line determine $N(>1\,\text{pe})$. The author also included a correlated fit in red according to equation (4.13) which, besides the crosstalk probability itself, includes an afterpulsing contribution, see next section. This was done for a range of bias voltages. The result of the crosstalk probability against the overvoltage can be seen on the right-hand side of figure 4.8, for both, the intersection method and the correlated spectrum function. The plot includes a linear fit with

$$p_{xt}(v_b) = \frac{\mathrm{d}p_{xt}}{\mathrm{d}v_b} \cdot (v_b - v_{bd}), \quad v_b > v_{bd}. \tag{4.20}$$

The result of this fit is also given in figure 4.8, where $v_{bd} \equiv 52.88\,\text{V}$ was fixed. A linear function describes the bias voltage relation of the crosstalk probability quite well. Typical crosstalk probabilities of modern SiPM series lie in the range between 1 % and 10 % [53]. The nominal operation point $v_{b,0}$ of roughly 3 V overvoltage, indicated by the vertical line, suggests a crosstalk probability of

$$p_{xt,\,6050\text{PE}}(v_{bd} + 3\,\text{V}) = 5.04\,\% \pm 0.05\,\% \text{ (stat.)} \pm 0.08\,\% \text{ (syst.)}. \tag{4.21}$$

The systematic error is a combination of the uncertainty on the breakdown voltage and the systematic difference between the intersection method and the correlated spectrum function. The result is larger than the value given by the manufacturer of 3% [53] yet smaller than values found in literature, e.g. 6% [89]. Differences in the results of the crosstalk probability obtained by different groups can be explained by systematics in the efficiency of the peak finding algorithm which typically overestimates the crosstalk probability, different definitions of the breakdown voltage itself, a different definition of the crosstalk probability other than the one introduced in equation (4.19) or its extraction analysis through pulse counting or correlated fits.

In the spectrum function from equation (4.13) above, the author parameterized the crosstalk probability with an exponential series which was

$$N(n) = N \cdot p_{xt}^{n-1} \cdot (1 - p_{xt}), \quad n \geq 1\,\text{pe}. \tag{4.22}$$

This relation returns the absolute abundance $N(n)$ as a function of the number of pe, n. It is compatible with the definition of the crosstalk probability from above, because

$$\frac{N(\geq 2\,\mathrm{pe})}{N(\geq 1\,\mathrm{pe})} \equiv \frac{\sum_{n=2}^{\infty} N(n)}{\sum_{n=1}^{\infty} N(n)} = p_{\mathrm{xt}}. \tag{4.23}$$

Its relative expected value is

$$\frac{\langle N(n) \rangle}{N} \equiv \frac{\sum_{n=1}^{\infty} n \cdot N(n)}{\sum_{n=1}^{\infty} N(n)} = \frac{1}{1 - p_{\mathrm{xt}}}. \tag{4.24}$$

That means that the response of the SiPM becomes on average $1/(1 - p_{\mathrm{xt}})$ as large as the incoming signal. For small crosstalk probabilities,

$$\frac{1}{1 - p_{\mathrm{xt}}} \approx 1 + p_{\mathrm{xt}}, \quad p_{\mathrm{xt}} \ll 1 \tag{4.25}$$

holds. For a real SiPM, $n \to \infty$ is not a realistic assumption as the cell occupancy saturates for large crosstalk probabilities or a large number of detected photons, which is not considered in the above considerations. Also, in a quadratic grid, it is expected that the intrinsic crosstalk probability for distant cells is smaller than that for neighboring cells. However, if p_{xt} is small, the above parameterization works fine. The advantage of using an exponential description is that analytical convolutions become more trivial. All calculations are shown in appendix A.1 starting on page 163 in detail.

4.3.5.2. Afterpulsing

The effect of afterpulsing on charge spectra   As introduced before, afterpulsing occurs randomly in single cells whose abundance decreases exponentially with time Δt since the initial cell breakdown. One or two time-constants τ_{ap} describe the afterpulsing probability quite well. The excess charge Δq generated in the cell is

$$\Delta q = 1 - \exp\left(-\frac{\Delta t}{\tau_r}\right), \tag{4.26}$$

in the presence of a single cell recovery time constant τ_r. When Δt is picked randomly from an exponential distribution of the form

$$f(t) = \frac{1}{\tau_{\mathrm{ap}}} \cdot \exp\left(-\frac{t}{\tau_{\mathrm{ap}}}\right) \tag{4.27}$$

it can be shown that the charge generated by a cell with an afterpulsing probability of $p_{\mathrm{ap}} = 1$ follows a distribution of the form

$$q_n(x) = \frac{\rho \cdot (Q_n + g - x)^{\rho-1}}{g^{\rho}} \cdot H(x - Q_n) \cdot \left(1 - H(x - Q_n - g)\right), \tag{4.28}$$

where $H(x)$ is the Heaviside function, and n is the number of photon equivalents in units of pe. A proof is given in appendix A.3 starting on page 164. The shape parameter $\rho = \tau_r / \tau_{\mathrm{ap}}$ relates the recovery time constant with the afterpulsing time constant. In the situation of equality, i.e. when $\tau_r = \tau_{\mathrm{ap}}$, above equation becomes constant $q_n(x) = \mathrm{const.}$ between $x = Q_n$ and $x = Q_n + g$. The charge generated in the abscence of afterpulsing is Q_n, which differs from the expected, resp. mean value $\langle q_n(x) \rangle > Q_n$ due to the afterpulsing excess. g is the gain. Both values are expressed in units of the histogram charge x.

The afterpulsing excess charge makes the single pe fingers asymmetric. In the case of $p_{\mathrm{ap}} \ll 1$ above distribution simply becomes

$$
\begin{aligned}
q_n(x) \approx {} & (1 - n\,p_{\mathrm{ap}}) \cdot \delta(x - Q_n) \\
& + n\,p_{\mathrm{ap}} \cdot \frac{\rho \cdot (Q_n + g - x)^{\rho-1}}{g^\rho} \cdot H(x - Q_n) \cdot \big(1 - H(x - Q_n - g)\big),
\end{aligned} \tag{4.29}
$$

with the Dirac function $\delta(x)$. The first summand is the single photon peak without any afterpulsing. Higher orders of the afterpulsing probability have been neglected, i.e. $p_{\mathrm{ap}}^n = 0$, $n \geq 2$. For large afterpulsing probabilities p_{ap}, the afterpulsing distribution needs to be folded with itself n times and multiplied with a combination of $\sum_i^n c_i \cdot p_{\mathrm{ap}}^i$. However, for the SiPMs used in this thesis, $p_{\mathrm{ap}} \sim 1\,\%$ was small enough to allow above simplification.

For a series of cells whose charge $\tilde{q}_i$ is normally distributed around Q_n with σ_n, $q_n(x)$ from above needs to be folded with a respective Gaussian function. While the first summand $1 - n\,p_{\mathrm{ap}} \cdot \delta(x - Q_n)$ becomes a Gaussian that is simply scaled vertically by $1 - n\,p_{\mathrm{ap}}$ at position $x = Q_n$, the second line has no analytical solutions but for integer values of ρ. However, as σ is usually smaller than g/p_{ap}, the Gaussian convolution of the second summand can be estimated by exchanging the two Heaviside functions with two error functions, to finally yield

$$
\begin{aligned}
\tilde{q}_n(x) \approx {} & \frac{1 - n\,p_{\mathrm{ap}}}{\sqrt{2\pi}\,\sigma_n} \cdot \exp\left(-\frac{(x - Q_n)^2}{2\,\sigma_n^2}\right) \\
& + \frac{n\,p_{\mathrm{ap}} \cdot \rho \cdot (Q_n + g - x)^{\rho-1}}{g^\rho} \cdot \left(\mathrm{erf}\left(-\frac{x - Q_n - \hat{g}}{\sqrt{2}\,\sigma_n}\right) - \mathrm{erf}\left(-\frac{x - Q_n}{\sqrt{2}\,\sigma_n}\right)\right).
\end{aligned} \tag{4.30}
$$

It shall be noted, that the excess charge as described above is only present in finger spectra which make use of signal integration over a significant fraction of the pulse. Then, $\hat{g} = g$. This means, that for ideal electronics no afterpulsing contribution will be found when only the amplitude value is filled into a histogram. For small, yet non-zero integration gates $\mathrm{d}t$, equation (4.27) is multiplied with a Heaviside function of the form $1 - H(t - \mathrm{d}t)$. Re-running all calculations results in equation (4.28) being multiplied with

$$
1 - H\left(x - Q_n - g\left(1 - \exp\left(-\frac{\mathrm{d}t}{\tau_r}\right)\right)\right). \tag{4.31}
$$

That simply means, that symbol $\hat{g}$ in the first error function of equation (4.30) has to be replaced with $g \cdot (1 - \exp(-\mathrm{d}t/\tau_r))$. A correlated fit including estimations of the afterpulsing contribution from above is shown in figure 4.5, and specifically in figure 4.8. The region between the fingers in both figures can only be described by an asymmetric contribution, like the afterpulsing excess charge from above, e.g. with equation (4.30).

Estimating afterpulsing from time spectra   SiPM pulses that originate from afterpulsing can usually not be distinguished from those of random origin on an event-by-event basis. From pulse height analyses it may be possible to distinguish afterpulsing from other cell breakdown events if the cell did not fully recover during the time difference between the afterpulsing and its initial event. On a statistical basis, one can estimate the afterpulsing probability by
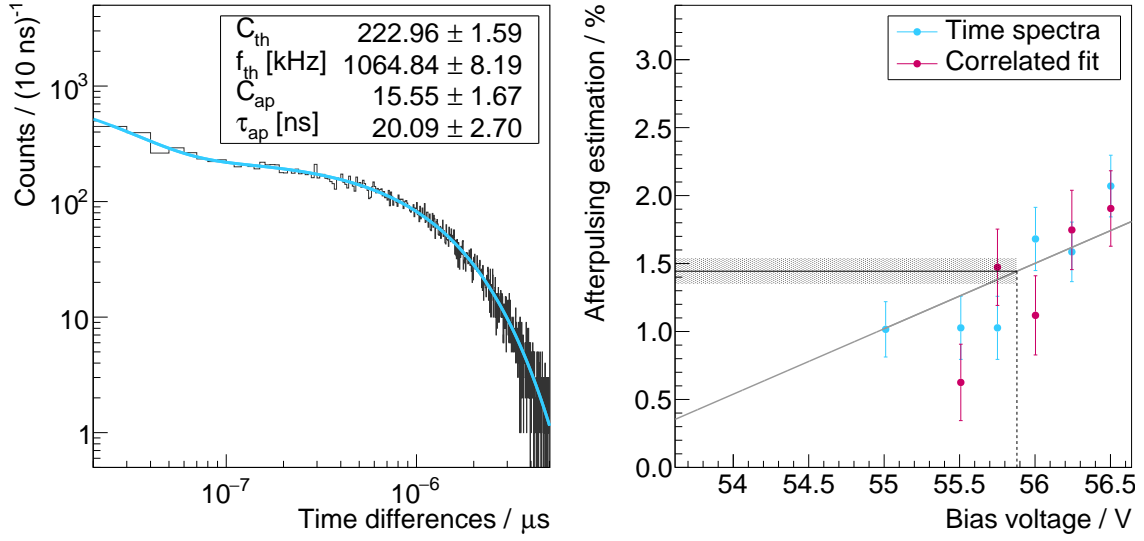
Figure 4.9.: *Left:* A time difference plot of consecutive SiPM pulses for a Hamamatsu S13360-6050PE [53] operated at 56.501 V from which the afterpulsing contribution and the thermal noise rate can be estimated by fitting equation (4.32). *Right:* Afterpulsing probability p_{ap} versus bias voltage v_b estimated independently with time spectra and correlated fits, plus a linear fit according to equation (4.35) where $v_b = 55.75$ V was fixed. The measurements were taken at room temperature of 20.1 °C.

determining time differences Δt between consecutive pulses. A random process will follow a natural exponential distribution.

In the case of an SiPM it is expected that the distribution can be described by a thermal and an afterpulsing contribution of the form

$$n(\Delta t) = n_0 \left(\frac{C_{ap}}{\tau_{ap}} \cdot \exp\left(-\frac{\Delta t}{\tau_{ap}}\right) + C_{th} \cdot f_{th} \cdot \exp\left(-f_{th} \cdot \Delta t\right) \right). \tag{4.32}$$

The normalization constant n_0 depends on the binning and is kept fixed during the fitting procedure. C_{ap} and C_{th} are the integrated afterpulsing and thermal noise contributions, respectively[3]. τ_{ap} is the afterpulsing time constant, whereas f_{th} is the thermal noise rate which dominates long time scales, so $f_{th} > \tau_{ap}^{-1}$, see also [90].

A time difference histogram obtained from a Hamamatsu S13360-6050PE is shown on the left-hand side of figure 4.9. The algorithm can not identify pulses that follow preceding pulses within a short time frame. This leads to an underestimation of the differential contribution from afterpulsing, i.e. the first bins in the histogram. To compensate for this effect, the first bin was ignored from which the systematics of the analysis was estimated.

A composition of two separate afterpulsing exponentials were claimed for example in [90]. In this work, however, no significant second afterpulsing contribution was found. This could originate from the limited number of events, i.e. approx. 20 000, and large bin sizes, i.e. 10 ns. As the first bin was ignored, the latter argument implied that no short but weak contribution would be resolved if the integrating constants C were in the same order of magnitude.

---

[3]The term *integrated* originates from the integrals of the individual contributions $\int d(\Delta t) \, n_i(\Delta t) \equiv C_i$.

By estimating the afterpulsing probability with

$$p_{\mathrm{ap}} = \frac{C_{\mathrm{ap}}^*}{C_{\mathrm{ap}}^* + C_{\mathrm{th}}} \tag{4.33}$$

its bias voltage dependence $p_{\mathrm{ap}}(v_{\mathrm{b}})$ and hence its dependence on the overvoltage can be investigated. C_{ap}^* is the integrated afterpulsing contribution that has been corrected for the cell recovery time τ_r, so

$$C_{\mathrm{ap}}^* = C_{\mathrm{ap}} \frac{\tau_{\mathrm{ap}}}{\tau_{\mathrm{ap}} + \tau_r}. \tag{4.34}$$

A recovery time constant of $\tau_r = (73.27 \pm 0.03)\,\mathrm{ns}$ was assumed, see specific topic about the SiPM recovery time.

The measurement was repeated for a range of bias voltages at the same temperature. This is shown on the right-hand side of figure 4.9. Due to the reduced afterpulsing probability p_{ap} of recent SiPM series of around 1 %, compared to above 40 % of older generations, its reconstruction only works well at high bias voltages, i.e. close to and above the nominal operating voltage. The author also included results of the afterpulsing estimator p_{ap} from the correlated spectrum function in equation (4.13) that were obtained through spectral fits to charge spectra. No significant difference between both methods was found, though the error bars on the individual data points are large.

If the afterpulsing probability scaled linear with the overvoltage, or whether it followed a different law could not be resolved here. But, because the afterpulsing probability of older SiPM generations behaved linear [90], a polynomial of first degree was fitted, i.e.

$$p_{\mathrm{ap}}(v_{\mathrm{b}}) = \frac{\mathrm{d}p_{\mathrm{ap}}}{\mathrm{d}v_{\mathrm{b}}} \cdot (v_{\mathrm{b}} - v_{\mathrm{bd}}), \quad v_{\mathrm{b}} > v_{\mathrm{bd}}, \tag{4.35}$$

where $v_{\mathrm{bd}} \equiv 52.88\,\mathrm{V}$ was fixed. An afterpulsing probability of

$$p_{\mathrm{ap,\,6050PE}}(v_{\mathrm{bd}} + 3\,\mathrm{V}) = 1.45\,\% \pm 0.09\,\%\ (\text{stat.}) \pm 0.12\,\%\ (\text{syst.}), \tag{4.36}$$

was found at the nominal operating voltage, i.e. at $v_{\mathrm{bd}} + 3\,\mathrm{V}$. This is indicated by the vertical and horizontal lines, and the shaded area in the right-hand side of figure 4.9. Again, the systematic error is a combination of the breakdown voltage uncertainty and the difference between both methods. For the lowest bias voltages, no significant afterpulsing contribution could be reconstructed.

In [91], Hamamatsu presents afterpulsing probabilities between 1 % and 2 % near the nominal operating point of 3 V overvoltage for an SiPM of the same series, which is compatible with the result presented here.

4.3.6. Random noise dependencies

Dark count rate versus temperature

As mentioned earlier, the dark count rate approximately doubles every 8 K for moderate temperatures between 0 °C and 25 °C. This can be verified by measuring the dark count rate versus ambient temperature. The measurement was done in [92] for a Hamamatsu S10362-11-100C
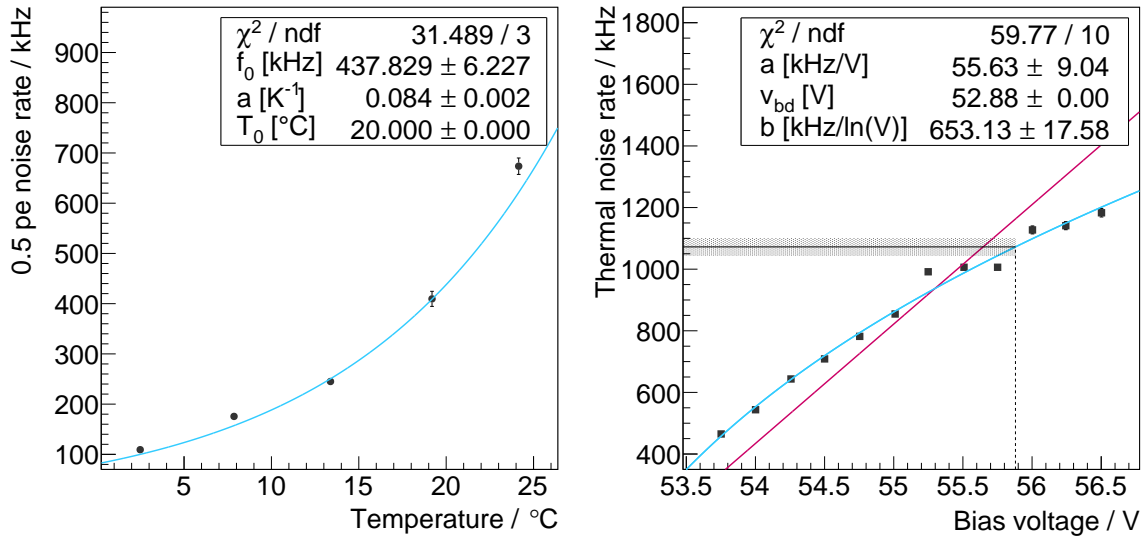
Figure 4.10.: *Left:* A measurement of the dark count rate of a Hamamatsu S10362-11-100C [62] SiPM versus temperature. The reference temperature T_0 for the exponential fit was fixed to 20 °C. All data points were extracted from [92]. *Right:* This plot shows the bias voltage dependence of the thermal noise rate of an SiPM of a different series, the Hamamatsu S13360-6050PE [53] and two different fits, see text. This measurement was performed at room temperature of 21.1 °C by the author.

[62], an early SiPM generation with $1\,\text{mm} \times 1\,\text{mm}$ and $100\,\mu\text{m}$ cell pitch. The result of this measurement is shown in the left-hand side of figure 4.10 indicated by the black squares.

By applying an exponential fit of the form

$$f(T) = f_0 \cdot \exp(a \cdot (T - T_0)) \tag{4.37}$$

the statement can be proven. The reference temperature $T_0 > 0\,°\text{C}$ lies within the range of the data points, i.e. between 2 °C and 25 °C and is kept constant in the fit procedure. $T_0 \equiv 20\,°\text{C}$ is chosen. The fit is also drawn in the left-hand side of figure 4.10 indicated by the blue curve.

The scaler rate $\phi(\Delta T) = f(T_0 + \Delta T)/f_0$ can be recovered from the fit by determining $\exp(a \cdot \Delta T)$. The fit yields $\phi(8\,\text{K}) = 1.96 \pm 0.03$ which is compatible with a factor of 2 increase every 8 K. Please note, that this plot and its result still include correlated noise.

Thermal noise versus bias voltage

The thermal noise rate increases with the bias voltage and hence with overvoltage which can be verified with the fast circuit described in the setup section. The SiPM was operated in the dark.

As the signal of an SiPM contains correlated noise, especially afterpulsing, the time differences of consecutive pulses were analyzed instead of the 0.5 pe dark noise rate. The thermal noise rate was recovered from time difference-histograms that were used to identify the afterpulsing contribution, see figure 4.9. The result is shown in the right-hand side of figure 4.10 for bias voltages from 53.75 V to 56.50 V. The increase of the thermal noise rate with bias voltage is not compatible with a single linear function

$$f_{th}(v_b) = \frac{df_{th}}{dv_b} \cdot (v_b - v_{bd}), \quad v_b > v_{bd}$$

indicated by the red line, but with the following empirical formula

$$f_{th}(v_b) = \frac{df_{th}}{dv_b} \cdot (v_b - v_{bd}) + \frac{df_{th}}{d\log(v_b)} \cdot \log(1 + v_b - v_{bd}), \quad v_b > v_{bd} \qquad (4.38)$$

represented by the blue line. $v_{bd} \equiv 52.88\,\text{V}$ was fixed. Even though the data points were also compatible with a linear function that did not originate in v_{bd}, i.e.

$$f_{th}(v_b) = \left(\frac{df_{th}}{dv_b}\right)^* \cdot (v_b - (v_{bd} - v_{off})), \quad v_{off} > 0\,\text{V}, \quad v_b > v_{bd}, \qquad (4.39)$$

the logarithmic fit from above describes the data better. This is most probably due to inefficiencies in the pulse identification analysis. Data points close to the breakdown voltage would have been needed to distinguish between the linear and non-linear behavior of the thermal noise rate versus bias voltage. However, as the gain decreases with decreasing overvoltage, it is difficult to differentiate 1 pe pulses from 2 pe pulses let alone SiPM pulses from electronic noise which is why no data points below 53.5 V were recorded. All fits yield compatible thermal noise rates of

$$f_{th,\,6050PE}(v_{bd} + 3\,\text{V}) = 1072.3\,\text{kHz} \pm 36.5\,\text{kHz (stat.)} \pm 8.5\,\text{kHz (syst.)}, \qquad (4.40)$$

for the 6 mm × 6 mm SiPM, Hamamatsu S13360-6050PE, with 50 μm cell pitch at room temperature of 21.1 °C and at the nominal operating voltage of $v_{bd} + 3\,\text{V}$. In relation to the size of the SiPM, this translates to a nominal thermal noise rate of 30 kHz mm^{-2} at room temperature.

4.3.7. Recovery time

The recovery time describes the timespan a single cell needs to recharge after a breakdown. Due to its exponential nature, the recovery time is usually expressed with the time constant τ_r of an exponential function, see equation (4.6). There are at least four ways to determine the recovery time of an SiPM:

- analyze afterpulsing from pulse height and time difference spectra,

- measure the electrical parameters of an SiPM and rely on the SiPM electrical model,

- perform a pulse shape analysis on the decay time of single photon pulses,

- trigger a light emitting device with consecutive pulses with variable interval and measure the response of the SiPM.

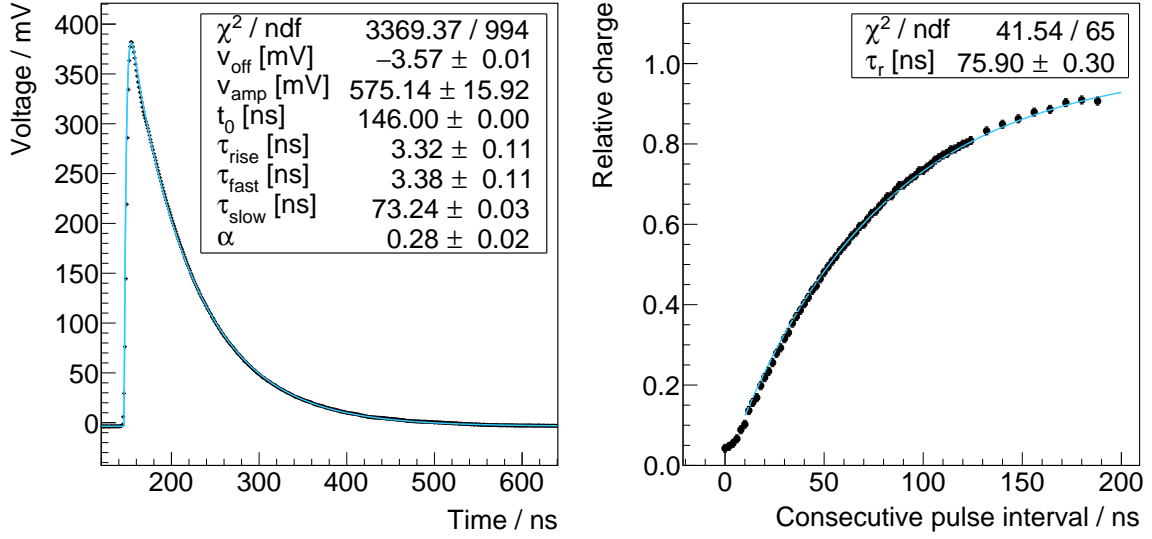In the following, the author will describe the last two solutions.

Figure 4.11.: *Left:* A histogram of decay times extracted from SiPM signals. *Right:* Relative charge versus consecutive light pulse interval. The SiPM is of type Hamamatsu S13360-6050PE [53] and was read-out with a transimpedance amplifier. Both measurements were taken at the nominal bias voltage of $v_{bd} + 3\,V$, see text for details.

Pulse shape analysis

According to the calculations done in [68], the recovery time of a cell is linked to the decay time of its signal. The calculations were based on the SiPM electrical model introduced earlier in this chapter.

To test this hypothesis, the SiPM was illuminated by a nano-second short light flash. As the transimpedance amplifier from figure 4.3 would have been saturated when all of its cells were breaking down instantaneously, the SiPM was read-out with two $51\,\Omega$ resistors in parallel, followed by the Texas Instruments THS3202 in the non-inverting configuration with an amplification of $-12\,dB$. Again, the output signal of this circuit was digitized by the Hameg HMO1002 oscilloscope and an exponential fit of the form

$$v(t) = v_{off} + v_{amp} \cdot H(t - t_0) \cdot \left(\alpha \frac{\tau_{fast}}{\tau_{fast} - \tau_{rise}} \cdot \left(\exp\left(-\frac{t - t_0}{\tau_{fast}}\right) - \exp\left(-\frac{t - t_0}{\tau_{rise}}\right) \right) \right.$$

$$\left. + (1 - \alpha) \frac{\tau_{slow}}{\tau_{slow} - \tau_{rise}} \cdot \left(\exp\left(-\frac{t - t_0}{\tau_{slow}}\right) - \exp\left(-\frac{t - t_0}{\tau_{rise}}\right) \right) \right) \tag{4.41}$$

was adjusted to the data. This function originates from an ideal exponential decay with two decay times τ_{fast} and τ_{slow}, weighted with $0 \leq \alpha \leq 1$, confer with equation (4.55), that is passing through an RC-low pass filter, with time constant $R \cdot C = \tau_{rise}$. The latter models the finite response function of the bandwidth-limited read-out, i.e. the THS3202 amplifier and especially the signal shaping of the 100 MHz oscilloscope. The convolution was calculated through Laplace transforms. The author also calculated the response of a bandpass filter which

is given in appendix A.5 starting on page 167. That function was used when a significant alternating current (AC) coupling constant was present in the data.

The left-hand side of figure 4.11 shows the response of an Hamamatsu S13360-6050PE SiPM to the setup described here and a fit to the data. Decay times of $\tau_{\text{fast}} = (3.38 \pm 0.11)\,\text{ns}$ and $\tau_{\text{slow}} = (73.24 \pm 0.03)\,\text{ns}$ were extracted. This result will be discussed after the next section.

Consecutive light pulses

A more direct way to determine the recovery time is the consecutive light pulses approach: The SiPM is illuminated by two light pulses which are separated by the interval Δt. When Δt is between $0 \times \tau_r$ and approx. $5 \times \tau_r$, where τ_r being the average SiPM recovery time, the charge generated by the SiPM in the second pulse will give a measure for the recovery status of the cells. Δt is swept and plotted against the charge of the SiPM. The recovery time can be extracted from this final interval-vs-charge distribution by fitting one or two natural exponential functions, confer with τ_{fast} and τ_{slow} from above.

A small circuit was developed that drove two LEDs independently. The circuit discriminated the input pulses with comparators on the inputs. The comparators drove NPN transistors that discharged 40 V from 100 pF capacitors whose charge loaded onto the LEDs. 100 kΩ resistors quenched the current. With this circuit, a current pulse with a full width at half maximum of about 1 ns was generated independently of the length or shape of the input pulse.

The initial trigger was generated by the commercial pulse generator Hewlett & Packard 8013B [93]. It was fed to the first LED driver. The trigger output of the 8013B was connected to a commercial passive delay module of type EG&G model DB463 whose output triggered a second 8013B which drove the second LED driver. The delay Δt through the DB463 cable delay box was programmed manually through switches between 0 ns and 120 ns in steps of 2 ns and from 128 ns to 184 ns in steps of 8 ns[4].

The LEDs were mounted on a printed circuit board (PCB) directly next to each other, generating a center-to-center distance of 5 mm. The PCB was positioned at a distance of approx. 20 cm from the SiPM.

The modified, highly-dynamic read-out was used for this measurement that was introduced before. The charge was determined through the integration over the baseline-subtracted trace. With 10 µs, the trace length was chosen long enough to minimize systematics: Otherwise, a fraction of the second pulse would have left the integration gate when time intervals Δt, or the SiPM decay time τ_{slow}, were longer than the trace length. Also, the trigger rate was fixed to 50 Hz to make sure that the LED-pulsers successfully recharged 40 V on the 100 pF capacitors through the 100 kΩ resistors.

When the total charge $q(\Delta t)$ is plotted versus the time interval Δt, it is expected to behave like

$$q(\Delta t) = q_{L,1} + q_{L,2} \cdot \left(1 - \exp\left(-\frac{\Delta t}{\tau_r}\right)\right), \tag{4.42}$$

in the presence of a single recovery time constant τ_r. Here, $q_{L,1}$ and $q_{L,2}$ is the mean charge initiated in the SiPM by the first and second LED, respectively. By measuring the response of the SiPM to the individual LEDs alone, i.e. when $q_{L,1}$ and $q_{L,2}$ were known, the equation from above reduces to

---

[4]Even though steps of 0.5 ns were possible, due to the manual *programming* of the delay box and for the author's sake, the steps were chosen larger.

$$r(\Delta t) \equiv \frac{q(\Delta t) - q_{L,1}}{q_{L,2}} = 1 - \exp\left(-\frac{\Delta t}{\tau_r}\right). \tag{4.43}$$

The setup and analysis described above was used for a series of measurements with the Hamamatsu S13360-6050PE, the 6 mm × 6 mm SiPM with 50 μm cell pitch. The results are shown in the right-hand side of figure 4.11. The relative charge $r(\Delta t)$ from equation (4.43) is fitted to the data points. The result is also shown in the right-hand side of figure 4.11. A recovery time of $\tau_r = (75.90 \pm 0.30)$ ns is retrieved – a value very close to the one obtained through the pulse shape analysis. Interestingly, the response of the SiPM deviates from its exponential behavior at small intervals.

Discussion

Both methods yield similar but not compatible values, i.e. (73.00 ± 0.03) ns against a value of (75.90 ± 0.30) ns. The difference is small, only 4 %, and can be neglected for most applications. However, the author tries to investigate whether the difference of both results is a matter of a yet unknown systematic effect due to electronics or optics, or *just* an underestimation of the statistical uncertainties from the fit values.

The author tried to reproduce the shape of the consecutive light pulse distribution by performing an electronic SPICE simulation of the SiPM. Every cell was treated individually as a separate G-APD. Due to the complexity of the simulation[5], the number of cells was shrunk from 14 400 down to 144.

The parameterization of the cells was taken from [72]. As the electrical parameters of the SiPM were not known, they were estimated either from data sheet values, from the signal shape, or from earlier measurements: $R_q = 924$ kΩ was taken from [94]. C_d and C_q were estimated from the data sheet value of the nominal gain at $v_{ov} = 3$ V through equation (4.3) to 60 fF and 30 fF, respectively. In addition, the grid capacitance C_g was extrapolated from smaller SiPM series in [72] and fixed to 10 pF. All cell parameters were smeared randomly by 1 % following a normal distribution.

In addition to this basic structure, every cell was able to break down twice. A fraction $\epsilon_{bd} \leq 1$ of the cells were randomly chosen to break down at time t_0, measured from the start of the simulation. The exact time of the breakdown was smeared normally within $t_{1/2}$ around t_0 full width at half maximum (FWHM). This mimicked the response of the SiPM to the initial LED pulse. At $t_1 = t_0 + \Delta t$, a second breakdown was executed. Its probability, i.e. the cell breakdown efficiency ϵ_{bd}, was chosen from an exponential distribution in each cell individually depending on the interval Δt, and a common time constant τ_ϵ, so

$$\epsilon_{bd}(\Delta t) = \epsilon_{bd} \cdot \left(1 - \exp\left(-\frac{\Delta t}{\tau_\epsilon}\right)\right), \tag{4.44}$$

reproducing the fact, that the PDE was expected to recover, too. Again, the exact time at which the cells experienced a breakdown, was chosen from a normal distribution with $t_{1/2} = 1$ ns FWHM around t_1.

Selecting $t_0 = 100$ ns was an arbitrary choice which left enough space before the pulse to estimate the baseline. Parameter $t_{1/2} = 1$ ns was chosen from a SPICE simulation of the LED-pulser. As the LED pulse presumably failed to initiate a breakdown in every single cell,

---

[5]The simulation took about one hour to finish on an Intel Core i7 2700K 3.50 GHz processor for 144 cells.
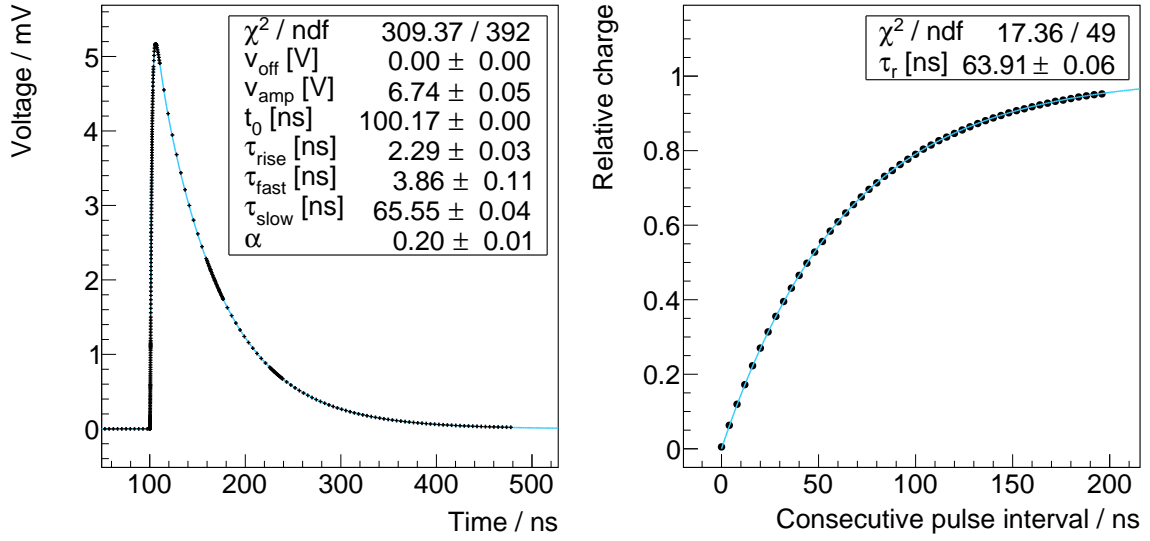
Figure 4.12.: The results of SPICE simulations of the consecutive light pulse experimental setup. The electrical parameters of the SiPM were estimated and the number of cells was reduced to 1 % to save computation time. *Left:* The response of the SPICE model to a single LED pulse. *Right:* The result of a full consecutive pulse simulation exposes similar features like the measurement in figure 4.11. See text for details.

$\epsilon_{bd} = 0.95$ was chosen and varied while several simulations were performed. τ_ϵ was probably the trickiest parameter to estimate. As the recovery time constants from the measurements for both methods differ only in 4 %, the time constant of the breakdown efficiency, i.e. PDE, could not be as large as the time constant of the gain. τ_ϵ was swept between 0 ns and 20 ns.

All the cells were read-out by a common 25 Ω resistor and filtered through a 1 GHz non-inverting amplifier which operated at unity gain. The signal passed through a SPICE model of a 3 m long, 50 Ω RG58 coaxial cable and was buffered by a 100 MHz amplifier. The output signal of the amplifier was integrated, and its value was stored in random access memory (RAM). For every interval, the simulation was performed ten times, to get an estimation of the variance on the result. The mean and standard deviation of the charge was calculated and stored on disk.

Figure 4.12 shows the result of the simulation. The left-hand side shows the transient response of the setup to a single LED pulse, like the one in figure 4.11. Equation (4.41) was adjusted to the data points. Its result is listed in the graph. The result of the consecutive pulse simulation is given on the right-hand side of figure 4.12. A fit with a single time constant as introduced in equation (4.43) suffices to describe the data very well.

As in the measurement, both methods yield different, statistically incompatible results for the recovery time of the SiPM, i.e. (65.55 ± 0.04) ns and (63.91 ± 0.06) ns. Two reasons were found that altered the results:

First, the width of the photon distribution affects the consecutive light pulse result at small intervals. No significant fast component can be found when the width of the photon distribution $t_{1/2}$ is equal to or larger than the fast recovery time constant $\tau_{fast} \lesssim t_{1/2}$. This is indicated by the result of the simulation. When $t_{1/2} = 0$ ns is chosen, the fit finds a fast recovery time constant. It is expected from calculations [68] that the fast time constant becomes more promi-

nent for SiPMs with small cell sizes, e.g. 25 μm instead of 50 μm, as the diode capacitance C_d becomes smaller, while the quenching capacitance C_q is in first approximation independent of the cell size.

The second reason comes from the PDE recharge time constant τ_ϵ. While its value is expected to be small, its effect cannot be found in the pulse shape analysis, as the pulse shape only describes the recovery of the gain. In the simulation, τ_ϵ needed to be implemented artificially, as the electrical model did not describe the optical response of the cells.

Conclusively it can be said, that the difference between both methods is most probably of systematic nature, occurring from the width of the light pulse, and the PDE recovery. Both effects could not be quantified with this setup but are under investigation, see for example [69].

4.3.8. Dynamic range

The dynamic range of an SiPM defines the number of photons that can be resolved from the analog signal within a given resolution. For an instantaneous photon distribution or a photon beam whose time spread is short against the recovery time of the G-APDs, only the number of cells and the PDE limit the dynamic range. A quantitative description of the effective number of cells through binomial statistics is

$$n(\gamma) = N \cdot \left(1 - \exp\left(-\frac{\text{PDE}^* \cdot \gamma}{N} \right) \right). \ [65] \tag{4.45}$$

N is the number of cells, PDE^* is the nominal PDE of the SiPM including crosstalk and afterpulsing, and γ is the number of photons. This relation originates from the change of active area when cells of the SiPM become occupied by avalanches. It holds for instantaneous photon pulses only, without the effects of over-saturation, see [95].

A quantitative derivation of equation (4.45) can be made by letting

$$\text{PDE}(m) = \text{PDE}^* \cdot \frac{N - m}{N}, \quad m \leq N \tag{4.46}$$

be the effective PDE while m cells are occupied. The last factor describes the loss of active area. Then the average number of photons γ needed to initiate n cell breakdowns becomes

$$\gamma(n) \rightarrow \int^N \frac{\text{d}m}{\text{PDE}(m)}$$

$$= -\frac{N}{\text{PDE}^*} \cdot \ln\left(\frac{N - n}{N} \right), \tag{4.47}$$

which can be solved for n to yield equation (4.45). To account for correlated noise, one can multiply equation (4.46) with the excess noise factor and solve the integral for n. The excess noise factor is in first approximation $1/(1 - p_{\text{xt}})$ for the SiPMs used in this thesis. However, this is mathematically the same as substituting PDE^* with $\text{PDE}/(1 - p_{\text{xt}})$. With this definition, the limit of the dynamic range approaches

$$\gamma_{\lim} \sim \frac{1}{2} (1 - p_{\text{xt}}) \cdot \frac{N}{\text{PDE}} \cdot \ln\left(\frac{N \cdot \text{PDE}^2}{(1 - p_{\text{xt}})^2} \right). \tag{4.48}$$

The author estimated γ_{lim} by solving for the number of photons at which the slope of $n(\gamma)$ becomes smaller than the square root of its variance. This only serves as a rough upper limit to quantify the dynamic range of an SiPM for short light pulses that are much shorter than the SiPM cell recovery time. In the real world, the limit on the resolution for short light pulses is usually smaller than γ_{lim} due to contributions of electronics noise and systematics from analytical extraction methods of the signal. However, for extended light pulses, the number of photons that can be reconstructed becomes typically larger than γ_{lim} because of the SiPM cell recovery.

For an application like SSD, two SiPM will be read-out in parallel due to reasons of increased optical acceptance, doubling the total number of cells N and thus increasing the upper limit of the dynamic range, see equation (4.45) and (4.48). For two Hamamatsu S13360-6050PE and for photons with wavelengths near the SiPM's peak efficiency, i.e. $N = 2 \times 14\,400$, PDE $= 40\,\%$, and $p_{\text{xt}} = 5\,\%$, the dynamic range is limited to $\gamma_{\text{lim}} \approx 290\,000$. For two Hamamatsu S13360-6025PE, on the other hand, the dynamic range approaches $\gamma_{\text{lim}} \approx 1\,900\,000$, where $N = 2 \times 57\,600$, PDE $= 25\,\%$, and $p_{\text{xt}} = 7\,\%$ was used.

At about

$$\text{NL}(1\,\%) \sim 0.02 \cdot \frac{N}{\text{PDE}} \cdot (1 - p_{\text{xt}}) \tag{4.49}$$

a non-linearity of 1 % is reached for instantaneous light pulses. For two Hamamatsu S13360-6050PE this is met at about $\text{NL}(1\,\%) = 1400$ photons or equivalently 14 MIP, whereas for two Hamamatsu S13360-6025PE the non-linearity is reached above $\text{NL}(1\,\%) = 8500$ photons or 85 MIP. The definition of one MIP is the most probable energy deposit of a minimum ionizing particle, equivalent to about 100 photons at the SiPMs' surfaces in the case of SSD, see also next chapter. Above these numbers, a reconstruction will be necessary for instantaneous light pulses to reach a resolution better than or equal to 1 %. However, this is only true for instantaneous light pulses. For signals that are extended in time, e.g. particles in the shower front of extended air showers, the limit on the non-linearity can be expected to be larger. For an application like SSD, a deconvolution of the SiPM signal will be necessary for showers whose core is close to the station in question and for high-energy events.

From the electronics point of view, the non-linear, yet well-defined response of an SiPM is of great advantage, as it reduces the electrical dynamic range compared to a linear detector. The consequence is that the electronics only has to offer a dynamic range in its amplitude proportional to the SiPMs' number of cells N instead of PDE $\cdot \gamma_{\text{lim}}$ which is usually larger. However, from the physicist's point of view, γ is the quantity of interest and not $n(\gamma)$. By measuring $n(\gamma_0)$, any error $\Delta n(\gamma_0)$ on that measurement translates to γ_0 through

$$\begin{aligned}
\Delta\gamma_0 &= \Delta n(\gamma_0) \cdot \left. \left(\frac{\mathrm{d}n}{\mathrm{d}\gamma}(\gamma) \right)^{-1} \right|_{\gamma=\gamma_0} \\
&= \frac{\Delta n(\gamma_0)}{\text{PDE}^*} \cdot \exp\left(+\frac{\text{PDE}^* \cdot \gamma_0}{N} \right).
\end{aligned} \tag{4.50}$$

The consequence is that the error on γ_0, i.e. $\Delta\gamma_0$ scales exponentially with γ_0.

At this point, it needs to be said that the response of SiPMs is in first order purely geometrical. It is expected that two SiPMs of the same type respond with the same signal within statistical uncertainties, when they are exposed to the same light flux, if both SiPMs are operated with
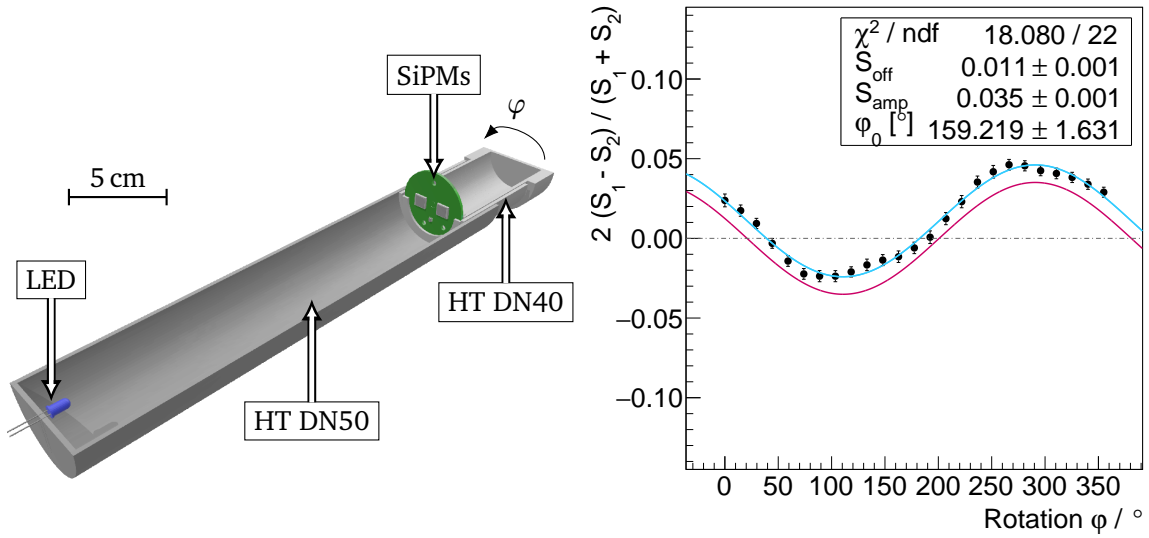
Figure 4.13.: *Left:* Setup for determining the homogeneity of SiPMs to short, intense light pulses, see text for details. The sketch was cut horizontally along the optical axis to expose the LED and the SiPMs. *Right:* Result of the rotation measurement. The blue line is an empirical fit to the data points according to equation (4.51). The *ideal* curve, i.e. with $S_{\mathrm{off}} = 0$ is indicated by the red line.

the same overvoltage, and if both SiPMs have, on average, the same electrical quantities, like R_q, C_d, and so on. The SiPM model only predicts changes in the amount of dark current and the signal shape through variations of the electrical quantities which are subject to production variation. However, since the recovery time is a function of these SiPM parameters, a variation of the dynamic range for extended light pulses cannot be excluded. Consequently, a small deviation in the response of two SiPMs would lead to a large systematic deviation at the upper limit of the dynamic range, as given by above's thoughts.

4.3.9. Homogeneity of the dynamic range

Here, the author tested the homogeneity of the response of SiPMs of the same species to a 100 ns-long and intense light pulse, i.e. at the upper limit of the dynamic range. An experiment was set up that allowed precise optical measurements of SiPMs. Two high-temperature drainage pipes with diameters of 50 mm and 40 mm, HT DN50 and HT DN40, respectively, were modified for a telescopic arrangement. A lid was inserted in the accessible side of HT DN50 which housed a blue LED. Two SiPMs of type Hamamatsu S13360-6025PE were soldered on a rotational symmetric PCB with a center-to-center distance of 15 mm. The company that soldered this PCB used a professional assembling machine, and it stated [96] that its precision was about 50 µm. In the telescopic arrangement, the inner pipe, i.e. the HT DN40 holding the PCB, was rotated around the optical axis of the LED. The SiPMs were read-out individually, with 25 Ω and unity gain. The left-hand side of figure 4.13 shows a 3-dimensional sketch of this experiment.

The signals of the two SiPMs, S_1 and S_2 were recorded by the Hameg HMO1002 100 MHz oscilloscope. The photon density on the surface of the PCB was expected to be inhomogeneous because the LED was not a perfect point source within the required precision of this experiment.

Therefore, the inner drainage pipe was rotated in steps of $\Delta\varphi = 15°$. After $180°$, both SiPMs changed the places in the light pool because the PCB was rotational symmetric in $d\varphi = \pi$. If both SiPMs were homogenous, the signal would behave like $S_1(\varphi) = S_2(\varphi + \pi)$.

By plotting the full difference $S_1 - S_2$ over the arithmetic mean $(S_1 + S_2)/2$, a rotational symmetric response was predicted, parameterizable through

$$2\frac{S_1 - S_2}{S_1 + S_2}(\varphi) \approx S_{\text{off}} + S_{\text{amp}} \cdot \sin\left(\varphi + \varphi_0\right), \tag{4.51}$$

in the absence of LED beam spot multipoles with a moment larger than a dipole. The systematic inhomogeneity of the photon flux could be identified as S_{amp}. S_{off}, on the other hand, included the inhomogeneous response of both SiPMs as well as systematics through the setup, e.g. misalignment of the rotational and the optical axis, as well as misplacement of the two SiPMs around the rotational axis. As the latter two were expected to be of random origin, i.e. the source of the error descended from the way the two pipes were installed, the experiment was dismantled and rebuilt several times.

Figure 4.13 shows the result of one rotational measurement. The left-hand side of equation (4.51) is plotted versus the rotational angle φ. Its right-hand side is fitted to the data points as indicated by the blue curve. To guide the eye, the red curve shows the same function but with $S_{\text{off}} \equiv 0$. This makes clear, that a mean difference of $S_{\text{off}} = (1.1 \pm 0.1)\,\%$ is extracted from the blue fit. The first SiPM responded with about $1\,\%$ more charge on average than the second. As stated above, the setup needed to be dismantled several times to get a hand on the setup systematics in S_{off}. After performing the measurement five times and averaging the individual S_{off} with a weighted arithmetic mean, the result was

$$\langle S_{\text{off}} \rangle = (0.7 \pm 0.4)\,\%. \tag{4.52}$$

Although this result is compatible with zero in less than two standard deviations, all five measurements return $S_{\text{off}} > 0$ individually with at least three σ or more. This indicates that $\langle S_{\text{off}} \rangle > 0$ from the result in equation (4.52) is a truly systematic difference between these two SiPMs.

A simple reason for this systematic is found quickly: The two SiPMs were operated with the same bias voltage. However, their breakdown voltages as given by Hamamatsu were off by $0.03\,\text{V}$. At a nominal overvoltage of $5\,\text{V}$ a gain difference of

$$\Delta g / \langle g \rangle = (0.6 \pm 0.1)\,\%. \tag{4.53}$$

was expected. This, however, is fully compatible with the systematics found in equation (4.52).

To show, that the measurements above were taken at the upper limit of the dynamic range, the individual SiPM responses, S_1 and S_2, were determined for various LED currents. The latter is a measure for the luminous intensity of the LED [97]. The inner pipe was turned into the phase $\varphi = -\varphi_0$ such that the right-hand side of equation (4.51) approached S_{off}.

Figure 4.14 shows the SiPM signal S_i as a function of the LED current, i.e. the number of photons. The measurement shown in figure 4.13 before was taken at an LED current of $12\,\mu\text{A}$ – the last data point in figure 4.14. Obviously, the response of the SiPM was well above the quasi-linear region.

The graph on the right-hand side of figure 4.14 exposes the full difference over the average SiPM signal from the data of the graphs from the left for the same range of LED currents. While
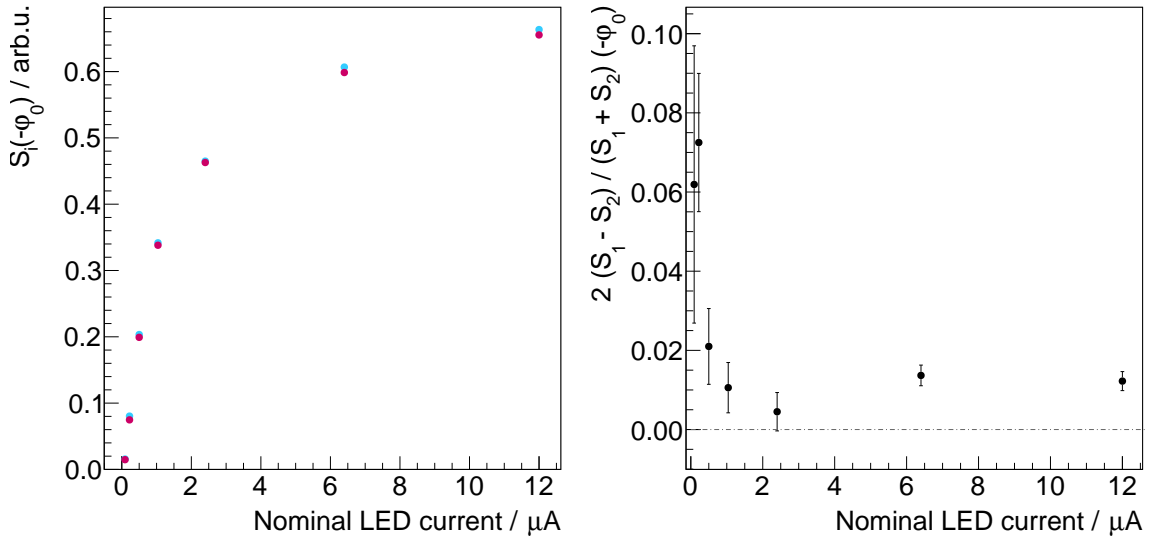
Figure 4.14.: *Left:* The individual SiPM response while the inner pipe was turned in the phase as a function of the LED current. *Right:* Full difference over the average SiPM signal as a function of the LED current. The current is a measure for the number of photons on the SiPMs.

the signal is dominated by Poisson fluctuations at small currents, the difference stabilizes above zero at about 1 %, see equation (4.52).

If SiPMs are operated at the same overvoltage, the response of the individual SiPMs is equivalent for the same light flux. In the particular case of two SiPMs, this means that the sum of the signals is equal to twice the individual response. For an application like SSD, see next chapter, the consequence is that two SiPMs can be operated in parallel and summed up in the analog front-end. Any deconvolution of the non-linear response can be made on the sum of the signal if both SiPMs are operated at the same overvoltage.

4.3.10. Signal-to-noise ratio (SNR)

One can also compare two SiPMs of different species when it comes to the signal-to-noise ratio (SNR), e.g. by comparing the gain and the PDE. In the following, the author will explain how the gain and the PDE relate to the signal amplitude, and thus, how they influence the SNR, as defined by

$$\text{SNR} \equiv \frac{v_{\text{amplitude}}}{\sigma_{\text{noise}}}. \tag{4.54}$$

The time-dependent voltage signal of a single cell breakdown at $t = 0$ for an SiPM, which is read-out with a shunt resistor R_s, is found to be

$$v(t) = v_0 \cdot \left(\alpha \cdot \exp\left(-\frac{t}{\tau_+}\right) + (1-\alpha) \cdot \exp\left(-\frac{t}{\tau_-}\right) \right), [68] \tag{4.55}$$

with

$$v_0 = \frac{v_{\text{ov}}}{N \cdot C_d/(C_d + C_q) + C_g/C_q}, \tag{4.56}$$

and

$$\int_0^\infty \mathrm{d}t \, v(t) = v_{\mathrm{ov}} R_s \left(C_d + C_q\right) \tag{4.57}$$

$$\equiv g \, e \, R_s.$$

Parameters α, τ_+ and τ_- are functions of R_s, N, R_q, C_d, C_q and C_g. While $\tau_+ < \tau_-$ and $0 \leq \alpha \leq 1$, the latter quantifies the fractional abundance of the fast component of the SiPM signal, represented by the time constant τ_+. α decreases inversely with R_s [68] while the voltage integral of the signal given in equation (4.57) increases linearly with R_s. For an ideal transmission of the signal, i.e. no losses at high frequencies, the signal amplitude is independent of R_s, see equation (4.56). However, as the fast component becomes more abundant for smaller R_s, it is beneficial to implement a larger shunt resistance when the read-out is slow and/or when long coaxial cables between the SiPM and the amplifier are used. A good value for R_s is $50\,\Omega$ and shall not exceed R_q/N by much, as the pulses get too long and pulse stacking might become an issue. Capacitances in parallel with R_s add up linearly to C_g and shall be avoided as they dampen the pulse amplitude, see again equation 4.56. Amplifiers close to the SiPM are essential for a good technical SNR.

When comparing two SiPMs where the RMS electronic noise can be assumed to be similar[6], the relation between the SNR of SiPM i and SiPM j can be written as

$$\left.\frac{\mathrm{SNR}_i}{\mathrm{SNR}_j}\right|_{\mathrm{pe}} = \frac{v_{0,i}}{v_{0,j}}. \tag{4.58}$$

For a photon signal, the PDE needs to be included, and the SNR becomes

$$\left.\frac{\mathrm{SNR}_i}{\mathrm{SNR}_j}\right|_{\gamma} = \frac{\mathrm{PDE}_i}{\mathrm{PDE}_j} \cdot \frac{v_{0,i}}{v_{0,j}}. \tag{4.59}$$

Above equations only hold for an ideal read-out that amplifies both, the fast and slow component. However, in the case of a slow read-out, i.e. where the effective bandwidth is (much) smaller than the inverse of the fast time constant $f_{\mathrm{bw}} \ll \tau_+^{-1}$ and/or the parasitic capacitance is (much) larger than the grid capacitance $C_s \gg C_g$, both equations need to be scaled with

$$\frac{1 - \alpha_i}{1 - \alpha_j}. \tag{4.60}$$

This is usually the case when amplifiers with high amplifications and/or long coaxial cables are used. Typical RG58 $50\,\Omega$ coaxial cables feature capacitances of about $100\,\mathrm{pF\,m^{-1}}$ [98], and consequently $2.5\,\mathrm{nH\,m^{-1}}$ while the grid capacitance is about $10\,\mathrm{pF}$ [72]. Estimations can be made by applying the measured parameters of various SiPMs from [72] to the equations from above and by using the parameterizations from [68], as well as $R_s = 50\,\Omega$:

$$\left.\frac{\mathrm{SNR}_{\mathrm{S10362\text{-}33\text{-}100C}}}{\mathrm{SNR}_{\mathrm{S10362\text{-}33\text{-}050C}}}\right|_{\mathrm{pe}} = 2.02 \pm 0.14 \qquad \left.\frac{\mathrm{SNR}_{\mathrm{S10362\text{-}33\text{-}050C}}}{\mathrm{SNR}_{\mathrm{S10362\text{-}33\text{-}025C}}}\right|_{\mathrm{pe}} = 1.25 \pm 0.16. \tag{4.61}$$

---

[6]This is usually not the case. As the impedance of the SiPM changes from size to size and cell-pitch to cell-pitch, the frequency-dependent electronic noise density changes, too – this can be neglected if the change in electronic noise is small, i.e. when comparing SiPMs of the same series and same size.

SiPM type	Nom. v_{ov}	p_{xt}	p_{ap}	$f_{\text{th}}/\text{mm}^2$
S13360-6025PE	5 V	$(7.0 \pm 0.2)\,\%$	$\leq 3\,\%$	35 kHz
S13360-6050PE	3 V	$(5.0 \pm 0.1)\,\%$	$(1.5 \pm 0.1)\,\%$	30 kHz
S12573-3580X	1.3 V	$(49.8 \pm 0.6)\,\%$	$(3.4 \pm 0.1)\,\%$	80 kHz
S10362-11-100C	1.3 V	$(23.7 \pm 2.0)\,\%$	$(33.0 \pm 3.1)\,\%$	600 kHz
MicroFJ-60035	5 V	$(34.3 \pm 0.1)\,\%$	$(4.0 \pm 0.1)\,\%$	55 kHz

Table 4.1.: This table summarizes results from several SiPM families of two manufacturers, Hamamatsu Photonics and SensL, determined through measurements in the scope of this thesis. v_{ov} is the nominal overvoltage, p_{xt} and p_{ap} the optical crosstalk and afterpulsing probabilities, and f_{th} the thermal noise rate at room temperature.

After dropping the fast time constant, i.e. by applying equation (4.60), the SNRs drastically change

$$\left.\frac{\text{SNR}_{\text{S10362-33-100C}}}{\text{SNR}_{\text{S10362-33-050C}}}\right|_{\text{pe}}^{1-\alpha} = 1.63 \pm 0.19 \qquad \left.\frac{\text{SNR}_{\text{S10362-33-050C}}}{\text{SNR}_{\text{S10362-33-025C}}}\right|_{\text{pe}}^{1-\alpha} = 4.97 \pm 1.50. \qquad (4.62)$$

The SNR for SiPMs with small cell sizes worsens when the PDE is included. The PDE decreases with decreasing cell size since the fill factor decreases. Conclusively, it can be said that SiPMs with larger cell sizes and smaller number of cells feature a better SNR than those with smaller cells and a larger number of cells.

In the case of pulse integration, equation (4.57) drives the separation power, i.e. the gain of the SiPM and the read-out impedance resp. shunt resistor R_s. Also, since the relative error on the number of detected photons scales inversely with the square root of the number of photons $\sigma_N/N \propto 1/\sqrt{N}$, the PDE also drives the quality of the reconstruction.

4.3.11. Results from other SiPM series

Table 4.1 includes the most important parameters of SiPMs of several series. Crosstalk and afterpulsing probabilities were measured at the nominal overvoltage given in the second column. The experiments were not performed in a temperature controlled environment which is why the reference temperature varies between 20 °C and 25 °C. With the exponential nature of the temperature dependence of thermal noise, systematic uncertainties between the SiPM species on f_{th} are typically in the order of 10 % to 50 %. The errors given in the table are of systematic nature due to reconstruction uncertainties of the SiPM breakdown voltages.

4.4. Conclusions

The right SiPM must be selected according to the needs of the experiment, and a compromise has to be found between size, SNR, and dynamic range. As the characteristics of today's SiPMs seem to be very similar across the portfolios of different manufacturers, the price will lastly be the decisive factor.

In the SSD application, the SiPM selection was constrained by the size of the fiber bundles. Also, a large dynamic range was more important than its SNR, see chapter 5. The UV sensitivity drove the needs in the FAMOUS telescope, i.e. the SNR below 400 nm and the size of the SiPM, while the dynamic range played a less prominent role, see chapter 6.

It needs to be said that no SiPM model was found that met all requirements from above. The ideal SiPM must be selected according to the individual needs of the application.

The optoelectronic module for SSD

This chapter discusses the development of the silicon photomultiplier (SiPM)-based optoelectronic module which was foreseen for the Surface Scintillation Detector (SSD) – a vital element of the Upgrade of the Pierre Auger Observatory *AugerPrime*. SiPMs, in contrast to vacuum photomultiplier tubes (PMTs), offer an intrinsic photon counting resolution, that allows monitoring their gain during data taking as long as the photocurrent is small. This is expected in the case of an SSD station. Also, SiPMs show no significant aging in an environment above cryogenic temperatures and without any large neutron fluence, see for example [99]. These are advantages that allow studying systematic changes of the detector, e.g. long-term aging of the scintillator or fiber optical power. Their reliability, homogeneity and the fact that no high voltage is needed makes SiPMs the ideal choice for detectors like SSD.

The IceCube Collaboration also uses SiPMs to read-out their scintillator upgrade of the surface detectors of the IceTop subdetector [100]. While the demands on the physics requirements are different from AugerPrime, the hardware of the IceTop upgrade, e.g. scintillators, fibers, and SiPMs, is very similar to the one that is planned for AugerPrime.

The term optoelectronic module is defined by the photosensor i.e. SiPM, the optical coupling between wavelength-shifting (WLS) fibers and the photosensor, i.e. light-guiding cones, and the front-end electronics. In the scope of this work, the front-end electronics of the SiPM optoelectronic module was developed. From 2015 on, prototype modules were designed, produced, characterized, and optimized. This included the temperature-adjusting bias voltage circuitry for SiPMs, the pre-amplifiers, their bipolar low voltage power supply, and the digital control. It was decided to use two 6 mm × 6 mm SiPMs. Devices in this size have already been introduced in the last chapter – the Hamamatsu S13360-series [53] and the SensL C-series [101] are just two examples. Four prototype detectors were equipped with single SiPMs to prove their promised photon-counting features and temperature stability in a real field environment. Finally, three modules were installed in the first pre-production SSD systems in Argentina whose results will be presented at the end of this chapter.

The SiPM-based optoelectronic module for SSD has already been pre-released in [54]. Its characteristics and first results are described in rich detail in that paper. Further publications exist, with a lesser amount of information about this module, these are [102, 103] and some are about to be published, for example [69]. Its results have been cited here appropriately.

5.1. Requirements on the optoelectronic module

The technical and physical requirements of the SSD optoelectronic module have already been introduced in chapter 3 on page 23ff. These points will be discussed in this section in more detail. The requirements on the SiPM optoelectronic module were

1. a dynamic range of at least 12 000 minimal ionizing particle (MIP) in the shower front, i.e. within 100 ns,

2. calibration options for monitoring of the long-term stability, i.e. single MIP, and single pe resolution if possible,

3. minimal changes on the baseline design of the SSD and Upgraded Unified Board (UUB) system,

4. a lifetime not much smaller than the expected lifetime of the experiment of seven years,

5. and a low power consumption of less than 500 mW.

The first two points affect the physics performance of the detector whereas the last three items needed to be fulfilled to be technically compatible with the baseline design of SSD, i.e. the PMT module.

5.1.1. Physics requirements

The physics requirements, i.e. the dynamic range and the MIP resolution, have been discussed thoroughly in the last two chapters: A larger dynamic range reduces the number of saturated stations that are usually close to the shower core. As the lateral distribution function is the steepest close to the shower core, its fit result would be greatly enhanced when close-by, yet non-saturated stations were included. This also applies to SSD and its optoelectronic module. From the last chapter it is known that the number of cells of an SiPM, its photon detection efficiency (PDE), and its recovery time affect the dynamic range. From this point of view, SiPMs with many cells, a low PDE, and a small recovery time are preferable. However, the first two points are typically in conflict with the second item on the bullet list: the single MIP and pe resolution. From the signal-to-noise ratio (SNR) definitions of the last chapter, see equations (4.58) to (4.59), an SiPM with a small cell size and low PDE offers a worse SNR on single MIPs than an SiPM with large cells and a high PDE. This can be quantified by comparing a Hamamatsu S13360-6050PE (6 mm × 6 mm, 50 μm) and a Hamamatsu S13360-6025PE (6 mm × 6 mm, 25 μm) both arbitrarily read-out with a transimpedance amplifier:

$$\left.\frac{\text{SNR}_{50}}{\text{SNR}_{25}}\right|_{\text{pe}} \approx 2.7 \quad \text{and} \quad \left.\frac{\text{SNR}_{50}}{\text{SNR}_{25}}\right|_{\gamma} \approx 4.3, \tag{5.1}$$

where the results of last chapter have been used. However, the dynamic range of the 50 μm SiPM is too limited. Its limit can be estimated in units of MIP when the number of photons per MIP is known. From prototype measurements done in the lab, it was found that the position of the MIP maximum was close to 40 pe for the Hamamatsu S13360-6050PE SiPM. With a PDE of about 40 %, one MIP generates most probably around 100 photons on the surface of the SiPMs in the case of SSD. According to last chapter's equation (4.48), the absolute dynamic range of two 50 μm and that of two 25 μm Hamamatsu SiPMs can be estimated with

$$\gamma_{\text{lim, 2x 50}} \approx 2900\,\text{MIP} \quad \text{and} \quad \gamma_{\text{lim, 2x 25}} \approx 19\,000\,\text{MIP}. \tag{5.2}$$

For two 25 µm SiPMs the limit is even larger than the physics requirement of 12 000 MIP as mentioned earlier. Note, that the dynamic range becomes even larger when the photon arrival time distribution is not instantaneous but spread over a time span in the order of the Geiger-mode avalanche photodiodes (G-APDs)' recovery times. For an arbitrary photon distribution, large photon numbers have to be deconvoluted from the signal with a dedicated analysis on signal traces, see also last chapter and [69].

Conclusively, it can be said, that if it was possible to resolve the single MIP and also the single pe with the 25 µm Hamamatsu SiPM, there would be no reason to choose the 50 µm over the 25 µm. On the other hand, when a proper resolution of the MIP was not achieved with the 25 µm Hamamatsu SiPM, the SiPM module would not fulfill the physics requirements – either different SiPMs needed to be chosen, e.g. the SensL MicroFC-60035-SMT [101], or SiPMs were no alternative to PMTs in SSD in general.

5.1.2. Technical requirements

Several technical requirements also needed to be fulfilled for the SiPM module to be a reasonable alternative to the PMT in the baseline design of SSD. Most importantly, no significant changes on the design could be made, neither on the SSD nor on the UUB as this would delay production. One of the minor changes was a redesign of the optical cookie. As stated in the introduction of this chapter, it was decided to use two 6 mm × 6 mm SiPMs. 96 WLS fibers, with a diameter of 1 mm each, do not fit on the photosensitive surface of those two SiPMs. Two quadratic SiPMs do not allow for a homogenous and rotational symmetric arrangement as a circular PMT entrance window does. Consequently, the optical cookie of the SSD was redesigned and the fibers were split equally into two circular fiber bundles. The optical path was compressed by two optical light guides made of plexiglass so that all fibers could be read-out equally homogenously by these two SiPMs. The geometry of the cones including simulations and laboratory measurements have been published in [54], see also [69] and will not be discussed here any further.

While its high-voltage supply was positive with respect to ground, the signal for the baseline PMT was planned to be decoupled from its high-side via a decoupling capacitor, generating a negative signal polarity. In the case of an SiPM, the signal is usually decoupled from its low-side, making high-voltage decoupling capacitors obsolete. The resulting voltage polarity, however, becomes positive. The UUB stringently required negative input polarities. The author had two options to invert the SiPM signals, by either decoupling the signal from their high-side or by adding inverters close to the SiPMs. The author favored the second solution. The author suspected that whence he decoupled the signal from the high-side, electronic switching noise from the bias voltage direct-current-to-direct-current (DC/DC) converters would mix onto the output signal. The author decided to implement inverting pre-amplifiers close to the SiPMs with sufficient amplification to improve SNR. In other words, the amplification of the signal was moved from the UUB to the SiPM module.

The next question was, how many channels would be needed to resolve the single photon equivalents, as well as to feature the full dynamic range of 115 200 cells. This depends strongly on the data acquisition (DAQ) that is used and its noise floor. At least 17 bit are necessary to map 1 to 115 200 cells onto a digital integer. If, for example, the single photon has to be

resolved with at least 3 bit, since the least-significant bits are often subjects to fluctuations through the electronic noise, the word size becomes larger than 20 bit wide. In the case of the UUB, every channel had a dynamic of 12 bit. Two channels were at least necessary to digitize the full dynamic extent of two 6 mm × 6 mm SiPMs with cell pitches of 25 μm. However, with only two channels, the overlap between both channels would have only been 4 bit wide. This would have complicated cross-calibrations between the two channels during operation. Consequently, all modules would have had to be characterized beforehand. Instead, the author decided to implement three inverting pre-amplifier channels on the SiPM module: A calibration channel for the single pe versus MIP calibration with a dynamic of a few MIP, a high-gain channel for the MIP versus physics calibration and also for small physics signals like distant or low-energy events up to a hundred MIP, and a low-gain channel for large physics events up to 12 000 MIP.

As the UUB featured three unused channels, only a minor change had to be made to the front-end of the UUB: The default amplification of 30 dB, −12 dB and 0 dB had to be set to 0 dB each. That was done by soldering surface-mounted device (SMD) resistors with different values than designated – an operation that could be performed easily.

Instead of the 12 V slow control supply, the author designed the SiPM module to operate from a Universal Serial Bus (USB) port. The reason to use USB was that a bias voltage generator chip manufactured by Hamamatsu Photonics was chosen to power both SiPMs. A single chip reduced the number of components on the SiPM module and its complexity. This usually simplifies debugging, makes the electronics more reliable and reduces costs, see requirement bullet point number four. The chip, however, runs only on 5 V but offers a digital interface which can be made USB compatible. It will be explained in more detail in the following sections. As the UUB offered a USB host connector, no changes had to be made to the UUB design.

The requirement on the power consumption of 500 mW originates from the USB standard which provides at least 100 mA on 5 V in the case of USB 2.0 [104]. Of course, the power consumption shall always be as low as possible to reduce the number of black stations due to a power outage. This problem could happen for example in winter when the electrical power generated by the solar modules during the day is too low to accumulate enough charge for the electronics to survive the night. The baseline PMT design estimates a power consumption of 400 mW [2] which will serve as a reference in the corresponding discussions that follow.

To test the physics calibration performance of SiPMs, that means point two: MIP and pe resolution, SiPMs of various types were installed in the scintillator prototype detector named Auger Scintillators for Composition – II (ASCII) in 2015. These detectors only held a single SiPM each. The former Unified Board (UB) read-out and power supply system was used as it had proven to run reliably in the past while the UUB had not been available at that time[1]. Also, pre-amplifiers based on the transimpedance technique with a good SNR, and low-noise SiPM bias supplies were developed. This will be described in the next section including first calibration and physics events. After that, the first modules holding two SiPMs, the SSD modules, were built. While the pre-amplifiers of the ASCII SiPM modules were supplied by the bipolar ±3.3 V rails of the UB, a bipolar, low-noise amplifier supply had to be developed for the SSD SiPM modules as the ±3.3 V feature was not available anymore on the UUB. Characterization studies followed, finalized by optimizations and physics results in the field. All this was done within the scope of this thesis.

---

[1] And even if it had, it would have introduced new systematics that had to be understood first.
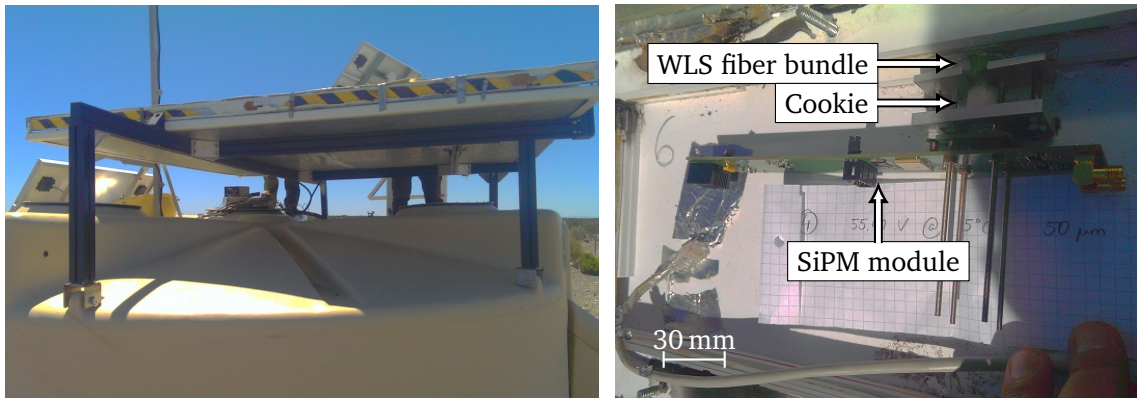
Figure 5.1.: *Left:* A picture of an ASCII detector mounted on top of a WCD tank. *Right:* A picture of the components inside the ASCII detector shows the fiber bundle, the cookie, and the front-end electronics. Picture credits belong to the author.

5.2. The ASCII SiPM modules

This section discusses the development of the ASCII SiPM modules – an essential milestone in the process of the SSD SiPM module development.

5.2.1. The ASCII detector

The Auger Scintillators for Composition – II (ASCII) [2] prototype was the predecessor of SSD and thus pioneered the hybrid, composition-sensitive detector architecture – a scintillator placed on top of a water-Cherenkov detector (WCD) tank. ASCII was developed and built in Bariloche, Argentina, and Malargüe, Argentina, and deployed in the Pampa Amarilla with the help of the local staff of the Pierre Auger Observatory. 27 WLS fibers picked up the scintillation light from a $2\,m^2$ plastic scintillator detector which was structured in 27 bars, each 1.8 m long. The fibers were guided onto a single photosensitive optoelectronic device, see figure 5.1. In the original report [105], this device had been an 0.5 inch PMT.

In the latest configuration, two ASCII modules were placed on a single WCD tank (twin configuration) which made high-level and low-level analyses possible. The ASCII optoelectronic module was powered and read-out by the UB. The UB has been introduced in chapter 3. As the UB only held analog-to-digital converters for the three WCD PMTs, one of the WCD PMTs was disconnected and not operational. In the twin configuration, only one WCD PMT was connected.

5.2.2. The ASCII SiPM module

At the beginning of 2015, an idea came up to replace the PMT of the ASCII baseline design with an SiPM whose sensitive area was artificially increased by a circular-to-quadratic shaped light-guiding cone made of plexiglass to fit the size of the fiber bundle – a diameter of more than 10 mm. Together with the heads behind the invention of the ASCII system, steps for a successful

---

[2]Internally, these modules were called milli-ASCII – ASCII was the name for the upgrade project which was named AugerPrime in later years, see [105].

PMT-to-SiPM replacement were discussed and finally, four ASCII systems were equipped with SiPM modules in Argentina [106].

Please note that the development of the ASCII SiPM modules was a complicated process which involved several prototype iterations of the electronics, especially of the bias voltage supply. Not all intermediate steps will be shown or explained in this thesis. The focus is given on the final revision instead. Also, since a poor layout of the electronic printed circuit board (PCB) increases electronic noise, the electronics presented here and in the following chapters follow low electromagnetic interference (EMI) guidelines [107, 108]. All developments were done by the author in close cooperation with co-workers of the Pierre Auger collaboration. Their results were never published.

5.2.2.1. Bias voltage supply

The requirement on the SiPM bias voltage supply for the ASCII SiPM module was that approx. 55 V needed to be generated from a 12 V supply and, as known from equation (4.2), regulated according to the ambient temperature near the SiPM with a precision of better than 30 mV. This value is equivalent to 1 % of a typical overvoltage of 3 V. There are several ways to implement this in electronics. The author will briefly explain the early revisions that the author developed since some of the ASCII detectors run with these prototype developments. Also, the First Auger Multi-pixel photon counter camera for the Observation of Ultra-high energy cosmic air Showers (FAMOUS) bias supply linear regulators which will be introduced in chapter 6 were based on the ASCII bias voltage supply design.

Early revisions The first revisions of the bias voltage circuitry were based on step-up boost generators, that generated $v_{\mathrm{boost}} \approx 60\,\mathrm{V}$ from $v_{\mathrm{UB}} = 12\,\mathrm{V}$, whose output voltage was filtered by RLC low-pass filters[3], and followed by a post-linear regulator circuit which programmatically set its output voltage to $v_{\mathrm{bias}} = 0\,\mathrm{V}\ldots 60\,\mathrm{V}$. The advantage of this design is the broadband noise suppression in the mid-frequency range above typ. 1 kHz by the post-linear regulator and in the high-frequency range above typ. 1 MHz by the RLC filters.

The bias voltage generators were based on inductive commercial DC/DC converters, e.g. the Maxim MAX15059 [109]. This DC/DC converter stored energy in an inductor and allowed for current limitation and monitoring. However, this specific device operated only on voltages of up to 5.5 V. The Fairchild LM7805 [110] served as a pre-linear regulator to create 5 V from v_{UB}. The post-linear regulator was a self-designed low-dropout linear regulator. This regulator was set up with discrete elements and similar to the ones developed in [68] and published in [111].

Although these solutions were installed in the first prototype PCBs, they were soon dismissed. The efficiency due to the pre-linear and post-linear regulator was very low. The circuitry consumed more than 300 mW in power but was otherwise practically noise-free. Instead, a self-designed capacitive Cockcroft-Walton multiplier was implemented. These step-up converters are known from low-current, high-voltage generators for PMTs, avalanche photodiodes, and Tesla coils, see also [112, 113]. For an ideal Cockcroft-Walton multiplier, the switched input voltage is multiplied by the number of stages. Every stage consists of capacitors and fast-switching diodes.

---

[3]RLC stands for **R**: resistor, **L**: inductor, **C**: capacitor. The RLC low-pass filter is a series combination of R, L and C. The resistor eliminates the pole of the LC filter reducing ringing for loads that follow a step function.

The Cockcroft-Walton circuit served as the voltage boost converter. A feedback system was added: The output voltage v_{out} of the Cockcroft-Walton multiplier was divided down with two resistors, R_1 and R_2. The divided voltage v_{fb} between R_1 and R_2 related to v_{out} as

$$v_{\text{out}} = \left(1 + \frac{R_1}{R_2}\right) \cdot v_{\text{fb}}. \tag{5.3}$$

An error amplifier compared v_{fb} with a reference voltage v_{ref}. The error amplifier drove the switching control circuit of the multiplier creating a simple, analog feedback system. Whenever the output voltage decreased below v_{ref}, the multiplier was enabled. The output of the multiplier was loaded with large-value capacitors of $C_{\text{out}} = 40\,\mu\text{F}$, in parallel with R_1 and R_2. This capacitance eliminated medium- to high-frequency switching noise and reduced the probability for oscillations of the feedback system. A feed-forward capacitor of 1 nF in parallel with R_1 improved the transient response of the feedback circuit.

This circuit tried to keep $v_{\text{fb}} = v_{\text{ref}}$, thus

$$v_{\text{out}} = \left(1 + \frac{R_1}{R_2}\right) v_{\text{ref}} + v_{\text{error}}. \tag{5.4}$$

The author added the arbitrary error term v_{error}. This succeeded as long as $v_{\text{out}}(v_{\text{ref}}) < v_{\text{out,max}}$, and $i_{\text{out}} < i_{\text{out,max}}$. v_{ref} was provided by a digital-to-analog converter (DAC) with $v_{\text{ref,max}} = 2.5\,\text{V}$ which allowed to sweep the output voltage from typically v_{in} to $v_{\text{out,max}}$. The DAC was programmed by a microcontroller – the Texas Instruments MSP430F2013 [85]. A digital temperature sensor of type Analog Devices ADT7310 [114] was connected to the serial peripheral interface (SPI) bus of the MSP430. The firmware of the MSP430 was designed to read out the temperature sensor regularly, approx. once every ten seconds. With the transfer functions in equation (5.4) and equation (4.2), the temperature depending bias voltage was applied to the SiPM.

For the supply of the digital components, i.e. the DAC, MSP430, and ADT7310, a voltage of 3.3 V needed to be generated from 12 V. The Texas Instruments LM1086 linear regulator [115] served well as the load of all digital components was typically below 1 mA. The power loss of less than 10 mW was negligible against the power consumption of the bias voltage generator.

Inaccuracies of this type of circuits are usually dominated by the absolute values of the feedback resistors R_1 and R_2 and their temperature dependence, by the DAC non-linearity and temperature dependence, and by the error amplifier input impedance R_{error} which adds up in parallel to R_2. To reduce those inaccuracies the following decisions were made: The two resistors R_1 and R_2 were chosen from the same family of 0.1 % and 25 ppm K^{-1} precision resistors. The advantage was that the temperature dependence of both resistors was expected to be very similar. Therefore, the major contribution of the temperature dependence cancelled out due to the relation $(1 + R_1/R_2)$, confer with equation (5.4). Mathematically, this can be proven with the parameterization of two resistors against temperature

$$R_i(T) = R_{i,0} \cdot \left(\frac{\text{d}\rho_i}{\text{d}T} \cdot (T - T_0) + \frac{\text{d}^2\rho_i}{\text{d}T^2} \cdot (T - T_0)^2 + \dots\right), \quad i = 1, 2. \tag{5.5}$$

If

$$\frac{\text{d}^n\rho_1}{\text{d}T^n} \approx \frac{\text{d}^n\rho_2}{\text{d}T^n}, \quad n = 1, 2, \dots \tag{5.6}$$

holds then the ratio

$$\frac{R_1}{R_2}(T) \approx \frac{R_{1,0}}{R_{2,0}} + \epsilon(T) \tag{5.7}$$

from equation (5.4) will become nearly independent of temperature T. The absolute precision of 0.1 % reduced the necessity for a voltage calibration. A DAC was chosen that offered high linearity and stability versus temperature, e.g. the AD5382 [116] with $5\,\mathrm{ppm\,K^{-1}}$ or the Microchip MCP4822 [117] with $50\,\mathrm{ppm\,K^{-1}}$ depending on the revision.

Finally, the STMicroelectronics TS912 [77], already introduced in the last chapter, was chosen to play the role of the error amplifier. The TS912 features an input bias current of only $i_{\mathrm{error}} = 150\,\mathrm{pA}$. A recalculation shows that the error term in equation (5.4) became $v_{\mathrm{error}} = R_1 \cdot i_{\mathrm{error}}$. Resistors R_1 and R_2 were chosen such that the desired $v_{\mathrm{out,max}}(v_{\mathrm{ref,max}}) = v_{\mathrm{bias,max}}$ and that the error terms in $R_2/R_{\mathrm{error}} \ll 1$ or $v_{\mathrm{error}} \ll v_{\mathrm{ref,max}}$. In this case, $R_1/R_2 = 60\,\mathrm{V}/2.5\,\mathrm{V} - 1 = 23$ worked well with $R_1 = 230\,\mathrm{k\Omega}$ and $R_2 = 10\,\mathrm{k\Omega}$. The error voltage became $v_{\mathrm{error}} \approx 35\,\mathrm{\mu V}$. For a 12 bit-DAC with $v_{\mathrm{ref,max}} = 2.5\,\mathrm{V}$ the voltage step, i.e. the change in output voltage with a change of the least-significant bit of the DAC becomes $\mathrm{d}v_{\mathrm{out}}/\mathrm{dDAC} \approx 15\,\mathrm{mV}$ which is much larger than the error voltage, i.e. $v_{\mathrm{error}} \cdot \mathrm{dDAC}/\mathrm{d}v_{\mathrm{out}} \approx 2.4 \cdot 10^{-3}$. As the error voltage only adds up linearly to equation (5.4), it is only important for small output voltages v_{out} and can be neglected for output voltages above the breakdown voltage, i.e. $v_{\mathrm{error}}/v_{\mathrm{bd}} < 1\,\mathrm{ppm}$.

To reduce the radiated noise density through the fast-switching diodes in the Cockcroft-Walton stage, resistors of $15\,\Omega$ were added. These resistors lowered the inrush current of the diode stages. On the other hand, the efficiency decreased, and the maximum achievable voltage was effectively reduced. The linearity from equation (5.4) was not affected thanks to the intelligent feedback system.

This modified Cockcroft-Walton circuit worked well for light loads, consumed less than $100\,\mathrm{mW}$, reduced the number of components compared to early revisions and allowed operation from 3 V to 16 V. However, due to the complexity and the risk of failure for self-designed solutions, i.e. overloading, short-circuiting, etc. and lack of features, e.g. current limiting and current monitoring, it was soon decided to go for a different design. However, for about the first year of operation between 2015 and 2016, all four SiPM modules ran with the latest bias voltage version of the early revisions, a solution based on a Cockcroft-Walton bias voltage generator and regulator, a microcontroller, DAC, and digital temperature sensor. Figure A.5 in appendix A.8 on page 169 contains a simplified circuit diagram of the Cockcroft-Walton bias voltage generator and regulator circuit.

Final revision – the Hamamatsu C11204-02   With the release of the Hamamatsu C11204-02 [118] a new bias voltage solution was available. The C11204-02 is a voltage generator and regulator manufactured by Hamamatsu Photonics. It runs on 5 V only and needs to be programmed digitally. The addition of a buck switching converter, a microcontroller, and an analog temperature sensor was all that was necessary to operate the C11204-02. The buck switching converter type Texas Instruments TPS62120 [119] generated 5 V from the 12 V rail, and supplied the C11204-02, the Atmel ATmega328P [120] microcontroller, and the Texas Instruments LM94021 [121] analog temperature sensor. At a load of approx. 20 mA the efficiency of the TPS62120 approached 90 % [119].

The C11204-02 is programmed via a universal asynchronous receiver-transmitter (UART) interface with a symbol rate of $38\,400\,\mathrm{baud\,s^{-1}}$, one stop bit and even parity. A broad functionality is available [122]: A bias voltage between 40 V and 70 V can be generated with a current

of up to $2\,\text{mA}$. In the typical setup, the C11204-02 is programmed with a desired nominal bias voltage $v_b(T_0)$ at a given temperature T_0. The C11204-02 automatically reads out the LM94021 analog temperature sensor and applies a voltage with two linear and two quadratic correction factors, $\gamma_\pm$ and $\delta_\pm$, respectively. The resulting bias voltage is calculated via

$$v_b(T) = \left\{ \begin{array}{ll} v_b(T_0) + \gamma_+ (T - T_0) + \delta_+ (T - T_0)^2, & T > T_0 \\ v_b(T_0) + \gamma_- (T - T_0) + \delta_- (T - T_0)^2, & T < T_0 \end{array} \right\}. \tag{5.8}$$

The nominal voltage $v_b(T_0)$ can be identified with the sum of the breakdown voltage and the nominal overvoltage at $T = T_0$, and $\gamma_\pm$ with the slope of the temperature dependent breakdown voltage, thus $v_{bd}(T_0)$ and $\mathrm{d}v_{\text{bd}}/\mathrm{d}T$, respectively, confer with equation (4.2). The quadratic temperature progression $\delta_\pm$ is usually set to zero and the linear progression below and above the reference temperature T_0 are not treated independently, i.e. $\gamma_+ = \gamma_-$. The voltage step size is $1.8\,\text{mV}$. The ambient temperature as given by the LM94021 analog temperature sensor and the current drawn by the SiPM can be accessed through the digital UART interface. The intrinsic temperature dependence of the C11204-02 was determined in [87] to be approx. $1.4\,\text{mV}\,\text{K}^{-1}$. This value needs to be included in $\gamma_\pm$.

In the final revision of the ASCII modules, the ATmega328P programmed the C11204-02 at start-up. The nominal temperature T_0 was identified with $25\,^\circ\text{C}$, and the nominal voltage $v_b(T_0)$ was calculated from the breakdown voltage at $25\,^\circ\text{C}$, i.e. $v_{\text{bd}}(25\,^\circ\text{C})$ and the nominal overvoltage v_{ov} of $3\,\text{V}$ and $5\,\text{V}$ for the $50\,\mu\text{m}$ and the $25\,\mu\text{m}$, respectively, in accord to equation (4.1) – thus $v_b(T_0) = v_{\text{bd}}(25\,^\circ\text{C}) + v_{\text{ov}}$. As described above, the linear progression factor was found to be $\gamma_\pm = 58\,\text{mV}\,\text{K}^{-1}$, see [87]. $\delta_\pm = 0\,\text{V}\,\text{K}^{-2}$ was fixed as no significant quadratic component was found in the characterization studies performed with Hamamatsu SiPMs within the temperature span of interest, see [68, 87, 90, 92]. After being programmed, the C11204-02 performed the temperature regulation of the bias voltage continuously. The ATmega328P microcontroller switched to sleep mode to minimize its power consumption.

5.2.2.2. Pre-amplifiers

As stated above, the development of the ASCII SiPM modules served the purpose of exploring SiPMs for the Upgrade of the Pierre Auger Observatory. That meant that the priority of the electronics was the single MIP and pe resolution. Without resolving the MIP, the measured photon signal could not be translated into a physical quantity which was necessary to determine the muon signal in air showers. Also, it was beneficial yet not necessary to identify the single photon equivalents. The pre-amplifiers were developed with the focus on small to medium signal sizes and did not cover the full dynamic range, see discussion above.

The technical requirement on the pre-amplifiers was an output voltage swing from $0\,\text{V}$ to $-2\,\text{V}$ at $50\,\Omega$, thus at least $40\,\text{mA}$. The bandwidth needed to be filtered according to the Nyquist-Shannon theorem because of the limited sampling rate of $40\,\text{MSa}\,\text{s}^{-1}$ of the analog-to-digital converters of the UB [123].

The Analog Devices AD8012 [124] current-feedback amplifier (CFA) was chosen. It offers a $-3\,\text{dB}$ unity-gain bandwidth of up to $350\,\text{MHz}$ and a slew rate of $2250\,\text{V}\,\mu\text{s}^{-1}$. It allows driving loads of up to $80\,\text{mA}$. Its small quiescent current of only $1.7\,\text{mA}$ per amplifier minimized the power consumption of the ASCII SiPM module. The AD8012 holds two amplifiers in one package. In the ASCII SiPM module, the two amplifiers formed the two stages of a single channel. Between the first and the second stage the anti-aliasing filter was implemented with
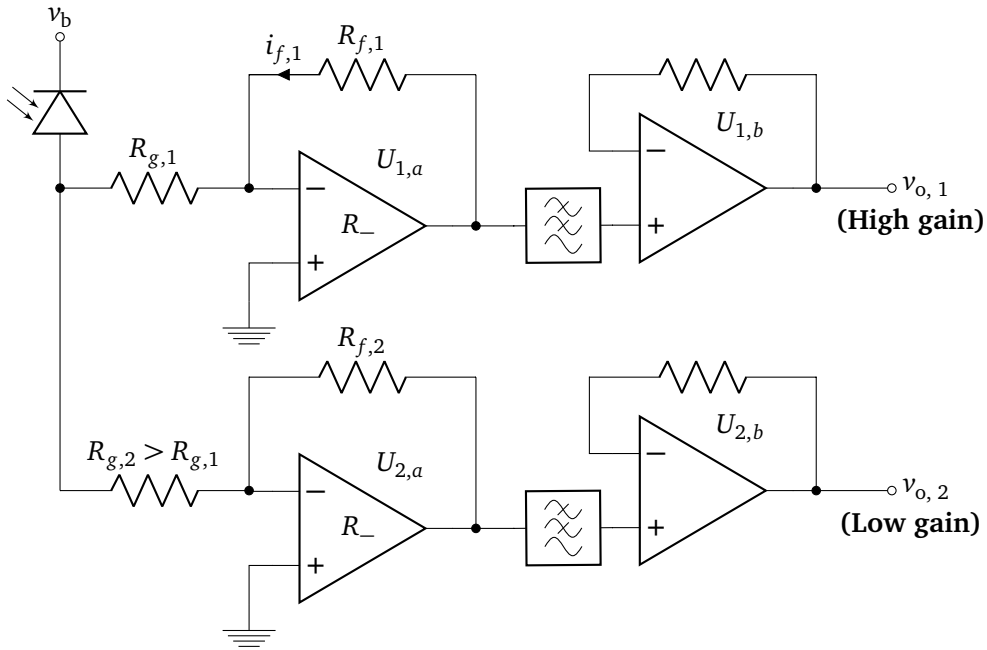
Figure 5.2.: This image shows simplified schematics of the pre-amplifiers of the ASCII SiPM module. Two channels were implemented, with two CFAs, the Analog Devices AD8012 [124], each. At the top: The high-gain stages, at the bottom: the low-gain stages. The SiPM was loaded with $R_{g,1} + R_- \parallel R_{g,2} + R_-$, where $R_{g,1} < R_{g,2}$. See text for details.

a 20 MHz -3 dB-bandwidth. The first stage inverted and amplified the signal, while the second stage buffered the shaped signal of the anti-aliasing filter and drove the coaxial cable.

Two pre-amplifier channels were foreseen which meant that two packages of the AD8012 were used per ASCII SiPM module. One channel was operated with a higher gain than the other. The high-gain channel resolved the pe pulses and the MIP up to about 3 MIP, whereas the low-gain channel resolved the MIP only and could be used for physics events up to a few 100 MIP. All values applied to the 50 μm SiPM, which was the baseline design for ASCII, due to its larger SNR as introduced above.

To improve the signal to noise ratio of the high-gain channel for small signals an asymmetric passive current divider was implemented. The divider was set up with two resistors, $R_{g,1}$ and $R_{g,2}$, see figure 5.2. It loaded the SiPM with about $R_{g,1} + R_- \parallel R_{g,2} + R_-$. The inverting input R_- of the AD8012 was low-ohmic during normal operation, and the SiPM drove both channels through $R_{g,1}$ and $R_{g,2}$. A smaller resistance $R_{g,1} < R_{g,2}$ at the input of the high-gain channel increased the amount of current relative to the low-gain channel, maximizing SNR for single pe pulses of the high-gain channel. It worked very well for small signals. But, as soon as the first stage of the high-gain channel got saturated, its feedback current $i_{f,1}$ distorted the low-gain channel, see again figure 5.2: When the output of U_1 saturated, current would flow through its feedback resistor $R_{f,1}$ into the current divider as the AD8012 inverting input became high-ohmic in the state of saturation. This current would have been picked up by the low-gain channel through $R_{g,2}$ and distorted the output voltage $v_{o,2}$ of U_2 through its own transimpedance $R_{f,2}$.
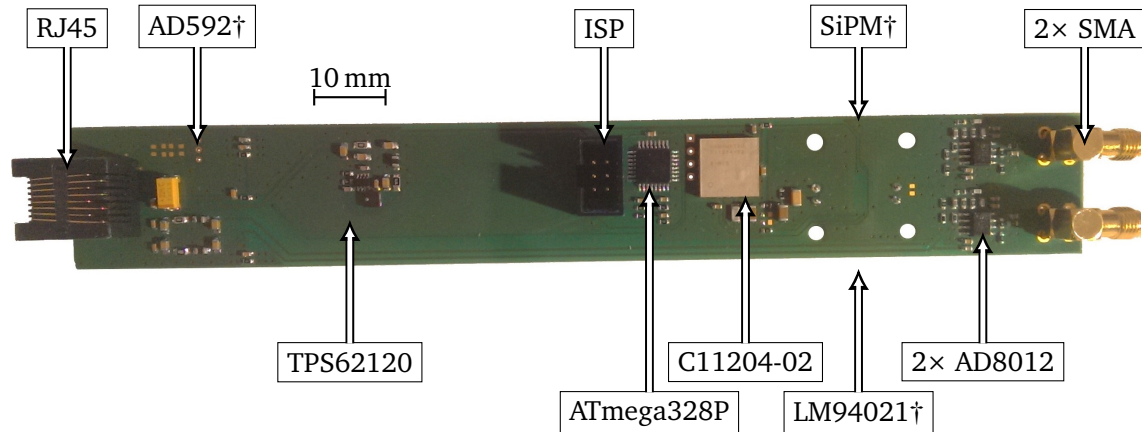
Figure 5.3.: This figure shows a vivid picture of the ASCII SiPM module of the final revision. Components marked with the †-symbol were placed on the back side of the PCB. The AD592 temperature sensor, the LM94021 temperature sensor, and the SiPM are thus not visible in the picture above.

However, the circuit worked great for exploring the single pe and MIP and for signals up to a few dozen MIP which was, once more, the purpose of the ASCII prototype SiPM modules.

5.2.2.3. PCB design

To be compliant with the ASCII baseline design, the PCB dimensions and its connectors were the same as those of the PMT version. The author designed and made a layout of a two-layer PCB, 200 mm long, 28 mm wide and 1.6 mm thick that held the circuits described above. A Registered Jack, RJ45 connector linked the SiPM module with the UB slow control over a standard CAT5 *Ethernet* cable. The analog outputs of the pre-amplifiers were routed through two sub-miniature version A (SMA) connectors and 2 m generic 50 Ω RG58 coaxial cable to the analog front-end of the UB. The firmware of the microcontroller was flashed via a six-pole, two-row 3x2 male pin header. With a dedicated Atmel AVR programmer, the microcontroller could be programmed live in the system. This is known as an in-system programmer, ISP. The Analog Devices AD592 [125] analog temperature sensor – also soldered to the ASCII SiPM module – was read out by the slow control of the UB.

The SiPMs were soldered by the electronics workshop of III. Physikalisches Institut A, RWTH Aachen University on a separate quadratic PCB, 28 mm wide and long and 1.6 mm thick. It was connected to the main PCB via two two-pole, single-row 2x1 pin headers.

Figure 5.3 shows a picture of the final revision. Four modules of the latest revision were successfully installed in Argentina in November 2016 and were operating for about one year. Two modules were equipped with 25 µm Hamamatsu SiPMs and two modules with 50 µm SiPMs, S13360-6025PE and S13360-6050PE, respectively. The pictures in figure 5.1 on page 77 above were taken during the installation campaign by the author of this thesis. Note, that the amplification of the pre-amplifiers was identical for the 25 µm and the 50 µm.

In total, the final revision of the ASCII SiPM module consumed about 125 mW on average during operation.
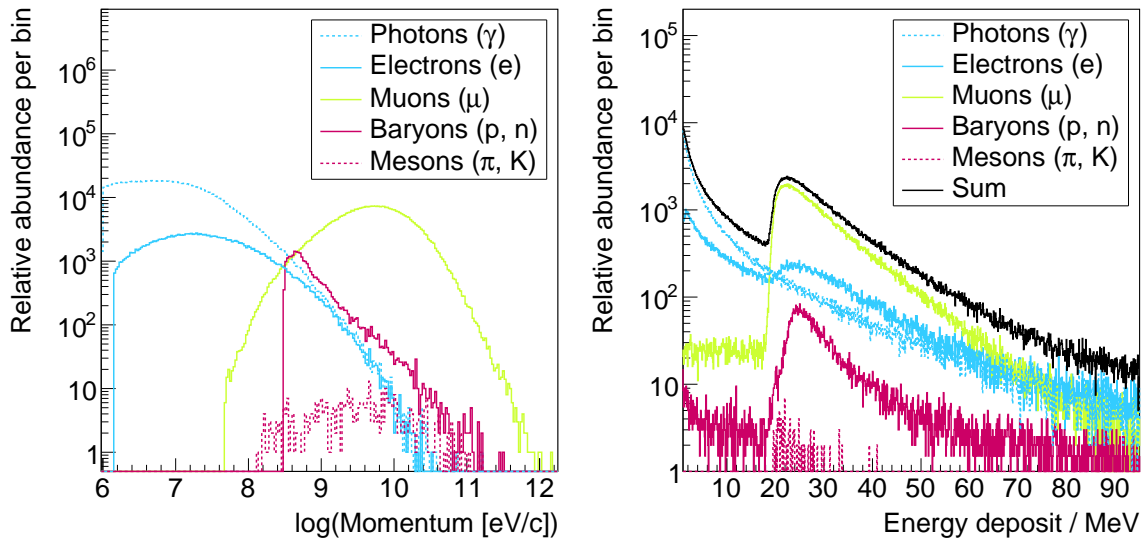
Figure 5.4.: *Left:* Momentum spectra of secondary particles simulated with CORSIKA [23] for proton primaries with energies between 100 GeV and 1 PeV for the observation at ground level in Malargue, Argentina and standard US atmosphere. *Right:* Energy deposit of the individual particle species from the *left* figure simulated with GEANT in version 4 [126] for polystyrene. Both simulations were performed by the author of this thesis.

5.2.3. Excursus – the expected secondary particle spectrum

The energy deposit of secondary particles can be used to calibrate the detector. The idea is that MIPs deposit a characteristic amount of energy in a plastic scintillator. This quantity is called the MIP peak. The clear majority of the secondary particles originate from low-energy cosmic rays which dominate the cosmic ray spectrum. In the following, the author tries to estimate the signal of a plastic scintillator that is exposed to those secondaries.

The relative abundance versus energy for secondary particle species in the air shower was estimated with a CORSIKA [23] simulation. 100 000 random showers of proton primaries with zenith angles between 0° and 70°, random azimuth, and energies between 100 GeV and 1 PeV were simulated with a spectral index of −2.7. The energy of the individual particle species at an observation height of 1412 m was extracted and filled into a histogram. The height corresponded to a detector operation in Malargue, Argentina. Thus, the horizontal and vertical magnetic field components were fixed to 19.2 µT and −14.3 µT, and the US standard atmosphere was used. The result of this simulation is given on the left-hand side of figure 5.4. It shows the relative abundance per logarithmic momentum bin versus the logarithm of the momentum in eV c^{-1} of the secondaries for electromagnetic particles (blue), muons (green) and hadrons (red). The fermions are encoded with solid lines while the bosons are indicated by the dashed lines. The hard cuts in the spectra, for example for baryons at 300 MeV c^{-1}, originate from the low-energy limits of the CORSIKA software.

Electromagnetic particles dominate the lower range of momenta between 1 MeV c^{-1} up to approx. 300 MeV c^{-1} while, due to their unstable nature, the momentum of muons has to be larger than typically 1 GeV c^{-1} for the muons to reach the surface of the Earth. Mesons are less abundant while baryonic hadrons like protons and neutrons can be found at medium momenta
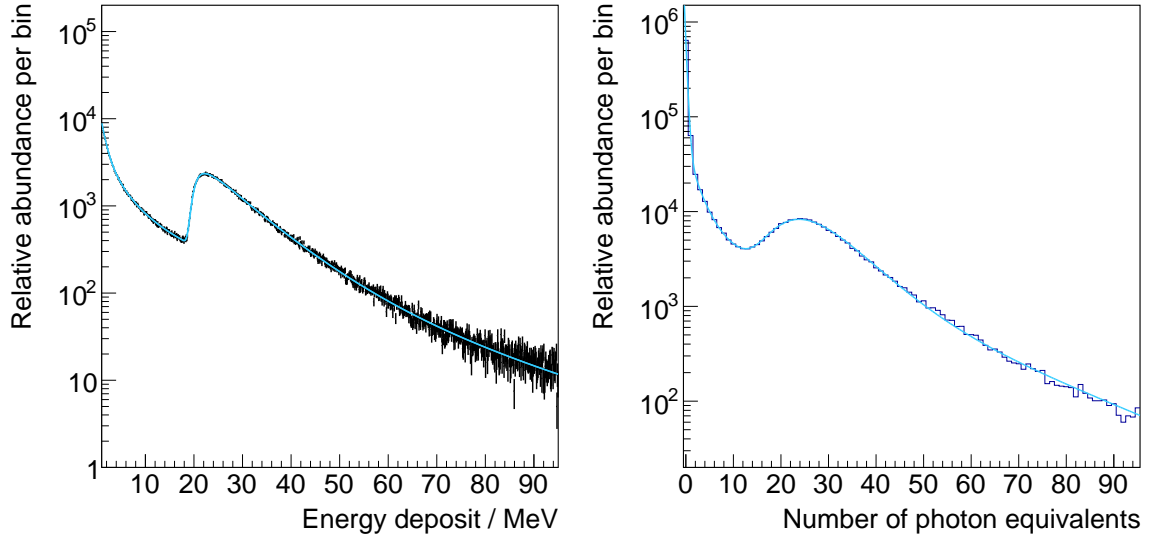
Figure 5.5.: *Left:* Typical integrated energy deposit of secondary particles in a plastic scintillator, confer with figure 5.4, including a parameterization through equations (5.9) to (5.11). *Right:* Estimated number of photon equivalents detected by an optical sensor like an SiPM and an empirical fit according to equation (5.13).

around $1\,\mathrm{GeV\,c^{-1}}$.

The relative abundance of the individual particle species was fed into a simplified Geometry and Tracking (GEANT) (version 4) [126] detector simulation. Here, the detector consisted of a single piece of polystyrene with dimensions $180\,\mathrm{cm} \times 110\,\mathrm{cm} \times 1\,\mathrm{cm}$. Wavelength shifting additives like POPOP and PPO were omitted. The total energy deposit of the particle species was simulated as shown on the right-hand side in figure 5.4.

The minimal ionizing leptons and hadrons deposit energy that correlates to a characteristic spectrum, peaking briefly above $20\,\mathrm{MeV}$. Landau distributions can approximate the underlying fluctuations. Natural exponential functions can describe the spectrum of photons and the spectra of low-energetic contributions of electrons. The left plot in figure 5.5 shows the sum of the all-particle spectrum versus the energy deposit as already shown in figure 5.4. An empirical fit with 20 parameters is added. The spectrum function reads

$$\frac{\mathrm{d}N}{\mathrm{d}E}(E) = \sum_{i=1}^{4} N_i \cdot \exp\left(-\frac{E}{E_i}\right) \qquad \text{(photons)} \qquad (5.9)$$

$$+ \sum_{i=5}^{6} N_i \cdot \exp\left(-\frac{E}{E_i}\right) + N_{\mathscr{L}} \cdot \mathscr{L}(E, E_{\mathrm{mpv}}, E_\sigma) \qquad \text{(electrons)} \qquad (5.10)$$

$$+ N_{\mathscr{G}} \cdot \mathscr{G}(E, E_\mu, E_{\mathrm{gr}}) \cdot \exp\left(-\frac{E - E_\mu}{E_7}\right). \qquad \text{(muons)} \qquad (5.11)$$

The first line, i.e. equation (5.9), describes the energy deposit of photons, parameterized through four independent natural exponential functions with eight parameters. The next line, equation (5.10) parameterizes the variations of the energy deposit of electrons and positrons. Two exponentials are used for the low-energy deposit and a Landau distribution denoted by

$\mathscr{L}$ represents MIP contributions of β-radiation. However, Landau or Landau-Vavilov functions [127, 128] fail to describe the MIP spectrum of muons. Instead, an empirical product of a sigmoid function, i.e. a Gompertz [129] distribution, denoted by $\mathscr{G}$, with a natural exponential function satisfies the muon contribution, see equation (5.11).

The energy deposit was converted into a photo signal by folding the histogram in figure 5.5 with a linear transfer function which included the

1. scintillation light yield,

2. internal scintillation WLS efficiency of the PPO and POPOP additive in the scintillator [55],

3. photon pickup, waveband shifting and photon transport efficiency by the WLS fibers, and

4. photon detection efficiency of the photosensor.

Molecular quenching that would have led to a non-linear fluorescence dS according to Birks' Law, i.e.

$$\frac{\mathrm{d}S}{\mathrm{d}x} = \frac{A \cdot \mathrm{d}E/\mathrm{d}x}{1 + kB \cdot \mathrm{d}E/\mathrm{d}x}, [130] \tag{5.12}$$

was neglected in this simulation. A and kB are constants, that depend on the target material. kB is about $85\,\mu\mathrm{m}\,\mathrm{MeV}^{-1}$ for polystyrene [131]. For small energy losses dS/dx, for example electrons above $100\,\mathrm{keV}\,\mathrm{c}^{-1}$ and muons above $100\,\mathrm{MeV}\,\mathrm{c}^{-1}$, its non-linearity becomes vanishingly small. This becomes clear when above equation is expanded in a Taylor series for $kB \to 0$ and higher orders of dE/dx are abandoned, which is a fair estimate for small dE/dx, i.e. minimal ionizing particles.

At the close of this procedure, optical crosstalk and dark noise, both originating from the SiPM, was added. Typical values were chosen for the optical efficiencies in the bullet list based on experimental findings of prototype experiments conducted by the author, while the results from the last chapter were used to describe the SiPM response. An optical crosstalk probability of 10 % was correlated with the number of detected photons using Monte Carlo methods. The amount of dark noise was calculated from Poisson statistics with the mean dark count rate at room temperature, i.e. 1 MHz, and the nominal integration window of 500 ns of the UB.

The result is shown in figure 5.5. Two fits were performed: At first, the 20-parameter strong empirical function from equations (5.9) through (5.11) was folded with the simplified detector response. The second, independent fit was a closed algebraic equation composed of three natural exponential functions and a Gumbel [132] distribution. The findings of the CORSIKA and GEANT simulations drove the motivation of the following algebraic spectrum function

$$\frac{\mathrm{d}N}{\mathrm{d}n}(n) = \sum_{i=0}^{2} N_i \cdot \exp\left(-\frac{n}{n_i}\right) + N_{\mathfrak{G}} \cdot \mathfrak{G}(n, n_\mu, n_\beta). \tag{5.13}$$

dN/dn is the relative abundance per number of photon equivalents n. $\mathfrak{G}$ is the Gumbel distribution. N_i and $N_{\mathfrak{G}}$ are differential constants, depending on the binning, and n_i, n_μ, and n_β are the spectral variables of the individual distributions. In contrast to a Landau distribution, the Gumbel distribution can be normalized through its integral as $\lim_{n \to +\infty} \mathfrak{G}(n, n_\mu, n_\beta) = 0$. Otherwise, both distributions are closely related.

This fit is also given in figure 5.5. While both fits performed well, the author decided to use the algebraic equation to describe the detector response from here on, as the number of free parameters was smaller and computational processing powers were much lower.

Equation (5.13) still needs to be transformed to a finger spectrum which will be discussed in the next section in detail.

5.2.4. Low-level results

The measurements with the ASCII detectors made low-level and high-level analyses possible. Low-level analyses were, for example, the SiPM gain stability versus time and temperature and the MIP long-term stability.

5.2.4.1. Calibration histograms

As shown above, the energy deposit of minimal ionizing secondary particles in the plastic scintillator shows a characteristic peak, i.e. the MIP peak. Once identified, the position of this peak can be used to characterize and calibrate the detector, and to correct for changes in the optoelectronic transfer function, i.e. scintillator and fiber light yield, as well as SiPM or PMT efficiency. Instead of the convoluted 23-parameter function, a simplified fit was performed. It will be discussed in this subsection.

The gain of an SiPM can be measured by identifying the Fingers in a charge or amplitude spectrum, see chapter 4 on page 35ff. The UB featured a separate logic for calibration purposes that triggered mainly on single muons whose rate was found to be 2 kHz for a single WCD station on average [123]. With a 2-fold coincidence on WCD tank PMTs [133], calibration histograms were generated based on the energy deposited by crossing secondary particles. The charge-monitoring allowed for continuous calibration of the Surface Detector (SD). These calibration histograms were sent to the central DAQ system e.g. whenever a high-level trigger condition for this station was met.

In the case of the ASCII detector, two ASCII scintillators were installed on a single WCD. While the UB only featured three independent analog signal inputs, two of the three WCD PMTs had to be disconnected. This led to somewhat complicated trigger conditions on a 2-fold of the single PMT and the two ASCII detectors. The ASCII detectors took calibration histograms. The UB integrated over an integration gate of 20 samples, i.e. 500 ns, around the trigger position and stored this value in a buffer. The author applied a fit of the form

$$\frac{\mathrm{d}N}{\mathrm{d}x}(x) = \sum_{n=0}^{\infty} \sum_{m=0}^{n-1} \left(\left(D\, p_{\lambda,n-m} + \sum_{i=1}^{2} E_i\, p_{\gamma i,n-m} \right) \cdot p_{\mathrm{xt},m} \cdot p_{\mathrm{xt},0}^{n-m-1} \cdot b_{m,n} \right) \cdot f(x - x_n, \sigma_n)$$
$$+ \sum_{n=1}^{\infty} M\, p_{\mu n,\beta} \cdot g(x - x_n, \sigma_n) \tag{5.14}$$

to the calibration histograms obtained from the ASCII stations. Here, x denotes the charge per analog-to-digital converter (ADC) count in the calibration histograms. This spectrum function is a semi-analytical convolution of the single cell response through equation (4.13) on page 47, and the fluorescence light yield, parameterized through equation (5.13) from above. Both spectral distributions influenced the spectrum function in equation (5.14). The substitutions

$$f(x,\sigma) = (1-\alpha) \cdot g(x,\sigma) + \alpha \cdot \frac{\rho \cdot (-x+g)^{\rho-1}}{2\,g^\rho} \cdot \left(\mathrm{erf}\left(-\frac{x-g}{\sqrt{2}\,\sigma} \right) - \mathrm{erf}\left(-\frac{x}{\sqrt{2}\,\sigma} \right) \right)$$

$$p_{\gamma i,k} = \gamma_i^k \cdot (1-\gamma_i)$$

$$p_{\mu n,\beta} = \exp\left(1 - \frac{n-\mu}{\beta} - \exp\left(-\frac{n-\mu}{\beta} \right) \right)$$

hold, together with the relations introduced in the last chapter. The dark noise of the SiPM was expected to occur randomly in the integration gate at any time. A Poisson distribution well described its abundance in the integration gate. The Poisson distribution is denoted $p_{\lambda,n}$ with its expected value λ being a function of the dark noise rate and the integration gate width. Due to its random nature, it so happened that only a fraction of the pulse was integrated, that was when only a part of the pulse was inside the integration gate. This effect leads to asymmetric *fingers*. Although this effect could be described analytically with $1/x$ and $1/(1-x)$ relations, folded with Gaussians, the author used a distribution $f(x,\sigma)$ which was similar to the afterpulsing excess charge from the last chapter to estimate this effect. $f(x,\sigma)$ contained a normal distribution with relative abundance $1-\alpha$ and an asymmetric excess proportional to α. In the event of $\alpha \to 0$, $f(x,\sigma)$ approached an ideal Gaussian. The author chose $\rho \equiv 2$ and left α free. The first summand in the first line of above equation describes the dark noise contribution mathematically.

The second summand of the first line estimates the low-energy deposit in the scintillator. Two exponential functions $p_{\gamma 1/2,n}$ were convoluted with the effect of optical crosstalk through its probability p_{xt}, also of exponential nature. Again, it was expected that this low-energy contribution did not prompt any trigger conditions. It was therefore folded with the asymmetric finger distribution $f(x,\sigma)$.

The last line describes the effect of minimal ionizing particles through a single Gumbel distribution $p_{\mu n,\beta}$. Here, it was expected that the signal was well contained in the integration gate, as the major MIP contribution was found to be originating from muons on which the WCD triggered efficiently. Confer with figure 5.4 from above. The MIP contribution was therefore multiplied with correlated, yet symmetric Gaussians.

Figure 5.6 contains two calibration histograms. Both histograms were recorded by UB electronics from operating ASCII detector stations of the Pierre Auger Observatory in Argentina in season 2016/2017. Its left-hand side shows the calibration histogram of an ASCII detector that ran a Hamamatsu S13360-6025PE, 25 μm, 6 mm × 6 mm SiPM. The right-hand side shows that of a Hamamatsu S13360-6050PE, 50 μm, 6 mm × 6 mm SiPM. Both figures include fits as per equation (5.14).

The single photon peaks are very prominent for the 50 μm SiPM, in contrast to the 25 μm. This can be quantified by the fit results of the gain versus the electronic noise root mean square (RMS) and the pe width, as

$$\left(\frac{g}{\sigma} \right)_{50\,\mu\mathrm{m}} \approx \frac{19.3}{3.6} \approx 5.3 \quad \text{and} \quad \left(\frac{g}{\sigma} \right)_{25\,\mu\mathrm{m}} \approx \frac{8.1}{4.0} \approx 2.0. \tag{5.15}$$

From the last chapter it is known, that the SNR is proportional to the gain in the case of random integration. While the *noise*, i.e. width in this context, is very similar for both types of SiPMs, the gain of the 25 μm is only 42 % of that of the 50 μm SiPM. This value fits nicely to the gain ratio of both SiPMs published in the datasheets by Hamamatsu, i.e. $7 \cdot 10^5$ versus
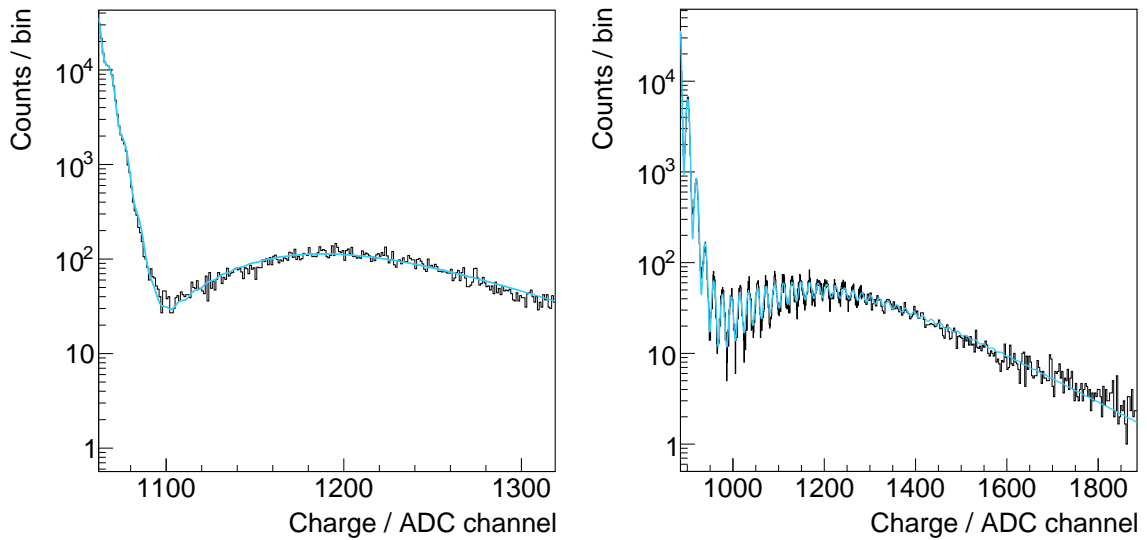
Figure 5.6.: *Left:* A Finger spectrum as obtained from the ASCII stations via the UB calibration histogram includes a correlated Gaussian fit, see equation (5.14), for a Hamamatsu S13360-6025PE and *right:* for a Hamamatsu S13360-6050PE. Notice the different scales of the horizontal axes. Credits to the data belong to the Pierre Auger collaboration.

$1.7 \cdot 10^6$ [53] which yields 41 %. This makes sense, as the SiPMs were scheduled to operate at their nominal operating voltages which was corrected for temperature changes. Also, the pre-amplifiers of both types of SiPM modules were running with the same gain, within the variation of the 1 % resistor tolerances. This indicates that the amplification of the high-gain pre-amplifier channels shall be increased by a factor of 2 to 3, when it is scheduled for a 25 μm SiPM in the future.

The most probable value of the MIP contribution was found at (16.1 ± 2.2) pe for the 25 μm and at (15.9 ± 1.2) pe for the 50 μm SiPM modules averaged over a three-month period. A quantitative comparison between the 50 μm and the 25 μm SiPM modules cannot be made, as the position of the MIP maximum not only depends on the PDE of the SiPM yet also on the quality of the optical coupling of the WLS fibers to the scintillator and to the SiPM. This underlies fluctuations whose width is expected to depend on the stability of the detector and coupling design. It seems that the optical efficiency of the 50 μm is much worse, about 50 % of that of the 25 μm ASCII station. It is, however, apparent that in both cases, the MIP maximum can be well separated from low-energy background and noise. Both types of SiPMs seem to be promising alternatives to PMTs.

The ASCII modules of the final revision operated for about one year. Once the gain of the SiPM and the MIP in units of pe was determined from the calibration histograms, the SiPM and scintillator long-term stability and temperature-dependence could be investigated. However, due to the low SNR of the 25 μm, the following results were taken from the data of the 50 μm SiPMs.
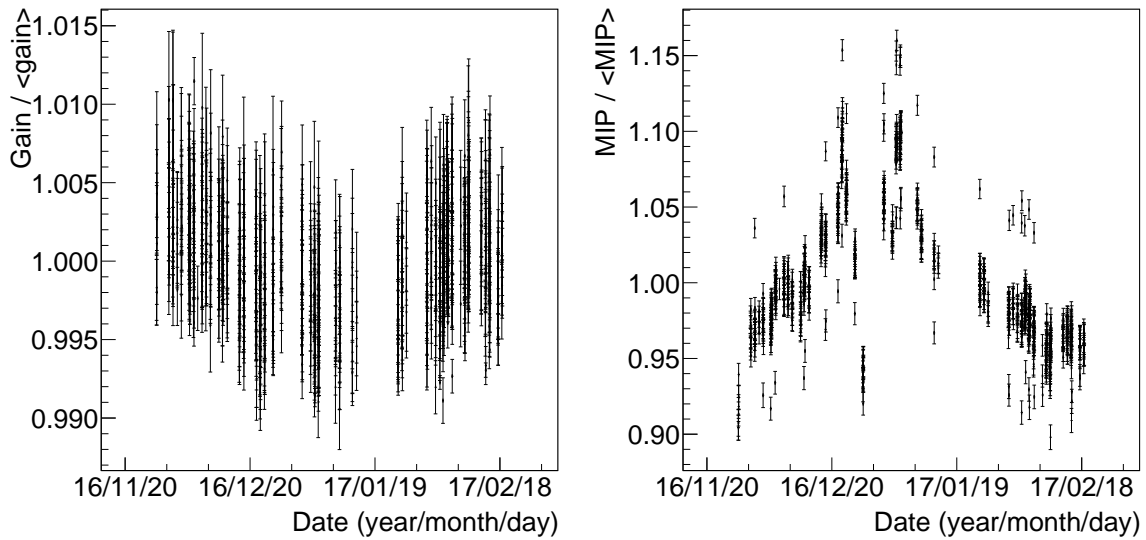
Figure 5.7.: *Left:* Evolution of the SiPM gain stabilized against temperature as extracted from finger spectra versus time and *right:* the evolution of the maximum of the MIP contribution versus time. Both figures were obtained from data of the Hamamatsu S13360-6050PE. Shown is a three-month period of the dataset during the summer of 2016/17 in the Southern hemisphere. The upper and lower bounds of the vertical axes are $\pm 1\,\%$ (*left*) and 15 % to $-10\,\%$ (*right*), respectively.

5.2.4.2. Time evolution of the SiPM gain and the MIP maximum

The SiPM gain and the most probable value, resp. the position of the maximum of the MIP distribution were extracted from calibration spectra with the help of spectral fits as introduced earlier, confer with equation (5.14). Only a three month period was analyzed towards gain and MIP stability as a long-term light loss of the scintillator due to aging of 2.8 % per year was expected [2]. Figure 5.7 shows the SiPM gain on the left and the position of the MIP maximum on the right, both normalized to their average values. The horizontal axes represent the time in equidistant bins, from November 20th, 2016 to February 18th, 2017.

Time periods exist where no data is shown. This had not been a problem with the data analysis. Merely, the whole detector did not transmit any data at these times, neither through its slow control nor physics triggers. This most probably originated from hardware failures, e.g. a problem related to the power supply, as no data was transmitted between dawn and dusk, see figure A.4 in appendix A.7.

The SiPM gain had been stable within $\pm 1\,\%$ in the time where data was available. Meanwhile, the position of the MIP maximum apparently changed more drastically, by up to 15 % to $-10\,\%$. However, it was found, that some of these changes were due to problems with the fitting algorithm. Since the position of the pedestal was on the far left of the histograms, see figure 5.6, the automatic spectrum fitting algorithm estimated the MIP maximum wrong by integer multiples of one pe. The data left from the margin was cut by the UB algorithm and was thus not available to the author. This cut happened to be on the left or on the right-hand side of the pedestal which worsened the fit result. This error probably originated from the fact that the UB algorithm was not designed for an operation of an ASCII detector running an SiPM. However, the reconstruction of the SiPM gain was not affected by this issue.
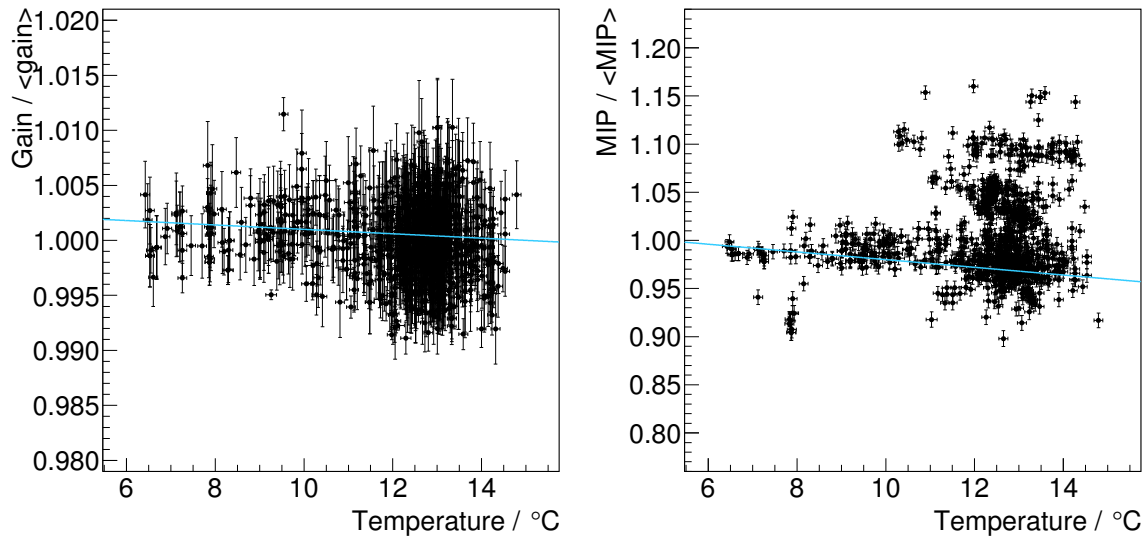
Figure 5.8.: *Left:* Temperature dependence of the SiPM gain as extracted from finger spectra and *right:* the temperature dependence of the MIP per pe corrected for the change in the SiPM gain, each normalized to the mean of its distribution. The same period as in figure 5.7 is shown for the same SiPM. Linear polynoms are shown to guide the eye (*left:* $-0.01\,\%\,\mathrm{K}^{-1}$, *right:* $-0.39\,\%\,\mathrm{K}^{-1}$).

It shall be noted, that a gain or MIP-stability of 100 % is not required since the live-monitoring of the single pe and MIP provides calibration data. However, it is desirable to operate the SiPM with a stable gain to reduce systematics through changes in PDE, afterpulsing, and crosstalk while the live-monitoring is unavailable or when data transmission is unstable.

5.2.4.3. Temperature dependence of the SiPM gain and the MIP maximum

The author correlated the SiPM gain and the position of the MIP maximum with temperature which will be presented in the following. Due to the number of black time periods, only a minimal number of monitoring data was available. The slow control data was transmitted in regular intervals which statistically did not coincide with the transmission of calibration histograms. For some events, no temperature was monitored in the last 30 min. The author did not use the monitoring data of a different, near-by ASCII station but removed these points from the plots.

While the temperature was monitored on the electronics board, the author expected it to reflect the core temperature of the SiPM because of its relatively large thermal conductivity. Atomic silicon, for example, has a thermal conductivity of $149\,\mathrm{W\,m^{-1}\,K^{-1}}$ [134, table 4.1]. On the other hand, polystyrene and plastics in general are good thermal isolators with thermal conductivities between $0.03\,\mathrm{W\,m^{-1}\,K^{-1}}$ and $0.3\,\mathrm{W\,m^{-1}\,K^{-1}}$ [134, table 10.2]. Due to the size of the ASCII scintillator, the author expected the temperature of the scintillator to react more slowly to ambient temperature changes. The author chose to apply a low-pass filter on the temperature data with a time constant of 30 min. The author varied the time constant between a few seconds, i.e. zero, and 90 min to estimate its systematic effect on the resulting distributions. Due to this artificial alteration of physical data, especially using arbitrary time constants, the results presented here shall be perceived only qualitatively.

The results are shown in figure 5.8. The change of the SiPM gain with temperature was compatible with zero. A linear fit produced a temperature progression of $(-0.01 \pm 0.02)\,\%\,\mathrm{K}^{-1}$, indicating that the width of the distribution, or more likely the errors on the SiPM gain, is too high to identify a non-zero temperature progression. It can be concluded, however, that the gain was stable within $\pm 1\,\%$.

In the case of the MIP maximum, the misidentification of the baseline becomes evident in this plot. Therefore, a fit was applied only to the majority of the data whose baseline was reconstructed with less than one pe off the mean. Its relative change with temperature was found to be $(-0.4 \pm 0.2)\,\%\,\mathrm{K}^{-1}$. The systematic error originated from the time constant of the temperature data that was introduced artificially. Typical plastic scintillators show temperature variations of their light output between $-0.2\,\%\,\mathrm{K}^{-1}$ and $-0.3\,\%\,\mathrm{K}^{-1}$ [135], not including the temperature effect of WLS fibers. In [136], it was reported that the average temperature dependence of the scintillators for SSDs was found to be less than $5\,\%$ during a day-and-night temperature cycle. In a different paper, it was published with $-0.26\,\%\,\mathrm{K}^{-1}$ [54]. All values were compatible with the result found here.

5.2.5. High-level results

Extensive high-level analyses on the ASCII SiPM dataset were performed in [137]. Its conclusion was that the measured value differed from the expected value through the universality theory by $20\,\%$ and $50\,\%$ in the case of the $50\,\mu\mathrm{m}$ and $25\,\mu\mathrm{m}$ SiPMs, respectively. Otherwise, the first results looked promising [137].

The author of this thesis further studied the response of an ASCII station in coincidence with SD of the regular array of the Pierre Auger Observatory. The scintillator light-yield per minimal ionizing particle was calibrated with the use of Finger spectra and correlated fits on an event-by-event basis. With the extraction of the most probable value of the underlying MIP distribution, ADC traces that were recorded by the UB, were converted from ADC counts into multiples of the position of the MIP maxima. For systematic studies and comparisons with simulations, the same procedure has to be applied to simulations. This, however, was not a part of this thesis.

As described above, the UUB integrated over $500\,\mathrm{ns}$ to accumulate data in its charge histograms by calculating the sum over 20 samples à $25\,\mathrm{ns}$. To simplify the analysis, the author also chose an integration gate width of $500\,\mathrm{ns}$. First, the author subtracted the baseline from ADC traces. In this analysis, the baseline was defined as the average value whose RMS was the smallest over 20 samples. Finally, 20 samples around the trigger position were summed up, starting from five samples prior to the trigger location. This value was converted into a number of MIPs by applying the results of the finger spectrum fits, i.e. the SiPM gain in units of pe per integrated ADC count and the most probable value of the MIP distribution in units of pe.

The left-hand side of figure 5.9 shows the ADC trace of one event recorded by the high-gain channel in one ASCII station that operated a $50\,\mu\mathrm{m}$ SiPM. The horizontal axis needs to be divided by the sampling rate of $40\,\mathrm{MSa\,s}^{-1}$, while the vertical axis has to be multiplied with the ADC voltage reference of $2\,\mathrm{V}$ divided by the sampling depth of $10\,\mathrm{bit}$ to obtain units according to the système international d'unités – International System of Units (SI). From left to right, the full scale of the horizontal axis corresponds to about $20\,\mu\mathrm{s}$. The author chose a logarithmic vertical axis to reveal the single photon equivalents, e.g. at the very beginning of the trace, and the prominent undershoot right after the main pulse starting at sample number 400. As the sample depth was $10\,\mathrm{bit}$, i.e. 1024 ADC counts, the high-gain channel was about to saturate
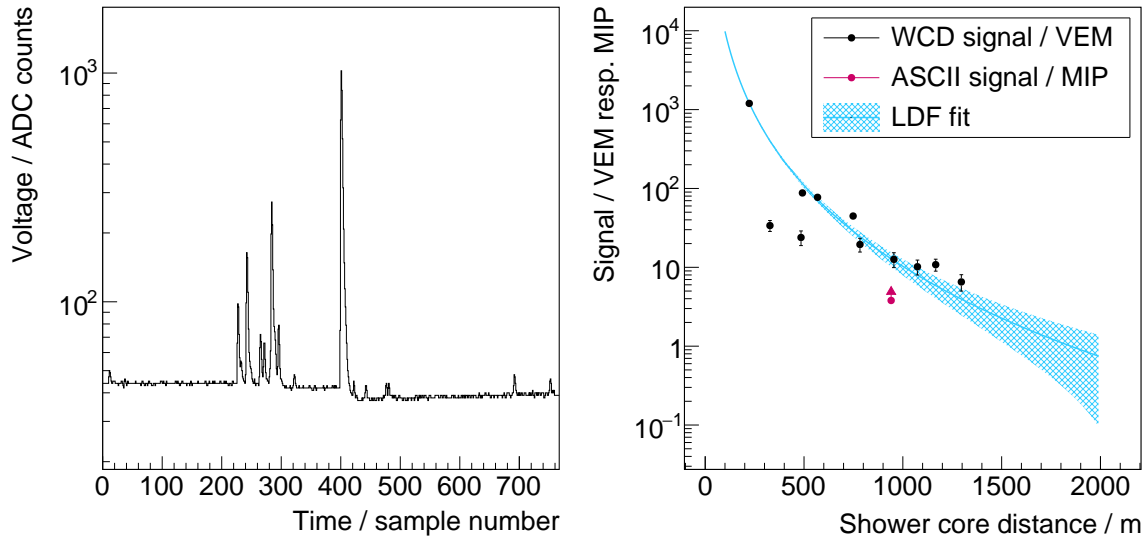
Figure 5.9.: *Left:* The ADC trace of an SiPM-equipped ASCII station that triggered on a cosmic ray event with event ID 40419594. *Right:* The signal in WCD stations (black points) that were read out in coincidence with event 40419594 versus their radial shower core distance. A fit through the standard SD reconstruction (blue curve) and the ASCII signal estimator (red point) is also given. The energy of that event was reconstructed as $2.5 \cdot 10^{18}$ eV with $\overline{\text{Off}}\underline{\text{line}}$ [138].

leading to the undershoot. If the signal was any larger, the signal size in MIP had to be extracted from the low-gain channel by multiplying its charge with the gain ratio between both channels of about 33 dB. The gain ratio can be determined a posteriori from non-saturating events or a priori in the lab.

For this particular event, the charge generated by the SiPM seemed to correspond to about 3 MIP, or equivalently close to 50 pe. With the standard reconstruction employed in the $\overline{\text{Off}}\underline{\text{line}}$-framework [138] developed by the Pierre Auger collaboration, the signal size of nearby WCD stations was extracted and plotted versus the reconstructed shower core radial distance. This is shown on the right-hand side in figure 5.9. The plot shows the lateral distribution of the shower. The signal size of every station was converted into multiples of a vertical equivalent muon (VEM), indicated by the black dots. A lateral distribution function (LDF) of the form

$$S(r) = \tilde{C} \cdot \left(\frac{r}{r_s} \right)^{-\beta} \cdot \left(1 + \frac{r}{r_s} \right)^{-\beta}, \quad \beta > 0 \tag{5.16}$$

can be used to parameterize the radial shower signal [19, p. 326]. Depending on the mixture of particle species that dominate the signal in the detector system, many variations of the above parameterization exist. From the fitted parameters and the zenith angle of the shower axis, the energy of the shower can be estimated. In the case of the event shown above, the energy was reconstructed with $2.5 \cdot 10^{18}$ eV [138].

The author also added the 3 MIP data point with a distance of about 940 m from the impact point of the shower to the WCD station on which this very ASCII module was installed. The data point is colored in red. The author included an error arrow to indicate that the high-gain channel was close to saturation and, due to the undershoot of the signal, the number of

MIP multiples was most probably larger. The number of particles crossing an ASCII station is expected to be smaller than for a WCD station because the aperture of an ASCII is smaller, about 40 % [136]. However, this does not directly translate to the signal size, as the response of the ASCII is different from that of a WCD, indicated by the different units of measure, i.e. MIP versus VEM. Also, for showers of rather low energy and stations far away from the shower core, fluctuations in the signal can be significant.

If more ASCII stations were deployed and fully operational, an LDF could be fitted to their signals. From the parameters obtained through the fits of both LDFs, i.e. the one for the WCDs and the ASCIIs, the muon signal could have been estimated, see chapter 3.

5.2.6. Conclusions

The following steps could be identified towards a successful SiPM module for SSD: The 25 µm performed well enough in ASCII to be chosen as the baseline design for the final SSD SiPM solution. Its MIP and pe resolution was satisfactory but could be improved with a reduced noise floor of the electronics, a higher amplification, and a faster DAQ. Nevertheless, 50 µm SiPM modules should be developed in parallel to check the systematics of the many changes in the detector environment: ASCII was being replaced with SSD, probably changing the optical output of the WLS fibers due to the changes in the detector system. The UUB relieves the UB, introducing an unknown DAQ system and its *features*. Two SiPMs needed to be supplied and read out instead of one, and the pre-amplifiers had to serve the full dynamic range from below 1 pe up to 12 000 MIP in amplitude which is a dynamic of more than 10^5, or equivalently 17 bit to 20 bit, depending on how 1 MIP translates to 1 pe. However, due to the success of the ASCII SiPM modules, it had been decided to equip three SSD stations in the field with SiPM modules which will be introduced in the following. The ASCII detectors were decommissioned in 2018, and their hosting WCD tanks continued to operate in the standard SD configuration.
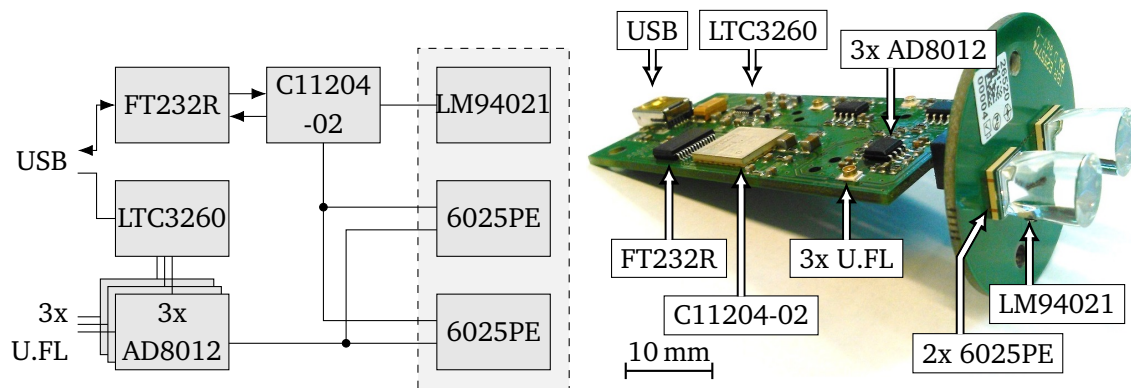
Figure 5.10.: *Left:* Schematic overview of the SSD SiPM optoelectronic module and *right:* a picture showing the electronics, the two SiPMs, type Hamamatsu S13360-6025PE [53], and the two light-guiding cones. The dashed box on the *left* indicates that these components are mounted on the circular board, see picture on the *right* – the picture was taken from [54]. Refer to the text for details.

5.3. The SSD SiPM module

The first step of the development process of the SSD SiPM module was the SiPM selection. The same light-guiding cones were used that had also been installed in the final ASCII prototypes, see the last section. A bipolar supply for the pre-amplifiers needed to be developed that was sourced from the 5 V 100 mA-limited USB host of the UUB with the use of the Linear Technology LTC3260 [139]. A redesign of the ASCII pre-amplifiers which were based on the Analog Devices AD8012 was necessary to serve the full dynamic range. The Hamamatsu C11204-02 bias voltage generator chip was reused from the ASCII modules, and its control was enabled through the FTDI FT232R [140] UART-to-USB bridge, without the need of a microcontroller.

Once again, the development process took several months and burned a lot of resources, prototype PCBs, and so on. Not all intermediate steps will be discussed in the following. The final pre-amplifier solution was developed in collaboration with colleagues from Istituto Nazionale di Fisica Nucleare, Sezione di Lecce, Italy. A schematic sketch and a picture are given in figure 5.10.

The SSD SiPM module consisted of two PCBs. A circular PCB held two SiPMs, the temperature sensor, and a connector while the rectangular PCB featured the power supply, the digital interface, and pre-amplifiers. Both PCBs were produced in industry. A professional soldering company [96] soldered the circular PCBs since the demands on the placement resolution of the two SiPMs was quite high [54]. The author soldered the rectangular PCBs.

5.3.1. SiPM selection

Two SiPMs of the same type needed to be supplied by the same bias voltage and read out in a single circuit. This meant that both SiPMs had to be as similar as possible, i.e. their breakdown voltages had to be as equal as possible. 20 SiPMs of type Hamamatsu S13360-6025PE and 20 of type Hamamatsu S13360-6025PE had been acquired, each type with a breakdown voltage span of ±150 mV. From these SiPMs, combinations of two devices were selected with a difference in the nominal overvoltage of less than 1 %, i.e. a breakdown voltage difference of max. 50 mV

and 30 mV for the 25 μm and 50 μm SiPMs, respectively. Within the resolution of the stated breakdown voltages, i.e. 10 mV, the selection succeeded.

With the results from the last chapter, the change in PDE, gain, crosstalk, and afterpulsing can be investigated for a change in bias voltage of up to 30 mV, in other words for the Hamamatsu S13360-6050PE, the worst case scenario: Given in absolute percentage points, the crosstalk probability would change by (0.055 ± 0.004) %, the afterpulsing probability by (0.040 ± 0.015) % and the PDE by approx. 0.5 %. The 1 % change in overvoltage becomes critical at the upper limit of the dynamic range where a 0.5 % change in PDE and gain goes along with a 10 % change in reconstructed photons. By determining calibration spectra and deconvolving the SiPM gain from the position of the MIP maximum with correlated spectral fits, the change in PDE can be reconstructed and accounted for in the analysis.

Both SiPMs were soldered on a circular PCB by an assembling expert [141] with professional machines and a placement resolution of about 50 μm [96]. The sensitive areas of the SiPM packages were arranged rotationally symmetric around the center of the PCB meaning that the active areas of both SiPMs switched places after a 180° rotation. Three holes were drilled on a circle of 26 mm diameter. The angular position of the three holes was asymmetric. This guaranteed that the SiPMs and their cones were directly beneath the fiber bundles after installation of the optoelectronic module.

5.3.2. The low-noise bipolar power supply

A clean power supply for the pre-amplifiers is as important as the design of the pre-amplifiers themselves. The power supply rejection ratio[4] of the AD8012, for example, worsens from -60 dB at about 200 kHz to about -30 dB to -20 dB at 100 MHz [124]. Inverting switching converters induce low-frequency ripple and high-frequency transient noise into the system. The latter also radiates on nearby traces and e.g. ground, making a professional PCB design essential. Otherwise, the electronic noise spikes would get amplified by the pre-amplifiers ruining any analysis on the single pe level.

Similar to the early revisions of the bias voltage design, it was decided in this work to go for a design that featured a switching converter, a post-linear regulator, and a RLC-filter to eliminate its electronic noise, for the negative as well as for the positive ± 3.3 V supply. The Linear Technology LTC3260 [139] is a capacitive switching converter that inverts its input voltage v_{in} to about $v_{neg} = -v_{in}$. The LTC3260 also features linear regulators for both voltage rails, v_{in} and v_{neg}. By adding external feedback resistors $R_{+,1/2}$ and $R_{-,1/2}$, the bipolar voltage supply $v_{\pm}$ can be set to about ± 3.3 V, in the same fashion as given by equation (5.4). The reference voltages are provided by the LTC3260.

The output voltages $v_{\pm}$ were filtered by external, single stage RLC filters with $R = 10\,\Omega$, $L = 100\,\mu H$ and $C = 10\,\mu F$. By probing the filtered voltages with an appropriate technique [108] (p. 549f.), the switching noise was found to be 100 μV peak-to-peak at a bandwidth of 100 MHz [54].

5.3.3. The final pre-amplifier design

The final pre-amplifier design allowed to resolve the single pe and technically served the complete dynamic range of up to 12 000 MIP. As the latter depended on the PDE and the efficiency

---

[4]The PSRR of an amplifier is a frequency-dependent quantity that describes what amount of power propagates from the amplifier's supply rails onto its output node.
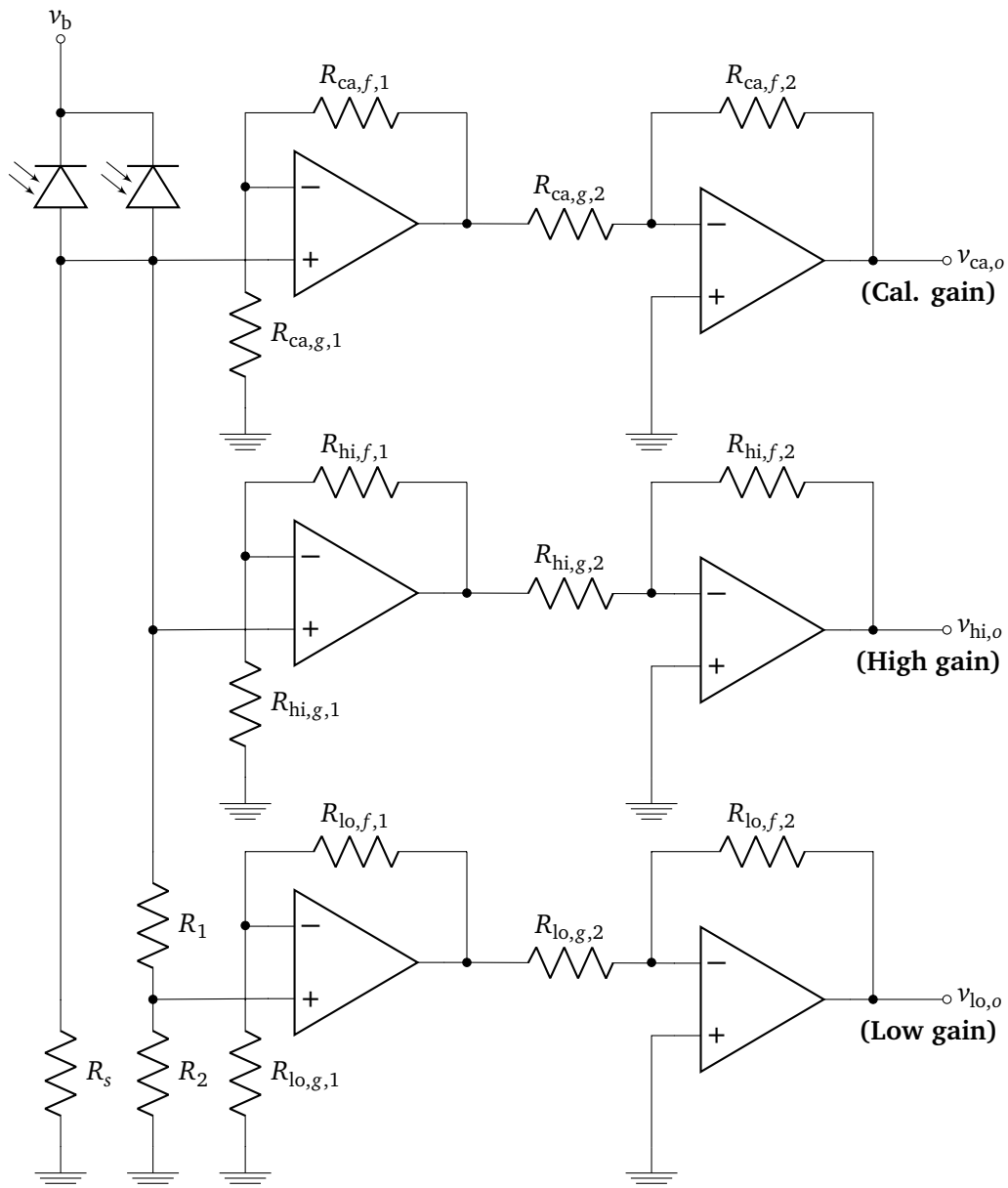
Figure 5.11.: This image shows simplified schematics of the pre-amplifiers of the SSD SiPM module. Three channels were implemented, from top to bottom: The calibration gain, the high-gain and the low-gain. The SiPMs were connected in parallel and loaded with $R_s \parallel (R_1 + R_2)$. See text for details.

of the optical system – scintillator, fibers, cookie, and cones – the technical phrasing of the dynamic range aspect was changed: The dynamic range needed to serve signal amplitudes of 28 800 pe and 115 200 pe for the Hamamatsu S13360-6050PE and the S13360-6025PE at the nominal overvoltage, respectively. These numbers originate from the number of cells which means that if all cells break down at the same time, the output voltage will not saturate the low-gain channel. The pre-amplifiers were structured in three channels, i.e. the calibration channel, the high-gain channel and the low-gain channel which was realized with three packages of the AD8012 CFA. The AD8012 holds two amplifiers in one chip. As one requirement was to generate negative pulses, and the signal was decoupled from the low-voltage side of the SiPM, one of the two amplifiers in the AD8012 had to invert the signal polarity exactly once for every channel individually.

The final solution was based on a shunt resistor bridge: The two SiPMs were connected in parallel. Both SiPMs were loaded with resistors R_s, R_1 and R_2 that introduced a load of $R_s \parallel (R_1 + R_2)$. Although R_s was optional, adding this resistor allowed for more combinations of total load impedance due to the limited number of E-series resistances, yielding higher flexibility. The calibration channel and the high-gain channel were decoupled from R_s, whereas the low-gain channel was split from R_2. The total load impedance was fixed to $50\,\Omega$ which was not an arbitrary choice – an optimum between a good SNR, i.e. a large impedance, and a small signal decay time, i.e. a small impedance, that was found through iterative testing and simulation. A rather large load was chosen since the integral of the signal is proportional to the load impedance, and the signal fraction of the slow decay time constant increases, too. Please refer to the SiPM chapter, for details on how the shunt resistor affects the signal shape.

The combination of R_1 and R_2 divided the total voltage drop across R_s at the input of the low-gain channel – a necessity to map the full dynamic range, e.g. 115 200 pe, to the technical dynamic range of 0 V to −1.9 V. With the passive voltage divider, any dynamic range should be achievable theoretically.

To overcome the problem of the feedback current distortion and its associated change of load impedance with signal size, see discussion in the ASCII pre-amplifier section, the first stage of the AD8012 was connected as a non-inverting amplifier. The non-inverting input of a CFA, i.e. of the AD8012, is high-ohmic and isolated from its output. Therefore, when the first stage of the calibration channel becomes saturated, the resistor bridge is kept isolated from the feedback current of the AD8012. To achieve a negative voltage swing between 0 V and −1.9 V, the second stage of the three channels had to be implemented as an inverting amplifier each, provided by the second AD8012 amplifier in each of the three packages. Figure 5.11 visualizes this concept.

For a given amplification a, that is the product of two amplifiers $a = a_1 \cdot a_2$ that are connected in series, the electronic noise n is expected to behave like $n \sim a_1^{-1}$ and $n \sim a_2$, for large a_1 resp. a_2. This is, because the second amplifier also amplifies the electronic noise of the first stage. A large a_1 and a small a_2 are therefore preferred.

The total transimpedance r_j of the three channels $j = \mathrm{ca, hi, lo}$ can be quantified with

$$r_j = \frac{R_1 + R_2}{1 + (R_1 + R_2)/R_s} \cdot a_j, \quad j = \mathrm{ca, hi, lo}, \tag{5.17}$$

where

$$a_j = -\left(1 + \frac{R_{j,\,f,\,1}}{R_{j,\,g,\,1}}\right) \cdot \left(\frac{R_{j,\,f,\,2}}{R_{j,\,g,\,2}}\right), \quad j = \mathrm{ca, hi} \tag{5.18}$$

and

$$a_j = -\frac{R_2}{R_1 + R_2}\left(1 + \frac{R_{\mathrm{j,\,f,\,1}}}{R_{\mathrm{j,\,g,\,1}}}\right)\cdot\left(\frac{R_{\mathrm{j,\,f,\,2}}}{R_{\mathrm{j,\,g,\,2}}}\right),\quad j = \mathrm{lo}\tag{5.19}$$

is the total voltage amplification of the calibration (ca), high-gain (hi) and low-gain (lo) two-stage channels, 1 and 2. Equations (5.17) through (5.19) only hold in the mid-frequency limit, i.e. at about 1 MHz.

As mentioned above, detailed simulations with the Simulation Program with Integrated Circuit Emphasis (SPICE) framework, and analytical calculations were performed to justify the choice of the feedback R_f and gain resistors R_g. These simulations were reviewed by dedicated lab measurements thereupon. Afterward, the SPICE simulations were tuned with the findings on the experimental data and the process started over. R_f and R_g were selected according to the following thoughts, described in detail for the two Hamamatsu S13360-6025PE 25 µm SiPMs:

The author reanalyzed the nonlinearity data from the SiPM homogeneity measurement, see last chapter. This time, the author extracted the pulse heights instead of the pulse integrals and plotted them against the light emitting diode (LED) current which was a measure for the number of photons on the SiPMs, consistently with figure 4.14 on page 68. The pulse height is the quantity that drives the selection of the amplification in the pre-amplifiers to avoid signal saturation and signal clipping. Ergo, the author applied equation (4.45) to the pulse height data versus LED current and extrapolated the maximum pulse height. The author found that the curve saturated below 4 V at a load of 50 Ω and a read-out bandwidth of 100 MHz. To map this quantity to the dynamic of the low-gain channel of about 2 V the SiPM signal had to be divided by a factor of 2.

By choosing $R_s = R_1 = R_2 = 75\,\Omega$, the transimpedance of the resistor bridge became $r_{\mathrm{ca/hi}}/a_{\mathrm{ca/hi}} = 50\,\Omega$ for the calibration and high-gain channel and $r_{\mathrm{lo}}/a_{\mathrm{lo}} = 25\,\Omega$ for the low-gain channel. The input for the low-gain channel was therefore divided by 2 in the resistor bridge. The feedback and gain resistors in the two stages 1 and 2 for the calibration, high-gain, and low-gain channel, i.e. $R_{\mathrm{ca,hi,lo;\,f,g;\,1,2}}$ were chosen to fulfill the dynamic range and to optimize SNR and cross-calibration of the three channels, see discussion above.

The purpose of the calibration channel was to amplify the SiPM signal in such a way that the single photon equivalents were distinguishable from electronic noise. Also, signals with equal to or more than 3 MIP[5] needed to be amplified without saturation of the channel, i.e. the output signal of 3 MIP must be smaller than 1.9 V, see chapter 3 on page 23ff. This allowed an identification of the number of MIP per pe, i.e. an in-situ characterization of the optical response of the detector. Arbitrary values were used at first that were motivated by the findings of the last chapters, and a characteristic signal size of about $30\,\mathrm{pe\,MIP^{-1}}$ was identified in a prototype detector. It was found that a single-stage voltage amplification of about 10^2 was necessary, to distinguish the single pe from each other. $R_{\mathrm{ca;\,f;\,1}} = 1\,\mathrm{k\Omega}$ and consequently $R_{\mathrm{ca;\,g;\,1}} = 10\,\Omega$ were chosen. The second stage did not improve SNR anymore as it also amplified the electronic noise of the first stage. Finally, $R_{\mathrm{ca;\,f;\,2}} = 750\,\Omega$ and $R_{\mathrm{ca;\,g;\,2}} = 220\,\Omega$ were chosen that mapped the output voltage to the desired range. A feedback resistance of 750 Ω is the preferred choice according to the manufacturer [124].

The situations for the high-gain and low-gain channel were different. The signal shape of the high-gain and low-gain channel at the ADC of the UUB should be as similar as possible

---

[5] Here, 1 MIP is the voltage amplitude of signals that correspond to the most-probable value of its contribution.

$i =$	ca	hi	lo
R_s	75 Ω		
R_1	75 Ω		
R_2	75 Ω		
$R_{i,f,1}$	1000 Ω	430 Ω	750 Ω
$R_{i,g,1}$	10 Ω	130 Ω	(open)
$R_{i,f,2}$	750 Ω	430 Ω	750 Ω
$R_{i,g,2}$	220 Ω	150 Ω	750 Ω
$\langle |r_i| \rangle$	17 216 Ω	617 Ω	25 Ω
$|a_{\text{calc}}|$	344.3 ± 1.4	12.35 ± 0.04	0.500 ± 0.002
$|a_{\text{simu}}|$	329.2 ± 1.3	12.09 ± 0.04	0.490 ± 0.001
$|a_{\text{meas}}|$	319.5	12.10	0.495

Table 5.1.: This table summarizes the resistor values and the transimpedance gain of the three SSD SiPM module amplifier channels, calibration, high-gain and low-gain for the 25 μm-SiPMs. The values for the 50 μm-modules are given in table A.1 in appendix A.9 on page 170. Resistors from the E-24-series were selected. Their impact on the transimpedance gain is given by equations (5.17) through (5.19). The errors on a_{calc} and a_{simu} are of systematic origin emerging from resistor tolerances.

to allow an inter-channel cross-calibration. That meant that the response of both channels against the signal frequency had to be flat or at least the same up to the corner frequency of the anti-aliasing filter of the UUB, i.e. up to 60 MHz. Also, the signal of a typical MIP should be distinguishable from the electronic noise in the case of the high-gain channel. The low-gain channel, on the other hand, should map the technical dynamic range of 1.9 V to the total number of cells of the SiPMs, i.e. to 10^5 pe. Furthermore, the overlap between the high-gain and low-gain channel should be large enough to allow a cross-calibration between the channels, to translate the signal in the low-gain channel into units proportional to a MIP. After dozens of iterations, resistor values were found that were in accord with the requirements listed above: $R_{\text{hi; f; 1,2}} = 430\,\Omega < R_{\text{lo; f; 1,2}} = 750\,\Omega$, $R_{\text{hi; g; 1}} = 130\,\Omega$ and $R_{\text{hi},g,2} = 150\,\Omega$ served the highest amplification possible for the AD8012 within the −3 dB frequency limit of 60 MHz. With $R_{\text{lo},g,1}$ left open, and $R_{\text{lo; g; 2}} = 750\,\Omega$, the high-gain to low-gain transimpedance ratio became about 25. The final resistor values, all complying with the E24-series of preferred numbers, are listed in table 5.1.

The outputs of the three amplifier channels were not optimized for any impedance system such as 50 Ω but they were expected to work with any standard impedance, i.e. 50 Ω, 75 Ω, or 93 Ω, as long as the coaxial cables were not long and the system was terminated correctly.

The output connectors were of type Hirose U.FL-R-SMT-1(10) [142]. These connectors are optimized for high-frequency 50 Ω signals. With U.FL to SMA pigtails and optional SMA to BNC connectors, the system matches the input specifications of most DAQ systems. Results of the pre-amplifier test procedures are given at the end of this chapter.

5.3.4. The digital control

Instead of using a microcontroller to program the C11204-02, a Mini USB type B connection was implemented. The FTDI FT232R [140] is a USB to UART bridge. Its library drivers on the host side are usually included in the kernel of the operating system which is the case for most Linux and Windows versions. The FTDI implements itself as a virtual serial port and can be written to and read out digitally. When this is not the case, for example for minimal operating systems that run on ARM processors (like the field-programmable gate array (FPGA) on the UUB), the FTDI driver library can be used. Both types of versions were implemented in simple C programs on Linux by T. Bretz [143] and on Microsoft Windows by the author of this thesis.

The FT232RL was used in the SiPM-based optoelectronic module for SSD. The housing of this chip is a shrink small-outline package with 28 leads arranged in a 0.65 mm pitch structure. This design allows soldering the device by hand which is essential for prototyping. The FT232RL can be seen in the picture in figure 5.10.

5.3.5. Electromagnetic interference reduction

Several improvements were made on the design and layout of the PCB against the ASCII solutions to minimize effects through EMI. The design was strictly split into digital and analog circuitry, and into digital and analog supply and return. The PCB was set up with four layers. All components, e.g. integrated circuits (ICs), and resistors, capacitors, etc. were placed on the top layer without exception, grouped into analog and digital circuitry. Signal and power traces were routed preferably on the top layer, too. For reasons of copper balancing, ground planes were added between the components and interconnected with the bottom layer. The bottom layer only held digital and analog ground planes. The upper inner layer was reserved for the positive and the lower inner layer for the negative bipolar supply. If necessary, the inner layers also served the routing of traces between the components when there was no space left on the top layer. The power planes in the inner layer were erased near any digital circuitry and hence between the digital ground planes to minimize capacitive coupling. After the placement of the components, the current density in the system was simulated. Resistances in the primary current paths were minimized, and inductance in high-frequency traces was optimized. On the intersections between the analog and digital circuitry, i.e. the 5 V USB supply, the common ground from the USB connection, and the bias voltage generated from the C11204-02, resistive π-filters were installed.

To reduce EMI of the digital communication between the USB host and the FTDI, as well as between the FTDI and the C11204-02, the wave impedance of the traces was matched. This was realized with 75 Ω-resistors in the fully-differential lines between the Mini USB type B connector and the FTDI. A 1 µH-inductor together with two 1 nF-capacitors formed an inductive π-filter on the 5 V USB supply which reduced the inrush current and hindered harmonic noise from spreading to or from the USB power source. Between the FTDI and the C11204-02 a combination of 75 Ω-resistors and 1 nF-capacitors were actively slowing down the rising and falling edges of the digital signals, minimizing high-frequency EMI during communication.

5.3.6. Component selection

All components were SMDs without exception. No electrolytic capacitors were used, especially no components with Tantalum electrolyte. These capacitors tend to create a short when they

break which will be problematic in harsh and remote environments like the Argentine Pampas. All capacitors were X7R and NP0 ceramic multi-layer chip capacitors in packages of sizes between 1210 and 0402 with appropriate voltage ratings manufactured by well-known companies. Ceramic capacitors usually offer a very low equivalent series resistance (ESR) which might be problematic for devices such as linear regulators which need ESR to operate stable, but the LTC3260 is robust against any capacitor [139]. NP0 ceramic capacitors maintain their capacitance over temperature, but are only available in small values, typically up to a few nF [144].

In the final design, all resistors had $\leq 1\,\%$ tolerance, $\leq 100\,\mathrm{ppm\,K^{-1}}$ temperature drift and had been manufactured by only one company – all but the three resistors that formed the resistor bridge at the SiPM load, i.e. R_s, R_1 and R_2, which were $0.1\,\%$ tolerance and $25\,\mathrm{ppm\,K^{-1}}$ drift precision components: As the voltage integral directly scaled with the load resistance, as in equation (4.57), it was decided to select components that were more stable against temperature. The other resistors only contributed relatively to the signal, i.e. via a ratio of the form R_f/R_g, see equations (5.17) through (5.19). A major contribution of the temperature drift was expected to cancel out – refer to earlier discussions.

5.3.7. Technical results from the lab

In the following, the author discusses performance measurements of the SSD front-end electronics that were done in the lab, before the modules were shipped to Argentina.

5.3.7.1. Power consumption

The module is dissipating about $190\,\mathrm{mW}$ [54]. This value was determined while the module was operating two Hamamatsu S13360-6025PE SiPMs in the dark at room temperature. As known from figure 4.4 on page 45, the current drawn by one SiPM in the dark at room temperature is typically less than $1\,\mu\mathrm{A}$. The power dissipation increases with increasing temperature, as the SiPM dark current rises exponentially, see figure 4.10 on page 58. It can be estimated that the power consumption of the module is typically less than $200\,\mathrm{mW}$ on average throughout one year of operation in Argentina. This value is less than half of the power budget of $500\,\mathrm{mW}$ and also less than the high-voltage PMT supply of the preliminary baseline design, see [2, table 4.2, p. 55], which is $400\,\mathrm{mW}$.

However, an alternative solution of the PMT high-voltage supply is being evaluated at the moment which promises a power consumption of $200\,\mathrm{mW}$ on a $12\,\mathrm{V}$ operation at an output voltage of $1500\,\mathrm{V}$ [145]. This value is competitive to the one of the SiPM module.

The rather high power consumption of the SiPM module is due to the integrated pre-amplifiers. From the datasheet values of the AD8012 amplifier [124] and of the LTC3260 DC/DC converter [139], the power quota of the pre-amplifiers can be estimated with about $100\,\mathrm{mW}$, or equivalently $30\,\mathrm{mW}$ per gain channel. The amplifiers account for more than half of the total power consumption.

In principle, the pre-amplifiers were not necessary to operate the SiPM module. The signal could be tapped from the high voltage side, decoupled through a capacitor to achieve a negative signal polarity. Without pre-amplifiers, the amplification had to be done by the UUB electronics as in the case of the PMT baseline design. In this case, however, it had to be feared that the single pe resolution was not preserved due to the capacitance of the coaxial cables and external noise pickup.
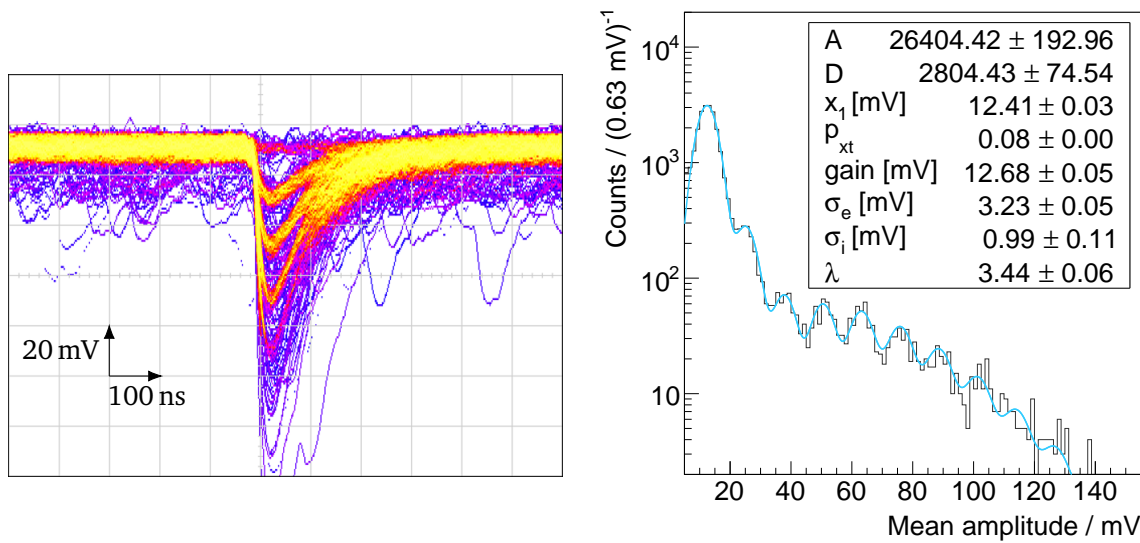
Figure 5.12.: *Left:* Similar to figure 4.1 on page 35, this oscilloscope screenshot shows the small signal response of SiPMs to a flashed LED, synchronized with the read-out. However, this time, two $6\,\text{mm} \times 6\,\text{mm}$ SiPMs with $25\,\mu\text{m}$ cell pitch were read out by the SSD optoelectronic module. The image was pre-released in [54]. *Right:* A finger spectrum taken with the same setup plus a correlated fit, see equation (4.13) on page 47.

5.3.7.2. Signal-to-noise ratio

The author measured the electronic noise for all channels individually by operating the module below the breakdown voltage of the SiPMs and by digitizing voltage traces with the Hameg HMO1002 oscilloscope. The author eliminated the effect of the DAQ by measuring the RMS noise of the HMO1002 and subtracting its squared value from the squared RMS values obtained for the individual channels. The results for the Hamamatsu S13360-6025PE module were $2.34\,\text{mV}$ for the calibration channel, and $0.31\,\text{mV}$ and $0.11\,\text{mV}$ for the high-gain and low-gain channel, respectively. The noise of the HMO1002 can be understood as a systematic resolution for these values, which was $0.04\,\text{mV}$.

In a first approximation, the electronic noise is random. Fast-Fourier transforms corroborated this idea, as the $500\,\text{kHz}$ switching noise of the DC/DC converter was only resolvable in the calibration channel. It can be concluded, that a significant fraction of the electronic noise in the calibration channel is of a harmonic nature, while the noise of the other two channels is much more random. Also, it stands to reason that the electronic noise in the calibration channel can be further reduced by additional RLC-low-pass filters at the supply pins of the AD8012 amplifier chips when the noise originated from the supply lines. In the case of ground noise, better signal-ground-decoupling could improve the SNRs.

Figure 5.12 shows the response of the SiPM module to small light levels, i.e. to a triggered LED. The left-hand side has been pre-released in [54]. It shows an oscilloscope screenshot, where the trigger has been synchronized with the flash of the LED. The persistence of the oscilloscope overlaid several thousand events making the prominent single p.e. features of the two $25\,\mu\text{m}$ SiPMs evident.

The right-hand side of figure 5.12 contains a histogram of signal amplitudes. Traces were

recorded and scanned with the algorithms that were introduced in the last chapter. A fit of equation (4.13) from page 47 is also shown.

From the quantitative results of the fit and the qualitative look of the oscilloscope screenshot, it is indisputable that the requirements on the single p.e. resolution have been met.

5.3.7.3. Pre-amplifier gain and saturation

The knowledge of the response of the pre-amplifiers over the total dynamic range is not only an asset but a requirement. The author could refer to the manufacturer, Analog Devices, for non-linearity studies as the AD8012 was implemented in *standard* non-inverting and inverting configurations, for which the AD8012 had been designed [124].

Nevertheless, the author performed a characterization measurement of the AD8012 amplification and saturation where a signal generator replaced the optoelectronic SiPMs. The Hameg HMO1002 oscilloscope features a programmable signal generator. The output of the signal generator was looped through an attenuator or an amplifier and connected to the input of the SSD module which had an input impedance of 50 Ω, confer with table 5.1. This signal was tapped directly from the input of the SSD module and served as a reference in the measurements that followed. The reference signal was connected to one of the inputs of the HMO1002 with an input impedance of 1 MΩ. Finally, the output of the SSD module, i.e. the low-gain, high-gain and calibration channels were connected sequentially to the second input of the HMO1002 with an input impedance of 50 Ω. U.FL to SMA pigtails, i.e. adapter cables with a U.FL connector on the one end and an SMA connector on the other, and 50 Ω-coaxial cables of type RG174 were used.

The signal generator was programmed to drive a 50 kHz sine wave. Effective amplitudes ranging from 130 μV to 4 V were generated at the input of the SSD module. Small amplitudes were obtained with the use of −20 dB-attenuators, whereas a separate amplifier drove large amplitudes. When the waveforms of both channels – the reference input voltage, and the output channel – were recorded, sine functions were fitted to their data whose amplitudes were saved to disk. Non-linearity and saturation studies were performed by investigating the ratio of the output against the input sine wave amplitude for various input sine wave amplitudes.

Figure 5.13 shows the results of this experiment. On its left-hand side, an example of the input and output signal is given. In this specific case, the output signal of the low-gain channel was recorded while it was responding to an input sine wave of an amplitude of about 200 mV. A phase shift of 180° is observable which is due to the inverting nature of the pre-amplifiers. The fit to the response of the low-gain channel reveals an amplitude of about 100 mV. By taking the ratio of the output to the input, an amplification of 0.495 or equivalently −6.10 dB is retrieved. This value is close to the design goal, see table 5.1, i.e. 0.5.

While this procedure was automated, the results were obtained for a wide range of sine wave amplitudes. This is shown on the right-hand side of figure 5.13. The diagram graphically represents the output voltage response of the calibration, high-gain and low-gain channel for various input voltage amplitudes. The author chose a logarithmic scale on both axes. This allows showing all three channels in a single diagram albeit their large differences in amplification. On a double-logarithmic scale, linear functions of different slopes are shifted by a constant offset, i.e. by the logarithmic ratio of their slopes. It thus becomes apparent, that the ratio of the calibration to the high-gain amplification is about the same as the ratio of the high-gain to the low-gain amplification. Linear fits yield amplifications of 50.1 dB, 21.7 dB and −6.1 dB.
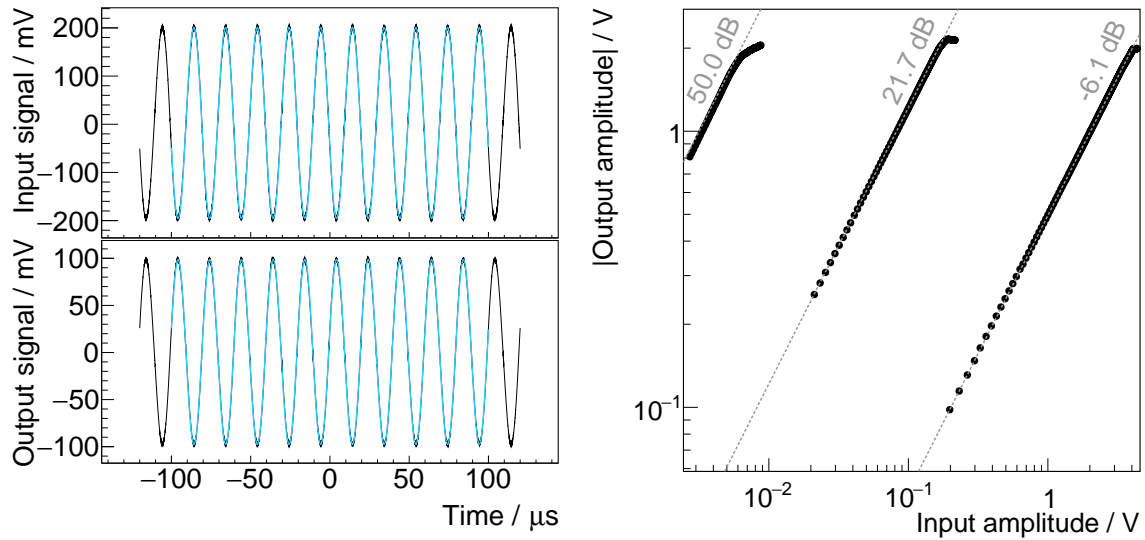
Figure 5.13.: *Left:* An example of the input-to-output signal ratio of the low-gain channel for non-linearity studies. A fit yields an amplification of −0.5. *Right:* The amplitude of the output sine wave for various input amplitudes at the same frequency for the calibration, high-gain and low-gain channel, from top to bottom on a double-logarithmic scale. The individual channel saturation at an output voltage of 2 V is observable. Also, the gain ratio between the high- and low-gain channel is comparable to that of the calibration and high-gain channel yielding the best inter-channel cross-calibration.

All measured amplification constants were systematically smaller than the expected values from table 5.1, i.e. 50.7 dB, 21.8 dB, and −6.0 dB. A systematic reduction of 1 % can be explained through resistive losses in the transmission line and voltage drops at the output impedance of the AD8012 amplifier chip. This assumption is supported by SPICE simulations based on datasheet values [124]. Reasons for the 10 % divergence in the case of the calibration channel most probably trace back to several sources: A high-pass filter with a cut-off frequency of 4 kHz had to be added to cancel the direct current (DC)-offset of the output voltage. This reduced the output voltage by about 1 % at 50 kHz. Also, the huge amplification of 40.1 dB in the first stage only applied to ideal amplifiers, where for real CFAs, the open-loop transimpedance gain needed to be considered. A dedicated SPICE simulation backed up these ideas, as it yielded an amplification of only 50.2 dB at 50 kHz – a value very close to the measurement. The values obtained from the simulation for the high-gain and low-gain channels were also closer to the measured ones than to the expected, resp. calculated ones, i.e. 21.6 dB, and −6.2 dB.

It is further evident that all channels saturated at output voltages of about 2 V. The requirement on the output voltage swing of 1.9 V was met. Additionally, the response of all channels was found to be linear up to their saturation limits.

The amplification ratios between calibration and high-gain, and between high-gain and low-gain are both about 25, i.e. 28.4 dB and 27.8 dB. The overlap between the channels is thus quasi-equally distributed and allows cross-calibration from pe to MIP to voltage or ADC counts. To estimate the overlap between two channels 1 and 2, the author calculated
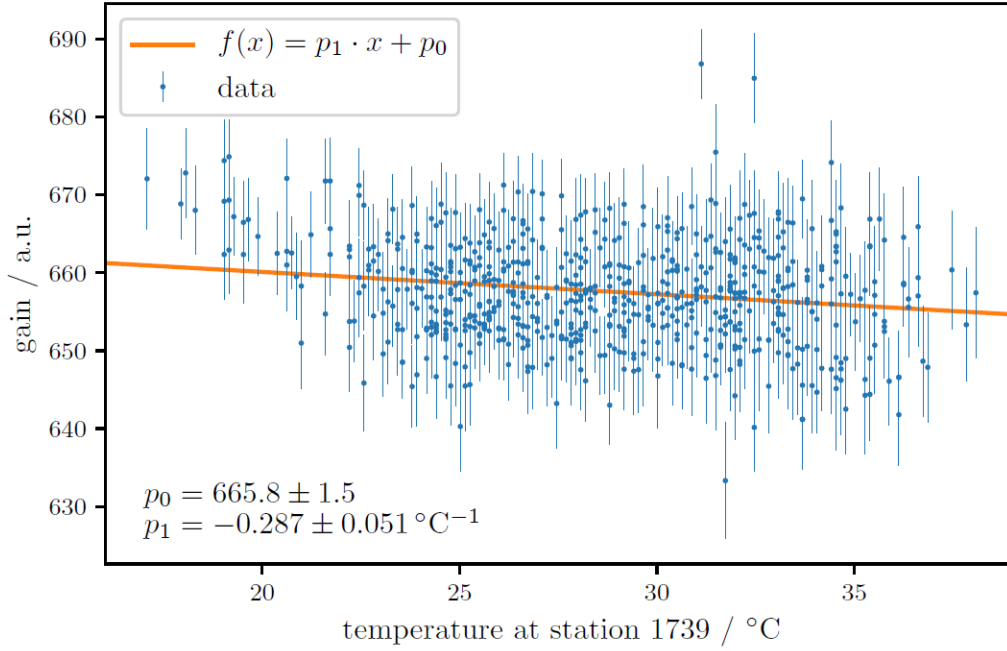
Figure 5.14.: This figure represents the SiPM gain in arbitrary linear units against the ambient temperature of an SSD station that operated an earlier revision of the SiPM optoelectronic module described above. The gain was extracted through correlated Gaussian spectral fits. A residual dependence of the SiPM gain of $-0.04\,\%\,\mathrm{K}^{-1}$ was found. The plot was taken from [54].

$$\log_2\left(\frac{v_{\mathrm{max}} - a_1/a_2 \cdot 5\,\sigma}{5\,\sigma}\right) \text{ bit.} \tag{5.20}$$

For an operation with the UUB, $v_{\mathrm{max}} = 1.9\,\mathrm{V}$ is the maximum voltage amplitude that can be digitized, and σ is the electronic noise of channel 2 folded with the UUB channel noise, thus $\sigma^2 = \sigma_2^2 + \sigma_{\mathrm{UUB}}^2$. Yet, the minimum value of σ is related to the resolution of the ADC, that is $2\,\mathrm{V}/2^{12}$ in the case of the UUB. With this definition, the overlap between the calibration and high-gain channel, and between the high-gain and low-gain channel was larger than 9 bit in both cases whence $\sigma_{\mathrm{UUB}} < 0.6\,\mathrm{mV}$, yielding excellent cross-calibration capabilities.

5.3.8. Low- and high-level results from the field

As of September 2018, SiPM modules of the final design have not been installed in the three SSD systems in Argentina. The final revision of the pre-amplifiers had not been finalized until the end of 2017, and there had not been the chance of an installation campaign in Argentina yet. The results shown in the following have been made with various intermediate module designs. The pre-amplifier layout of its latest version is attached to this thesis in figure **??** in appendix A.10

The Upgrade of the Pierre Auger Observatory was well underway during the writing of this thesis. As a result, many problems occurred that were traced back to the UUB electronics, like malfunctioning of ADC channels and data transmission. Only a small amount of data,
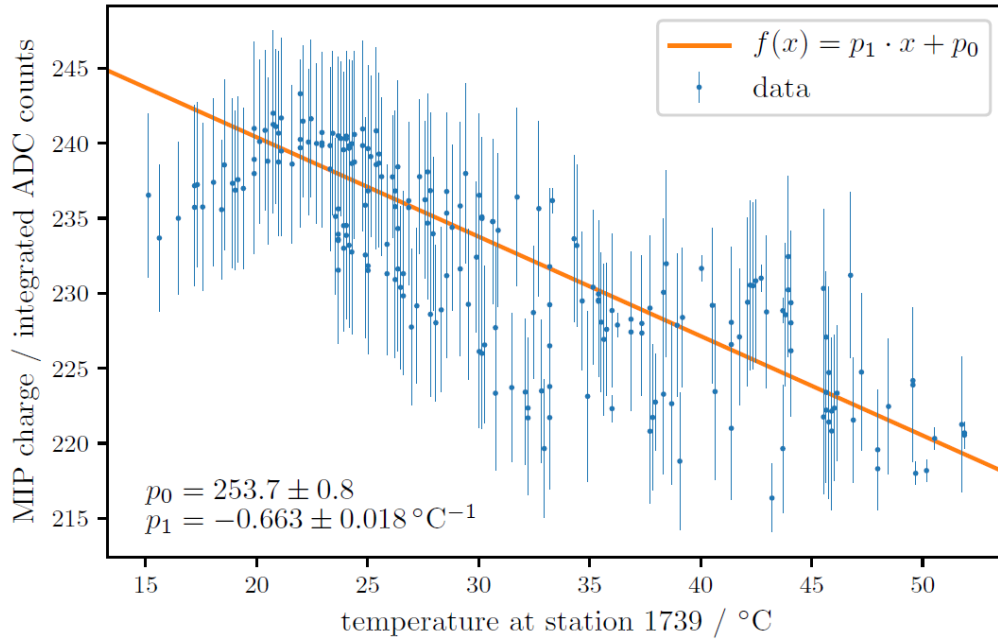
Figure 5.15.: The MIP charge is shown against ambient temperature. The MIP was extracted through log-normal spectral fits. A linear fits yielded a temperature dependence of about $-0.26\,\%\,\mathrm{K}^{-1}$ of the total light yield and spectral response which included the scintillator, WLS fibers and SiPMs. The figure was taken from [54].

low-level in particular, was available from the field by now, yet still analyzed by J. Kemp and published collaboratively in a journal paper, see [54]. The results presented in the following were analyzed by J. Kemp, RWTH Aachen University, and published in [54].

5.3.8.1. Temperature dependence of the SiPM gain and the MIP maximum

By extracting the SiPM gain with correlated Gaussian functions, the stability of the SiPM gain versus temperature was investigated [54] analog to the way presented in the ASCII section. The result is shown in figure 5.14 and published in [54]. The plot shows the gain in arbitrary, linear units against the temperature recorded at station number 1739, which was the detector under investigation. A linear fit yields a temperature dependence of

$$\frac{1}{g(0\,°\mathrm{C})} \cdot \frac{\mathrm{d}g}{\mathrm{d}T} = \frac{-0.287 \pm 0.051}{665.8 \pm 1.5}\,\mathrm{K}^{-1} \approx -0.04\,\%\,\mathrm{K}^{-1}. \tag{5.21}$$

However, by taking the width of the distribution into account, the significance of the temperature progression can be challenged. The quality of these studies will benefit from a better SNR which was promised by the final electronics revision described above.

Like the studies done on the ASCII data, the position of the MIP maximum was extracted from charge histograms and plotted versus temperature. The result is an indication for the temperature dependence of the light yield of the scintillator bars and the WLS fibers. However, it also contains the temperature dependence of the SiPM gain and PDE when the latter was not unfolded. Figure 5.15 shows the result of this study.
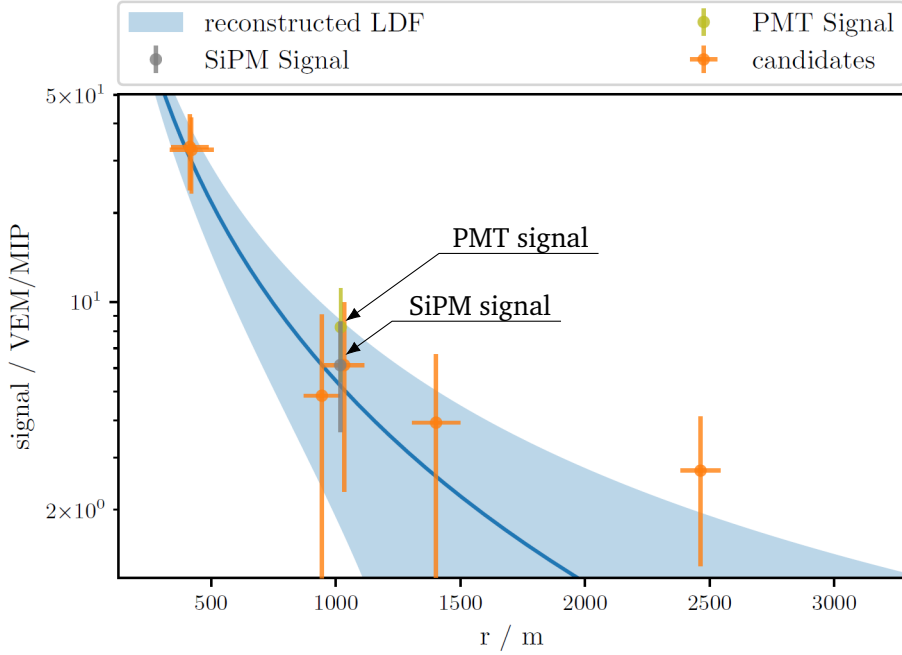
Figure 5.16.: The reconstructed lateral distribution function (blue) together with candidate signals of the Pierre Auger WCD (orange) in units of VEM. The individual responses of two SSD stations in units of MIP are also shown, yet not included in the fit – an SiPM-based station (dark green) and a reference PMT-based station (light green) at distances of about 1000 m. Both data points are very close to each other, indicated by the two arrows. The image was taken from [54].

The plot shows the baseline-subtracted position of the MIP maximum against the ambient temperature. A linear function with a slope of

$$\frac{1}{\text{MIP}(0\,°\text{C})} \cdot \frac{\text{dMIP}}{\text{d}T} = \frac{-0.663 \pm 0.018}{253.7 \pm 0.8}\,\text{K}^{-1} \approx -0.26\,\%\,\text{K}^{-1} \tag{5.22}$$

is added to the data to guide the eye of the reader, see also [54]. Its absolute value is nearly an order of magnitude larger than that of the SiPM gain. However, it still includes the temperature dependence of the two SiPMs. On the other hand, it is compatible with the SiPM-gain-corrected value found for the ASCII detector, as discussed above. In both cases, i.e. the gain-temperature dependence and the MIP-temperature dependence, a deviation from linearity for small temperatures is observed which is not understood by now.

In conclusion, it can be said that even with two 6 mm × 6 mm SiPMs with more than 100 000 cells in total, the SiPM gain and scintillator light yield can be extracted.

5.3.8.2. High-level events – a qualitative comparison to PMT data

The ADC trace of every event can be transformed into MIP equivalents with the help of charge, resp. calibration spectra. This was done in [54] for a series of events. One event is shown in figure 5.16. It shows the signal recorded in several stations that triggered in coincidence against their radial distance to the shower core. In orange, the signal of the regular WCDs is

given which also provide the basis for the LDF fit in blue. The response of a PMT-based SSD and that of an SiPM-based SSD is indicated by the light and dark green points, at a radial distance of about 1000 m. While the signal of the WCD candidates is expressed in units of VEM, the response of the two SSD stations was converted to MIPs. The two SSD stations are operated at a distance of about 10 m to each other [54].

Within their errors, both the SiPM station and the PMT station registered the same amount of light in MIP equivalents. This is an indication that the calibration of both types of stations worked equally well. Also, the response of the two SSD stations did not differ much from the signal expected from the WCD stations, in VEM. Dedicated analyses follow "in the near future" [54].

5.3.9. Conclusions

The SiPM module presented here is a low-power, low-cost optoelectronic module dedicated for the read-out of two bundles of WLS fibers with a dynamic range of more than $2 \cdot 10^6$ photons. Three independent pre-amplifier channels map the dynamic range of two $6\,\mathrm{mm} \times 6\,\mathrm{mm}$ Hamamatsu SiPMs with $25\,\mu\mathrm{m}$ cell pitch equally to three ADC channels, with negative polarity and an output voltage swing of up to $-2\,\mathrm{V}$ on $50\,\Omega$ each. The pre-amplifiers are supplied by an onboard bipolar low-noise switching regulator circuit that is directly sourced from the $5\,\mathrm{V}$ USB line. The nominal SiPM bias voltage at a given reference temperature can be controlled via USB, together with a programmable temperature progression factor. The system consumes less than $200\,\mathrm{mW}$ [54].

The electronics was optimized for low-noise, high-linearity operation, whose performances was checked in the scope of this thesis. The design profited from experiences with the SSD-predecessor, ASCII. Low-level analyses were performed, that proved that the light-yield of scintillator and fibers could be disentangled from the response of the SiPMs and electronics. This worked best with the $50\,\mu\mathrm{m}$ SiPMs due to advantages of the SNR over the $25\,\mu\mathrm{m}$ versions, confer with figures 5.6 to 5.8. This is a feature that will allow long-term systematic detector studies in the future.

Furthermore, a glance was cast on physics events, showing that the calibration of the ASCII prototype performed well. Studies on preliminary SSD data promised a similar performance for the SSD module as pre-released in the journal paper [54], see also figures 5.14 to 5.16.

With costs of about 530€ per module for small quantities and 180€ for large quantities [54], the module is expected to be cheaper than the single PMT that was foreseen as the baseline design of SSD [2, p. 127, figure A.1], without taking its electronics into account.

5.3.10. Outlook & further applications

The module described here was optimized for a specific application: The read-out of SSD with SiPMs. It is currently discussed to add the VULCAN [146] chip to the module, that was initially developed for the JUNO experiment by ZEA-2, Forschungszentrum Jülich, Germany. This makes the need for an external DAQ obsolete, while still allowing operations in SSD stations [147].

Further improvements include the read-out of both SiPMs in series instead of in parallel to reduce capacitance. This will reduce pulse-width and accompanying pulse stacking while increasing the signal amplitude to further improve SNR. However, this will only be possible
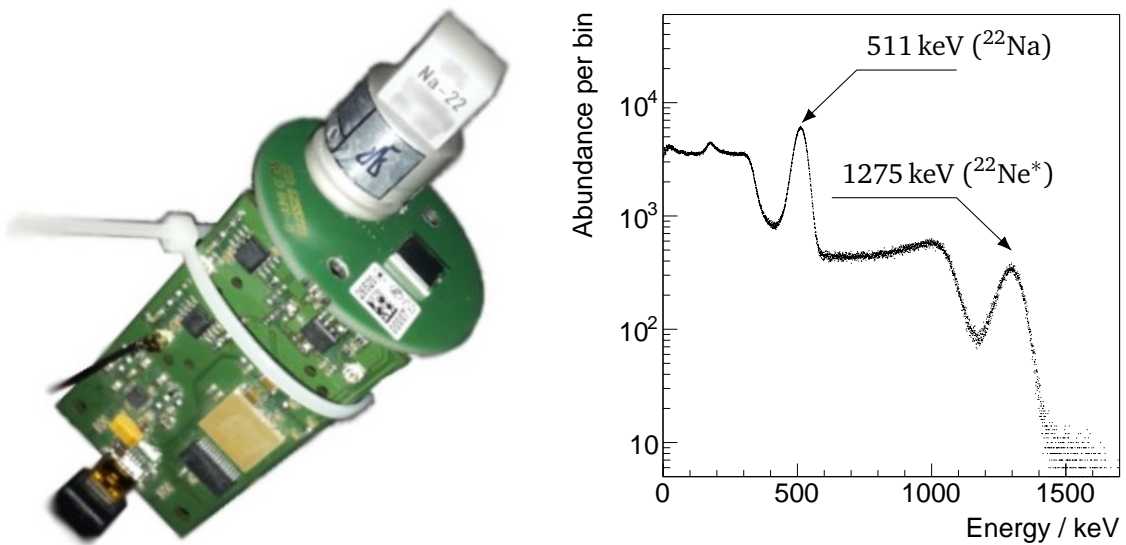
Figure 5.17.: *Left:* A measurement setup featuring the SSD optoelectronic SiPM module equipped with an NaI crystal. *Right:* The spectrum of ^{22}Na-measured with the setup on the *left* shows the 511 keV and 1275 keV lines. The data was taken from [150]. Picture credits belong to F. Reisenhofer.

with SiPMs that operate at smaller voltages because of the voltage limit of the Hamamatsu C11204-02 bias voltage generator chip.

The low-cost, low-power, high-stability and wide-dynamic range design of this module opened possibilities for a series of various applications. These include calibration of optical light guides for telescopes designated for the IceCube Observatory [148], exploring of large-sized SiPMs for the SHiP experiment [149], and gamma spectroscopy with LYSO or NaI crystals [150].

One example is shown in figure 5.17. As a proof of principle, the SSD optoelectronic module was equipped with a Sodium-Iodide (NaI) crystal which is shown in the picture on the left-hand side of above figure. F. Reisenhofer [150] performed the measurement in close cooperation with the author of this thesis. A spectrum of ^{22}Na is shown on the right-hand side of figure 5.17. The 511 keV annihilation peak is visible which originates from β^+-radiation in the decay of ^{22}Na into ^{22}Ne*. The latter is an excited state of Neon which emits 1275 keV γ-radiation during the transition into its ground state ^{22}Ne. The non-linearity of the crystal and the module were calibrated with known radioactive sources. The data was taken from [150].

FAMOUS

With the great success of the First G-APD Cherenkov Telescope (FACT), see for example [83, 151], silicon photomultipliers (SiPMs) have proven to be the most favorable choice for the detection of light emitted in the process of extensive air showers. Advantages over traditional vacuum photomultiplier tube (PMT) have already been introduced in the last chapters, which are for example excellent optical efficiency, robustness, and costs. FACT, for instance, is optimized for the detection of air-Cherenkov light. In the early 2010s, the idea came up to equip SiPMs in the Fluorescence Detector (FD) of the Pierre Auger Observatory [152]. Feasibility studies were driven by the III. Physikalisches Institut A, RWTH Aachen University. It was decided that a small prototype instrument had to be built [153] to better understand the advantages of SiPMs in the context of air shower detection: The First Auger Multi-pixel photon counter camera for the Observation of Ultra-high energy cosmic air Showers (FAMOUS) project was born.

It was later found that the design of FAMOUS was also suitable for the detection of air-Cherenkov light emitted by secondary particles in an air shower due to its lower energy threshold. Consequently, the electronics used and developed in the scope of this thesis targets the air-Cherenkov technique, which fundamentally differs from the idea of air-fluorescence light detection. However, with the original idea in mind, the author designed the electronics in a way that will allow a design upgrade for the air-fluorescence case in the future. The optics, on the other hand, was already optimized for air-fluorescence light detection [6].

While the author introduces the physics reach of FAMOUS in the following, he will also go into detail about the technical differences between air-Cherenkov and air-fluorescence detection in terms of energy threshold, event rate, and hardware selection.

6.1. Physics performance

The optical efficiency of early SiPMs was paid dearly for with a high correlated noise, e.g. the Hamamatsu S10362-series [62]. Nowadays, with improved quality and new optimizations regarding low-noise applications, SiPMs outperform comparable photodetectors, like traditional PMTs when it comes to optical efficiency and robustness. A telescope like FAMOUS allows various applications in astroparticle physics, which is the topic of this section.

6.1.1. Telescope design

The telescope design was driven by developments performed in [6] following design guide-lines from the fluorescence telescopes used at the Pierre Auger Observatory, HiRes, and the Telescope Array. These observatories made use of PMTs, e.g. the Photonis XP3062 1.5 inch device [154]. However, it became soon apparent that the original Schmidt telescope design of the fluorescence telescopes of the Pierre Auger Observatory was ineligible for the use of SiPMs, due to the enormous difference in pixel size: While the XP3062 covered an active area of more than $1000\,mm^2$, the largest SiPMs in the early 2010s were only as large as $9\,mm^2$.

For any optoelectronic instrument, the number of pixels drives the cost. Therefore, it was decided [6] to introduce a Fresnel lens which allowed the operation of SiPMs in large pixels of 1.5°, compatible with the design in the Schmidt telescopes of the Pierre Auger Observatory, see earlier chapters. However, the consequence was a small aperture of 0.5 m diameter, lowering the optical signal-to-noise ratio (SNR), which is about to scale with

$$\text{SNR} \propto \sqrt{\frac{\epsilon A}{d\Omega}}. \quad [155] \tag{6.1}$$

ϵ, A, and $d\Omega$ are the optical efficiency, the aperture size, and the angular pixel size, respectively. Although the decrease of $d\Omega$ would have improved SNR, the number of channels had to be increased to retain the same field of view of the telescope, inevitably increasing costs. Lowering the field of view, on the other hand, would have decreased the number of events observed in the camera. Larger Fresnel lenses were usually not economical [6].

The final design included an 0.5 m diameter Fresnel lens, 61 pixels with 1.5° field of view each, leading to a total field of view of about 15°.

6.1.2. Physics applications

With its large field of view, FAMOUS was the perfect candidate for large-scale observations above approx. 50 TeV in the case of air-Cherenkov detection for proton primaries, and due to its low weight, small size, and low costs, it matched the needs for many physics applications [59, 74, 76].

These included the original idea of a feasibility study to detect air-fluorescence light with SiPMs. As SiPMs benefit from outstanding optical efficiencies, the implementation of SiPMs in air-fluorescence telescopes will improve the SNR, as given by equation (6.1), see [6].

Furthermore, the telescope seems to be an ideal candidate for vetoing of cosmic and gamma rays at the South pole [74] by detecting air-Cherenkov light, and even improving cosmic ray composition studies along with IceTop [156], the on-ice extension of the IceCube observatory.

Hybrid operations in coincidence with surface detectors [75] also promise improvements concerning energy reconstruction and angular resolution.

While the costs for construction and execution are small, and the optics and electronics are robust, the telescope is also a perfect candidate for outreach applications, such as educational laboratory experiments.

6.2. Estimations of the telescope performance

In the following, the author tries to estimate the performance of FAMOUS by relating its SNR to that of other telescopes – for the air-Cherenkov and the air-fluorescence case individually.

6.2.1. Air-fluorescence detection

6.2.1.1. Estimation of the fluorescence rate

The expected fluorescence rate can be estimated without full Monte Carlo simulations, by relating the energy threshold and field of view of a FAMOUS-like telescope to an FD-telescope of Auger.

In good conscience, the rate of ultra-high energy cosmic rays (UHECRs) for a given optical instrument is proportional to the inverse of the energy threshold squared E_{th}^{-2} multiplied with its solid angle Ω for energies above $3 \cdot 10^{18}$ eV. The square in energy threshold comes from the integral of the differential cosmic ray spectrum which drops with E^{-3} above these energies. For two comparable instruments, it means that

$$f_1 \approx f_2 \cdot \left(\frac{E_{\mathrm{th},1}}{E_{\mathrm{th},2}} \right)^{-2} \cdot \frac{\Omega_1}{\Omega_2} \tag{6.2}$$

holds, when trigger efficiencies and differences in the uptime, i.e. duty cycle are neglected. f_1 and f_2 are the event rates of the two telescopes, and Ω_1 and Ω_2 their respective field of view. By estimating the energy threshold with

$$E_{\mathrm{th}} \propto (\mathrm{SNR})^{-1}, \tag{6.3}$$

and by making use of equation (6.1), the expected event rate for the detection of fluorescence light of air showers for a FAMOUS telescope can be estimated with

$$f_{\mathrm{FAMOUS}} \approx f_{\mathrm{FD}} \cdot \frac{A_{\mathrm{FAMOUS}}}{A_{\mathrm{FD}}} \cdot \frac{\epsilon_{\mathrm{FAMOUS}}}{\epsilon_{\mathrm{FD}}} \cdot \frac{\Omega_{\mathrm{FAMOUS}}}{\Omega_{\mathrm{FD}}}, \tag{6.4}$$

where $\mathrm{d}\Omega_{\mathrm{FD}} = \mathrm{d}\Omega_{\mathrm{FAMOUS}}$ was used. Equation (6.1) can be used, when the dominating noise source is the night-sky background, which is usually the case, see dedicated section below.

During standard operation, the event rate of FD per eye, i.e. for six telescopes, is about 12 mHz [3]. That means, that per telescope, the rate is approximately $f_{\mathrm{FD}} = 2$ mHz. The aperture diameter of FD's diaphragm is stated to be 1.7 m [36], thus $A_{\mathrm{FD}} = 2.27\,\mathrm{m}^2$, or $1.5\,\mathrm{m}^2$ when the shadowing of the camera is subtracted [36]. The light collection area of FAMOUS, on the other hand, is about $A_{\mathrm{FAMOUS}} = 0.25\,\mathrm{m}^2$. While the solid angle of FAMOUS is $\Omega_{\mathrm{FAMOUS}} = 0.07\,\mathrm{sr}$ [6], the one of a single FD telescope is approx. $\Omega_{\mathrm{FD}} = 0.21\,\mathrm{sr}$ [36]. The transmittance of both optical systems is about the same [6, 59], i.e. round about 50 % to 60 %. The light detection efficiencies of the SiPMs used in FAMOUS and the PMTs used in FD folded with the fluorescence spectrum given in the first chapter, is also roughly the same, deviating from unity by 3 % only. Thus, $\epsilon_{\mathrm{FAMOUS}} \approx \epsilon_{\mathrm{FD}}$.

Putting all these numbers into the equation from above, it follows that the expected fluorescence event rate is about

$$f_{\mathrm{FAMOUS}} \approx 100\,\mu\mathrm{Hz}. \tag{6.5}$$

That means that per night, i.e. a six-hour measurement, about two events can be expected on average. This will only hold when the telescope is operated under the same conditions as the FD telescopes, i.e. a low night-sky background and a high trigger efficiency. Please be aware that a trigger inefficiency in the FAMOUS telescope can alter above numbers drastically.

Subsidiary, it shall be noted that the duty cycle, resp. up-time fraction can be larger for an SiPM telescope than for a PMT telescope, since SiPMs can also be operated during full moon [83] and closer to sunset and sunrise without optoelectronic degradation. In [2], an increase of the uptime of 50 % was estimated for PMT-based FD telescopes that operated with a lower gain. A similar increase would be expected if SiPMs were used.

Finally, the above numbers are expected to be valid for an operation of FAMOUS comparable to standard FD telescopes. If the FAMOUS telescope is tilted in a way like the High Elevation Auger Telescopes (HEAT), the energy threshold can be reduced which on the other hand increases the detected fluorescence rate by a factor of five, estimated with the HEAT event rate [3].

6.2.1.2. Estimation of the signal duration

The expected signal duration per pixel can be estimated from simple geometric considerations. For showers that propagate vertically to the optical axis of a given pixel, the time an air shower remains in the field of view of that pixel is

$$\mathrm{d}t \sim 2\,\frac{d}{c} \cdot \sin(\Delta\alpha/2). \tag{6.6}$$

While d is the shower distance, c the speed of light, and $\Delta\alpha$ the field of view of a single pixel in radians. Any impact of the atmosphere has been neglected in this estimation. For a close shower, i.e. $d = 1\,\mathrm{km}$, $\mathrm{d}t$ becomes 100 ns. $\mathrm{d}t$ maximizes when the shower moves away from the camera. In this specific case, the above equation needs to be modified with the sine of the angle between the shower axis and the optical axis of the pixel. For a highly inclined shower with respect to the optical axis, $\mathrm{d}t$ can easily reach several µs. For example, $\mathrm{d}t$ is 2 µs for a shower at a distance of 10 km with an inclination of 25°.

With these numbers, a draft of the timing requirements on the data acquisition (DAQ) can be drawn. For a telescope with a field of view of 15°, an event can last several ten µs. The DAQ needs to feature a long sample buffer. On the other hand, a fine sampling will not be needed. In the case of the Auger FD telescopes, the DAQ makes use of a buffer length of 100 µs and a sampling rate of $10\,\mathrm{MSa\,s^{-1}}$ with 12 bit [157]. For a telescope like FAMOUS, the buffer length could be reduced by a factor of two to four, since the size of its field of view is about a quarter of that of the FD telescopes.

6.2.2. Air-Cherenkov detection

6.2.2.1. Estimation of the energy threshold

While FACT was designed for the detection of gamma rays with energies as low as "several hundred GeV" [151], one can estimate the expected energy threshold for the detection of gamma rays for FAMOUS using the air-Cherenkov technique from the optical efficiency, aperture size, and pixel size of FACT compared to the numbers of FAMOUS.

With the values published in [151] and [6], and following the definition of the energy threshold and SNR from above, the energy threshold of a FAMOUS-like telescope can be expected to be about two orders of magnitude higher than that of FACT, i.e.

$$E_{\mathrm{th,FAMOUS},\gamma\text{-rays}} \approx \text{several ten TeV.} \tag{6.7}$$

6.2.2.2. Estimation of the signal duration

The signal length in a pixel depends, of course, on the size of the pixel, but also on the geometry of telescope and shower axis, production height of the air-Cherenkov light emitted by secondary particles and their energy, i.e. the Cherenkov angle θ_C. An oversimplified guess of the signal duration can be made, by a simple scenario in which the shower propagates in the direction of the optical axis of the telescope, and by estimating the Cherenkov production height with a few tens of km. For a high-energy shower, it follows with $\theta_C \sim 1°$, that the signal duration can last a few tens of ns.

The different demands on the electronics for air-fluorescence and air-Cherenkov light detection become evident. To estimate the temporal evolution of the shower in the camera, high-speed electronics with sampling rates in the order of $\mathrm{GSa\,s^{-1}}$ is necessary. Furthermore, for the trigger circuitry to react on those fast signals, its analog bandwidth needs to be in the region above a hundred MHz. Otherwise, the associated shaping will reduce the electronic SNR, defined by the amplitude over the root mean square (RMS), see last chapters. On the other hand, the buffer depth can be small, i.e. in the order of the photosensor decay time, since the event only lasts a few ten ns.

6.2.3. Night-sky background

The diffuse night-sky background flux impinging on the individual pixels of FAMOUS can be estimated from the measurements of the mean detected photon fluxes done in [158, p. 176], and the FAMOUS telescope parameterization from [6, p. 135f] to somewhere between 10 MHz per pixel during a clear night with ultraviolet (UV)-passing filters installed, and 1 GHz per pixel without filters and during a cloudy night. With a nominal gain of $2.8 \cdot 10^6$ and the elementary charge $1.6 \cdot 10^{-19}$ C, this translates to currents of $10\,\mu$A and $400\,\mu$A, respectively, excluding correlated noise. In the presence of star- or moonlight in the field of view of a pixel, the current can exceed 1 mA.

Again, these numbers allow to estimate the requirements of the bias voltage supply system. The bias supply needs to source up to 1 mA per pixel, and 60 mA in total. The maximum current drawn by an SiPM can be estimated from the resistance of its parallel combination of N quenching resistors R_q and the applied excess voltage v_{ov} with

$$i_{\max} = \frac{R_q}{N} \cdot v_{\mathrm{ov}}. \tag{6.8}$$

That is the case when all cells are triggering continuously. $i_{\max}$ is typically found in the range of a few mA.

6.2.4. Conclusions

To conclude, the demands on air-Cherenkov detection are different from those of air-fluorescence detection. While the sampling rate for the detection of air-Cherenkov light needs to be large, and the buffer depth can be small, the situation is the other way around in the case of air-fluorescence detection. Due to the smaller energy threshold in the air-Cherenkov case, its expected event rate was higher. That simplified debugging and testing and was, therefore, the primary goal of the developments done in the extent of this thesis. More details follow in the upcoming section.

Lens mounting ring

300 mm

Fresnel lens

Carbon fiber lens barrel

Bottom baseplate

Winston cone mount

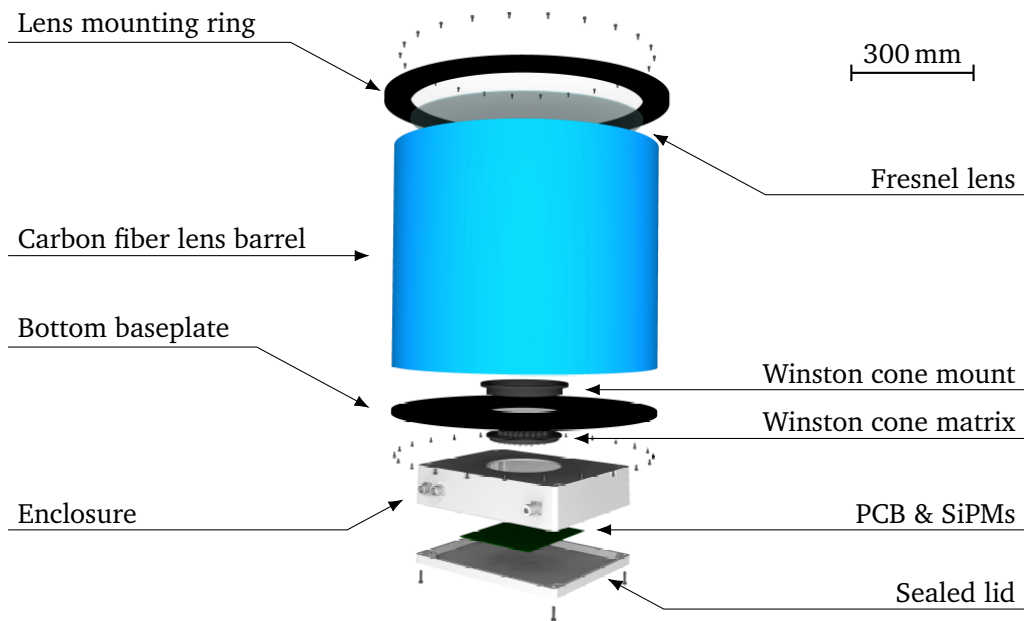Winston cone matrix

Enclosure

PCB & SiPMs

Sealed lid

Figure 6.1.: A sketch of the optical and mechanical components of the FAMOUS telescope. A Fresnel lens focusses incoming light onto a 61-pixel camera consisting of 61 Winston cones and 61 SiPM packages. The image was taken from [59]. Image credits belong to M. Schaufel.

6.3. Hardware

This section describes the hardware of the FAMOUS telescope in varying levels of detail. While the optics were mainly developed in [6], this work focusses on the electronics whose realization was a result of this thesis. Nevertheless, an overview is given on the individual optical components, and their parameters are summarized. Figure 6.1 shows a sketch of the optical and mechanical components of FAMOUS.

6.3.1. Optics

The primary optical components of the telescope are

- a 0.5 m-diameter Fresnel lens,

- a triangular matrix of 61 light-guiding cones, and

- 64 SiPM packages of which 61 were actively monitoring the night sky.

6.3.1.1. Fresnel lens

A Fresnel lens is a refractive element which has superior transmitting properties compared to regular lenses. This comes from the low material volume which reduces absorption, especially in the UV range. Concentric grooves are cut from the bulk material of a regular lens generating the Fresnel lens. However, the focal length f of an ideal Fresnel lens is a function of the light's
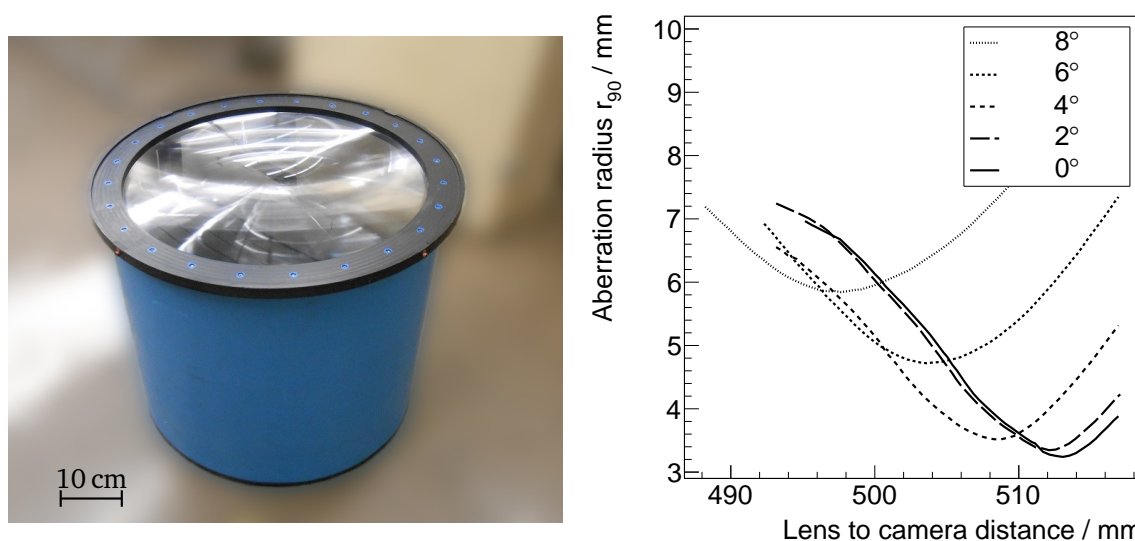
Figure 6.2.: *Left:* A picture of the Fresnel lens assembled on the light-weight carbon fiber tube of FAMOUS. *Right:* The aberration radius r_{90} versus the lens-camera distance for incident angles between 0° and 8°. The plot was adapted from [6, 59].

wavelength and the radial distance on the lens, leading to imaging errors such as chromatic and spherical aberration. Both effects can be reduced by dedicated techniques [6, 159].

The Fresnel lens of FAMOUS was made of UV-transparent polymethyl methacrylate (PMMA), manufactured by ORAFOL Fresnel Optics GmbH [59]. Full Monte Carlo simulations were developed [6] and improved with results from experimental studies [6, 92, 160, 161]. A picture of the lens mounted on a carbon fiber tube is given in figure 6.2.

The physical parameters of the lens are a nominal planar conjugate[1] of 502.1 mm for a wavelength of 546 nm, an aperture diameter of 549.7 mm and a thickness of 2.5 mm with a tolerance of ±5 % [159].

The point spread function of the Fresnel lens was measured in [160] as a function of the incident angle of light with a wavelength of 550 nm. A recent analysis [6] showed that the minimum aberration radius was found at a distance of (513.2 ± 0.4) mm for light that passed the Fresnel lens perpendicular to its surface, see figure 6.2. The minimum spot size defined in [6] as the minimum aberration radius of an imaginable circle that encloses more than 90 % of the light, was found to be about $r_{90,min}(0°) \equiv r_{90}(0°, f(0°)) \approx 3.2$ mm for an incident angle of 0° in a plane with a distance of $f(0°)$ from the lens, and about $r_{90}(8°, f(8°)) \approx 5.9$ mm for 8°. Both values are smaller than the pixel size, i.e. 6.71 mm. However, the planar conjugate decreased by about 15 mm from 0° to 8° with the result that the maximum aberration radius for 8° becomes drastically larger when the lens is not in focus, i.e. larger than $r_{90}(8°, f(0°)) > 8$ mm in the conjugate $f(0°)$ for 0°. The optimum camera lens distance is therefore between $f(0°)$ and $f(8°)$ where the average $\langle r_{90} \rangle$ becomes minimal. A distance of 508 mm was chosen [6].

The transmittance of 2.5 mm PMMA itself including surface reflections exceeds 90 % above 300 nm, see also figure 6.5. With the photon spectra of air-Cherenkov and air-fluorescence light from figure 2.7 on page 19 it becomes evident that a Fresnel lens is ideally suited to allow the detection of air-Cherenkov as well as air-fluorescence light. Both spectra are also given

---

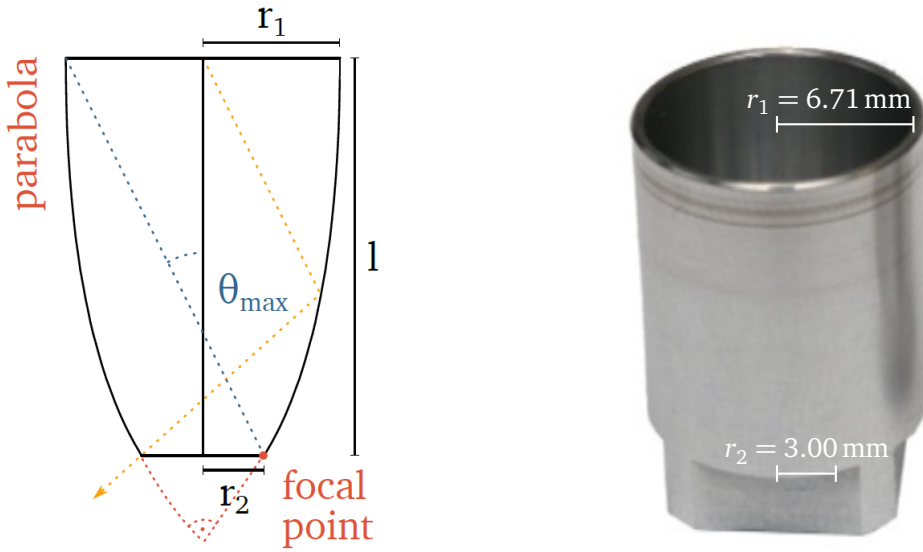[1]The conjugate of a negligibly thin lens is identical with its focal length.

Figure 6.3.: *Left:* A sketch of a Winston cone with quantities r_1, r_2, and θ_{max} defined in the text, see equation (6.10). *Right:* A picture of a single Winston cone used for the FAMOUS telescope. The sketch was taken from [6]. Sketch credits belong to T. Niggemann. Picture credits belong to L. Middendorf.

in figure 6.5. Its discussion will be postponed to a later point of this section. However, the implementation of the Fresnel lens was found to lose about 50 % of vertically incident light in total [59, 160].

6.3.1.2. Focal plane

For an ideal thin lens, the relation between pixel size Δx and field of view, resp. opening angle $\Delta\alpha$ can be shown to be

$$\Delta x = f \cdot \tan(\Delta\alpha), \tag{6.9}$$

by the means of geometrical optics. f is the focal length of the lens. This means, that in order to get a field of view per pixel of about $\Delta\alpha = 1.5°$, a pixel size of $\Delta x \approx 13.4\,\text{mm}$ is needed for a focal length of $f = 510\,\text{mm}$. A pixel radius of 6.71 mm was chosen as the baseline design for FAMOUS [162], closely meeting the demands from above.

The largest SiPMs available at that time were $3\,\text{mm} \times 3\,\text{mm}$ SiPMs which were packed in a symmetric 2×2 array, yielding a total sensitive area of $6\,\text{mm} \times 6\,\text{mm}$, i.e. the Hamamatsu S10943-series. These were, however, too small for a requested pixel size of 13.4 mm. Non-imaging optical components like Winston cones, also known as *compound parabolic concentrators* [163], allow to increase the pixel size, albeit their accompanying degradation of optical quality and angular acceptance.

For an ideal Winston cone, see figure 6.3, it follows from Fermat's principle that the maximum acceptance angle of a Winston cone θ_{max} is defined by the ratio of the radii of exit r_2 and entry aperture r_1 with

$$\sin(\theta_{max}) = \frac{r_2}{r_1}. \ [163] \tag{6.10}$$

Within this angle, all the light is transmitted to the exit aperture with only one or no reflection per photon. This holds for an ideal, that means round-to-round, hollow Winston cone that works as a reflector, i.e. the medium inside the cone is the same as outside. r_2 and r_1 were defined through the thoughts from above as 3 mm and 6.71 mm, respectively, which fixed the maximum acceptance angle to $\theta_{\mathrm{max}} \approx 26.6°$. The optical response of these Winston cones was studied extensively in [161]. It was concluded, that depending on the definition of $\theta_{\mathrm{max,\ data}}$ in the data, the measured response agreed very well with the prediction from above's formula.

However, hollow Winston cones with a round-to-round geometry are not perfectly suited for this application for several reasons:

- the active area of SiPMs is quadratic – not round,

- insensitive gaps emerge between the triangular pattern of SiPMs if the cones' entry apertures were not hexagonal but round, and

- the maximum entry angle of light rays that were refracted at the outer edge of the lens can be as large as $\theta_{\mathrm{in,\ max}} \approx 33.9° > \theta_{\mathrm{max}} \approx 26.6°$.

$\theta_{\mathrm{in,\ max}}$ is estimated by the following thought: With the lens diameter D, camera diameter d, lens-camera distance f, it follows from $2f \cdot \tan(\theta_{\mathrm{in,\ max}}) = D + d$ that $\theta_{\mathrm{in,\ max}} \approx 33.9°$.

In [148], solid hexagonal-to-quadratic cones were developed, optimized for the detection of air-Cherenkov light with a FAMOUS-like telescope. For a solid, yet round-to-round cone with an ideal Winston shape, the maximum acceptance angle increases to

$$\sin(\theta_{\mathrm{max,\ solid}}) = n \cdot \frac{r_2}{r_1}, \tag{6.11}$$

where n is the index of refraction of the solid cone. $n_0 \equiv 1$ was used for air, outside the cone. With a refractive index of $n = 1.5$, and r_2 and r_1 from above, $\theta_{\mathrm{max,\ solid}} \approx 42°$. Hexagonal cones increase the entry aperture by approx. 10 % compared to round entry windows by means of close-packing of equal spheres. The quadratic exit aperture now covered the full SiPM sensitive area of 6 mm × 6 mm.

It was found that the hexagonal-to-quadratic cones doubled the individual pixel performance [148]. A camera featuring the new solid cones was brought to the South pole in the season of 2017/2018.

In this thesis, however, the hollow Winston cones were used. Hollow cones benefit from simpler maintenance as camera and cones were screwed and not glued together. That means that in the case of hollow cones, SiPMs and electronic components could be replaced rather easily if necessary. Hollow Winston cones also allowed the operation of thin UV passing filter glasses between cones and SiPMs.

The mechanical workshop of the III. Physikalisches Institut A, RWTH Aachen University designed, drilled, and polished a matrix of 61 Winston cones. All cones were made of aluminum which simplified mechanical machining. The individual cones were glued into an aluminum support frame. The support frame itself was fixed to the camera printed circuit board (PCB) with up to eight metric machine screws. 64 notches matched the SiPMs' packages and fixated PCB and frame. 61 of which contained aluminum Winston cones, while the remaining three were covered by aluminum to shield these pixels from any light. These three channels were used for debugging and testing. Figure 6.4 shows pictures of the Winston cones and their aluminum frame for structural support.
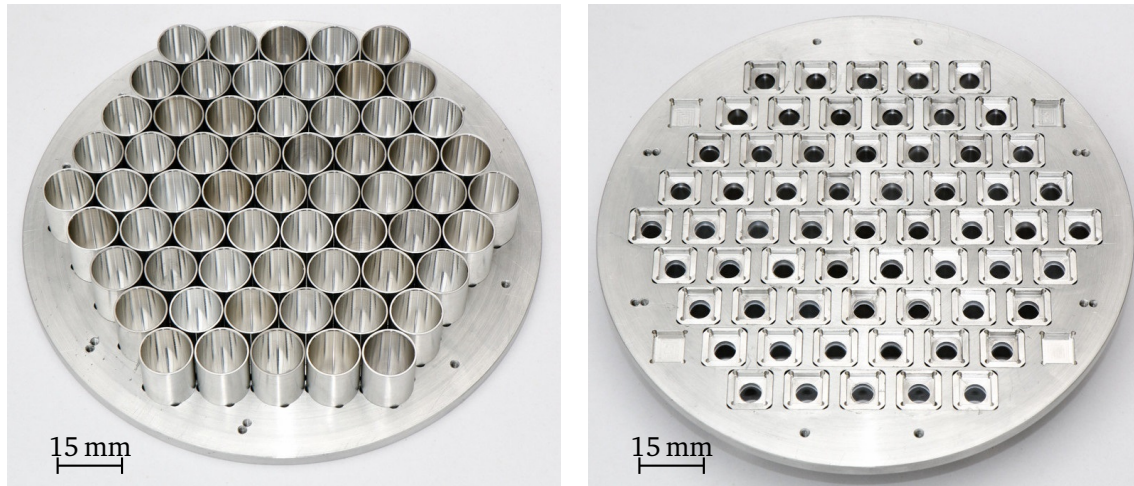
Figure 6.4.: Pictures of the Winston cone matrix of the 61-pixel camera that was manufactured by the mechanical workshop of the III. Physikalisches Institut A, RWTH Aachen University. *Left:* Top view, showing the circular entry windows in a close-packing of equal spheres and *right:* Bottom view. Rectangular notches allow to align SiPM packages. Up to four notches for so-called blind-pixels are visible along with 61 notches for regular pixels. The left picture was published in [59]. Credits for the pictures belong to L. Middendorf.

The center-to-center distance of the individual pixels on the triangular pattern was chosen to be 15.00 mm, leaving room of $(15.00\,\text{mm} - 2 \cdot 6.71\,\text{mm})/2 \approx 0.80\,\text{mm}$ per pixel for the non-zero wall thickness of the aluminum Winston cones.

61 UG-11 UV passing filters [164] could be mounted between the exit aperture of the Winston cones and the active area of the SiPMs with the idea to eliminate a significant fraction of the night-sky background.

The pixels were SiPM packages of type Hamamatsu S12573-3580X [165] a custom successor of the S10985-100C [166] with an increased UV sensitivity and reduced afterpulsing. Consisting of $3\,\text{mm} \times 3\,\text{mm}$ SiPMs, every package housed 2×2 individual SiPMs. These four SiPMs shared the same cathode yet remained individual anodes. However, all four SiPMs per pixel were shorted on the camera PCB and thus read-out in parallel, see also next section. Characterization measurements of the S12573-3580X can be found in chapter 4 see table 4.1.

The left-hand side of figure 6.5 shows the efficiency curve of the SiPMs, together with the transmittance of 2.5 mm PMMA including surface reflections, and that of the 1 mm thick UG-11 UV passing filters. All components were chosen for an optimal SNR in the case of air-fluorescence light, see also the right-hand side of figure 6.5. The use of the UG-11 optical filters in the case of air-Cherenkov detection is optional as the filters reduce not only night-sky background but also a significant fraction of the signal. The data was taken from [59].

6.3.2. Mechanics

A cylindrical tube made of 6 mm thick aluminum kept the camera in the focal plane of the Fresnel lens at a nominal distance of 508 mm [6]. Incidentally, the tube shielded the camera from the night-sky background that approached from the side. As an improvement, the tube
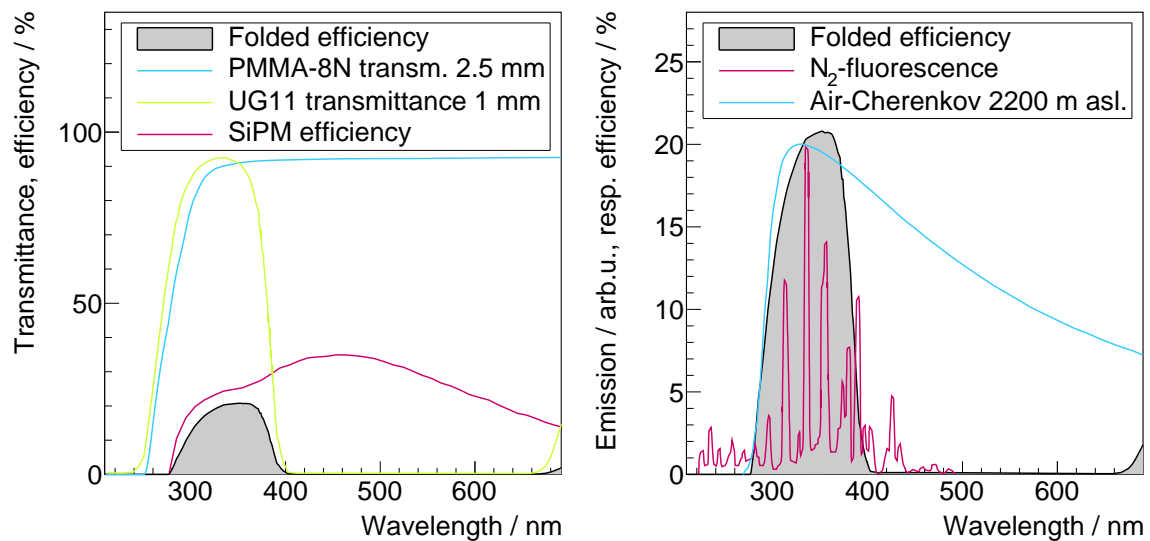
Figure 6.5.: *Left:* The sensitivity of the optical components of the FAMOUS telescope as a function of the wavelength in the ideal case of perpendicular incidence. *Right:* The folded efficiencies from the left together with the emission spectra of air-fluorescence and air-Cherenkov as from the first chapter. All curves were taken from [59].

was later made from carbon fibers to reduce weight to 15 kg and costs to about 200 USD [59]. The Fresnel lens was fixed with a clamping ring, while black velour adhesive foil absorbed stray light on the inner walls of the tube.

A highly-durable aluminum enclosure box protected focal plane and the direct-current-to-direct-current (DC/DC) bias supply PCB from environmental stress. The latter will be introduced in a later section. Figure 6.2 shows a picture of a next-generation reinforced carbon tube with the Fresnel lens assembled on the top.

6.3.3. Electronics

The DAQ system was a loan of the FACT collaboration [83]. Details about which can be abstracted from there. The bias supply was developed by the electronics workshop of the III. Physikalisches Institut A, RWTH Aachen University, Germany, by D. Louis in close cooperation with the author of this thesis. The author improved the performance of the bias supply by implementing hardware changes over the years. Furthermore, the author drove the development of further electronic components, e.g. the SiPM camera PCB, the trigger routing PCB, and the trigger master PCB and its firmware. Testing and debugging was done in cooperation with the FAMOUS and IceAct groups, see e.g. [76, 167].

6.3.3.1. Focal plane

The centerpiece of the SiPM camera was a six-layer PCB that was designed, developed, and tested by the author. It held all 64 SiPM packages, the same quantity of temperature sensors, and resistors and capacitors for signal filtering, as well as six connectors to access the signals externally. Pictures of the fully-assembled SiPM camera are given in figure 6.6.
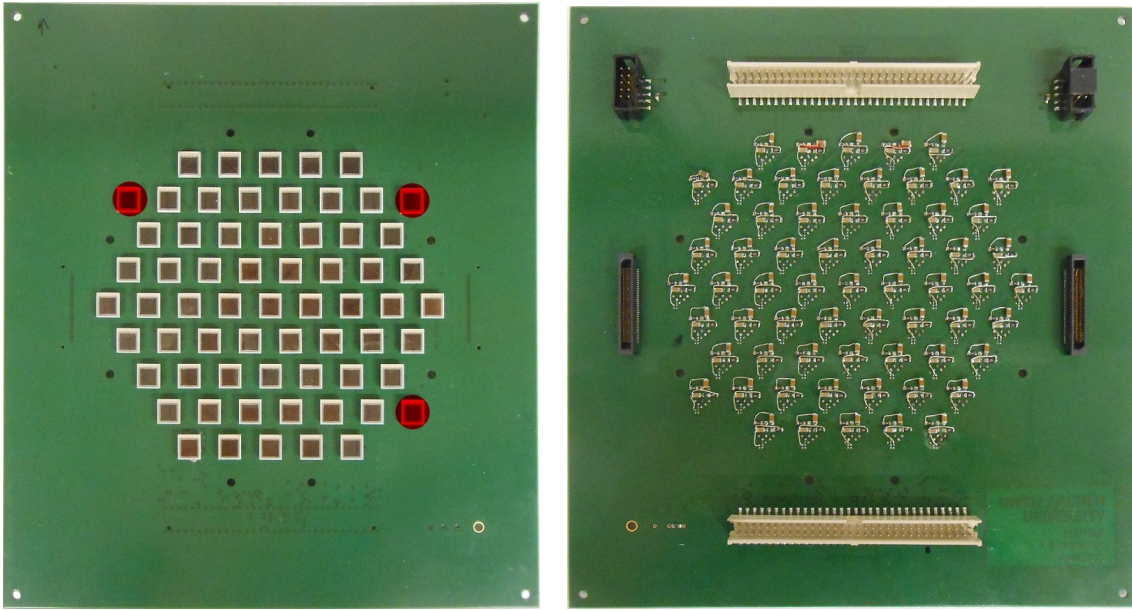
Figure 6.6.: Pictures of the 61-pixel camera. *Left:* The top view allows to inspect all 61 regular and three additional *blind* pixels, with the latter encircled in red. 64 analog temperature sensors are placed locally beneath the SiPM packages and are not visible in this view. *Right:* Any other electronic component is assembled on the bottom side, like resistors, capacitors, and connectors. Solder patches are visible, see text for details. The left image was pre-released in [59]. Picture credits belong to the author of this thesis.

64 SiPM packages were soldered onto its top side, along with 64 analog temperature sensors of type Texas Instruments LMT87 [168]. Any other component was placed on the bottom side of the PCB, which included RC low-pass filters for the bias voltages of every individual SiPM with initially $R = 10\,\Omega$ and $C = 100\,\text{nF}$, as well as connectors. The reason for placing the components on the bottom layer was to have an insulated surface on the top side of the PCB since the Winston cone matrix was embedded in an aluminum disc and in direct contact with the PCB. Aluminum is electrically conductive. With this approach, accidental shorts were avoided. Please refer to the pictures in figure 6.4. The LMT87 chips were mounted directly beneath the SiPM packages with thermal pads between SiPMs and the LMT87. This complicated refurbishing in the case of a component failure but guaranteed the best thermal conductivity between SiPM and temperature sensor. Placing the LMT87 chips beneath the SiPMs was only possible because the SiPM packages were not surface-mounted devices (SMDs), but leaded.

Because of the electrically conducting aluminum Winston cone disk, the author selected connectors that were SMD. The connectors that collected the 64 individual SiPM bias voltages, the 64 analog output voltages of the LMT87 temperature sensors, and their supply voltage of 3.3 V and ground were from the HTSS-1 series of Samtec [169]. These connectors were compatible with standard flat ribbon cables. For the 64 SiPM signals, the author chose the TEM-135-02 from Samtec [170]. The TEM-series are high-frequency, high-density connectors that directly connect PCBs with each other with mating connectors [171] and without the use of cables. A piggyback PCB was sitting on the focal plane, interconnected through two TEM-
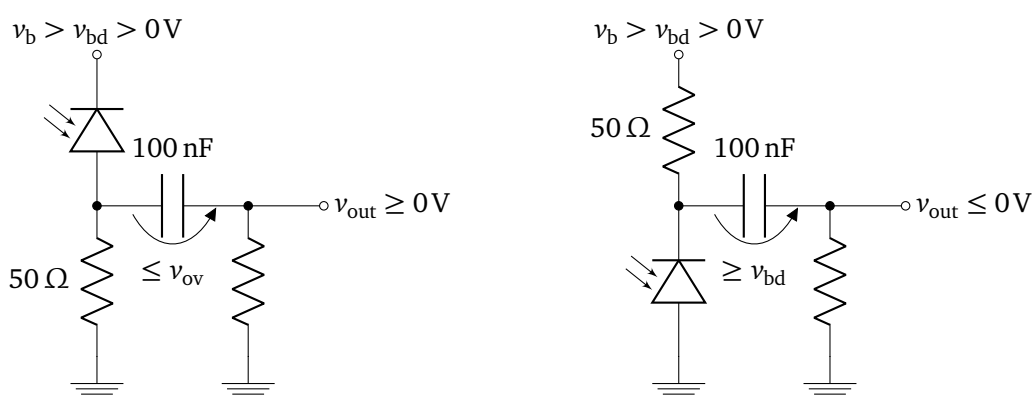
Figure 6.7.: *Left:* The initial SiPM read-out on the focal plane PCB was designed to achieve positive output polarities. *Right:* One way to modify the read-out from the left to achieve negative polarities was to do the de-coupling from the high-voltage side. The change was necessary to operate the DAQ borrowed from the FACT [151] collaboration. Refer to the text for details.

135-02 and their mating connectors. This PCB was designed to group the signals of pre-defined pixels onto connectors depending on the DAQ and its trigger implementation. Outsourcing the trigger grouping into a small piggyback PCB made the focal plane more versatile for different application scenarios. Two examples of this *trigger routing* PCB will be introduced in the next section.

Initially, the focal plane foresaw that its SiPMs were read-out at their low-voltage side, i.e. at their anodes, while their cathodes were biased with positive voltages, exceeding the SiPMs' breakdown voltages. This is indicated in the circuit on the left-hand side of figure 6.7. The reason was simply that no high-voltage capacitor was necessary to decouple the SiPM signal since the maximum voltage drop at the 100 nF capacitor was expected to be smaller than the overvoltage. The resulting voltage polarity at the anode would have been positive, as the technical current flows from the high- to the low-voltage side, introducing a voltage drop at the shunt impedance, e.g. at the 50 Ω resistor. However, the DAQ in the baseline design demanded negative signal polarities for its analog trigger circuitry to operate correctly. The DAQ will be introduced after the next section.

The author thought of three ways to change the SiPM signal polarity from positive to negative since the SiPMs had already been soldered to the PCB:

- with the use of inverting, low-gain amplifiers between the focal plane and the DAQ,

- by operating the SiPMs with a negative bias voltage and swap connections of cathode and anode, or

- by reading out the SiPMs at their high-voltage sides, de-coupled through high-voltage capacitors.

For the first solution, amplifiers with small amplification had to be designed. The gain had to be small not to saturate the input of the DAQ, which had been optimized for naked SiPM signals only. However, the SNR would have decreased significantly, since the electronic noise of the inverting amplifier would have been amplified in the DAQ along with the signal. This

would have denied single pe calibrations. The second solution would have generated the need for a new bias supply with negative output voltages, delaying the operational availability of the telescope. The last solution could be performed rather easily with solder patches, bridges and flying leads on the focal plane PCB itself. The feasibility of that operation was proven for one pixel by the author. All the other pixels were modified by the electronic workshop of III. Physikalisches Institut A, RWTH Aachen University, once the author finished testing the first pixel. Figure 6.7 shows simplified schematics of the read-out circuitry before and after the modification.

However, operating the PCB with solder patches was not without risk as the bridges were uninsulated. Also, when the high-voltage capacitor shortened, the bias voltage v_b or at least the breakdown voltage of about 60 V would drop at the input of the DAQ, probably destroying the system. The solder patches are visible in the picture on the right-hand side of figure 6.6.

Incidentally, the author developed a negative bias voltage module which was sent to the South pole on behalf of the IceCube collaboration along with a FAMOUS-like telescope in the season of 2017/2018. A negative bias module became necessary after cathode and anode of the SiPMs had been mixed up in the soldering process. A brief outlook is given in the bias supply topic.

6.3.3.2. Trigger layout & routing

For most DAQ systems that feature trigger groups of several channels, the trigger circuitry is not freely configurable in software but set up with discrete or integrated circuits. One example is the DAQ system of the FACT project [151] based on the Domino Ring Sampler (DRS) in version 4 [172]. Another example is the prototype electronics of the Cherenkov Telescope Array (CTA) based on the TARGET7 application-specific integrated circuit (ASIC) [173].

Practically, this means that the signal input connectors of these DAQ systems are already hardwired to the trigger logic in individual groups, and the trigger routing must be done electrically between the focal plane and the DAQ. The most straightforward approach is to use a dedicated PCB that is plugged onto the focal plane PCB, as introduced earlier. This piggyback board routes the signal lines of the individual pixels to connectors in predetermined groups which depend on the DAQ system and the desired trigger layout. The DAQ is then connected to this piggyback board with standard or dedicated coaxial cables.

The first trigger routing boards were developed by the author. The very first one routed the individual pixel signals from the focal plane to individual vias, i.e. to through-hole solder pads, without any trigger layout in mind, simply, because no DAQ was available at that time. This board was used in the first measurements with the TARGET7 [173] DAQ, for example in [174, 175]. Single RG174 50 Ω-coaxial cables were soldered to that board by N. Höflich and B. Pestka. Air-Cherenkov candidates were measured with the TARGET7 DAQ and the central section of the camera. Those results will be summarized at the end of this chapter.

Dedicated layouts were created in cooperation with J. Auffenberg and T. Bretz targeting the FACT [151] DAQ which became the de-facto standard of the FAMOUS project. After fruitful discussions, the author created the trigger routing PCB according to the layout shown on the left-hand side of figure 6.8. A picture of the fully-assembled PCB including coaxial cables is shown on the right-hand side of the same figure. Both images were pre-released in [59], the left sketch was designed by M. Schaufel, the right picture was taken by the author.

Eight trigger groups were available, comprised of up to nine pixels each, indicated by the color-coding. The blind pixels formed a separate group and were usually taken out of any
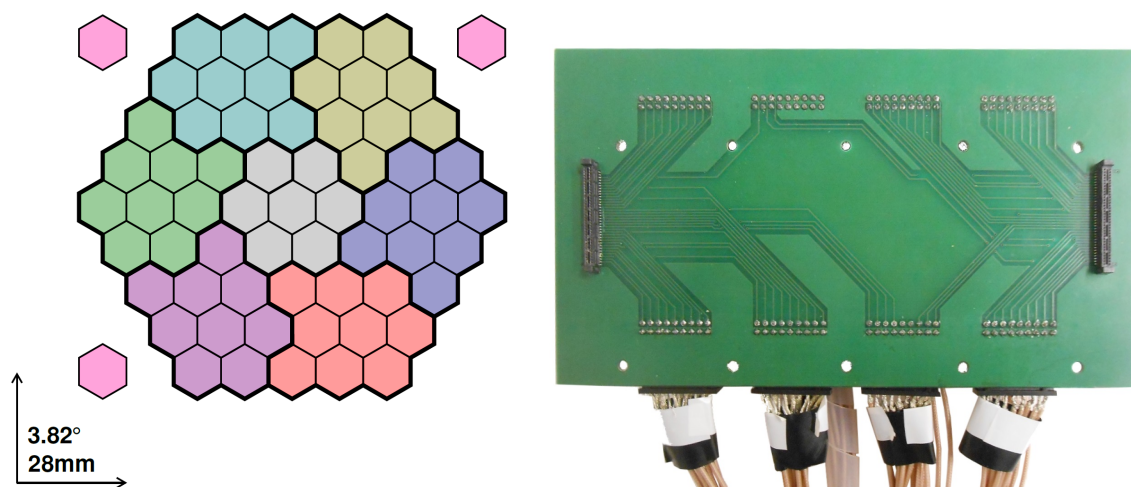
Figure 6.8.: *Left:* The final trigger layout of the FAMOUS telescope when operated with the FACT DAQ system [151]. Pixels were combined in groups of up to nine in an almost symmetric arrangement. The layout was done in cooperation with J. Auffenberg and T. Bretz. Image credits belong to M. Schaufel. Taken from [59]. *Right:* This picture shows the back side of the PCB that routed the pixels from the focal plane to eight connectors according to the trigger layout on the left. The PCB was designed and soldered by the author. Picture credits belong to the author. The picture was pre-released in [59].

trigger decision. The seven central pixels were grouped, while the pattern of all other pixel groups resembled trapezia, symmetrically arranged around the center. The 64 coaxial cables can be seen at the bottom of the picture on the right-hand side. The author fabricated one cable bundle prototype, one was made by M. Schaufel, and the remaining cable bundles were done by the electronics workshop of the III. Physikalisches Institut A, RWTH Aachen University.

A. Bogner made further studies with a focus on the TARGET7 DAQ in [167]. All layouts were tested extensively with Monte Carlo methods in terms of symmetry and unidirectionality. His final trigger layout is shown on the left-hand side of figure 6.9. The image shows a virtual view of the camera. The TARGET7 DAQ requires trigger groups of four pixels. On the right-hand side of the same figure, its electronic implementation is shown. The picture shows the trigger routing PCB plugged on the back side of the focal plane in piggyback fashion.

For all trigger routing PCBs that have been introduced here, care was taken to minimize the number of overlapping traces, to avoid right-angled traces, and to decrease the spread of trace lengths within a trigger group. The idea was to eliminate electronic crosstalk between overlapping traces, radiated noise by right-angled traces and the time jitter between pixels of the same trigger group. For the latter, the trace lengths of the focal plane were also considered. This usually succeeded well, within the temporal resolution of the SiPMs and the read-out, i.e. better than 100 ps which is equal to about 20 mm.

T. Niggemann discussed theoretical implementations of a trigger layout dedicated for air-fluorescence detection extensively in [6] which were based on the trigger system of the fluorescence telescopes of the Pierre Auger Observatory. Hardware implementations were never pursued due to the lack of suitable DAQ systems dedicated for air-fluorescence detection, see
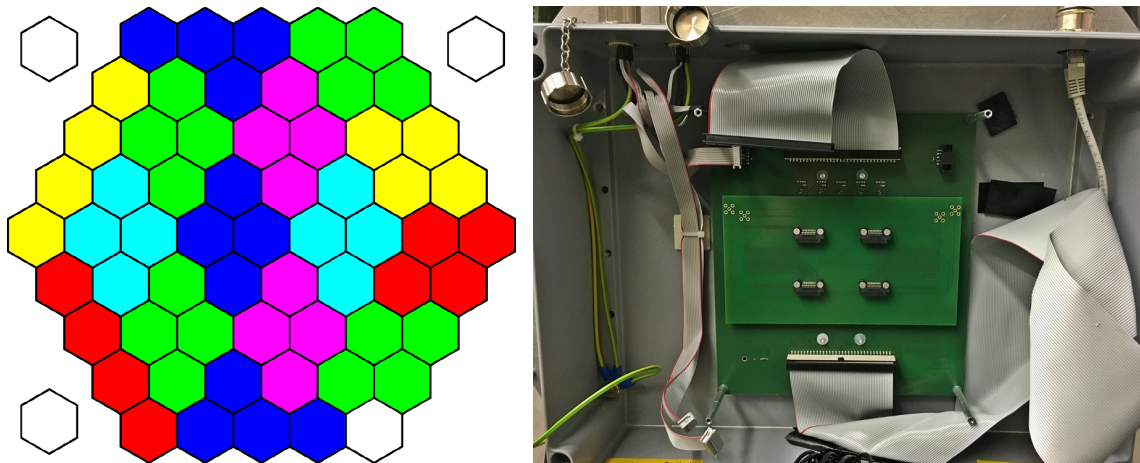
Figure 6.9.: *Left:* The final trigger layout of the trigger routing board developed for the read-out with the TARGET7 DAQ in [167] by A. Bogner. *Right:* Its implementation by A. Bogner as a PCB, assembled, and plugged on the focal plane. The four connectors allowed a direct connection to the TARGET7 DAQ [173] with coaxial flat ribbon cables. Both images were taken from [167]. Image credits belong to A. Bogner.

also next section and earlier discussions. However, this could change in the future as plans were made to send the telescope to the Pierre Auger Observatory in Argentina [143].

6.3.3.3. Data acquisition

The DAQ that the author describes in the following was a loan of the FACT collaboration. The system was specifically designed for the operation with FACT where its performance was studied in detail [151]. Because of the enormous number of channels of FACT, i.e. 1440, the DAQ was conceptualized modularly. One set of the DAQ consisted of one pre-amplifier board (FPA), one trigger unit (FTU), and one digitizer board (FAD). Every set was able to amplify, trigger, and digitize 36 channels. While 40 sets were used in FACT, two sets were sufficient for the FAMOUS telescope to read out 61 regular and three additional blind pixels. A very simplified sketch of one FACT DAQ set is shown in figure 6.10, on the left-hand side.

The FPA held pre-amplifiers for 36 channels, together with four individual trigger modules that were initiated on the voltage threshold on the sum of nine pre-amplifier channels each. The pre-amplified signals were routed through a FAMOUS-specific backplane to the FAD, where they were buffered and sampled by four DRS4 chips. The DRS4 chip, holding nine input channels each, was developed by PSI [172]. These four DRS4 chips were connected to two Analog Devices AD9238-40 [176], two-channel analog-to-digital converters, which were finally read-out by a single field-programmable gate array (FPGA) of the Xilinx Spartan 3-series [177]. The trigger from the four FPA trigger modules was passed to the FTU where a threshold on the sum of the four trigger signals was set. When the threshold was exceeded, a common high-ohmic trigger signal was generated and sent through a LEMO cable.

As every set handled 36 channels, two sets were needed for the full FAMOUS camera to be operated. A common backplane was developed and assembled by the electronics workshop of III. Physikalisches Institut B, RWTH Aachen University, with modest contributions by the author.
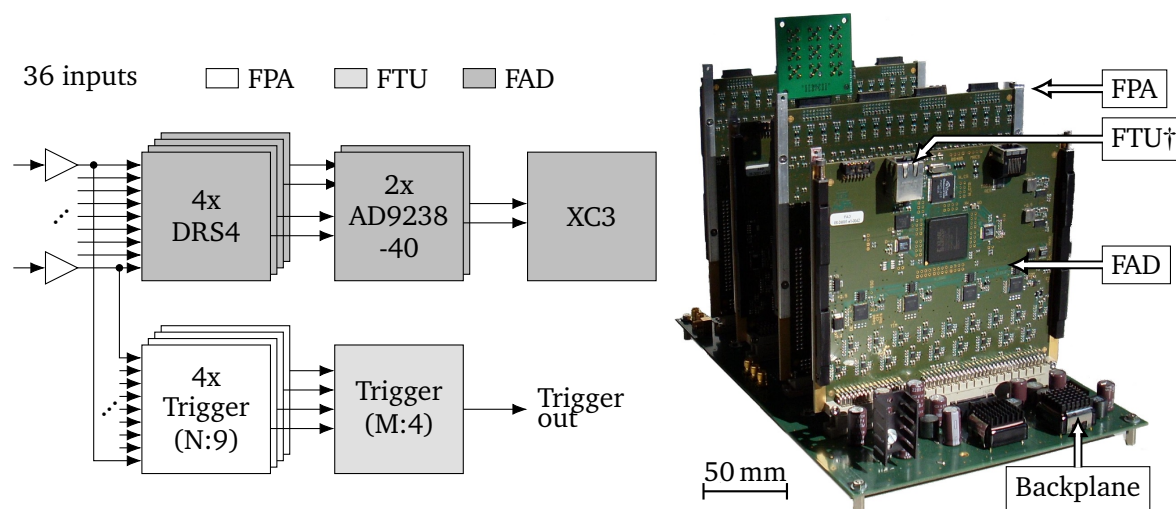
Figure 6.10.: *Left:* Oversimplified schematic diagram of one set (FPA, FTU, FAD) of the DAQ developed by the FACT collaboration [151] for FACT. The fill color indicates on which module the individual components are located: FPA (non-filled), FTU (light-grey), FAD (dark-grey). Two sets were lent to the FAMOUS project. Image credits belong to the author. *Right:* A picture of two FACT DAQ sets plugged into a FAMOUS-specific backplane, and a single SMA-adapter card connected to one FPA input socket. The picture was taken from [59].

A prototype was tested, debugged, and retrofitted by T. Bretz and the author. M. Schaufel tested later revisions. The backplane routed signals, e.g. the pre-amplified SiPM signals, between the FPA and FAD within the same set. It also provided individual power rails from a common ±5 V supply, for the pre-amplifiers and digital components on the FPA, FTU, and FAD.

The trigger system only handled negative input signals, which was why the SiPM de-coupling had to be retrofitted on the focal plane, see earlier discussions. The final integration of the DAQ system was driven by T. Bretz and M. Schaufel, in close collaboration with the author of this thesis. However, two FACT DAQ sets had to be synchronized. In the FACT project, this is done by the trigger master board (FTM) [151]. The author developed a slim version of the trigger master, called miniFTM, which is subject of the next section.

6.3.3.4. Trigger master

As described before, two sets of the FACT DAQ needed to be synchronized. The author developed a system that made use of a Texas Instruments MSP430 microcontroller in a mixed signal environment. In the FACT project, this task was done by the FACT trigger master board, abbreviated FTM, synchronizing 40 DAQ sets. The FTM was not available for the FAMOUS project, and an in-house development was performed by the author of this thesis. In accord to this nomenclature, the module described here was named miniFTM. The author made two versions of miniFTM. In the following, the author concentrates on the last and final one.

To synchronize two FACT DAQ sets miniFTM needed to fulfill the following requirements:

- four low-voltage differential signaling (LVDS) lines duplicated on two RJ45 connectors with
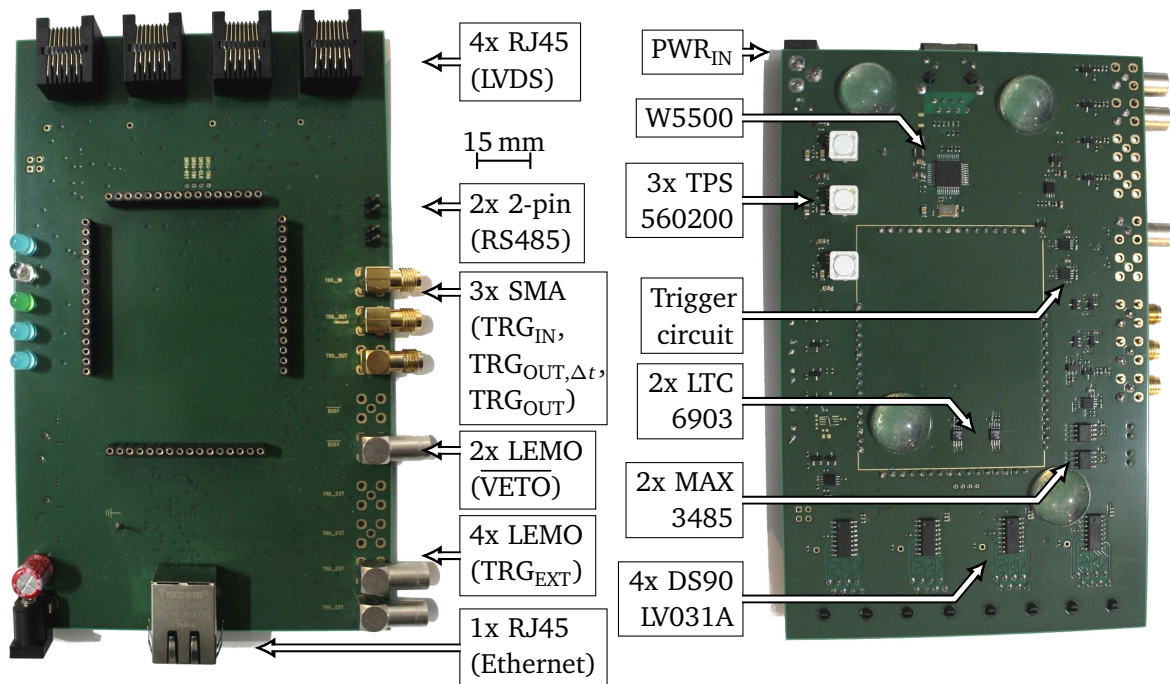
Figure 6.11.: Two pictures of one trigger master module, named miniFTM, developed and soldered by the author. *Left:* The top side and *right:* the bottom side of the same module. The microcontroller board was removed in these pictures. All connectors and LEDs were mounted on the top side which allowed direct access. Meanwhile, the electronic components were soldered on the bottom side. Not all LEMO connectors were populated. Picture credits belong to the author.

- a programmable, highly accurate clock with a frequency of around 1 MHz,

- a main trigger output with a logic consisting of

  - two trigger inputs connected through OR logic on LEMO 00 [178] connectors,

  - one trigger veto added to the OR logic on a LEMO 00, and

  - a programmable, jitter-free trigger delay.

- a reset logic which can be set by the microcontroller, and

- an optional time marker for timing characterizations of the DRS4 sampling chips.

- two differential RS485 lines duplicated on arbitrary connectors with

  - one universal asynchronous receiver-transmitter (UART) port for sending trigger IDs, and

  - one UART port for sending and receiving threshold information.

- powering options from less than 5 V and up to more than 12 V,

- the possibility to upgrade the system to FPGA logic, and finally

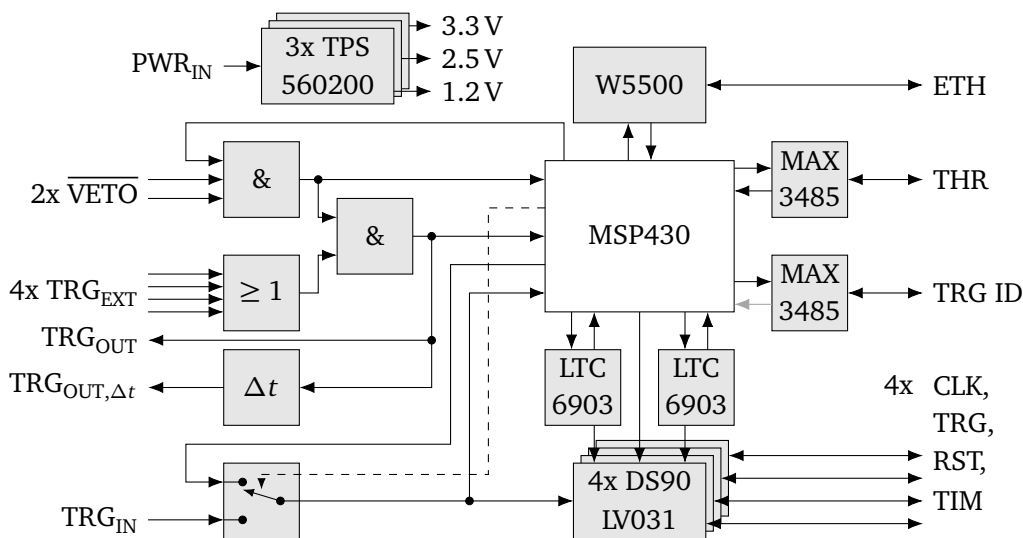- the possibility to be configured via Ethernet.

Figure 6.12.: Schematic diagram of miniFTM. This system is used to synchronize up to four individual FACT DAQ sets. Please refer to the text for details. Image credits belong to the author.

In its 2nd version, miniFTM was designed to synchronize up to four FACT DAQ sets. This allowed stereo observations with two FAMOUS-like telescopes.

Overview   MiniFTM consisted of two PCBs – a main board and a microcontroller board. The latter hosted the MSP430 microcontroller, a 25 MHz quartz oscillator, four LEDs for debugging, and a Spy-bi-wire programming connector. The PCB was attached to the main board in mezzanine fashion with four 16 pin headers. The main board hosted three switching converters of type Texas Instruments TPS560200 [179] which provided 1.2 V, 2.5 V, and 3.3 V, respectively, with output currents of up to 500 mA from a common supply voltage between 4.5 V and 17 V. In the standard configuration, only the 3.3 V rail was used, while the other two were foreseen for an optional FPGA upgrade. The trigger was implemented with fast trigger logic elements that allowed to accept active-high triggers from four connectors and active-low vetoes from two connectors. A fixed delay line of about 400 ns provided a delayed output with the intention to move the trigger position close to the center of the readout window. A non-delayed output allowed the usage of an external delay circuit, or a delay provided by the microcontroller or FPGA instead. Fixed rate and random triggering were implemented in the microcontroller to take calibration data. Threshold information and trigger IDs were sent and, in the case of the threshold, received through two separate RS485 lines translated to low-voltage transistor-transistor logic (LVTTL), and vice versa, by two Maxim Integrated MAX3485 [180] chips. The clock and the time marker were generated through two independent clock generators of type Linear Technology LTC6903 [181]. The MSP430 was able to reset the FACT module through LVDS lines which were grouped with the DRS4 clock, a trigger indicator signal and time marker via four Texas Instruments DS90LV031A [182] chips. The Wiznet W5500 [183] chip provided Ethernet communication with the user. Figure 6.11 shows a picture of a miniFTM main board and of a microcontroller board, while figure 6.12 shows a simplified schematic diagram of miniFTM.

Trigger implementation The trigger was implemented with discrete logic elements from the SN74LVC-family of Texas Instrument's little logic, which included the SN74LVC1G08, a two-input AND gate, the SN74LVC1G123, a monostable multivibrator, and the SN74LVC1G3157, a two input analog switch [184, 185, 186]. Buffers and line drivers were implemented with fast bipolar transistors of type NXP BFR93A and BFT93 [187, 188]. The BFR93A is a 6 GHz NPN transistor that can source up to 35 mA. The BFT93 is the PNP complementary of the BFR93A with similar characteristics, i.e. a transition frequency of 5 GHz and a direct current (DC) of up to 35 mA.

MiniFTM featured four LEMO 00 connectors which provided the input for four external triggers. Every input was buffered by a single BFR93A whose input resistance was set with a 10 kΩ resistor due to the rather large output impedance of the FACT DAQ trigger output. A 50 Ω resistor would not have worked. The emitters of the four NPN transistors were shorted together generating a simple OR logic while every BFR93A held a single 200 Ω emitter resistor.

Two further LEMO 00 connectors were used for external vetoing of the trigger. The veto condition was active low meaning that when the veto was idle, its voltage was near the supply voltage of 3.3 V. This is indicated by the symbol $\overline{\text{VETO}}$ in figure 6.12. The veto was used to discard triggers if the DAQ was busy, for example at the time when a preceding trigger was processed. This, of course, reduced the effective uptime of the telescope. The microcontroller set an additional veto. These three veto signals were added in AND logic which meant that as soon as one veto was active, i.e. at low voltage, the output of the logic element went low, too.

The output of the discrete OR logic of the four external trigger inputs and the output of the AND logic was connected to a further AND logic element generating the main trigger TRG_{OUT}. This circuitry accepted only triggers where the veto was inactive, i.e. high at the same time. The trigger output was fed into the MSP430 which further processed the trigger digitally. The MSP430 registered transitions from low to high and generated interrupts. More information can be found in the section about the firmware.

The author developed a fixed delay with analog components. It generated a pulse of fixed width in the event of an initial rising edge yet delayed by Δt. Consisting of two stages the first stage discharged a capacitor C instantly on the initial rising edge of the input pulse, setting its output voltage to 3.3 V. While the voltage on that capacitor recharged through a resistor R, the output of that stage remained high. When the voltage across C exceeded the voltage threshold v_{thr}, its output toggled to the low level, i.e. GND. The second stage registered the falling edge of the first stage and performed a similar process with a second resistor and capacitor circuit, generating an output pulse with a fixed length. However, the resulting pulse was delayed by Δt.

The total delay Δt was therefore defined over the width of the output pulse of the first stage plus any transition delay Δt_t of the discrete components and traces. Its value could then be estimated with

$$\Delta t \approx R\,C \cdot \ln\left(\frac{1}{1 - v_{\text{thr}}/3.3\,\text{V}}\right) + \Delta t_t. \tag{6.12}$$

Originally, v_{thr} was fixed by a device-specific value. R and C were chosen in a way to generate a fixed delay period of $\Delta t \approx 330\,\text{ns} + \Delta t_t$. The delay was thus not programmable. In a later revision, v_{thr} was set by a digital-to-analog converter, adding a programmable feature to the delay circuitry. This revision, however, was never built. Additional delay summed up through the finite response by individual components, propagation and line delay through traces, as

well as finite rise times, in the order of $\Delta t_t \sim 50\,\text{ns}$ in total. Note, that Δt was not linear in v_{thr} as evident from above formula.

The purpose of the delay was to shift the trigger position t_0 in the read-out window to $t_0 - \Delta t$. A subsequent timespan Δt after the trigger was thus recorded in the data stream. Without this delay, only the rising edge of the pulses that initiated the trigger would have been recorded, together with everything that had happened before, yet nothing afterward. Typically, the trigger position should be moved to the end of the first third of the read-out window, due to the temporal asymmetry of the SiPM pulse shape. This allowed estimating the baseline of the trace and its electronic noise, any single photon pulses that did not exceed the threshold level as well as the decaying signal after the trigger. With a sampling rate of $2\,\text{GSa}\,\text{s}^{-1}$ and a buffer length of $1024\,\text{Sa}$, i.e. a sample length of $512\,\text{ns}$, the total delay should be set to about $400\,\text{ns}$ which moved the rising edge of the trigger near cell $200 \approx 1024 - 800$. If a different sample rate were chosen the values of R and C would have to be changed according to the above equations. In the latest revision, however, the delay could be changed by programming the digital-to-analog converter (DAC). In the original miniFTM, the author chose $R = 2.2\,\text{k}\Omega$ and $C = 100\,\text{pF}$ to generate $380\,\text{ns}$ from connector to connector.

The delayed and the non-delayed trigger output, $\text{TRG}_{\text{OUT},\Delta t}$ and TRG_{OUT} were directed to SMA connectors. Likewise, a trigger input TRG_{IN} was accepted from an SMA connector. The idea here was to either connect a coaxial cable from $\text{TRG}_{\text{OUT},\Delta t}$ to TRG_{IN}, or from TRG_{OUT} to TRG_{IN}. In the case of TRG_{OUT}, an external delay had to be placed between both SMA connectors. Per default, $\text{TRG}_{\text{OUT},\Delta t}$ was connected to TRG_{IN}.

TRG_{IN} was connected to a single pole-double throw switch, type SN74LVC1G3157. Its purpose was to switch off any external triggers, for example during startup, to prevent any triggers from reaching the DAQ during initialization. A digital pin of the MSP430 was connected to the other input of the switch. This pin was used to generate a fixed rate or a pseudo-random trigger. The MSP430 could change the state of the switch.

In the end, the final trigger signal was sent to the MSP430 and the DAQ through LVTTL to LVDS converters of type DS90LV031A. All signals that were transmitted to the MSP430 were artificially stretched to at least $50\,\text{ns}$, to guarantee that the microcontroller registered the low-to-high transition in its interrupt routines. Outgoing signals were about $2.4\,\text{V}$ in size at a load of $50\,\Omega$, about $100\,\text{ns}$ long and active high. Again, figure 6.12 shows a simplified sketch of the trigger circuit.

Clock generation for the DRS4 sampling rate   One of the two LTC6903 chips was programmed to generate the clock frequency f_{LTC6903}. This clock was sent to all FADs through one channel of every DS90LV031A LVDS drivers. The DRS4 sampling rate ζ_{DRS4}, a quantity given in $\text{Sa}\,\text{s}^{-1}$, related to this clock through

$$\zeta_{\text{DRS4}} = 2 \cdot 1024\,\text{Sa} \cdot f_{\text{LTC6903}}. \quad [172] \tag{6.13}$$

$1024\,\text{Sa}$ is the DRS4 ring buffer size in number of samples Sa. As described above, miniFTM was optimized for an operation at $\zeta_{\text{DRS4}} = 2\,\text{GSa}\,\text{s}^{-1}$, because the author initially designed a fixed delay of about $400\,\text{ns}$. Therefore, the LTC6903 nominal target frequency was targeted to be

$$f_{\text{LTC6903, nom}} = \frac{2\,\text{GSa}\,\text{s}^{-1}}{2048\,\text{Sa}} = 976.5625\,\text{kHz}. \tag{6.14}$$

The LTC6903 is programmed with one 4 bit and one 10 bit integer, i.e. OCT and DAC, whose combination sets the output frequency according to

$$f_{\text{LTC6903}}(\text{OCT}, \text{DAC}) \equiv 2^{\text{OCT}} \cdot \frac{2078\,\text{Hz}}{2 - \text{DAC}/1024}. \; [181] \qquad (6.15)$$

By setting OCT = 9 and DAC = 932, a sampling rate close to $2\,\text{GSa}\,\text{s}^{-1}$ is obtained. Although $f_{\text{LTC6903}}(9, 932)$ is smaller than $f_{\text{LTC6903, nom}}$ by about $3 \cdot 10^{-4}$, the typical initial absolute accuracy of $5 \cdot 10^{-3}$ [181] is even worse. If the sampling rate needed to be known by better than 0.5 %, the LTC6903 clock frequency would have to be calibrated. As long as the value did not change with time, an absolute knowledge better than 0.5 %, i.e. 3 ns on 1024 samples sampled at $2\,\text{GSa}\,\text{s}^{-1}$, would not be necessary. With a frequency drift of only $10\,\text{ppm}\,\text{K}^{-1}$ [181], the LTC6903 was perfectly suited for operations over a wide temperature range.

Communication   Inter-Communication between the DAQ and the user was implemented with RS485, LVDS and TCP/IP standards. The latter will be discussed in a later section.

As already introduced above, miniFTM sent trigger information to the DAQ, resp. to the FADs, whenever a trigger event occurred. The communication protocol was RS485, a differential bus, as chosen by the engineers who developed the FACT DAQ electronics. A baud rate of about $250\,\text{kbaud}\,\text{s}^{-1}$, two stop bits and no parity bit realized its logical implementation, while the MAX3485 translated the single-ended LVTTL logic from the MSP430 to differential RS485 logic levels for transmission to the DAQ.

The trigger information contained the type of trigger, i.e. internal or external, and a running number which indicated the trigger counter, resp. event number. This information was received by the FADs and saved in the event header, identifying the time and event number in the rare case of desynchronization of two or more FADs.

The trigger itself, i.e. the switched TRG_{IN} signal, the LTC6903 clock for the DRS4 sampling rate generation, i.e. f_{LTC6903}, the DAQ reset and time marker were converted from single-ended LVTTL into differential LVDS by the use of four 4-input DS90LV031A driver chips. The communication was implemented unidirectionally, i.e. receiving was not foreseen. For every DAQ set, a separate DS90LV031A routed its signal to one generic RJ45 connectors.

Firmware   The following describes the firmware loaded onto the MSP430. It was programmed in C code and compiled and debugged with the help of Texas Instruments' Code Composer Studio [189]. After initialization of its central processing unit (CPU) clock, general purpose inputs and outputs, timers, analog-to-digital converter (ADC), UART and serial peripheral interface (SPI) buses, and registration of its interrupts, the MSP430 entered an infinite loop. In this loop, the MSP430 checked for the status of its interrupts through flag polling. In the respective interrupt procedures, these flags were set or unset on receiving an interrupt, after which, the procedures terminated. Otherwise, the interrupt procedures would have blocked the CPU and prevented further quasi-parallel critical real-time interrupts.

Interrupts   When an interrupt flag was polled, the busy indicator was set, leading to $\overline{\text{VETO}}$ going low and any succeeding triggers being ignored. The following interrupts were implemented:

1. internal trigger generation through a timer overflow,

2. external trigger capture through low-to-high transition on the trigger input,

3. periodic data transmission through yet another timer overflow, and

4. Ethernet state change interrupts through low-to-high transition on the Ethernet interrupt pin.

In any case, the flag was unset after the interrupt handler was processed. The internal trigger timer period could be set via Ethernet. A fixed rate trigger and a random trigger were implemented, also selectable through Ethernet. While the fixed rate trigger generated timer periods $\Delta t = 1/f$, where f was the target frequency, the random trigger determined Δt through the probability density function

$$p(\Delta t) \cdot \mathrm{d}\Delta t = \frac{\exp(-f \cdot \Delta t)}{f} \cdot \mathrm{d}\Delta t, \tag{6.16}$$

whose expected value was the inverse of the target frequency $1/f$. f had to be selected appropriately via Ethernet. Small timer periods $\Delta t < 10\,\mathrm{ms}$ were discarded, in both cases. Also, both implementations checked whether the DAQ was busy by polling $\overline{\mathrm{VETO}}$.

As the MSP430 did not feature a random number generator, T. Bretz and the author developed a rather simple code that generated pseudo-random numbers in C/C++ based on arithmetic integer operations and bit manipulation, i.e. bitwise operations and bit shifts [143]. Its implementation is attached to this thesis, in appendix A.11 starting on page 172. The purpose of the random trigger was to study systematics by emulating triggers originating from the night-sky background.

The implementation of the external trigger has already been discussed above. Also, a timer was used to send trigger numbers via Ethernet periodically. The data contained a 32 bit counter which was incremented whenever a trigger was sent to the DAQ. In the latest revision 2.b, clock cycles were counted at which the DAQ was busy $n_{\overline{\mathrm{VETO}}=0}$ and at which the DAQ was not, n_1. Both values were sent in two separate 32 bit integers. By taking the ratio of both integers, i.e. $n_1/(n_1 + n_0)$, the measured uptime of the telescope could be estimated.

Finally, an interrupt was raised whenever the state of the W5500 changed, for example during connecting, disconnecting, error raising or data reception. When the MSP430 handled the interrupt it would set the busy flag, i.e. $\overline{\mathrm{VETO}} = 0$. In the event of connecting or disconnecting, the MSP430 changed its state which was indicated to the user by lighting up or switching out an LED, respectively. Also, automatic transmissions were activated or deactivated. Timeouts and the like raised an error interrupt which led to all LEDs blinking synchronously. The system had to be reset in that state. When data was received through its port, the MSP430 checked the command by interpreting the byte string received.

Ethernet commands The default IP 10.0.131.222 and MAC 00:08:DC:4F:0D:FE were loaded onto the W5500 Ethernet chip during startup. Every command was embedded in a 16 B-long byte frame. Every frame started and ended with two FF frame bytes. Three command bytes followed, whose first byte indicated a read (00) or write (04) procedure. Eight optional data bytes and a checksum byte completed a frame. The checksum byte was simply the least significant byte of the arithmetic sum of all preceding bytes except for the first two. The communication protocol is attached to this thesis, see appendix A.12 on page 173. Table A.2 visualizes a single

command frame used for communication with miniFTM, while table A.3 summarizes all commands that were implemented in the FAMOUS miniFTM microcontroller up to this point (30th of June 2018).

Characterization & calibration MiniFTM was tested and debugged intensively by T. Bretz and me. Its results will be summarized qualitatively in the following.

The trigger delay circuit was tested with regard to temporal jitter with a 500 MHz bandwidth oscilloscope and a sampling rate of $2\,\mathrm{GSa\,s^{-1}}$. A pulse generator created an artificial trigger and the time difference between the input and output trigger was measured with the oscilloscope. It was found that the temporal jitter was compatible with the resolution of the oscilloscope, i.e. a width smaller than 500 ps was found.

Similar tests were performed for the random trigger generator, with the result that the time distribution followed an exponential function. However, due to its integer implementation, the exponential function was not continuous. The DRS4 clock generator was tested with the FACT electronics. The FADs successfully locked the clock generated by the LTC6903 on the miniFTM. The total power consumption of miniFTM during standard operations was determined with a multimeter and found to be about 650 mW on a 12 V supply, where more than half of the power was dissipated by the W5500 Ethernet chip.

All in all, miniFTM successfully synchronized two sets of FACT DAQ electronics.

6.3.3.5. Bias supply

The purpose of an SiPM bias supply has already been introduced in chapter 5: It keeps an SiPM biased with a constant overvoltage over time, temperature, and load. The main differences between the SiPM bias supply for the FAMOUS telescope and the one for the scintillator module are

1. the number of channels,

2. the output current, and

3. the operation from alternating current (AC) mains.

The bias supply of the scintillator module sourced two SiPMs from the same voltage. The current drawn by the SiPMs was dominated by the dark current of the SiPMs and was usually found below 1 μA. As the nominal operating voltages of all FAMOUS SiPMs scattered around 65.74 V by 0.15 V, i.e. more than 10 % of the nominal overvoltage, all 64 SiPMs packages had to be biased with individual voltages. Every channel needed to source currents of up to 1 mA.

Furthermore, all voltages needed to be generated from either 110 V 60 Hz or 230 V 50 Hz mains instead of a DC voltage. A low power consumption, on the other hand, was not required as the system did not rely on a limited power budget through the operation of a battery rather than on the quasi-unlimited power of the mains.

The SiPM power supply was developed in cooperation with the electronics workshop of the III. Physikalisches Institut A, RWTH Aachen University, Germany. While its main features have already been pre-released in [111], the author will focus on hardware improvements, the microcontroller firmware and the hardware calibration which have not been discussed in above publication.

Overview The FAMOUS power supply was split into an alternating-current-to-direct-current (AC/DC) module and a DC/DC module. The latter was composed of self-designed linear regulators and offered current and temperature monitoring.

The total number of channels was 64, equal to the number of SiPM arrays in the SiPM camera. For newer SiPM generations, the number of bias channels could be reduced as the production quality improved over the years and the typical standard deviation of the breakdown voltages of a sample size of 146 590 SensL B-series SiPMs was found to be 0.073 V [64]. For an operation of nominal 5 V overvoltage, this is approx. 1.5 %. In the case of the FAMOUS camera, the standard deviation is about 0.15 V, generating a fluctuation of 11.6 % at the nominal overvoltage of 1.3 V. It was thus decided to bias all 64 SiPMs individually. However, the SiPM camera that was operating at the South pole season 2017 to 2018, for example, was equipped with the SensL C series SiPMs, and its power supply featured only a single channel biasing all 64 SiPMs with the same voltage, due to its predicted homogeneity.

Temperature monitoring is essential due to the temperature dependence of the SiPM breakdown voltage, see again equation (4.2) on page 37. It was chosen to utilize one temperature sensor for every single SiPM array, as the temperature spread across the camera ΔT was expected to introduce a significant change in the gain, i.e. $\Delta T \cdot \mathrm{d}v_{\mathrm{bd}}/\mathrm{d}T/v_{\mathrm{ov, nom}}$, particularly because of the large temperature dependence given in the second product. While the temperature dependence of the gain of recent SiPM species has been about $5\,\%\,\mathrm{K}^{-1}$ [62], new generations promise temperature dependences of as low as $0.5\,\%\,\mathrm{K}^{-1}$ [101]. For a new version of the FAMOUS SiPM camera, the number of temperature channels could be reduced. In that case, however, interpolation between neighboring temperature sensors had to be done in software or the microcontroller firmware.

Measuring the current in every bias channel allows to perform optical alignment measurements, see [6], as the current, once calibrated, is a direct measure for the photon flux on an SiPM, see preceding chapters. This quantity is averaged over an extended period, i.e. fractions of seconds and does not qualify for air-shower measurements. However, the trigger thresholds in the DAQ could be adjusted to the night-sky background in an automated process when the pixel currents were known. The value of the thresholds for pixels with, e.g. a star in the field of view can be increased to suppress background events. This, of course, needs to be reported such that analyses take the actual live-time of the instrument into account.

The former unit, the AC/DC module generated DC voltages from the AC mains with the use of transformers, bridge rectifiers, electrolytic capacitors, and linear regulators. This module will be described here only briefly. Although the technology is free of high-frequency noise and very durable, it has many disadvantages, like a high power consumption, heavy weight, high costs, and large physical dimensions. A new solution has not yet been finished, but an outlook onto a prototype system based on switching converters is given at the end of this chapter.

The AC/DC module The power supply was initially designed to operate from 230 V AC mains or from 115 V AC with either 50 Hz or 60 Hz. An intelligent circuit was developed, that detected the operating voltage and switched the number of primary windings of the transformers with electromagnetic relays by a factor of two to ensure that roughly the same AC voltage was available behind the transformers' secondary windings in either case – for operation in Europe, i.e. 230 V and 50 Hz, and in North America, i.e. 120 V and 60 Hz.

Bridge rectifiers created unidirectional alternating voltages. Large-sized capacitors with aluminum electrolyte smoothed the output voltage. Care was taken to choose capacitors with an
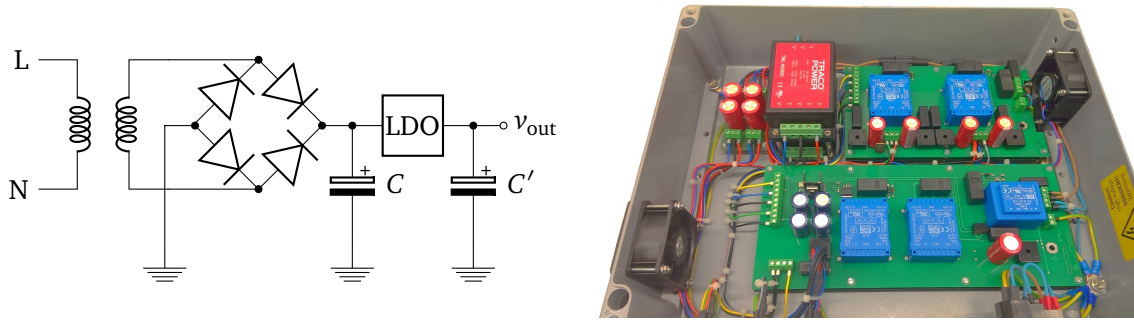
Figure 6.13.: *Left:* An equivalent circuit of a transformer-based bridge rectifier with capacitive ripple suppression and a LDO linear regulator. These circuits were used to generate DC voltages from AC mains. *Right:* This picture shows the top side of the AC/DC module PCBs surrounded by the aluminum enclosure. Image and picture credits belong to the author.

appropriate voltage rating, expected lifetime, i.e. low equivalent series resistance, and capacitance. The left-hand side of figure 6.13 shows an equivalent circuit of one out of six AC/DC channels, while its right-hand side shows a picture of its implementation in the FAMOUS AC/DC power supply.

The following estimation can be made to estimate the size of the capacitor: Assume a diode operating in forward direction, with infinite off-resistance $R_{d,\,off}$. An alternating voltage with amplitude v_{amp} and wave frequency $\omega = 2\pi f$ is connected to the anode of the diode. The diode charges a capacitor C through the output voltage v_{out}. A current load i_L is connected in parallel with the capacitor. The peak-to-peak ripple voltage, that is $v_{pp\text{-}ripple} \equiv v_{amp} - v_{out,min}$ can then be shown to be

$$v_{pp\text{-}ripple} \approx i_L \cdot \left(\frac{1}{f \cdot C} + R_C \right), \tag{6.17}$$

where $R_{d,\,off} \cdot C \gg 1/f$ has been used, i.e. higher geometrical orders of the exponential decay have been dismissed. R_C is the equivalent series resistance (ESR) of the capacitor which is typically a few $100\,\text{m}\Omega$ [190]. In the case of a bridge rectifier, f in above equation becomes twice the input frequency, e.g. $f = 100\,\text{Hz}$ in the case of European mains and $120\,\text{Hz}$ in the case of North American mains, due to its full-wave rectification. However, above relation only holds for large v_{amp}, where $v_{pp\text{-}ripple} < v_{amp}$ or equivalently only for small loads i_L. In other words, the above equation is only valid when the output voltage $v_{out}(t)$ can be parameterized with a saw-tooth function. In the case of the FAMOUS power supply system, this was always the case.

With the rule-of-thumb

$$C \geq 10 \cdot i_L\, \mu\text{F}\,\text{mA}^{-1}, \quad \text{see for example [191]} \tag{6.18}$$

the peak-to-peak ripple voltage becomes typically $v_{pp\text{-}ripple} = 1\,\text{V}$ while neglecting the ESR of the capacitor. Post-linear regulators offer great ripple rejection in the order of $70\,\text{dB}$, for example the LM7800-series [110], which further damps the ripple by 10^{-3} to 10^{-4} in this frequency band.

The AC/DC module was comprised of a high-voltage and a low-voltage section: The high-voltage PCB featured two transformers with two primary and two secondary windings each. The secondary windings were cascaded in series. Depending on whether the module was operated with 110 V or with 230 V mains, the primary windings were operated in parallel or in series, respectively, with the use of magnetic relays. The secondary windings of the transformers were connected to bridge rectifiers and converted to DC voltages with the use of two 330 μF capacitors in parallel, each with a voltage rating of 160 V. A capacitance of 660 μF was chosen from the requirement of sourcing 64, resp. 61 SiPMs with a maximum current of 1 mA each and the rule-of-thumb from equation (6.18). The result was a DC voltage of approx. $84 \, V^2$ with $v_{\text{pp-ripple}} < 20 \, \text{mV}$ at a load of 1 mA and $v_{\text{pp-ripple}} < 1 \, \text{V}$ at a load of 60 mA.

The peak-to-peak ripple was further reduced with the use of a high-voltage, high-power low-dropout linear regulator of the kind that had been developed in [68]. The discussions on the linear regulator will be postponed to the section about the DC/DC module as it shares the same features as the ones described below. A full Simulation Program with Integrated Circuit Emphasis (SPICE) simulation of this circuit estimated a remaining peak-to-peak ripple voltage of less than 90 μV with a load of 60 mA. This was less than $7 \cdot 10^{-5}$ of the nominal overvoltage of 1.3 V of the SiPMs. This was tested with an oscilloscope and a programmable load and found to be true, resp. less than 100 μV in the resolution of the measurement.

The average output voltage was set to 73 V with the use of a resistor pair and a voltage reference, according to the last chapter's equation (5.4). As this circuit was capable of sourcing more than 100 mA, a Zener diode was added that limited the current to 100 mA, i.e. 1.5 mA per channel on average. This was part of the improvements done by the author, along with aluminum electrolytic capacitors of larger capacitance i.e. two times 330 μF instead of one 100 μF, the addition of ceramic capacitors in parallel to reduce the effective ESR at intermediate and high frequencies above 100 Hz. Furthermore, a potentiometer was removed and replaced by two resistors to fix the output voltage to 73 V. Its incentive becomes evident in the next section.

Similar thoughts applied to the low-voltage section of the AC/DC module. Four individual secondary transformer windings were used to supply the temperature sensors on the SiPM camera, the analog electronics on the high-voltage section and DC/DC module, the main digital electronics like the micro-controller and digital-to-analog converters, and the Ethernet controller. Bridge rectifiers and 2200 μF electrolytic capacitors created DC voltages of approx. 8 V. No significant load was expected during a healthy operation i.e. in the case of no shorts on the camera or the DC/DC module. Only the W5500 Ethernet controller dissipated a significant amount of current, namely 132 mA on a 3.3 V operation, yet typically less [183]. The 8 V voltages were followed by commercial on-chip linear regulators e.g. the Texas Instruments LM1086 [115] in the case of the Ethernet, digital and analog voltages, and by the Fairchild LM7805 [110] in the case of the temperature sensors, generating two times 3.3 V (Ethernet and digital) and two times 5 V (analog and temperatures sensors). The peak-to-peak ripple was expected to be less than 600 μV in a worst-case scenario, i.e. in the case of the W5500 operating at full load.

The complexity and costs of this solution become evident in the description above which have been made on purpose for reasons of safety and stability.

---

[2] The secondary windings created 15 V AC from the primaries' 115 V AC. Then, four windings in series gives $4 \times 15 \, V \, AC \times \sqrt{2} \approx 85 \, V$ DC, where the forward voltage drop across the diodes has not been considered, yet.
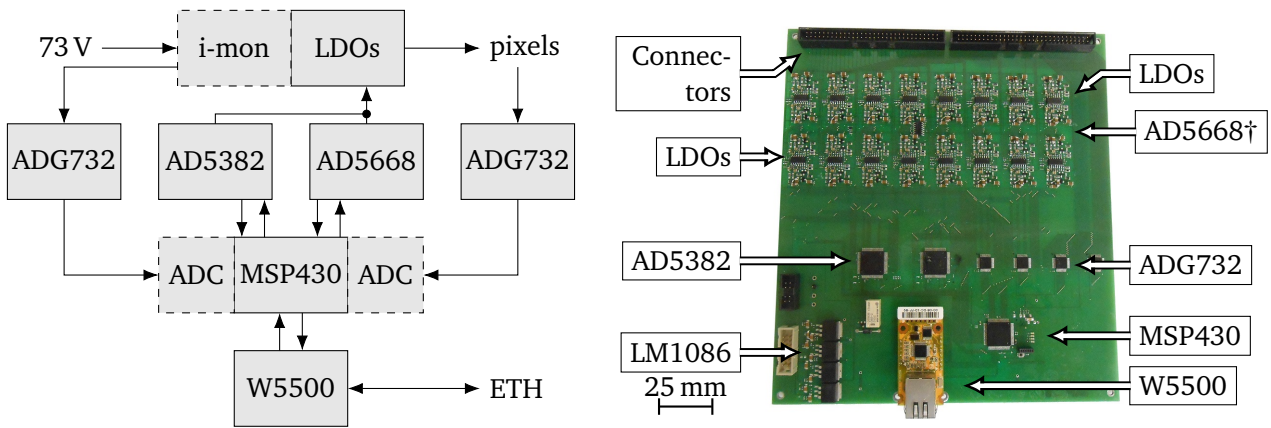
Figure 6.14.: *Left:* This sketch of the DC/DC module shows the design principle of the mixed-signal feedback system of the FAMOUS bias supply. *Right:* A picture of a fully-assembled DC/DC module PCB. The picture was pre-released in [59]. The eight AD5668 chips are soldered on the back side, not visible in this picture and thus marked with the †-symbol. Circuit diagrams of the current monitoring i-mon and the LDO linear regulators are explicitly shown in figure 6.15. Image and picture credits belong to the author.

The DC/DC module   The DC/DC module contained 64 bias channels, with individual current, and external temperature monitoring. A Texas Instruments MSP430F5659 [85] microcontroller operated at the heart of the DC/DC module. The MSP430 controlled the 14 bit and 16 bit DACs, the multiplexers, MUXs, and digitized the voltage of the analog temperature sensors and the voltage of the analog current measurement with its built-in 12 bit ADCs. Communication with the user was made available through the Wiznet W5500 [183] Ethernet controller. A sketch is given in figure 6.14, together with a picture of a fully assembled PCB as pre-released in [111].

The bias voltage controllers were of a similar type as the ones described in the last chapter. Again, the bias voltage controllers were discretely-built low-dropout linear regulators. The technical design was based on the solution described in [68]. Every channel was built from one PNP series pass transistor, type Nexperia PBHV9040T [192], one NPN sink transistor, type Diodes Inc FMMT458 [193], one error amplifier utilized by one of the four channels of the STMicroelectronics TS914 [77] operational amplifier, a precision resistor pair and several standard resistors and capacitors. Simplified schematics are given on the right-hand side in figure 6.15. v_b is set through the ratio of the precision resistor pair R_1 and R_2 and the voltage reference, allocated by the DACs, according to equation (5.4) on page 79.

The DC/DC module featured current monitoring for every individual bias channel. These circuitries were set up electronically between the 73 V of the AC/DC module and every individual LDO linear regulator. A shunt resistor of 1 kΩ introduced a voltage drop whenever a current i_L was drawn. This is shown on the left-hand side in figure 6.15. The resistor also worked as a current limiter, limiting the current to $i_{lim} \approx (73 \, V - v_b)/1 \, k\Omega$, which is typically less than 10 mA while $v_b > 63 \, V$.

The reason for arranging the current monitoring physically between the 73 V and the LDO, and not between the LDO and the SiPM was that the voltage drop across the 1 kΩ shunt resistor did not affect the SiPM operating voltage in the case of the former arrangement. On the other
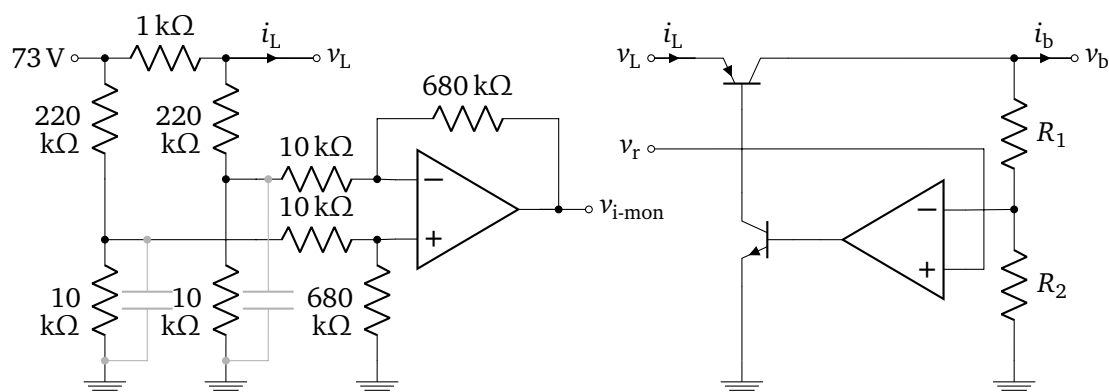
Figure 6.15.: This figure shows simplified circuit diagrams of the analog feedback system of a single FAMOUS bias channel. *Left:* The current monitoring measures the voltage drop across a shunt resistor of $1\,\text{k}\Omega$. This takes place in front of the bias channel, such that the SiPM bias voltage is unaffected by the voltage drop. *Right:* An over-simplified circuit diagram of a single bias voltage channel set up in the tradition of an LDO linear regulator. v_b is set depending on the value of the reference voltage v_r and the resistor pair R_1 and R_2. Image credits belong to the author.

hand, the current i_L did not only include the load of the SiPM i_b, rather than the sum of the LDO's own base current i_LDO and i_b. This had to be calibrated. As the common-mode voltage at the shunt resistor was quite high, about $73\,\text{V}$, the voltage was divided down with the $220\,\text{k}\Omega$ and $10\,\text{k}\Omega$ resistor bridge. A difference amplifier eliminated a significant fraction of the remaining common-mode voltage allowing the output voltage v_i to be digitized by the MSP430's ADCs. D. Louis of the electronics workshop of III. Physikalisches Institut A, RWTH Aachen University designed that circuit.

The current measurement circuitry was subject to electronic noise fluctuations on the output node v_i, due to the voltage divider, i.e. attenuator, and the following amplifier circuit. Two capacitors were added by the author to counteract the noise sources after experiencing large fluctuations in the monitoring data during the first years of operation. Both capacitors are drawn in gray in parallel to the two $10\,\text{k}\Omega$ resistors in the figure 6.15. They form an RC low-pass filter with the $220\,\text{k}\Omega$ resistors. Instead of a cut-off frequency of about $160\,\text{kHz}$ which was dominated by the bandwidth of the TS914, the corner frequency could be decreased to less than $20\,\text{Hz}$ by choosing $1\,\mu\text{F}$ capacitors. The effective noise density with and without the two capacitors is quantified in the upcoming calibration section.

Calibration Due to the relatively large number of resistors in every bias channel, i.e. 17, its associated resistance variance, and the deviating nature of transistor properties, it was decided to calibrate all 64 bias channels. The bias voltage was calibrated against the digital, integer DAC code. The current drawn by the SiPM, on the other hand, was determined as a function of the current monitoring digital integer ADC code and the bias voltage DAC code.

Bias voltage setting The electronics workshop of III. Physikalisches Institut A, RWTH Aachen University calibrated the transfer function between the bias voltage in système international d'unités – International System of Units (SI)-units and the DAC codes. As described

above, one 16 bit DAC channel and one 14 bit DAC channel were mixed to create the reference voltage of the LDO. It was later found that if only a single 16 bit DAC per bias channel was used the bias voltage resolution would not have dramatically worsened, i.e. only by 1/4. However, costs and complexity would have dropped dramatically, reducing the need for calibration.

Both channels were averaged with the use of a resistive divider, with two input resistors R_{16} and R_{14} and one output resistor R_r. Its transfer function was

$$v_r(v_{16}, v_{14}) = \left(R_{16} \parallel R_{14} \parallel R_r\right) \cdot \left(\frac{v_{16}}{R_{16}} + \frac{v_{14}}{R_{14}}\right), \tag{6.19}$$

with

$$v_{16} = \frac{3.3\,\mathrm{V}}{2^{16}} \cdot \mathrm{DAC_{off}}, \text{ and} \tag{6.20}$$

$$v_{14} = \frac{2.5\,\mathrm{V}}{2^{14}} \cdot \mathrm{DAC_{reg}}. \tag{6.21}$$

Here, v_{16} and R_{16} is the voltage and the resistance of the 16 bit DAC and its series resistor. Respective thoughts apply to v_{14} and R_{14}. All resistances need to be high-ohmic to neglect the DACs output resistances, though not too high-ohmic that the input impedance of the error amplifier must be considered. The choice of the electronics workshop was $R_{16} = 10\,\mathrm{k\Omega}$, $R_{14} = 27\,\mathrm{k\Omega}$, and $R_r = 10\,\mathrm{k\Omega}$. $\mathrm{DAC_{off}}$ and $\mathrm{DAC_{reg}}$ are the integer DAC values for the 16 bit and 14 bit DAC, respectively.

The 16 bit DAC originally served to specify the range of the bias voltage by providing a constant offset. Only the 14 bit DAC was used to fine-tune the bias voltage for example against temperature, or to compensate the different breakdown voltages of the SiPMs. According to equation (5.4), the bias voltage could be expressed as

$$v_b(v_{16}, v_{14}) = \left(R_{16} \parallel R_{14} \parallel R_r\right) \cdot \left(1 + \frac{R_1}{R_2}\right) \cdot \left(\frac{v_{16}}{R_{16}} + \frac{v_{14}}{R_{14}}\right), \tag{6.22}$$

and equivalently

$$\begin{aligned} v_b(\mathrm{DAC_{off}}, \mathrm{DAC_{reg}}) = &\left(R_{16} \parallel R_{14} \parallel R_r\right) \cdot \left(1 + \frac{R_1}{R_2}\right) \\ &\cdot \left(\frac{3.3\,\mathrm{V}}{R_{16}\,2^{16}} \cdot \mathrm{DAC_{off}} + \frac{2.5\,\mathrm{V}}{R_{14}\,2^{14}} \cdot \mathrm{DAC_{reg}}\right). \end{aligned} \tag{6.23}$$

$R_1 = 205\,\mathrm{k\Omega}$ and $R_2 = 5.1\,\mathrm{k\Omega}$ is the resistor pair that can be seen in the right-hand side of figure 6.15. Both resistors were chosen from the same manufacturer and the same series, for reasons that were explained in an earlier chapter. Due to the resistor tolerances, a calibration was performed for every channel individually. The electronics workshop set up an experiment: The bias supply was deployed in a climate chamber which was set to 25 °C. With the use of a precision multimeter, the 16 bit DAC value $\mathrm{DAC_{off}}$ of every channel was trimmed such that v_b was to yield 54.000 V within the resolution of one LSB, i.e. 0.001 V, while the value of the 14 bit DAC $\mathrm{DAC_{reg}} = 0$ was kept at zero. Next, a voltage calibration of the 14 bit DAC was performed, where the bias voltage was measured with the Fluke multimeter while the 14 bit DAC value was swept. Figure 6.16 shows the results of the calibration.
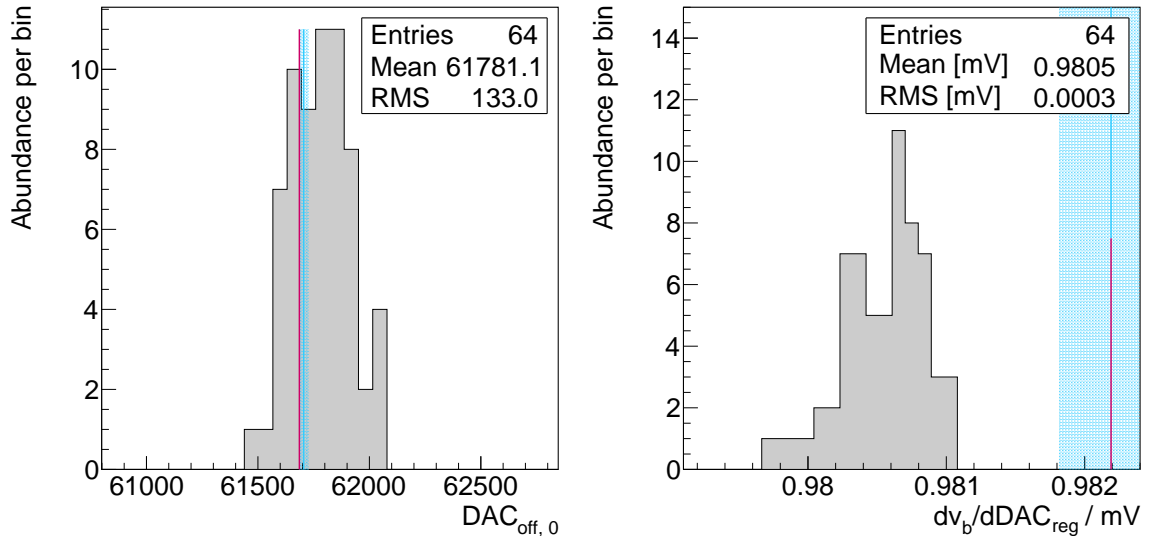
Figure 6.16.: Voltage calibration of the FAMOUS PSU bias channels as performed by D. Louis. *Left:* A histogram of the 16 bit offset DAC integer values that correspond to a voltage of $(54.000 \pm 0.001)\,\mathrm{V}$, denoted $\mathrm{DAC_{off,\,0}}$ in the text. *Right:* Slope parameter of the 14 bit DAC channels that indicate the voltage change by a change of one DAC count, i.e. the resolution. The blue and red lines represent the theoretical value from circuit calculations and the mean values obtained from a complete SPICE simulation, respectively.

The left- and right-hand side of the figure shows histograms of the parameters $\mathrm{DAC_{off,\,0}}$ and $\mathrm{d}v_b/\mathrm{dDAC_{reg}}$ in

$$v_b(\mathrm{DAC_{off}}, \mathrm{DAC_{reg}}) = v_b(\mathrm{DAC_{off,\,0}}, 0) + \frac{\mathrm{d}v_b}{\mathrm{dDAC_{off}}} \cdot (\mathrm{DAC_{off}} - \mathrm{DAC_{off,\,0}})$$

$$+ \frac{\mathrm{d}v_b}{\mathrm{dDAC_{reg}}} \cdot (\mathrm{DAC_{reg}} - \mathrm{DAC_{reg,\,0}}), \tag{6.24}$$

where

$$v_b(\mathrm{DAC_{off,\,0}}, 0) = (54.000 \pm 0.001)\,\mathrm{V},$$

$$\frac{\mathrm{d}v_b}{\mathrm{dDAC_{off}}} = \frac{\left(R_{16} \parallel R_{14} \parallel R_r\right) \cdot (1 + R_1/R_2)}{R_{16}} \cdot \frac{3.3\,\mathrm{V}}{2^{16}},$$

$$\frac{\mathrm{d}v_b}{\mathrm{dDAC_{reg}}} = \frac{\left(R_{16} \parallel R_{14} \parallel R_r\right) \cdot (1 + R_1/R_2)}{R_{14}} \cdot \frac{2.5\,\mathrm{V}}{2^{14}},$$

$$\mathrm{DAC_{off,\,0}} = \frac{R_{16}}{\left(R_{16} \parallel R_{14} \parallel R_r\right) \cdot (1 + R_1/R_2)} \cdot \frac{v_b(\mathrm{DAC_{off,\,0}}, 0)}{3.3\,\mathrm{V}} \cdot 2^{16}, \quad \text{and}$$

$$\mathrm{DAC_{reg,\,0}} = \frac{R_{14}}{\left(R_{16} \parallel R_{14} \parallel R_r\right) \cdot (1 + R_1/R_2)} \cdot \frac{v_{\mathrm{bd}}(T_0) + v_{\mathrm{ov}} - v_b(\mathrm{DAC_{off,\,0}}, 0)}{2.5\,\mathrm{V}} \cdot 2^{14}.$$

Parameter $\mathrm{d}v_b/\mathrm{dDAC_{off}}$ was not explicitly calibrated since $\mathrm{DAC_{off}} \equiv \mathrm{DAC_{off,\,0}}$ was usually kept constant during operation while only $\mathrm{DAC_{reg}}$ was a function of temperature. The regulator voltage swept the bias voltage from $v_b(\mathrm{DAC_{off,\,0}}, 0) = 54\,\mathrm{V}$ to about $v_b(\mathrm{DAC_{off,\,0}}, 2^{14}-1) = 70\,\mathrm{V}$. The nominal operating voltage of the Hamamatsu SiPMs was expected to be less than $66\,\mathrm{V}$ at room temperature, see [6].

The author included the ideal values obtained through calculations from the equations above in the histograms. Both theoretical values are drawn as solid blue lines. Parameters estimated from full SPICE Monte Carlo simulations are printed as solid red lines. The shaded areas indicate the expected spread originating from resistor and reference voltage tolerances. While the expectation of the offset of the 16 bit DAC is met the value for the regulating 14 bit DAC deviates significantly from the quantities obtained through the calibration, i.e. $5.6\,\sigma$ of the distribution. However, the deviation could be explained by a systematic shift in one of the parameters, e.g. the reference voltage of the AD5382. This explanation seems to fit the circumstance that the offset DAC values behave as expected, as the regulator DAC is set to zero during this measurement. Although the shift seems to be large in respect to the width of the distribution, the ideal line is only shifted by less than 0.2 %, compatible with the width of the offset distribution on the left. The width of the regulator distribution is nearly one order of magnitude smaller than the distribution of the offset DAC integers, as it does not contain variations on its offset. Other systematics originating from the calibration method cannot be ruled out.

One can conclude that a calibration is necessary when the absolute voltage needs to be known with high precision as the spread between the channels is about 0.1 V. Although it deviates from expectation, the spread of the relative slope between the channels is very small.

A new revision of the FAMOUS bias supply foresaw only one 16 bit DAC channel per bias channel, discarding the two 14 bit AD5382 wholly. A prototype was successfully tested by the author between 2017 and 2018, reducing costs[3] and complexity significantly by eliminating two AD5382 chips, 192 precision resistors, and PCB traces.

Bias voltage temperature stability   The temperature stability of the FAMOUS bias voltage supply was investigated in cooperation with the electronics workshop of the institute. The system was cycled in a climate chamber while the bias voltage and temperature were logged. As mentioned before, see equation 5.7 on page 80, it was expected that a significant fraction of the temperature dependence of the resistors canceled out. However, a small remaining temperature dependence was expected.

On a further note, the DAC reference voltages were stated to be temperature dependent, although by a small amount, i.e. $5\,\mathrm{ppm\,K^{-1}}$ [194]. Figure 6.17 shows the measured result of the intrinsic temperature dependence of a single bias channel. For that channel, both DAC values $\mathrm{DAC_{reg}}$ and $\mathrm{DAC_{off}}$ were kept constant while the temperature in the climate chamber was swept. The left-hand side of that figure shows the bias voltage versus temperature together with a linear fit. The range of the y-axis is chosen to yield 1.3 V from top to bottom, which is the nominal overvoltage of the SiPMs of the baseline design of FAMOUS. Hardly any temperature dependence can be seen by the naked eye on a temperature range of 90 K. The linear fit yields a slope of about $-0.4\,\mathrm{mV\,K^{-1}}$ which is rather small compared to the expected temperature dependence of the SiPM breakdown voltage of about $60\,\mathrm{mV\,K^{-1}}$. The relative temperature dependence is only

---

[3]The two 32 channel AD5382 cost about 85 USD per piece – quoted from Mouser Electronics on May 2$^{\text{nd}}$ 2018.
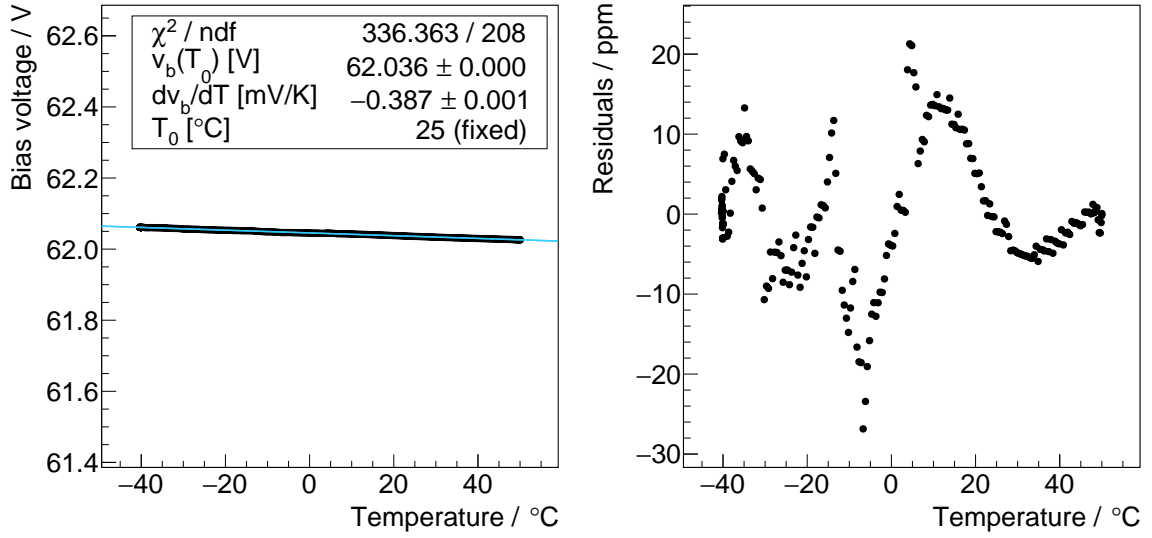
Figure 6.17.: *Left:* Native temperature dependence of a single bias voltage channel of the FAMOUS bias supply as measured by D. Louis. A linear fit yields a relative slope of about $-6\,\mathrm{ppm\,K^{-1}}$. The scale of the vertical axis corresponds to the nominal overvoltage of FAMOUS SiPMs of $1.3\,\mathrm{V}$. *Right:* The associated residuals in parts per million against temperature. The data was taken from the publication in [111].

$$\left|\frac{\mathrm{d}v_b}{\mathrm{d}T}\cdot\frac{1}{v_b(T_0)}\right|\approx 6.2\,\mathrm{ppm\,K^{-1}}. \tag{6.25}$$

The overall linear dependence on the temperature probably came from the precision resistors whose temperature dependence did not cancel out, as a control measurement with standard non-precision resistors suggested. Also, the voltage reference of the DAC is based on a bandgap difference and stated to be non-linear versus temperature [195].

By looking at the residuals, a non-linearity can be observed. This, probably, was an effect of the two different voltage references, the internal reference of the 14 bit DAC, i.e. AD5668, as well as the Analog Devices REF196 3.3 V reference used for the 16 bit DAC.

To conclude, one can say that the bias voltage supply is remarkably stable over a wide temperature range. If necessary, the remaining temperature dependence of $-0.4\,\mathrm{mV\,K^{-1}}$, resp. $-6.2\,\mathrm{ppm\,K^{-1}}$, can be accounted for in the temperature dependence of SiPMs, thus

$$\mathrm{d}v_{\mathrm{bd}}/\mathrm{d}T\rightarrow\mathrm{d}v_{\mathrm{bd}}/\mathrm{d}T+0.4\,\mathrm{mV\,K^{-1}}. \tag{6.26}$$

The bias supply promised a stability of better than $\pm30\,\mathrm{ppm}$ after compensation of the $-0.4\,\mathrm{mV\,K^{-1}}$, i.e. after calibration, over the whole temperature range. This is equal to about $1.4\cdot10^{-3}$ of the nominal overvoltage of the FAMOUS SiPMs.

Current monitoring With the help of Kirchhoff's circuit laws and Ohm's law, the transfer function

$$v_{\mathrm{i}}(i_{\mathrm{L}})\approx 1.5\,\mathrm{k\Omega}\cdot i_{\mathrm{L}}+0.5\,\mathrm{V} \tag{6.27}$$

could be extracted from figure 6.15 in dependence of the current drawn by the load i_L, i.e. by the LDO regulator i_{LDO} and the SiPM i_b, thus

$$i_L = i_{LDO}(v_b, T) + i_b. \tag{6.28}$$

It was found that i_{LDO} was a function of the bias voltage v_b, i.e. DAC_{off} and DAC_{reg}, and temperature T. The first dependence is not surprising, as v_b introduces a current through the resistor pair $R_1 + R_2$.

More interestingly, the current drawn by the LDO was temperature-dependent, denoted with the symbol T in preceding's equation, due to the temperature dependence of the PNP transistor's base current. However, with the help of SPICE simulations and calculations from the manufacturer's data sheet, this effect, i.e. di_{base}/dT was found to be small, about $6\,\mu A$ over $80\,K$. Moreover, a temperature effect of $25\,ppm\,K^{-1}$ was expected from the precision resistors, as equation (6.27) is not dimensionless. This would introduce a change of about $2 \cdot 10^{-3}$ on $80\,K$ – which is also negligible.

For a $3.3\,V$ 12 bit ADC, like the one used in the MSP430, the transfer function from equation (6.27) was reorganized and solved for the SiPM current by using equation (6.28), thus

$$i_b(ADC_i, v_b) \approx 0.536\,\mu A \cdot ADC_i - 320\,\mu A - i_{LDO}(v_b). \tag{6.29}$$

In principle, the bias voltage dependence of the LDO current $i_{LDO}(v_b)$ could be solved with the use of SPICE simulations. When the base current tolerance from transistor-to-transistor was too high, or any other component was inhomogeneous over a production batch, an inter-channel variation on $i_{LDO}(v_b)$ would be expected. The author performed a calibration measurement for that reason:

At first, the author made improvements on the DC/DC module PCB to reduce the variance on the ADC_i value through electro-magnetic noise. The procedure has already been mentioned above: Two $1\,\mu F$ capacitors were added in parallel to the $10\,k\Omega$ load resistors in figure 6.15 which formed low-pass filters with the $220\,k\Omega$ resistors. This reduced the RMS on the measured i_b from about $12\,\mu A$ [111] to $0.6\,\mu A$ [59]. After that, the following transfer function was postulated, driven by equation (6.29) above, where it was assumed that $i_{LDO}(v_b)$ scaled linearly with v_b

$$i_b = \frac{di_b}{dADC_i} \cdot \left(ADC_i - ADC_{i,0} - \left(\frac{dADC_i}{dDAC_{off}} \right) \cdot \left(DAC_{off} - DAC_{off,\,0} \right) \right.$$
$$\left. - \left(\frac{dADC_i}{dDAC_{reg}} \right) \cdot \left(DAC_{reg} - DAC_{reg,\,0} \right) \right). \tag{6.30}$$

$di/dADC_i$ converts ADC integers into SI-units, i.e. μA. This parameter needs to be calibrated with an active load, for instance. All the other parameters carry the dimensions of DAC and ADC integers. Two of the three offset parameters are redundant. $DAC_{off,\,0}$ can be identified with the offset DAC integer that generates $54.000\,V$ which are graphically represented on the left-hand side in figure 6.16.

$$\frac{dADC_i}{dDAC_{reg}} = \left(\frac{dv_b}{dDAC_{reg}} \right) \cdot \left(\frac{dADC_i}{dv_b} \right), \quad \text{and} \quad \frac{dADC_i}{dDAC_{off}} = \left(\frac{dv_b}{dDAC_{off}} \right) \cdot \left(\frac{dADC_i}{dv_b} \right) \tag{6.31}$$
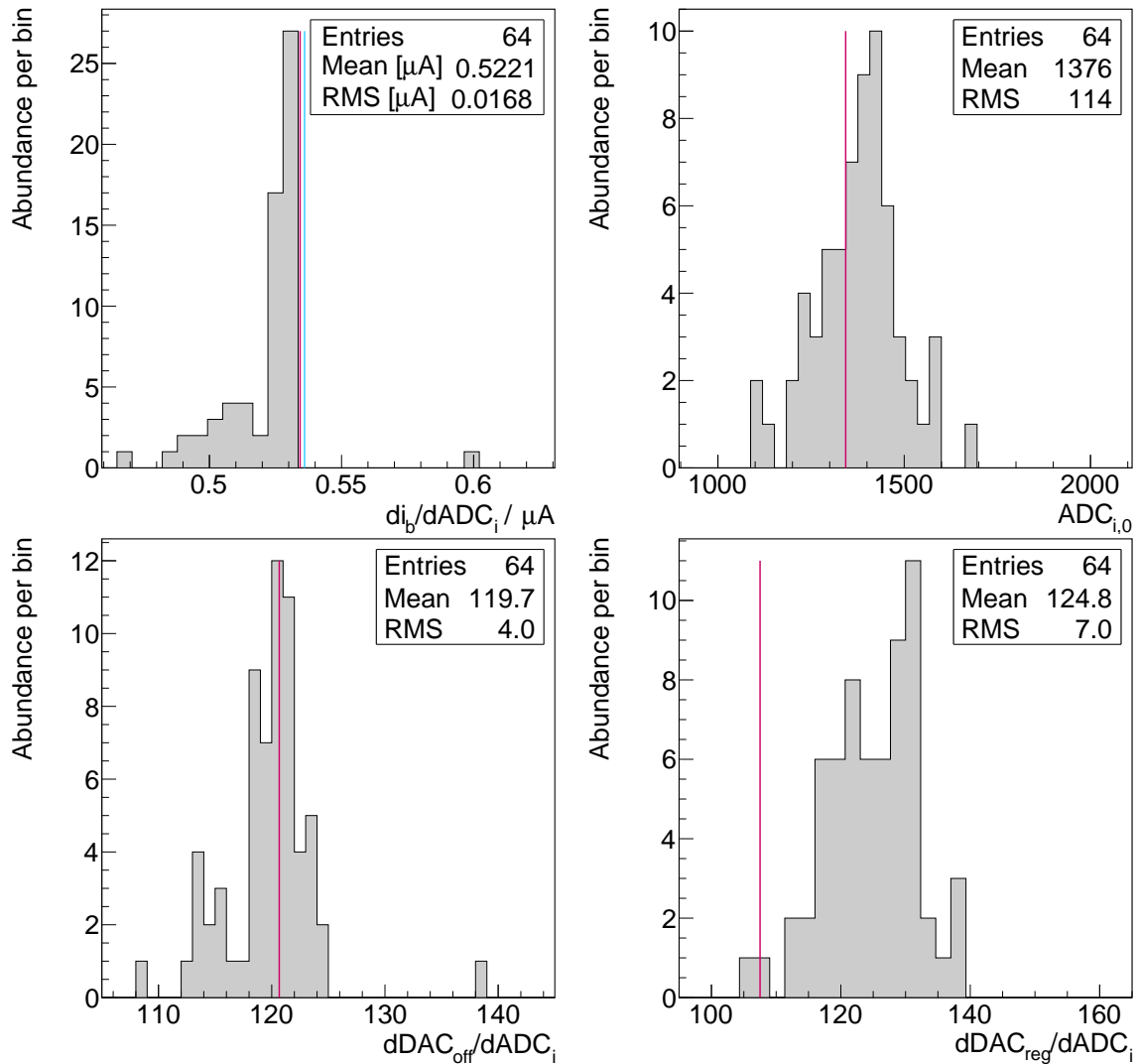
Figure 6.18.: This figure shows the result of the current calibration of the 64 FAMOUS PSU bias channels. The variables come from the parameterization in equation (6.30), confer with figure 6.16. The blue and red lines represent the theoretical value from circuit calculations and the mean values obtained from a complete SPICE simulation, respectively.

could have been combined. As $dDAC_{off}/dv_b$ was not calibrated, both parameters were treated independently, leading to systematics in both parameters originating from the voltage calibration.

The only remaining free offset parameter, $ADC_{i,0}$, was extracted from data by setting $DAC_{off} = DAC_{off,0}$ and $DAC_{reg} = DAC_{reg,0}$, and removing any load from the bias voltage, such that $i_b = 0\,\mu A$. $ADC_{i,0}$ was then identified as the ADC integer in the data stream.

After that, $dADC_i/dDAC_{off}$ was determined by keeping $DAC_{reg} = DAC_{reg,0}$ and $i_b = 0\,\mu A$ and sweeping DAC_{off}. The same procedure applied to $dADC_i/dDAC_{reg}$, where $DAC_{off} = DAC_{off,0}$ and $i_b = 0\,\mu A$.

With the help of an active load, the transfer variable $di_b/dADC_i$ was determined for every

channel. This was, by far, the most tedious task: the author developed an active load that sourced a current between $0\,\mu A$ and $1400\,\mu A$ with a programmable resolution of about $0.5\,\mu A$ from any voltage between $4\,V$ and $100\,V$. The author calibrated the active load with the Fluke 8842A [80] precision multimeter. Programmed and powered over Universal Serial Bus (USB), the active load was connected to every bias channel individually in sequence. Starting with the first bias channel the load was swept automatically between $0\,\mu A$ and $1000\,\mu A$ while the monitored data was stored on disk, after which the author proceeded with the next channel. The channels had to be connected to the load manually. Figure 6.18 shows the results of the calibration.

Again, the blue and red lines indicate values obtained through circuit calculations and full SPICE simulations, respectively. The author only performed calculations in the case of parameter $di/dADC_i$. Like before, all parameters are well represented by the theoretical predictions – all, but $dADC_i\;/\,dDAC_{reg}$. This, however, is probably a systematic that originates from the systematic deviation between the theoretical and experimental results of parameter $dv_b/dDAC_{reg}$ in figure 6.16. When the expectation for $dv_b/dDAC_{reg}$ is systematically larger than the observed value, the prediction for $dDAC_{reg}/dADC_i$ will be systematically smaller, as the values inversely scale with each other according to equation (6.31). This prognosis is met.

The spread of the distributions is a few percents. A calibration is useful to reduce systematics.

The effect of the bias voltage change on the LDO current is approximately

$$\frac{di_{LDO}}{dv_b} = 5.3\,\mu A V^{-1}. \tag{6.32}$$

This means, that, if the bias voltage is increased by $dv_b = 1\,V$, through either DAC_{off} or DAC_{reg}, the LDO draws about $di_{LDO} = 5.3\,\mu A$ more current than before. This effect is small compared to the night-sky background which is about $100\,\mu A$ in Aachen, Germany [59], yet strongly varying from night to night. However, compared to the dark current of the SiPMs which is less than $1\,\mu A$ at room temperature, see chapters before, the effect is not negligible. Depending on the application, $dADC_i/dDAC_{off}, dADC_i/dDAC_{reg} = 0$ can be set to zero. This had been the case in [6] during the measurement of star trails with the FAMOUS camera.

In conclusion, during an observation in a single night, this effect can be neglected, as the temperature changes only by about $10\,K$ between dusk and dawn, introducing a bias voltage change of about $600\,mV$ and thus $di_{LDO}/dv_b \cdot 600\,mV \approx 3\,\mu A$ which is a few percent during a dark night or less than one percent in a cloudy night, confer with figure 6.21. However, as the bias voltage supply could also be used with different SiPM cameras that operate at lower or higher voltages, e.g. with a SensL J-series [60] camera, this effect of close to $200\,\mu A$, i.e. a change from bias voltages above $65\,V$ to less than $30\,V$, cannot be neglected anymore and needs to be considered.

Temperature monitoring   The LMT87 temperature sensors generate an output voltage $v_T(T)$ depending on the ambient temperature T. The transfer function

$$v_T(T) = v_T(T_r) + \left(\frac{dv_T}{dT}\right) \cdot (T - T_r) \tag{6.33}$$

is linear [168] within less than $\pm 0.4\,°C$ for a temperature range that is typical for the observation in European nights, i.e. $0\,°C$ to $30\,°C$. By choosing the reference temperature as $T_r \equiv 25\,°C$, the average voltage offset becomes $\langle v_T(25\,°C)\rangle = 2.298\,V$ and its slope typically

$\langle \mathrm{d}v_T/\mathrm{d}T \rangle = -13.6\,\mathrm{mV\,K^{-1}}$ [168]. As the LMT87 were read-out by the internal 12 bit ADC of the MSP430 microcontroller, the following relation holds

$$\mathrm{ADC}_T(T) = \mathrm{ADC}_T(T_0) + \left(\frac{\mathrm{dADC}_T}{\mathrm{d}T} \right) \cdot (T - T_0), \tag{6.34}$$

where

$$\mathrm{ADC}_T(T_0) = \frac{2^{12}}{3.3\,\mathrm{V}} \cdot v_T(T_r) - \left(\frac{\mathrm{dADC}_T}{\mathrm{d}T} \right) \cdot (T_r - T_0), \quad \text{and} \quad \left(\frac{\mathrm{dADC}_T}{\mathrm{d}T} \right) = \frac{2^{12}}{3.3\,\mathrm{V}} \cdot \left(\frac{\mathrm{d}v_T}{\mathrm{d}T} \right). \tag{6.35}$$

Firmware D. Louis developed the original firmware. Internally, all computations were implemented with floating point numbers, e.g. for the calculations of bias voltages depending on temperature. Since the MSP430F5659 did not feature a hardware-based floating-point unit, the processing of the code was inefficient and slow; the MSP430 took typically more than 1 s for a single loop. The author programmed a new version of the firmware in cooperation with T. Bretz with focus on implementation in the FACT++ user framework. All operations were soon carried out with integer divisions, multiplications, bit shifting and simple addition as well as subtraction without the use of floating point numbers. Additionally, the latest firmware version also offered new features.

After configuring its clock, ports, and interrupts, the MSP430 ran a continuous loop in which the current and temperature of all 64 channels were digitized with its built-in ADC. After that, yet still in the main loop, the MSP430 checked for interrupts: These were timer interrupts, error interrupts as well as interrupts raised by the W5500 Ethernet chip. All features could be disabled and enabled by the user by sending the corresponding Ethernet command. With all features enabled, the maximum loop frequency was about 15 Hz.

Two types of operations were foreseen: The standard operation included an automatic adaption of the bias voltage with respect to temperature, to compensate for the temperature dependence of the breakdown voltages of the SiPMs. In that case, the 64 regulator channels were set with individual nominal values at reference temperatures $\mathrm{DAC}_{\mathrm{reg}}(\mathrm{ADC}_T(T_0))$ and positive slopes, which were composed of a 16 bit integer numerator and a 16 bit integer denominator, each, according to

$$\mathrm{DAC}_{\mathrm{reg}}(\mathrm{ADC}_T(T)) = \mathrm{DAC}_{\mathrm{reg}}(\mathrm{ADC}_T(T_0)) + \left(\frac{\mathrm{dDAC}_{\mathrm{reg}}}{\mathrm{dADC}_T} \right) \cdot (\mathrm{ADC}_T(T) - \mathrm{ADC}_T(T_0)). \tag{6.36}$$

With the support of above equations, the SI-based units of the temperature dependence of the SiPM breakdown voltage can be identified as follows

$$\frac{\mathrm{d}v_{\mathrm{bd}}}{\mathrm{d}T} \equiv \left(\frac{\mathrm{d}v_b}{\mathrm{d}T} \right) = \left(\frac{\mathrm{d}v_b}{\mathrm{dDAC}_{\mathrm{reg}}} \right) \cdot \left(\frac{\mathrm{dDAC}_{\mathrm{reg}}}{\mathrm{dADC}_T} \right) \cdot \left(\frac{\mathrm{dADC}_T}{\mathrm{d}T} \right). \tag{6.37}$$

ADC routine All 64 temperature sensors channels, as well as all 64 current monitoring channels, were connected to four Analog Devices ADG732 [196] 32:1 multiplexers, MUX. The outputs of the two ADG732 which were used for the temperature sensors were tied together. The same applied to the two ADG732 for the current monitoring. The two combined outputs were connected to two independent ADC channels.

In the ADC procedure, the MSP430 activated the first of the 64 channels, waited for a short period Δt, digitized both the current and the temperature, and moved to the next channel by setting the bits to select the right channels from the four ADG732 multiplexers. The author determined the period by estimating $\Delta t \equiv 5 \cdot \max(R \cdot C)$, where R was the output impedance, resp. resistance, of the monitoring circuits and C the total line capacitance. Both parameters were dominated by the $R = 1\,\text{k}\Omega$, $C = 100\,\text{nF}$ low-pass filters of the analog temperature sensors which were included on the SiPM camera PCB. This lead to a deliberate time delay of $\Delta t = 500\,\mu\text{s}$.

To reduce the scattering of the temperature and current data 16 values were summed up for every channel individually. The author did not choose this number arbitrarily, yet deliberately from the digital size of one word, i.e. 16 bit and the native resolution of the ADC, i.e. 12 bit, such that with

$$2^{16-12} = 16 \tag{6.38}$$

aggregated values, its sum still occupied only one word, i.e. 16 bit. This 16 bit word, resp. unsigned short, was finally transmitted to the user who needed to divide the word by 16 to obtain the averaged monitoring value with the help of equation (6.30) in the case of the current and with equation (6.34) in the case of temperature.

Interrupts If an interrupt occurred, a flag was set in a global variable. The flags of this variable were polled in the main loop. These were

- the Ethernet interrupt,

- the timer interrupt for the automatic data transmission,

- the timer interrupt for the automatic regulation, and

- the error interrupt.

The Wiznet W5500 Ethernet controller was configured to toggle the binary voltage on a pin whenever an Ethernet event occurred. This pin was connected to the MSP430. The MSP430 caught the transition and raised an internal interrupt. Whenever the flag was set in the main loop, the MSP430 asked the W5500 for the type of the interrupt:

- a new connection was established to one of the W5500 sockets,

- a connection was closed,

- data was received on an open socket, or

- an error was detected, e.g. IP conflict, client unreachable, timeout, after which the error interrupt was raised.

The MSP430 responded appropriately. More information can be found in the next subsection.

Two low-frequency timers were used to regularly raise interrupts, to remind the MSP430 to either transmit data automatically or perform the bias voltage regulation. Corresponding Ethernet commands set the timer frequencies.

Ethernet commands A list of all commands that have been implemented in the FAMOUS bias supply firmware is attached with this thesis, in table A.5 in appendix A.13 on page 174. All commands were supposed to be received and transmitted in frames of 1024 B. The Ethernet socket listened on port 5000 for any commands. The IP address and the MAC address were hard-coded in firmware and set to 10.0.131.223 and 00:08:DC:1D:FF:89, respectively. The bias supply was set up as a host while the user connected as a client at will. Every command sent to the bias supply was acknowledged by a response, containing the data that was asked for. The communication protocol is very similar to that of miniFTM and can be found in appendix A.13 on page 174 in detail.

Improvements At the end of 2017, the author proposed a new version of the FAMOUS PSU with the following improvements.

- Reducing the number of transformers,

- removing electromagnetic relays,

- removing the two 32-channel AD5382 14 bit DACs and 192 associated precision resistors, and

- moving and simplifying the current measurement circuitry.

Applying all these changes makes a calibration mandatory due to the reduced number of tolerances. The current measurement could be simplified using a Texas Instruments LMP8480 [197], or a Linear Technology LTC6101HV [198] current sensing amplifier with a gain of 100. The circuitry can be moved to v_b such that the shunt resistor is placed between the LDO and the SiPM. Its value can be decreased to 15 Ω to offer the same transimpedance of 1.5 kΩ as before, cf. with equation (6.27), along with the same digital resolution from the ADC integer on i_b of about 0.5 µA. Only one, or two precision resistors will be needed instead of nine. Although the channel-to-channel variation will be in the same order of magnitude, no offset current needs to be calibrated, reducing the calibration parameterization of equation (6.30) to

$$i_{\mathrm{b}} = \frac{\mathrm{d}i_{\mathrm{b}}}{\mathrm{d}\mathrm{ADC}_i} \cdot \left(\mathrm{ADC}_i - \mathrm{ADC}_{i,0} \right). \tag{6.39}$$

The voltage drop across the 15 Ω resistor will only be 15 mV at a full load of 1 mA, but typically 1 mV to 2 mV during operation in a dark night. This means that the voltage at the SiPM is up to 15 mV smaller than intended. It can be compensated in firmware by increasing the bias voltage depending on the load current, but its effect on the gain will only be 1 % at most for the FAMOUS SiPMs and about 0.3 % for newer generations, yet typically less.

Above improvements will reduce costs, as well as complexity and the necessity for calibration, yielding an even better 64 channel precision bias voltage supply for SiPMs. Tests of prototypes have already demonstrated the feasibility of above improvements. A picture of a new bias supply version as developed exclusevily by the author of this thesis is attached in appendix A.14 on page 175.

Outlook　Due to the large overvoltage and excellent fabrication homogeneity of today's SiPMs, the question arose whether every SiPM needed to be supplied by an individual bias voltage. With an estimated breakdown voltage variation of 73 mV and an overvoltage of 5 V, confer with earlier chapters, a variation on the gain of only 1.5 % would be expected, when all SiPMs were operated with the same bias voltage.

The number of channels can be reduced to eight, instead of 64, for example. By sorting the SiPMs to bias channels groups by their breakdown voltage, the variation on the gain while operating eight SiPMs with the same bias voltage can be decreased by about one order of magnitude on average, i.e. from 1.5 % to 0.2 %.

The author already developed a one-channel DC/DC solution for a 64 SiPM camera. It provided a bias current of up to 100 mA and a temperature-stabilized bias voltage. Programmable through USB, the module was operating at the South Pole during the 2017/2018 season. Some of the improvements from above influenced the development of this bias supply, like a single DAC channel and simplified current monitoring circuitry. This all means that it is technically possible to operate several SiPMs with a single bias channel.

On a further note, the author designed and built an AC/DC module that was based on a commercial AC/DC switching converter. This architecture was small, about 10 cm × 6 cm × 4 cm and low-weight, about 100 g, as well as cheap, about 35 € and allowed operation from 85 V AC to 264 V AC and 47 Hz to 63 Hz. All numbers included PCB, components, and housing, but neither assembling nor VAT. Inductive filtering with chip ferrites and a post-linear regulator reduced electromagnetic noise to about 2 mV peak-to-peak on a DC to 1 MHz bandwidth which could be further reduced by a following DC/DC module. However, only SiPMs with a bias voltage smaller than 45 V could be supplied. This solution was proposed for the FAMOUS follow-up instruments that make use of 30 V SiPMs like the SensL FC- and FJ-series.

The bias voltage developed in the scope of this thesis, together with the electronics workshop of III. Physikalisches Institut A, RWTH Aachen University, was calibrated for the use with the FAMOUS telescope. Its final revision worked reliably and was used in high-level measurements and analyses that followed over the years. Some of which will be introduced in the following.

6.4. Physics results

The FAMOUS system as described above had already been used in many occasions by now. In [6], for example, due to the lack of any DAQ, the bias supply current monitoring was used to check the reliability of the optical system and its simulations. In [76] the complete system was operated at the High-Altitude Water Cherenkov observatory (HAWC) site in Mexico. Also, a series of test measurements were performed [174, 175]. Further results were pre-released in [59].

6.4.1. Prototype detector results

While no DAQ was available at the beginning, T. Niggemann and the author performed the first measurements with the telescope's slow control only, i.e. with all optical components, the SiPM focal plane, the bias supply, and a telescope mount that fixed the telescope direction. We obtained the current per pixel, which was a measure of the average photon flux in the camera, folded with the SiPMs' correlated noise and optical efficiency. Together with simulations and measurements of the optical response of the telescope, the photon flux on the lens was
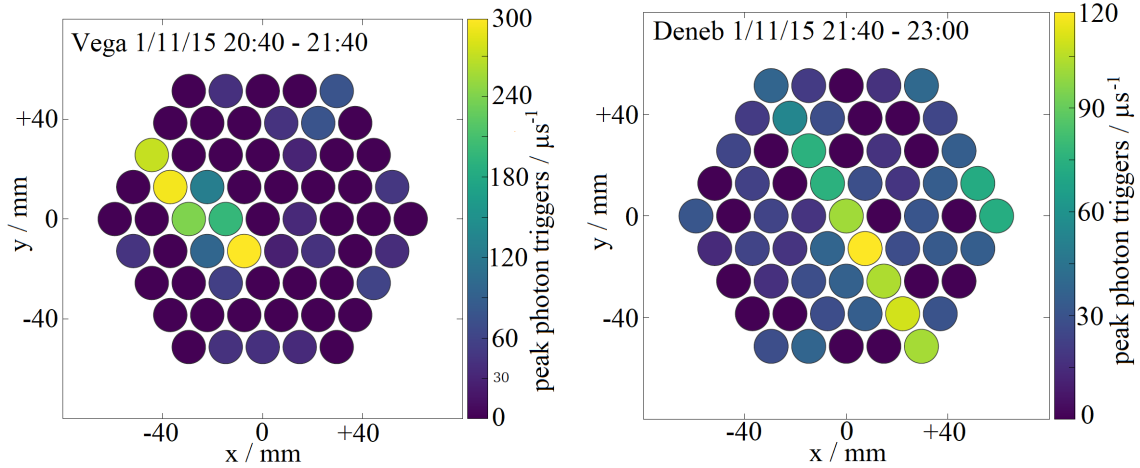
Figure 6.19.: The number of photon triggers per unit time obtained from star trails in the field of view of the telescope measured with the current monitoring feature of the bias supply. *Left:* Vega. *Right:* Deneb, in the night of November 1st, 2015, both taken from [6], yet the labels and titles of the axes were modified to fit the size of the body text.

reconstructed and compared to the apparent magnitude of stars whose trails were recorded over an extended period. T. Niggemann analyzed these measurements [6]. Figure 6.19 shows the number of photon triggers per unit time of star trails for Vega and Deneb in the 61-pixel camera of FAMOUS. Both plots were taken from [6].

While the reconstructed photon flux was about 20 % smaller than the expected photon flux for both, Vega and Deneb, the ratio of both, i.e. the reconstructed photon flux ratio between Vega and Deneb, compared to the expected one were quite consistent [6]. This was an indication that either the optical efficiency of the telescope or the expected photon flux were overestimated. While the latter could be an effect of environmental conditions [6], an overestimation of the optical efficiency would also bias the expected physics performance of the instrument. T. Niggemann concluded that dew on the lens had a "large negative influence (...) on the detection efficiency of the telescope", and that a "prevention mechanism" was needed to counter these influences in the future [6, p. 182]. However, this issue was never addressed again.

The first DAQ obtained for the FAMOUS telescope was a loan of the CTA consortium based on the TARGET chip [173] in version 7. Originally developed for the small-sized and medium-sized dual-mirror telescopes of CTA, the TARGET DAQ incorporated pre-amplifiers and ADCs for 64 channels, including an integrated trigger on the sum of four channels. Please refer to the trigger layout studies earlier. The DAQ system was designed for the use of SiPMs. The TARGET chip itself had 16 channels with a buffer depth of 16 384 cells, meaning that a total of more than $16\,\mu s$ could have been recorded per channel at a sampling rate of $1\,GSa\,s^{-1}$, or $33\,\mu s$ at $500\,MSa\,s^{-1}$.

N. Höflich and B. Pestka calibrated the TARGET7 DAQ in [174, 175], and performed the first measurements with the telescope in Aachen, Germany, together with the author of this thesis. However, due to complications with the hardware, firmware, and software, only 16 channels of the TARGET7 DAQ were operable, and the trigger system was not working correctly. Conse-
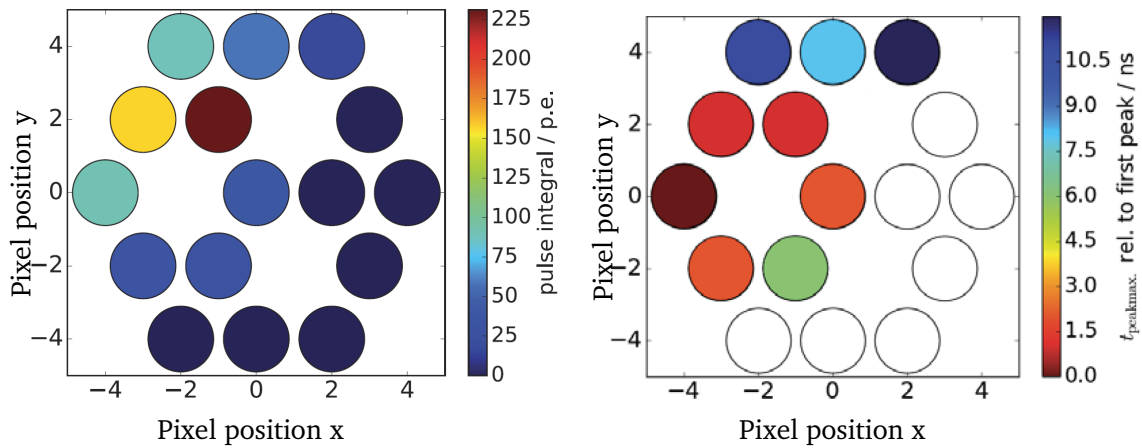
Figure 6.20.: These images show the camera display of the same event, taken with the camera's center only. *Left:* Signal integral color-coded in the individual pixels and *right:* Signal timing, also color-coded. See text for details. Both images were taken from [174, 175], yet slightly modified.

quently, the author developed a trigger system with discrete electronics on a separate PCB. The trigger was raised whenever the voltage on its input exceeded a certain threshold, configurable via software due to an onboard microcontroller and a digital-to-analog converter, and the use of fast comparators. The threshold was fixed before the run to a level that corresponded to a trigger rate of about 0.5 Hz. Three pixels were connected to the trigger and taken out of the DAQ. Since only 16 channels could be recorded, only the center of the camera was instrumented. The telescope was pointed to the night-sky and operated for about one hour. N. Höflich and B. Pestka analyzed the data and found several events. One candidate of air-Cherenkov light emitted by an extended air shower is given in figure 6.20. Both images were taken from [174, 175].

The left plot shows the location of the 16 instrumented pixels in the camera layout, with the color scale indicating the integrated charge in units of photon equivalents, i.e. the signal size, resp. number of detected photons. The plot on the right-hand side shows the time of the signal in the corresponding pixel with respect to the time of the pixel that responded first. The three empty spaces around the central pixel express that these pixels were used for triggering and were not recorded by the TARGET7 DAQ. From the left image, we see that the peak signal was exceeding 200 pe, which could only have originated from an external signal, i.e. a light flash. The figure on the right indicates that the signal did not occur simultaneously but within a concise time window of about 10 ns. This means that the signal in the individual pixels did not come from electronic crosstalk. Both plots suggest that a short, yet intense photon flash was collected in the camera, i.e. an air-Cherenkov candidate of an extended air shower.

6.4.2. Final detector results

With the FACT DAQ finally set up, M. Battermann, M. Schaufel, and the author performed first light measurements with the full 61-pixel camera. In two nights in summer 2017, the telescope was set up in the yard of the physics department of the RWTH Aachen University in Aachen, Germany, N 50.780 820°, E 6.049 149° [59]. While the first night was used to test and debug
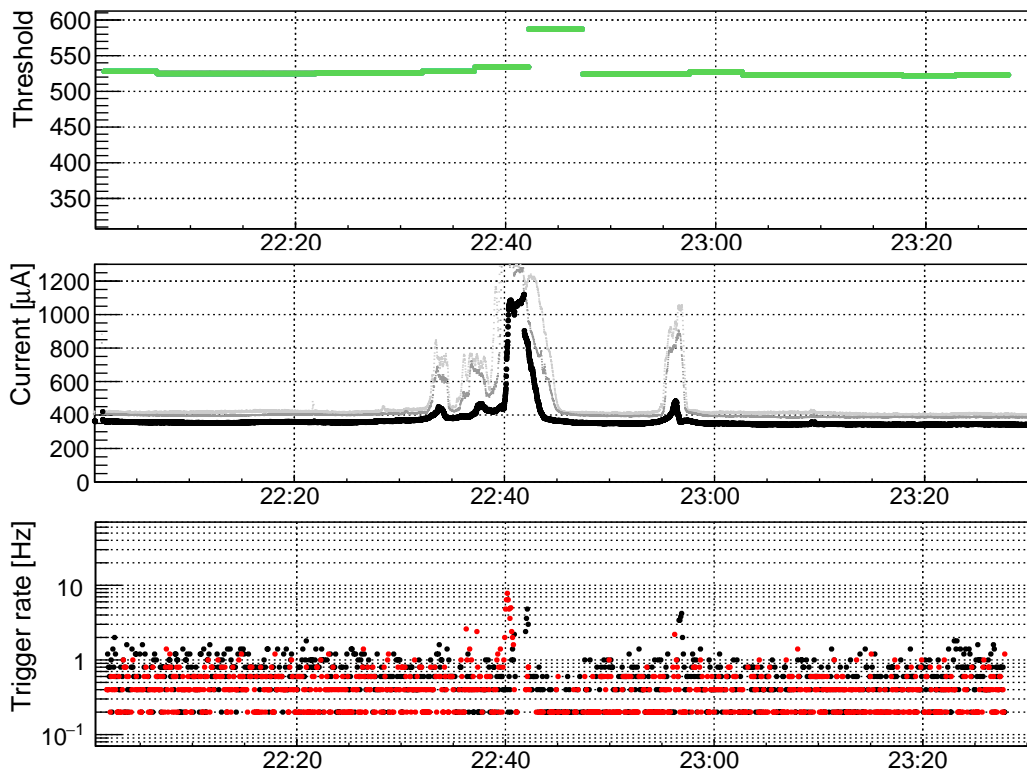
Figure 6.21.: A quality plot taken during a measurement campaign in June 2017. *Top:* Trigger threshold in integer units, *center:* Average pixel current (black) and peak current (grey), and *bottom:* Average trigger rate. Even though the current increased significantly, the trigger rate was adapted every 5 min (before each run) by an intelligent trigger threshold adjustment, see text for details. Taken from [59].

the system during realistic operational conditions, the second night allowed continuous night sky observations. The data of the second night was analyzed by M. Schaufel, some of which was published in a collaborative journal paper [59].

Figure 6.21 shows the quality plot of the measurement taken in the second night on June 21st 2017. The plot shows slow control data over 90 minutes of continuous observation. This figure can be used to check the stability of the system. The top row shows the trigger threshold in internal integer units of the FACT trigger system. The larger the trigger threshold in integers, the larger the input signals must be to initiate a trigger. The next row holds the average pixel current in μA in black, and that of the *hottest* pixels in grey. The current was calibrated in accord to above thoughts. The average trigger rate of both FACT DAQ sets is indicated in the last row by the black and red dots. The time is given in Coordinated Universal Time (UTC). The local time was UTC+2. The figure was taken from [59].

While the overvoltage was kept constant during operation, the increase in current at about 22:30 UTC was an indication for an increase of the average background photon flux. Most probably, this was a cloud whose stray light entered the field of view of the camera. At the same time, the average trigger rate increased. However, the system was configured in such a way that it adjusted the trigger threshold according to the pixel current at the beginning of each run, similar to the algorithm implemented in [83, p. 29, eq. (5.5)]. As a rule of thumb,
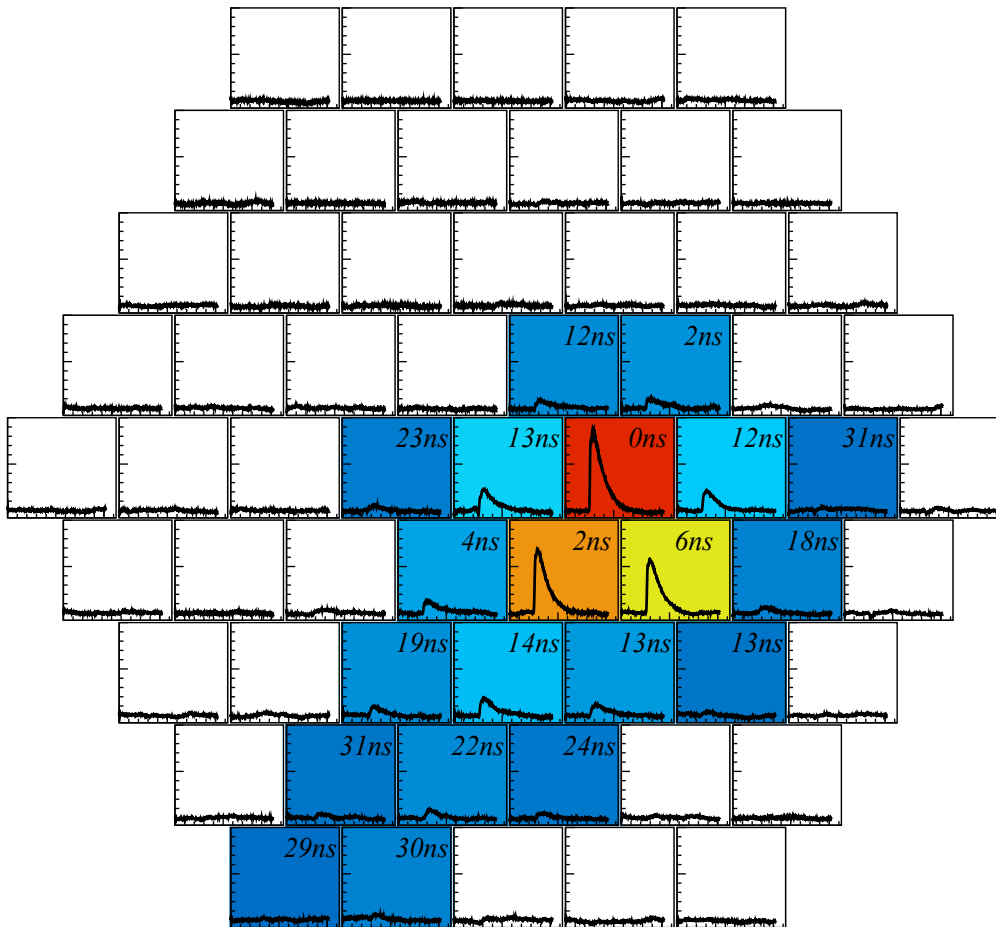
Figure 6.22.: This image shows the camera display of an event taken with the FACT DAQ. The timing of the individual pixel signals is printed in the pixels, while the individual signal size is color-coded and indicated by the plots in the pixels. The traces shown are 512 ns long and about 1 V high. The nominal 1 pe amplitude was about 3 mV, see text for details. Taken from [59].

the threshold should increase with the square root of the current $\sqrt{i}$, as apparent from equation (6.1). M. Battermann and M. Schaufel managed its implementation in FAMOUS. Five minutes runs were chosen for this measurement campaign. After the previous run ended at about 22:42, the threshold was increased, and the trigger rate settled to the targeted default value close to 1 Hz. With this approach, the number of background events could be reduced significantly.

Figure 6.22 shows an event in the camera display of FAMOUS. This time, all 61 pixels, resp. 64 channels of FAMOUS were instrumented. The event was published in [59]. The signal size is color-coded with red indicating large signals and blue small signals. The raw signal trace recorded by the FACT DAQ is also shown for every pixel, as is the timespan between the signal in each pixel with respect to the first pulse. Like the event recorded by the 16-pixel camera shown before, this event is also a candidate for air-Cherenkov light emitted during an extended air shower, due to the correlation in time, and an excessive yet instantaneous increase of the

signal. With a nominal single photon amplitude of 3 mV [59], the event shown here had a peak amplitude of about 300 pe. Again, correlated electronic or dark noise could be excluded.

From the peak amplitude of 300 pe in the brightest pixel alone, it can be concluded that this pulse could not have originated from the diffuse night-sky background. With the individually calibrated single bias channel current i_b, the average detected photon flux ϕ can be recovered with

$$i_b = \phi \cdot e \cdot g \cdot \frac{1}{1 - p_{\mathrm{xt}}}, \tag{6.40}$$

see for example [6], where e is the elementary charge, g the SiPM charge gain, and p_{xt} the SiPM's crosstalk probability as introduced in earlier chapters. With $i_b = 400\,\mu\text{A}$, see figure 6.21, the average detected photon flux becomes approximately

$$\phi = 500\,\text{MHz}. \tag{6.41}$$

With the decay time constant $\tau = 65\,\text{ns}$, estimated from figure 6.22, the average number of simultaneously occupied cells can be estimated with

$$\lambda = 30. \tag{6.42}$$

Assuming that the diffuse night-sky background is purely Poissonian, its variance becomes λ. For large λ, the Poisson distribution approaches the Normal distribution with a mean value of λ and a standard deviation of $\sqrt{\lambda}$. From this information, the probability for getting a 300 pe excess from the diffuse night-sky background can be estimated with

$$P_{\sqrt{\lambda}}(\geq 300\,\text{pe}) = \frac{1}{2} - \frac{1}{2} \cdot \mathrm{erf}\left(\frac{300\,\text{pe}}{\sqrt{2\,\lambda}}\right) \tag{6.43}$$

to

$$P_{\sqrt{30}}(\geq 300\,\text{pe}) \ll 10^{-100}. \tag{6.44}$$

This value is still minuscule when the crosstalk probability is included. The diffuse night-sky and optical crosstalk of the SiPM can be ruled out.

Another explanation includes artificial light sources, e.g. human-made photon pulses like position and anti-collision lights of aircraft. However, according to the advisory circulars of the Federal Aviation Administration (FAA), the duration of these pulses shall be between 0.05 s and 0.2 s for reasons of efficiency and visibility [199]. The bias supply current monitoring would have recognized this amount of light. The traces in figure 6.22 also indicate that the measured light flux was only nano-seconds long. One may argue that high-pass filtering could have converted a step function into an exponential function, resembling the traces shown before. However, the missing undershoot contradicts this hypothesis.

To finally give proof that the event shown in figure 6.22 is due to air-Cherenkov light emitted during the evolution of an extensive air shower, FAMOUS was operated at the HAWC site in coincidence with the HAWC detector in 2017 [59, 75]. M. Schaufel performed an intensive study of these results in [76] showing that events like the one shown before are indeed of extraterrestrial origin. Although the average current per pixel was quite high, i.e. around 400 μA, many events of similar size and shape were triggered by the FAMOUS telescope in that night [59].

6.4.3. Conclusions

For a prototype, the FAMOUS telescope performed extraordinarily well. With the optics developed by T. Niggemann in [6], and the electronics developed in this thesis, the FAMOUS telescope finally allowed air-Cherenkov measurements.

While the first candidates were recorded with a limited number of pixels by N. Höflich and B. Pestka, the integration of the FACT DAQ allowed the instrumentation of the full camera. Its integration was done in cooperation with M. Batterman, T. Bretz, and M. Schaufel, which was followed by a measurement campaign in the yard of the physics department of the RWTH Aachen University, in Aachen, Germany, in summer 2017. For the first time, FAMOUS measured candidate events of air-Cherenkov light emitted during the evolution of extended air showers. One of which was published in a journal paper [59].

The telescope was further operated at the HAWC site [26] by M. Schaufel after the successful commissioning in Aachen, which culminated in his Master's thesis [76]. This hybrid setup, i.e. the surface detector of HAWC and the optical telescope FAMOUS, allowed detailed studies on the physics performance of FAMOUS. The proton energy threshold at the altitude of 4100 m, for example, was found to be as low as 22 TeV [76], coinciding with the energy threshold estimated in equation (6.7).

Even though the hardware of the telescope is inexpensive – estimated with 10 000 € not including the DAQ [59] – the excellent optical efficiency and robustness of a FAMOUS-like instrument promise benefits for many applications.

6.4.4. Future prospects and trends

So far, variants of the telescope were operated in Germany, Mexico and at the South Pole [59, 75, 200]. While those instruments targeted the detection of air-Cherenkov light of extended air showers, the telescope is scheduled to be brought to Argentina to measure air-fluorescence light in coincidence with the Fluorescence Detector of the Pierre Auger Observatory [143]. This concept, however, needs a different DAQ system than the one borrowed from the FACT collaboration because of the longitudinal observation of the air shower which leads to larger time scales than for air-Cherenkov detection. This idea will target the initial objective [162] to study SiPMs as an alternative to PMTs for the detection of air-fluorescence light.

Summary & final remarks

Silicon photomultipliers (SiPMs) promise to become the next-generation de-facto standard in photon detection in the scope of astroparticle physics, superseding vacuum photomultiplier tubes in many applications. Mass-production of these silicon-based semiconductors has lead to device-homogeneities that allow precision measurements without intense calibrations.

The author showed in chapter 4 that inhomogeneities that were found between two SiPM specimens of the same series were related to differences in the relative overvoltage, i.e. gain. This was an indication that SiPMs could be commonly parameterized as a function of overvoltage and temperature across a series and family, and only the breakdown voltage had to be characterized for every device individually.

In the case of the operation of individual devices, the homogeneity of the breakdown voltages could be made use of to characterize the devices in situ. With their intrinsic single photon resolution, the gain of SiPMs can be monitored during operation as long as the cell breakdown rate is low. The author made use of this technique in the case of the Auger Scintillators for Composition – II (ASCII) prototypes in chapter 5. In this detector, the optical output of the scintillator and the wavelength-shifting fibers could be separated from the gain of the SiPM. This allows studying devices stabilities individually from the average signal charge against temperature and time. Prospects for the future include the Surface Scintillation Detector (SSD) stations that were equipped with SiPMs. The development of the optoelectronic module excluding the light guides was done in this work, whose results were pre-released in [54].

The optical telescope – the First Auger Multi-pixel photon counter camera for the Observation of Ultra-high energy cosmic air Showers (FAMOUS) – was finally commissioned as soon as its electronic system was finalized by the author of this thesis. These included a calibrated, highly precise power supply unit (PSU) for SiPM-biasing, the data acquisition (DAQ) synchronization module miniFTM, the focal plane printed circuit board (PCB), the trigger layout and grouping PCB, as well as its inter-connection and programming, see chapter 6. The FAMOUS telescope and its spin-offs, HAWC's eye and IceAct, have been operated with great success at several sites, including Germany [59], Mexico [76], and the South pole [200].

Appendix

A.1. SiPM – optical crosstalk

The number of dark count events with n simultaneous cell breakdowns is given by the crosstalk probability p_{xt}, and can be approximated with

$$N(n) = N(1\,\mathrm{pe}) \cdot p_{\mathrm{xt}}^{n-1}.$$ (A.1)

This function fulfills the definition of the crosstalk probability, that p_{xt} is defined by the number of events larger $1\,\mathrm{pe}$ over all events, because

$$
\begin{aligned}
\frac{N(n \geq 2\,\mathrm{pe})}{N(n \geq 1\,\mathrm{pe})} &= \frac{\sum_{m=2}^{\infty} p_{\mathrm{xt}}^{m-1}}{\sum_{n=1}^{\infty} p_{\mathrm{xt}}^{n-1}} \\
&= p_{\mathrm{xt}} \cdot \frac{\sum_{m=2}^{\infty} p_{\mathrm{xt}}^{m-2}}{\sum_{n=1}^{\infty} p_{\mathrm{xt}}^{n-1}} \\
&\overset{m\,=\,k+1}{=} p_{\mathrm{xt}}.
\end{aligned}
$$ (A.2)

While the integrated number of events is given by the geometric series, i.e.

$$\sum_{n=1}^{\infty} N(n) = \frac{N(1\,\mathrm{pe})}{1 - p_{\mathrm{xt}}},$$ (A.3)

and the expected value by

$$\sum_{n=1}^{\infty} n \cdot N(n) = N(1\,\mathrm{pe}) \cdot \sum_{n=1}^{\infty} n \cdot p_{\mathrm{xt}}^{n-1}$$

$$= N(1\,\mathrm{pe}) \cdot \sum_{n=1}^{\infty} \frac{\mathrm{d}}{\mathrm{d}p_{\mathrm{xt}}} p_{\mathrm{xt}}^{n}$$

$$= N(1\,\mathrm{pe}) \cdot \frac{\mathrm{d}}{\mathrm{d}p_{\mathrm{xt}}} \left(p_{\mathrm{xt}} \cdot \sum_{n=1}^{\infty} p_{\mathrm{xt}}^{n-1} \right)$$

$$\overset{(A.3)}{=} N(1\,\mathrm{pe}) \cdot \frac{\mathrm{d}}{\mathrm{d}p_{\mathrm{xt}}} \frac{p_{\mathrm{xt}}}{1 - p_{\mathrm{xt}}}$$

$$= \frac{N(1\,\mathrm{pe})}{(1 - p_{\mathrm{xt}})^2}. \tag{A.4}$$

Then, the relative mean value follows, that is

$$\frac{\sum_{n=1}^{\infty} n \cdot N(n)}{\sum_{n=1}^{\infty} N(n)} = \frac{1}{1 - p_{\mathrm{xt}}}. \tag{A.5}$$

That means, that for small crosstalk probabilities $p_{\mathrm{xt}} \ll 1$, the signal gets larger by about p_{xt} on average.

A.2. SiPM – spectrum

The following abbreviations hold

$$b_{m,n} = n - 1 + \sum_{j=2}^{m} \binom{n-m}{j} \cdot c_{j,m}, \quad b_{0,n} = 1$$

$$c_{0,m} = c_{1,m} = 1, \quad c_{2,m} = m - 1, \quad c_{3,m} = 0.5 \cdot (m-3)^2 + 1.5 \cdot (m-3) + 1,$$

$$c_{4,m} = 1.5 \cdot (m-4)^2 + 1.5 \cdot (m-4) + 1, \quad c_{5,m} = 3 \cdot (m-5)^2 + 3 \cdot (m-5) + 4, \quad \dots$$

A.3. SiPM – afterpulsing

Let's assume that U is a random variable drawn from its cumulative distribution function $F_U(u)$. Then, $V = g(U)$ defines a new random variable on $F_V(v)$. It can be shown that

$$F_V(v) = F_u(g^{-1}(v)) \tag{A.6}$$

holds if g is invertible, see for example "Introduction to Probability" by J. K. Blitzstein and J. Hwang (2014). By differentiating both sides of the above equation, and making use of the chain rule of calculus, the relation of the probability density function (PDF)

$$f_V(v) = f_U(g^{-1}(v)) \cdot \left| \frac{\mathrm{d}g^{-1}}{\mathrm{d}v}(v) \right| \tag{A.7}$$

is retrieved, where $f_X(x) = \mathrm{d}F_X/\mathrm{d}x(x)$ is the PDF of X on F.
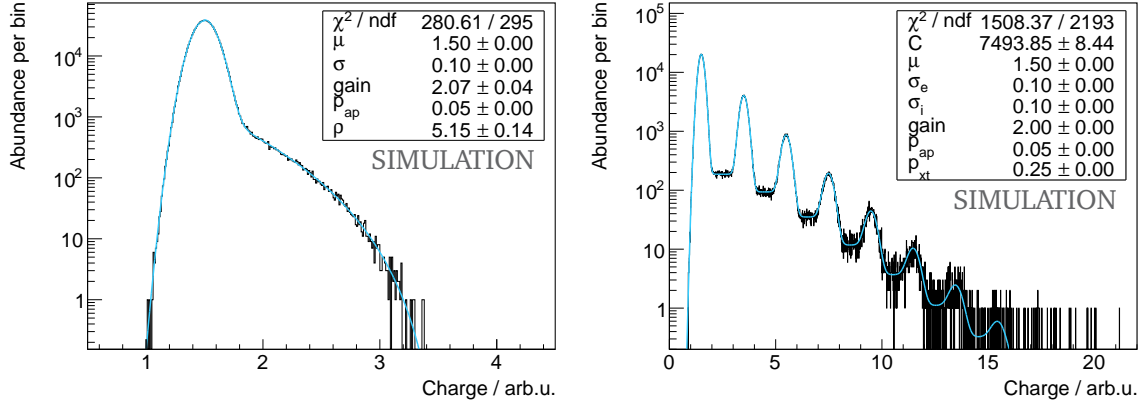
Figure A.1.: *Left:* Simulated afterpulsing of 5 % on a 1 pe finger including a fit. *Right:* A simulated finger spectrum with 25 % crosstalk, 5 % afterpulsing with $\rho = 1$, plus correlated spectrum fit, see text for details.

After a breakdown in a cell of an silicon photomultiplier (SiPM), p_{ap} defines the integral probability that an afterpulsing event is triggered. Its PDF is given by

$$f_U(t) = \frac{p_{\mathrm{ap}}}{\tau_{\mathrm{ap}}} \exp\left(-\frac{t}{\tau_{\mathrm{ap}}}\right), \tag{A.8}$$

where t expresses the time since the initial cell breakdown. The gain of the SiPM recharges with time t according to

$$g(t) = 1 - \exp\left(-\frac{t}{\tau_{\mathrm{r}}}\right). \tag{A.9}$$

Then, with

$$g^{-1}(y) = -\tau_{\mathrm{r}} \cdot \ln(1 - y) \tag{A.10}$$

it follows from above that

$$
\begin{aligned}
f_V(v) &= \frac{p_{\mathrm{ap}}}{|1-v|} \cdot \frac{\tau_{\mathrm{r}}}{\tau_{\mathrm{ap}}} \cdot \exp\left(\ln(1-v) \cdot \frac{\tau_{\mathrm{r}}}{\tau_{\mathrm{ap}}}\right) \\
&= p_{\mathrm{ap}} \cdot \frac{\tau_{\mathrm{r}}}{\tau_{\mathrm{ap}}} \cdot \frac{(1-v)^{\tau_{\mathrm{r}}/\tau_{\mathrm{ap}}}}{|1-v|} \\
&= p_{\mathrm{ap}} \cdot \frac{\tau_{\mathrm{r}}}{\tau_{\mathrm{ap}}} \cdot (1-v)^{\tau_{\mathrm{r}}/\tau_{\mathrm{ap}}-1}, \quad 0 \le v \le 1 \\
&= p_{\mathrm{ap}} \cdot \frac{\tau_{\mathrm{r}}}{\tau_{\mathrm{ap}}} \cdot (1-v)^{\tau_{\mathrm{r}}/\tau_{\mathrm{ap}}-1} \cdot H(v) \cdot (1 - H(v-1)), \quad \forall v \in \mathbb{R}.
\end{aligned}
\tag{A.11}
$$

expresses the PDF of the excess charge Δv given in pe as defined in equation (4.13).

Figure A.1 shows an example of the above equation applied to a Monte-Carlo simulation on its left-hand side. In the simulation, the charge of 1 pe was simulated, estimated with a normal distribution to account for the variance of the individual cell gain. For every event, afterpulsing was added with a probability of 5 %. The charge excess was computed by pulling
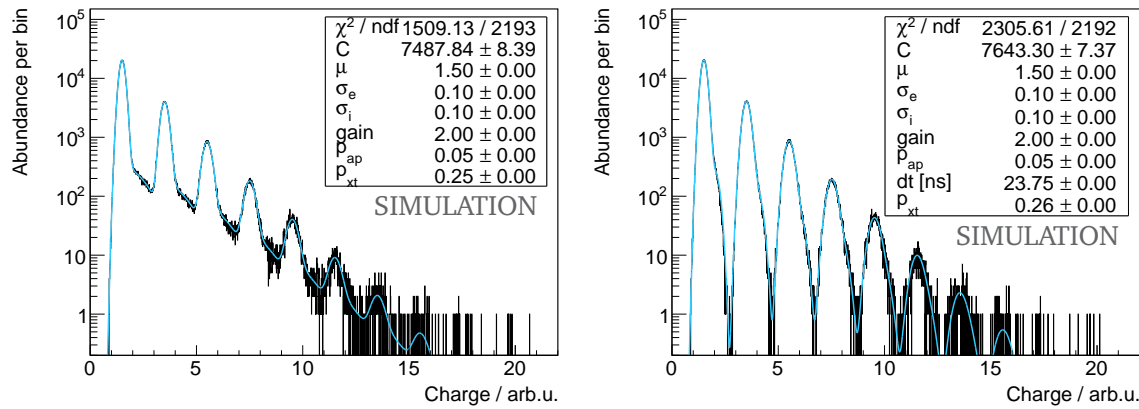
Figure A.2.: Simulated finger spectra with *left:* $\rho = 2$, and *right:* same as left but with $\mathrm{d}t = 25\,\mathrm{ns}$, confer with figure A.1, and with equation (4.13) on page 47.

a random number which was exponentially distributed. This random number was inserted into an exponential equation of the form of $g(x)$ from above.

The following parameter set was chosen:

$$\mu = 1.5,\ \sigma = 0.1,\ \text{gain} = 2,\ p_{\mathrm{ap}} = 0.05,\ \rho \equiv \frac{\tau_{\mathrm{ap}}}{\tau_{\mathrm{r}}} = \frac{50\,\mathrm{ns}}{10\,\mathrm{ns}} = 5$$

which was reconstructed well by the fit.

A.4. SiPM – spectrum function

Figure A.1 and figure A.2 show simulated finger spectra that were generated with the following ROOT [201] C-code:

```
const int N = 1e6;
TRandom *r;
TH1D *h;
double q, t;

r = new TRandom(160487);
h = new TH1D("h", "", 2200, 0, 22);

for (int i=0; i<N; i++) {
  q = r->Gaus(0, SIGMA_E) + MU - GAIN;
    do {
       q += r->Gaus(0, SIGMA_I) + GAIN;
       if (r->Uniform() < P_AP) {
         t = r->Exp(TAU_AP);
         q += GAIN * (1 - TMath::Exp( - t / TAU_R )) * (1 - TMath::Exp( -
             DT / TAU_R ));
       }
    } while ( r->Uniform() < P_XT );
    h->Fill(q);
}
```

The simulation included electronic noise through SIGMA_E, the intrinsic G-APD gain width SIGMA_I, the G-APD gain GAIN, all in arbitrary units, afterpulsing with its probability P_AP and
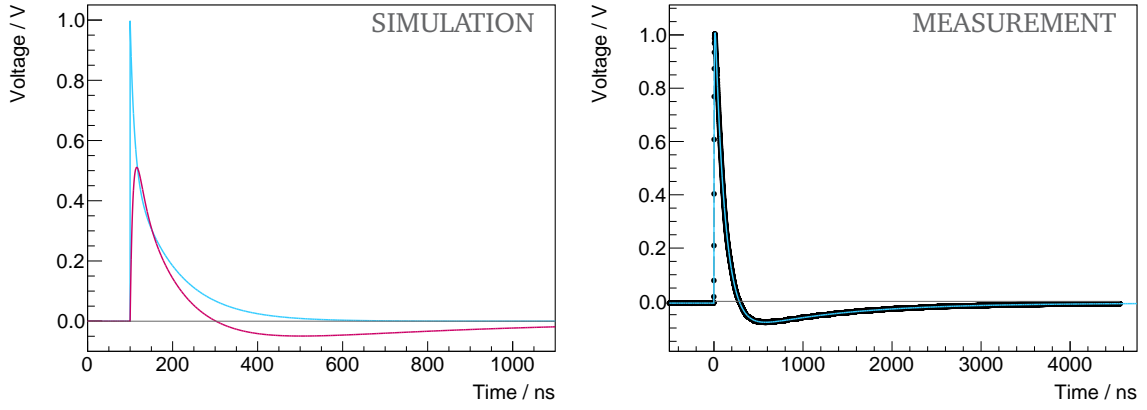
Figure A.3.: *Left:* Bandpass filter response in red to the original input voltage in blue. Depending on the choice of the bandpass filter AC-coupling parameters, a large undershoot is observed. *Right:* A SensL FJ-60035 [60] SiPM read-out with a 10 nF AC-coupling plus a fit according to equation (A.14).

its time constant `TAU_AP`, and the cell recovery time `TAU_R`, as well as optical crosstalk through its probability `P_XT`.

The simulations are well described by the fits.

A.5. SiPM – bandpass filter response

When a signal of the type

$$v_{\text{in}}(t) = v_0 \cdot \left(a \cdot \exp\left(-\frac{t-t_0}{\tau_1}\right) + (1-a) \cdot \exp\left(-\frac{t-t_0}{\tau_2}\right) \right) \cdot H(t-t_0) \tag{A.12}$$

is transmitted through an RC high-pass filter with time constant $RC = \tau_{\text{AC}}$, buffered, and then passed through an RC low-pass filter with time constant $RC = \tau_{\text{DC}}$, i.e. when the following s-domain transfer function holds

$$\frac{V_{\text{out}}}{V_{\text{in}}}(s) = \frac{\tau_{\text{AC}} \cdot s}{1 + (\tau_{\text{AC}} + \tau_{\text{DC}}) \cdot s + \tau_{\text{AC}} \tau_{\text{DC}} \cdot s^2}, \tag{A.13}$$

the output voltage is found to be

$$\begin{aligned}
v_{\text{out}}(t) = \frac{\tau_{\text{AC}} v_0 \cdot H(t-t_0)}{(\tau_{\text{AC}} - \tau_1)(\tau_{\text{AC}} - \tau_2)(\tau_{\text{AC}} - \tau_{\text{DC}})(\tau_{\text{DC}} - \tau_1)(\tau_2 - \tau_{\text{DC}})} \cdot \bigg(\\
+ \left((1-a)\tau_2 \tau_{\text{AC}} + a \tau_1 \tau_{\text{AC}} - \tau_1 \tau_2\right)(\tau_{\text{DC}} - \tau_1)(\tau_2 - \tau_{\text{DC}}) \cdot \exp\left(-\frac{t-t_0}{\tau_{\text{AC}}}\right) \\
+ \left((1-a)\tau_2 \tau_{\text{DC}} + a \tau_1 \tau_{\text{DC}} - \tau_1 \tau_2\right)(\tau_{\text{AC}} - \tau_2)(\tau_{\text{AC}} - \tau_1) \cdot \exp\left(-\frac{t-t_0}{\tau_{\text{DC}}}\right) \\
+ a \tau_1 (\tau_{\text{AC}} - \tau_{\text{DC}})(\tau_{\text{AC}} - \tau_2)(\tau_2 - \tau_{\text{DC}}) \cdot \exp\left(-\frac{t-t_0}{\tau_1}\right) \\
+ (1-a)\tau_2 (\tau_{\text{AC}} - \tau_{\text{DC}})(\tau_{\text{AC}} - \tau_1)(\tau_1 - \tau_{\text{DC}}) \cdot \exp\left(-\frac{t-t_0}{\tau_2}\right) \bigg).
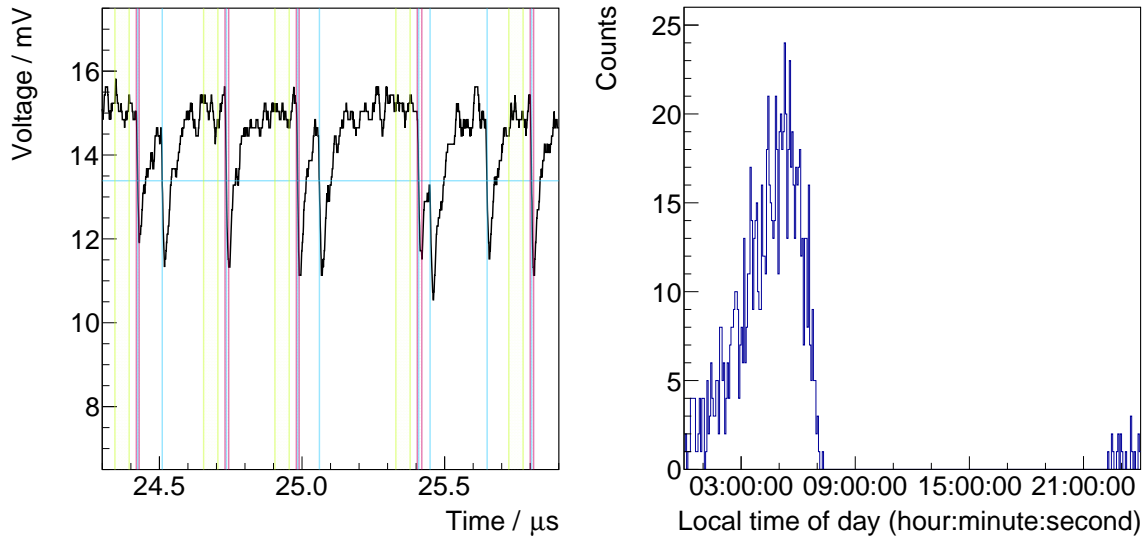\end{aligned} \tag{A.14}$$

Figure A.4.: *Left:* Signal extraction procedure as used in chapter 4 in this thesis visualized for instructive purposes. *Right:* A histogram of the time of day of events measured with one of the ASCII stations indicates that the stations failed to either record or send data during the day.

Figure A.3 shows an example of $v_{in}(t)$ in blue and $v_{out}(t)$ in red with the parameter set

$$v_0 = 1\,V, \ t_0 = 100\,ns, \ a = 0.5, \ \tau_1 = 10\,ns, \ \tau_2 = 100\,ns,$$
$$\tau_{AC} = 50\,\Omega \cdot 10\,nF, \ and \ \tau_{DC} = (100\,MHz)^{-1}.$$

These are quite typical values for SiPMs and a non-ideal read-out with about 100 MHz. While the low-pass filter affects the slope of the instantaneous rise, the high-pass filter leads to a significant undershoot of the output signal. For large values of τ_{AC}, the amplitude of the undershoot becomes negligibly small, yet the undershoot itself becomes long. Typical values are found in the range between $50\,\Omega \cdot 10\,nF$ and $50\,\Omega \cdot 1\,\mu F$. The integral over v_{out} becomes zero when it is integrated over the complete pulse. In the author's developments, it was tried to avoid any AC-coupling. When this was not possible, the author chose 1 μF, e.g. for the Surface Scintillation Detector (SSD) and for the Auger Scintillators for Composition – II (ASCII), or 100 nF capacitors, e.g. for the First Auger Multi-pixel photon counter camera for the Observation of Ultra-high energy cosmic air Showers (FAMOUS) telescope, at the output of the front-end.

On the right-hand side of figure A.3, the author shows a measurement of the signal of a SensL FJ-series SiPM that was flashed by an LED pulse. The author intentionally placed a 10 nF capacitor at the input of the oscilloscope. A fit to the data according to equation (A.14) is also given which successfully reconstructs the shape of the pulse.

A.6. SiPM – signal extraction procedure

The left-hand side of figure A.4 illustrates the signal extraction procedure used in this work to identify SiPM pulses in a given trace (voltage versus time). The blue horizontal line shows the global trace threshold estimated from the baseline noise. More information can be found
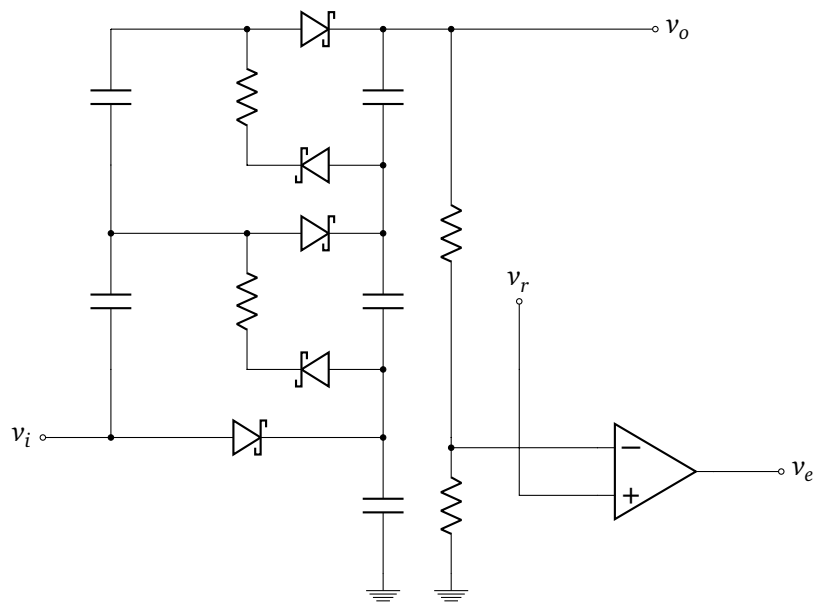
Figure A.5.: Simplified circuit diagram of the Cockcroft-Walton voltage generator and feedback circuit based on an error amplifier. The inductor-based DC/DC-converter that generates the rectangular input voltage v_i driven by the output of the error amplifier v_e is not shown in this sketch.

in chapter 4. The blue vertical lines show where the signal exceeded the trigger threshold. Whenever a stable baseline was found in the green region the algorithm started to integrate over 25 samples of the leading edge of the pulse indicated by the red area. Some pulses were discarded because the baseline before the pulse was not stable enough.

A.7. ASCII – event time of day

The right-hand side of figure A.4 illustrates the local time of the day of events taken with the ASCII-station introduced in chapter 5. The blank region between 08:00 AM and 10:00 PM proofs that either the station was not operational during the day or the data was not transmitted in that time. One of several possible explanations was that a light leak in the ASCII-detector drained the battery because of the excessive photo current drawn by the SiPM module. The battery then recovered in the evening and the early morning when the solar panel's battery recharge rate was higher than the power consumption of the SiPM module.

A.8. ASCII – Cockcroft-Walton voltage regulator

In the early ASCII optoelectronic modules, the author implemented a self-designed DC/DC-converter that generated and regulated the SiPM bias voltage from a 12 V input according to a reference voltage v_r between 0 V and 2.5 V. The reference voltage v_r was provided by a highly-precise digital-to-analog converter (DAC) that was programmed by a micro-controller.

The DC/DC-converter was based on a Cockcroft-Walton design, see figure A.5. Its input was driven by a periodic rectangular voltage v_i, provided by an inductor-based DC/DC-converter.

The input was boosted by the stages of the Cockcroft-Walton circuit and converted to a direct current (DC) signal with the use of capacitors. The output voltage was divided down by two resistors whose voltage was compared to a reference voltage v_r by an error amplifier. The output of the amplifier v_e enabled or disabled the inductor-based rectangular input voltage v_i, depending on the signum of the reference voltage v_r minus the divided voltage.

This circuit was able to provide output voltages of more than 50 V with high precision, typically in the order of a few 1 mV, with an absolute precision of some 10 mV, while consuming less than 100 mW.

A.9. SSD – $50\,\mu m$ amplification

The resistor values for the $50\,\mu m$ SSD optical module are summarized in table A.1.

$i =$	ca	hi	lo
R_s		50 Ω	
R_1		0 Ω	
R_2		*(open)*	
$R_{i,f,1}$	1000 Ω	430 Ω	750 Ω
$R_{i,g,1}$	10 Ω	130 Ω	*(open)*
$R_{i,f,2}$	750 Ω	430 Ω	750 Ω
$R_{i,g,2}$	750 Ω	150 Ω	750 Ω
$\langle |r_i| \rangle$	5050 Ω	617 Ω	50 Ω
g_{calc}	101.0 ± 0.4	12.35 ± 0.04	1.000 ± 0.003
g_{simu}	97.5 ± 0.4	12.09 ± 0.04	0.980 ± 0.003

Table A.1.: This table summarizes the resistor values and the transimpedance gain of the three SSD SiPM module amplifier channels, calibration, high-gain and low-gain for the Hamamatsu S13360-6050PE [53] ($50\,\mu m$) SiPMs. Resistors from the E-24-series were selected. Their impact on the transimpedance gain is given by equations (5.17) through (5.19). The errors on g_{calc} and g_{simu} are of systematic origin.

A.10. SSD – final yet preliminary pre-amplifier design

Figure A.6 shows the final pre-amplifier design created by the author of this thesis to read out two 6 mm × 6 mm SiPMs of type Hamamatsu S13360-6025PE [53]. The output gets split into three channels, mimicking the input current of the two SiPMs. With simple current-to-voltage converters, i.e. single resistors or transimpedance amplifiers, the output currents of channels one through three can be converted into proportional voltages with independent amplification gain.

Pre-amplifiers of this design are currently (2017 and 2018) installed in the SiPM-based SSD systems in Argentina. Details have been left out on purpose, e.g. frequency stabilization through capacitors and inductors, voltage conversion, and the like.
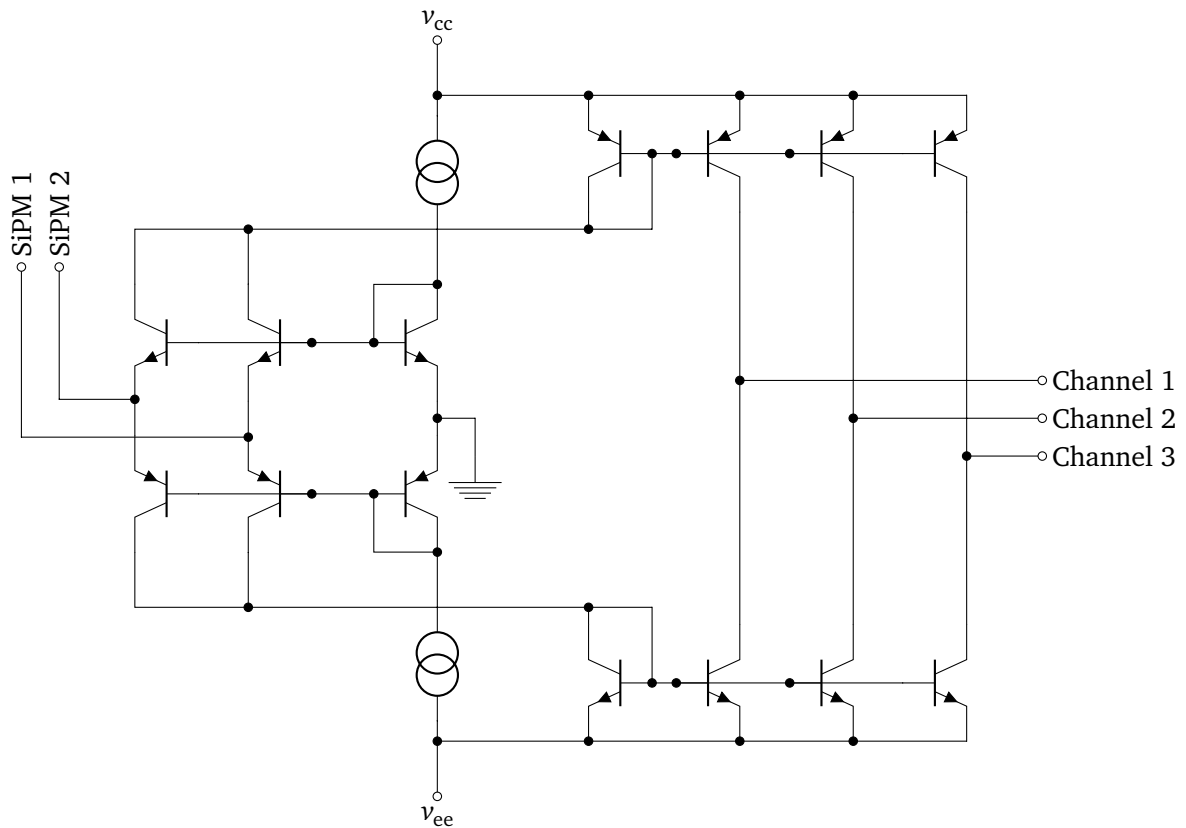
Figure A.6.: Simplified circuit diagram of the final pre-amplifier revision based on a two-input three-output active current mirror. Channel one through three need to be converted to a voltage externally, for example with the use of single resistors or transimpedance amplifiers. The transimpedance gain is then given by the shunt resistor or feedback resistor value. In the case of SSD, shunt resistors of $10\,\Omega$, $100\,\Omega$, and $1\,k\Omega$ were chosen.

A.11. FAMOUS – miniFTM random trigger implementation

The period Δt between two triggers can be defined as

$$
\begin{aligned}
\Delta t &= -\frac{\ln(u)}{f} \\
&= \frac{\ln(2)}{f} \cdot \left(16 - \log_2(\bar{u})\right).
\end{aligned}
\tag{A.15}
$$

$u = 0\ldots1$ is a uniform random number. The second line of above equation has made use of $\bar{u} = 0\ldots65536$, $\ln(x) \equiv \ln(2) \cdot \log_2(x)$ and $\log_2(65536) = 16$. In the first order, the binary logarithm can be calculated through bitshifting the floor function of $\log_2$, i.e.

$$
x \approx 1 \ll \lfloor \log_2(x) \rfloor.
\tag{A.16}
$$

In the next order, a linear interpolation to $\lfloor \log_2(x) \rfloor + 1$ is done, such that above equation can be expressed as

$$
\Delta t \approx \frac{\ln(2)}{f} \cdot \left(16 - \left(\lfloor \log_2(x) \rfloor + \frac{\bar{u} - 1 \ll \lfloor \log_2(x) \rfloor}{1 \ll \lfloor \log_2(x) \rfloor - 1 \ll (\lfloor \log_2(x) \rfloor + 1)}\right)\right).
\tag{A.17}
$$

In the next step, the above equation had to be multiplied by the timer frequency of 8300 Hz to estimate the number of cycles Δc. By using

$$
\ln(2) \approx \frac{9}{13},
\tag{A.18}
$$

calculating $\lfloor \log_2(x) \rfloor$ with the following C code function

```c
uint8_t log2(uint16_t x) {
        uint8_t l2 = 0;
        while (x >>= 1) l2++;
        return l2;
}
```

and defining

$$
\begin{aligned}
l_2 &\equiv \lfloor \log_2(\bar{u}) \rfloor \\
x_0 &\equiv 1 \ll l_2 \\
x_1 &\equiv 1 \ll (l_2 + 1) \\
dx &\equiv x_1 - x_0,
\end{aligned}
$$

Δc finally becomes

$$
\begin{aligned}
\Delta c &\equiv 8300\,\text{Hz} \cdot \Delta t \\
&\approx \frac{1196648 \cdot dx - 74791 \cdot dx \cdot l_2 - 74791 \cdot (\bar{u} - x_0)}{13 \cdot dx \cdot f\,[\text{Hz}]}.
\end{aligned}
\tag{A.19}
$$

A.12. FAMOUS – miniFTM communication table

Table A.2 visualizes a single command frame used for communication with miniFTM, while table A.3 summarizes all commands that were implemented in the FAMOUS miniFTM micro-controller up to this point (30th of June 2018).

Byte index i	0 - 1	2	3 - 4	5 - 12	13	14 - 15
Description	Frame	R/W	Command	Data	Checksum	Frame
Content $B[i]$	FF FF	00/04	[00 .. FF]	[00 .. FF]	$\sum_{j=2}^{12} B[j]$	FF FF

Table A.2.: This table visualizes a 16 B long Ethernet frame used to communicate with miniFTM. All bytes are in hexadecimal code.

Command bytes	R/W	Description
00 00	R	Product ID
00 01	R	Firmware ID
00 10	W	DRS4-Clock enable, disable, shutdown
00 11	R/W	DRS4-Clock frequency
00 20	R/W	Trigger mode internal, external, random, random-log
00 21	R/W	Trigger frequency
00 22	R/W	Trigger control
00 30	W	FAD reset
00 31	R/W	FAD reset timer
00 32	R/W	FAD reset active low, high
00 40	R	ADC channel 1 (temperature)
00 41	R	ADC channel 2 (temperature)
00 42	R	ADC channel 1 & 2 (temperature)
00 50	R/W	Event counter
00 51	R/W	CRC counter
00 52	R/W	Event type
00 53	R/W	Event number
00 5E	W	Trigger single shot
00 5F	R	Trigger counter
00 60	R/W	ATM enable
00 A0	R/W	Error flag

Table A.3.: A summary of all commands that the author had implemented in the miniFTM MSP430 firmware by the time of this writing. All bytes are in hexadecimal code.

A.13. FAMOUS – bias supply communication table

Tables A.4 and A.5 summarize all FAMOUS bias supply commands.

Byte index i	0 - 1	2	3 - 4	5 - 1020	1021	1022 - 1023
Description	Frame	R/W	Command	Data	Checksum	Frame
Content $B[i]$	FF FF	00/04	[00 .. FF]	[00 .. FF]	$\sum_{j=2}^{1020} B[j]$	FF FF

Table A.4.: This table visualizes a 1024 B long Ethernet frame used to communicate with the FAMOUS bias supply. All bytes are in hexadecimal code.

Command bytes	R/W	Description
00 00	R	Product ID
00 01	R	Firmware ID
10 00	R	Get DAC_{off}, DAC_{off}, $ADC(i_L)$, $ADC(T)$ for all channels
10 00	W	Set DAC_{off}, DAC_{off} for all channels
10 01	R	Get DAC_{off}, DAC_{off}, $ADC(i_L)$, $ADC(T)$ for a single channel
10 01	W	Set DAC_{off}, DAC_{off} for a single channel
10 02	R/W	Get/set $dDAC_{reg}$, $dADC_T$, $ADC(T_0)$ for all channels
10 03	R/W	Get/set $dDAC_{reg}$, $dADC$, $ADC(T_0)$ for a single channel
20 00	R/W	Get/set i_{lim} enable
20 01	R/W	Get/set T_{lim} enable
20 10	R/W	Get/set i_{lim} flags
20 11	R/W	Get/set T_{lim} flags
20 20	R/W	Get/set i_{lim} value
20 21	R/W	Get/set T_{lim} value
20 30	R/W	Get/set LED enable
30 00	R/W	Get/set ATM enable
30 01	R/W	Get/set AAM enable
30 02	R/W	Get/set ARM enable
30 10	R/W	Get/set ATM frequency [CPU cycles]
30 11	R/W	Get/set AAM S/H time [ADC cycles]
30 12	R/W	Get/set ARM frequency [CPU cycles]
30 F0	R/W	Get/set DAC power up enable
40 00	R/W	Get/set STATE, i_{lim}, T_{lim}, ATM cycles, AAM S/H time cycles, ARM cycles

Table A.5.: A summary of all commands that the author had implemented in the bias supply MSP430 firmware. All bytes are in hexadecimal code.

A.14. FAMOUS – bias supply version 2

The author of this thesis developed a 2nd version of the FAMOUS bias supply. This new version featured only a single 16 bit DAC per bias channel. A relative resolution of about 1.1 mV was achieved. Also, all 64 linear regulators were moved from the mainboard to small single printed circuit boards (PCBs). The bias supply became thus more maintenance-friendly. A picture is shown in figure A.7.
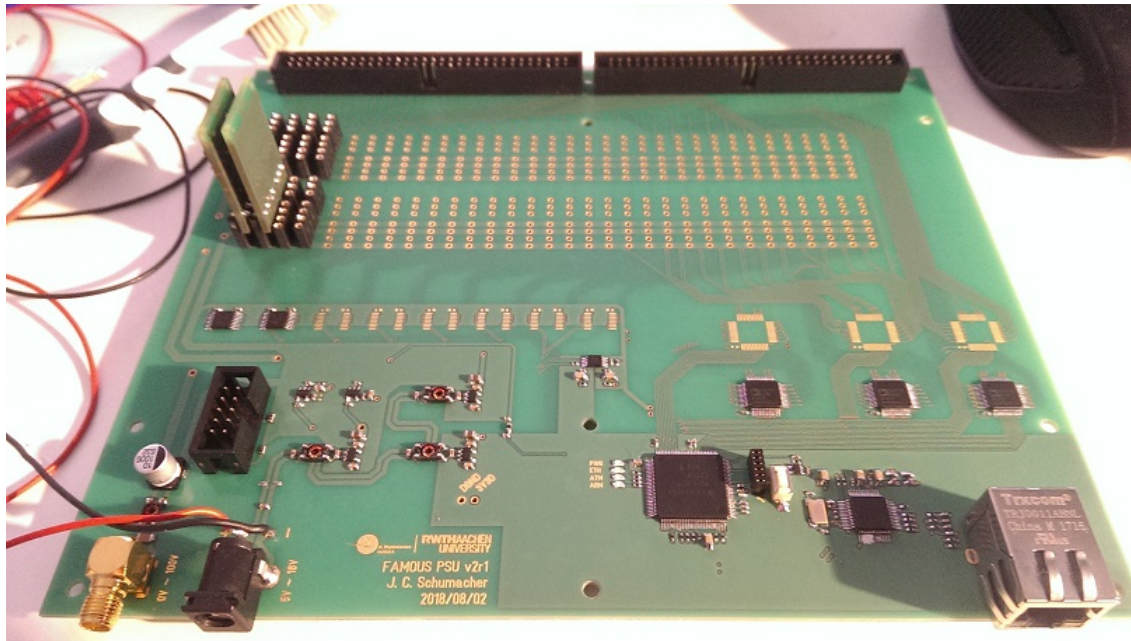

Figure A.7.: A picture of the 2nd version of the FAMOUS bias supply developed by the author of this thesis, see text for details. Picture credits belong to the author.

References

[1] International Cosmic Ray Conference (ICRC). URL: http://www.icrc2017.org/.

[2] A. Aab et al. "The Pierre Auger Observatory Upgrade - Preliminary Design Report". In: *ArXiv e-prints* (2016). arXiv: 1604.03637 [astro-ph].

[3] The Pierre Auger Collaboration. "The Pierre Auger Cosmic Ray Observatory". In: *Nuclear Instruments and Methods in Physics Research Section A: Accelerators, Spectrometers, Detectors and Associated Equipment* 798.Supplement C (2015), pp. 172–213. ISSN: 0168-9002. DOI: https://doi.org/10.1016/j.nima.2015.06.058.

[4] R. R. Engel. "Upgrade of the Pierre Auger Observatory". In: *proceedings of the 34th International Cosmic Ray Conference* [PoS (ICRC2015) 686] (2015).

[5] D. Martello. "The Pierre Auger Observatory Upgrade". In: *proceedings of the 35th International Cosmic Ray Conference* [PoS (ICRC2017) 383] (2017).

[6] T. Niggemann. "The Silicon Photomultiplier Telescope FAMOUS for the Detection of Fluorescent Light". PhD Thesis. RWTH Aachen University, Oct. 2016. URL: http://publications.rwth-aachen.de/record/673852.

[7] M. G. Aartsen et al. "Measurement of the cosmic ray energy spectrum with IceTop-73". In: *Phys. Rev.* D88.4 (2013), p. 042004. DOI: 10.1103/PhysRevD.88.042004. arXiv: 1307.3795 [astro-ph.HE].

[8] T. Antoni et al. "KASCADE measurements of energy spectra for elemental groups of cosmic rays: Results and open problems". In: *Astropart. Phys.* 24 (2005), pp. 1–25. DOI: 10.1016/j.astropartphys.2005.04.001. arXiv: astro-ph/0505413 [astro-ph].

[9] D. J. Bird et al. "The cosmic-ray energy spectrum observed by the Fly's Eye". In: *Astrophysical Journal* 424 (Mar. 1994), pp. 491–502. DOI: 10.1086/173906.

[10] D. Ivanov. "Energy spectrum measured by the telescope array surface detector". PhD Thesis. Rutgers, The State University of New Jersey, Oct. 2012.

[11] F. Fenu. "The cosmic ray energy spectrum measured using the Pierre Auger Observatory". In: *proceedings of the 35th International Cosmic Ray Conference* [PoS (ICRC2017) 486] (2017).

[12] D. Ivanov. "Report of the Telescope Array - Pierre Auger Observatory Working Group on Energy Spectrum". In: *proceedings of the 35th International Cosmic Ray Conference* [PoS (ICRC2017) 498] (2017).

[13] A. Aab et al. "Observation of a large-scale anisotropy in the arrival directions of cosmic rays above 8 × 1018 eV". In: *Science* 357.6357 (2017), pp. 1266–1270. ISSN: 0036-8075. DOI: 10.1126/science.aan4338.

[14] P. J. Lundquist, P. Sokolsky, and P. Tinyakov. "Evidence of Intermediate-Scale Energy Spectrum Anisotropy in the Northern Hemisphere from Telescope Array". In: *proceedings of the 35th International Cosmic Ray Conference* [PoS (ICRC2017) 513] (2017).

[15] J. Bellido. "Depth of maximum of air-shower profiles at the Pierre Auger Observatory: Measurements above 1017.2 eV and Composition Implications". In: *proceedings of the 35th International Cosmic Ray Conference* [PoS (ICRC2017) 506] (2017).

[16] M. Erdmann et al. "A Method of Searching for Origins of Cosmic Rays correcting for Galactic Field Deflections and Charge Composition". In: *proceedings of the 35th International Cosmic Ray Conference* [PoS (ICRC2017) 518] (2017).

[17] W. Hanlon et al. "Telescope Array Composition Summary". In: *proceedings of the 35th International Cosmic Ray Conference* [PoS (ICRC2017) 536] (2017).

[18] J. Vicha et al. "Mass Composition of Cosmic Rays with Combined Surface Detector Arrays". In: *proceedings of the 35th International Cosmic Ray Conference* [PoS (ICRC2017) 482] (2017).

[19] T. K. Gaisser. *Cosmic Rays and Particle Physics*. 2nd ed. Cambridge University Press, 2017. ISBN: 978-0-52101-646-9.

[20] M. Wang et al. "The AME2016 atomic mass evaluation (II). Tables, graphs and references". In: *Chinese Physics C* 41.3 (2017), p. 030003. URL: http://stacks.iop.org/1674-1137/41/i=3/a=030003.

[21] A. Letessier-Selvon et al. "Layered water Cherenkov detector for the study of ultra high energy cosmic rays". In: *Nuclear Instruments and Methods in Physics Research A* 767 (Dec. 2014), pp. 41–49. DOI: 10.1016/j.nima.2014.08.029. arXiv: 1405.5699 [astro-ph.IM].

[22] A. S. Chou et al. "An Universal Description of the Particle Flux Distributions in Extended Air Showers". In: *proceedings of the 29th International Cosmic Ray Conference* ICRC2005 (2005).

[23] D. Heck et al. "CORSIKA: A Monte Carlo code to simulate extensive air showers". In: *Wissenschaftliche Berichte, FZKA-6019* (Feb. 1998).

[24] C. Patrignani et al. "Review of Particle Physics". In: *Chin. Phys.* C40.10 (2016), p. 100001. DOI: 10.1088/1674-1137/40/10/100001.

[25] T. Abu-Zayyad et al. "The surface detector array of the Telescope Array experiment". In: *Nuclear Instruments and Methods in Physics Research Section A: Accelerators, Spectrometers, Detectors and Associated Equipment* 689.Supplement C (2012), pp. 87–97. ISSN: 0168-9002. DOI: https://doi.org/10.1016/j.nima.2012.05.079. URL: http://www.sciencedirect.com/science/article/pii/S0168900212005931.

[26] A. U. Abeysekara et al. "Observation of the Crab Nebula with the HAWC Gamma-Ray Observatory". In: *Astrophys. J.* 843.1 (2017), p. 39. DOI: 10.3847/1538-4357/aa7555. arXiv: 1701.01778 [astro-ph.HE].

[27] L. Sonnenschein. "CMS: Cosmic muons in simulation and measured data". In: (2011). arXiv: 1107.0427 [hep-ex].

[28] K. Greisen. "Highlights in air shower studies". In: *Proceedings of the 9th International Cosmic Ray Conference* ICRC1965 (1965).

[29] A. N. Bunner. "Cosmic ray detection by atmospheric fluorescence". PhD Thesis. Cornell University, Feb. 1967.

[30] G. Hartmann and P. C. Johnson. "Measurements of relative transition probabilities and the variation of the electronic transition moment for N_2 $C^3\Pi_u$-$B^3\Pi_g$ second positive system". In: *Journal of Physics B: Atomic and Molecular Physics* 11.9 (1978), p. 1597. URL: http://stacks.iop.org/0022-3700/11/i=9/a=013.

[31] J. V. Greisen and N. A. Porter. "Cerenkov Radiation from the Night Sky". In: *Quarterly Journal of the Royal Astronomical Society* 4 (1963), p. 275.

[32] A. Bouvier et al. "Photosensor Characterization for the Cherenkov Telescope Array: Silicon Photomultiplier versus Multi-Anode Photomultiplier Tube". In: *Proc. SPIE Int. Soc. Opt. Eng.* 8852 (2013), 88520K. DOI: 10.1117/12.2023778. arXiv: 1308.1390 [astro-ph.IM].

[33] C. Leinert et al. "The 1997 reference of diffuse night sky brightness *". In: *Astron. Astrophys. Suppl. Ser.* 127.1 (1998), pp. 1–99. DOI: 10.1051/aas:1998105. URL: https://doi.org/10.1051/aas:1998105.

[34] F. E. Roach and J. L. Gordon. *The Light of the Night Sky*. 1st ed. D. Reidel Publishing Company & Springer Netherlands, 1973. ISBN: 978-9-02770-293-7.

[35] M. Unger et al. "Reconstruction of longitudinal profiles of ultra-high energy cosmic ray showers from fluorescence and Cherenkov light measurements". In: *Nuclear Instruments and Methods in Physics Research Section A: Accelerators, Spectrometers, Detectors and Associated Equipment* 588.3 (2008), pp. 433–441. ISSN: 0168-9002. DOI: https://doi.org/10.1016/j.nima.2008.01.100.

[36] G. Matthiae on behalf of the Pierre Auger Observatory. "Optics and Mechanics of the Auger Fluorescence Detector". In: *proceedings of the 27th International Cosmic Ray Conference* ICRC 2001 (2001).

[37] T. Bretz and M. Ribordy. "Design constraints on Cherenkov telescopes with Davies-Cotton reflectors". In: *ArXiv e-prints* (Jan. 2013). arXiv: 1301.6556 [astro-ph.IM].

[38] H. Tokuno et al. "New air fluorescence detectors employed in the Telescope Array experiment". In: *Nuclear Instruments and Methods in Physics Research Section A: Accelerators, Spectrometers, Detectors and Associated Equipment* 676.Supplement C (2012), pp. 54–65. ISSN: 0168-9002. DOI: https://doi.org/10.1016/j.nima.2012.02.044.

[39] T. AbuZayyad. "Cosmic Rays Energy Spectrum observed by the TALE detector using Cerenkov light". In: *proceedings of the 34th International Cosmic Ray Conference* [PoS (ICRC2015) 422] (2015).

[40] J. Sitarek. "Performance of the MAGIC telescopes after the major upgrade". In: *proceedings of the 34th International Cosmic Ray Conference* [PoS (ICRC2015) 981] (2015).

[41] J. Cortina et al. "Technical Performance of the MAGIC Telescopes". In: *ArXiv e-prints* (July 2009). arXiv: 0907.1211 [astro-ph.IM].

[42] H. Falcke et al. "Detection and imaging of atmospheric radio flashes from cosmic ray air showers". In: *Nature* 435 (2005), pp. 313–316. DOI: 10.1038/nature03614. arXiv: astro-ph/0505383 [astro-ph].

[43] P. W. Gorham et al. "Observations of microwave continuum emission from air shower plasmas". In: *Phys. Rev. D* 78 (3 Aug. 2008), p. 032007. DOI: 10.1103/PhysRevD.78.032007. URL: https://link.aps.org/doi/10.1103/PhysRevD.78.032007.

[44] I. A. Samarai and O. Deligny. "Intensity of Microwave Signals Expected from Molecular Bremsstrahlung Radiation in Extensive Air Showers". In: *proceedings of the 34th International Cosmic Ray Conference* [PoS (ICRC2015) 417] (2015).

[45] C. Glaser. "The Energy Content of Extensive Air Showers in the Radio Frequency Range of 30-80 MHz". In: *proceedings of the 34th International Cosmic Ray Conference* [PoS (ICRC2015) 364] (2015).

[46] T. Suomijarvi. "New electronics for the surface detectors of the Pierre Auger Observatory". In: *proceedings of the 35th International Cosmic Ray Conference* [PoS (ICRC2017) 450] (2017).

[47] R. Šmída. "Scintillator detectors of AugerPrime". In: *proceedings of the 35th International Cosmic Ray Conference* [PoS (ICRC2017) 390] (2017).

[48] M. J. Figueira. "An improved reconstruction method for the AMIGA detectors". In: *proceedings of the 35th International Cosmic Ray Conference* [PoS (ICRC2017) 396] (2017).

[49] A. Castellina. "The dynamic range of the AugerPrime Surface Detector: technical solution and physics reach". In: *proceedings of the 35th International Cosmic Ray Conference* [PoS (ICRC2017) 397] (2017).

[50] G. Salina. "Automated procedures for the Fluorescence Detector calibration at the Pierre Auger Observatory". In: *proceedings of the 34th International Cosmic Ray Conference* [PoS (ICRC2015) 594] (2015).

[51] N. Barenthien et al. "Scintillator Surface Detectors of the Engineering Array: Production and Validation (GAP2016-040)". In: *The Pierre Auger Observatory – internal GAP notes* (June 2016).

[52] Hamamatsu Photonics. *R9420 photomultiplier tube datasheet*. URL: http://www.hamamatsu.com/.

[53] Hamamatsu Photonics. *S13360-series silicon photomultiplier datasheet*. URL: http://www.hamamatsu.com/.

[54] T. Bretz et al. "An integrated general purpose SiPM based optical module with a high dynamic range". In: *Journal of instrumentation* 13.06 (2018), P06001. URL: http://stacks.iop.org/1748-0221/13/i=06/a=P06001.

[55] A. Pla-Dalmau, A. D. Bross, and K. L. Mellott. "Low-cost extruded plastic scintillator". In: *Nuclear Instruments and Methods in Physics Research Section A: Accelerators, Spectrometers, Detectors and Associated Equipment* 466.3 (2001), pp. 482–491. ISSN: 0168-9002. DOI: https://doi.org/10.1016/S0168-9002(01)00177-2.

[56] Kuraray. *Y11 wavelength shifting fiber*. URL: http://kuraraypsf.jp/psf/ws.html.

[57] C. Peters et al. "The muon detector prototype AMD for the determination of the muon content in UHECRs". In: *proceedings of the 34th International Cosmic Ray Conference* [PoS (ICRC2015) 596] (2015).

[58] A. Aab et al. "Muon counting using silicon photomultipliers in the AMIGA detector of the Pierre Auger observatory". In: *Journal of Instrumentation* 12.03 (2017), P03002. URL: http://stacks.iop.org/1748-0221/12/i=03/a=P03002.

[59] T. Bretz et al. "A compact and light-weight refractive telescope for the observation of extensive air showers". In: *Journal of instrumentation* 13.07 (2018), P07024. URL: http://stacks.iop.org/1748-0221/13/i=07/a=P07024.

[60] SensL. *J-series silicon photomultiplier datasheet*. URL: http://sensl.com/products/j-series/.

[61] SensL. *R-series silicon photomultiplier datasheet*. URL: http://sensl.com/products/r-series/.

[62] Hamamatsu Photonics. *S10362-series silicon photomultiplier datasheet*. URL: http://www.hamamatsu.com/.

[63] F. Nagy et al. "A model based DC analysis of SiPM breakdown voltages". In: *Nucl. Instrum. Meth.* A849 (2017), pp. 55–59. DOI: 10.1016/j.nima.2017.01.002. arXiv: 1606.07805 [physics.ins-det].

[64] C. Jackson et al. "High-volume silicon photomultiplier production, performance, and reliability". In: *Optical Engineering* 53 (2014), p. 10. DOI: 10.1117/1.OE.53.8.081909. URL: https://doi.org/10.1117/1.OE.53.8.081909.

[65] D. Renker and E. Lorenz. "Advances in solid state photon detectors". In: *Journal of Instrumentation* 4.04 (2009), P04004. URL: http://stacks.iop.org/1748-0221/4/i=04/a=P04004.

[66] Hamamatsu Photonics. *S10943-series silicon photomultiplier datasheet*. URL: http://www.hamamatsu.com/.

[67] SensL. *Technical note – Introduction to SiPM Technology*. URL: http://www.sensl.com/.

[68] J. Schumacher. "Front-end electronics for silicon photomultipliers". Master's Thesis. RWTH Aachen University, Jan. 2014.

[69] J. Kemp. "t.b.a." PhD Thesis. RWTH Aachen University, 2020, to appear.

[70] F. Corsi et al. "Electrical Characterization of Silicon Photo-Multiplier Detectors for Optimal Front-End Design". In: 2 (Oct. 2006), pp. 1276–1280. ISSN: 1082-3654. DOI: 10.1109/NSSMIC.2006.356076.

[71] F. Corsi et al. "Modelling a silicon photomultiplier (SiPM) as a signal source for optimum front-end design". In: *Nuclear Instruments and Methods in Physics Research Section A: Accelerators, Spectrometers, Detectors and Associated Equipment* 572.1 (2007). Frontier Detectors for Frontier Physics, pp. 416–418. ISSN: 0168-9002. DOI: https://doi.org/10.1016/j.nima.2006.10.219.

[72] F. Scheuch. "Measurement and simulation of electrical properties of SiPM photon detectors". Master's Thesis. RWTH Aachen University, Nov. 2012.

[73] T. Bretz et al. "FAMOUS – a fluorescence telescope using SiPMs". In: *proceedings of the 34th International Cosmic Ray Conference* [PoS (ICRC2015) 649] (2015).

[74]   J. Auffenberg et al. "Design Study of an Air Cherenkov Telescope for Efficient Air-Shower Detection at 100 TeV at the South Pole on Top of IceCube". In: *proceedings of the 34th International Cosmic Ray Conference* [PoS (ICRC2015) 1155] (2015).

[75]   M. Schaufel et al. "Small size air-Cherenkov telescopes for ground detection arrays - a possible future extension?" In: *proceedings of the 35th International Cosmic Ray Conference* [PoS (ICRC2017) 786] (2017).

[76]   M. Schaufel. "Implementing Hybrid Detection by Combining a Compact Air-Cherenkov Telescope with the HAWC Gamma-Ray Observatory". Master's Thesis. RWTH Aachen University, Oct. 2017.

[77]   STMicroelectronics. *TS912 – voltage feedback amplifier datasheet*. URL: http://www.st.com/en/amplifiers-and-comparators/ts912.html.

[78]   Texas Instruments. *THS3202 – 2 GHz Current Feedback Amplifier datasheet*. URL: http://www.ti.com/product/ths3202.

[79]   Rohde & Schwarz. *HMO1002 mixed signal oscilloscope datasheet*. Sept. 2016. URL: https://www.rohde-schwarz.com/us/brochure-datasheet/hmo1002/.

[80]   Fluke. *8842A digital multimeter datasheet*. Dec. 1991. URL: http://assets.fluke.com/manuals/8842a___imeng0300.pdf.

[81]   Linear Technology. *LTspice software*. URL: http://www.linear.com/docs/42781.

[82]   L. Nagel and R. Rohrer. "Computer analysis of nonlinear circuits, excluding radiation (CANCER)". In: *IEEE Journal of Solid-State Circuits* 6.4 (Aug. 1971), pp. 166–182. ISSN: 0018-9200.

[83]   A. Biland et al. "Calibration and performance of the photon sensor response of FACT – the first G-APD Cherenkov telescope". In: *Journal of Instrumentation* 9.10 (2014), P10012. URL: http://stacks.iop.org/1748-0221/9/i=10/a=P10012.

[84]   Analog Devices. *AD22100 – Voltage Output Temperature Sensor with Signal Conditioning datasheet*. URL: http://www.analog.com/ad22100.

[85]   Texas Instruments. *MSP430 family – ultra-low-power MCUs*. URL: http://www.ti.com/microcontrollers/msp430-ultra-low-power-mcus/overview.html.

[86]   Lecroy. *WaveJet 354A digital signal oscilloscope datasheet*. Apr. 2009. URL: http://teledynelecroy.com/doc/docview.aspx?id=1800.

[87]   C. Günther. "Temperature dependence of the SiPMs and the front-end electronics for AugerPrime". Bachelor's Thesis. RWTH Aachen University, Aug. 2016.

[88]   L. L. Futlik et al. "Methodical problems of crosstalk probability measurements in solid-state photomultipliers". In: *Bulletin of the Lebedev Physics Institute* 38.10 (Oct. 2011), pp. 302–310. DOI: 10.3103/S1068335611100058. URL: https://doi.org/10.3103/S1068335611100058.

[89]   V. Oleynikov and V. Porosev. "After-pulsing and cross-talk comparison for PM1125NS-SB0 (KETEK), S10362-11-100C (HAMAMATSU) and S13360-3050CS (HAMAMATSU)". In: *Journal of Instrumentation* 12.06 (2017), p. C06046. URL: http://stacks.iop.org/1748-0221/12/i=06/a=C06046.

[90]   M. Lauscher. "Characterisation Studies of Silicon Photomultipliers for the Detection of Fluorescence Light from Extensive Air Showers". Master's Thesis. RWTH Aachen University, Jan. 2012.

[91]   Hamamatsu Photonics. *MPPC Technical note*. URL: http://www.hamamatsu.com/.

[92]   J. Schumacher. "Characterization Studies of Silicon Photomultipliers: Noise and Relative Photon Detection Efficiency". Bachelor's Thesis. RWTH Aachen University, Feb. 2011.

[93]   Hewlett & Packard. *8013B 50 MHZ Dual-Output Pulse Generator*. Sept. 1976. URL: https://literature.cdn.keysight.com/litweb/pdf/08013-90006.pdf.

[94]   A. Gutsche. "Measurement of the dynamic range of SiPMs for AugerPrime". Bachelor's Thesis. RWTH Aachen University, Aug. 2016.

[95]   L. Gruber et al. "Over saturation behavior of SiPMs at high photon exposure". In: *Nuclear Instruments and Methods in Physics Research Section A: Accelerators, Spectrometers, Detectors and Associated Equipment* 737 (2014), pp. 11–18. ISSN: 0168-9002. DOI: https://doi.org/10.1016/j.nima.2013.11.013. URL: http://www.sciencedirect.com/science/article/pii/S0168900213015520.

[96]   Kuttig Electronic GmbH. *private communication*.

[97]   Würth Elektronik. *WL-TMRW THT Mono-color Round Waterclear LEDs*. URL: http://katalog.we-online.de/de/led/WL-TMRW.

[98]   Lappkabel Deutschland. *RG58 C/U coaxial cable*. URL: https://www.lappkabel.de.

[99]   A. Biland. "FACT - Status and Experience from Three Years Operation of the First SiPM Camera". In: *proceedings of the 34th International Cosmic Ray Conference* [PoS (ICRC2015) 1032] (2015).

[100]   T. Huber et al. "The IceTop Scintillator Upgrade". In: *proceedings of the 35th International Cosmic Ray Conference* [PoS (ICRC2017) 401] (2017).

[101]   SensL. *C-series silicon photomultiplier datasheet*. URL: http://sensl.com/products/c-series/.

[102]   T. Bretz et al. "SiPMs – A revolution for high dynamic range applications". In: *proceedings of the 35th International Cosmic Ray Conference* [PoS (ICRC2017) 472] (2017).

[103]   C. Peters et al. "Prospects of Silicon Photomultipliers for Ground-Based Cosmic Ray Experiments". In: *Proceedings of 2016 International Conference on Ultra-High Energy Cosmic Rays (UHECR2016)* (2016). DOI: 10.7566/JPSCP.19.011030. eprint: http://journals.jps.jp/doi/pdf/10.7566/JPSCP.19.011030. URL: http://journals.jps.jp/doi/abs/10.7566/JPSCP.19.011030.

[104]   USB Implementers Forum, Inc. *A Technical Introduction to USB 2.0*. URL: http://www.usb.org/developers/docs/whitepapers/.

[105]   X. Bertou. *Presentation on "ASCII Auger Scintillators for Composition - II"*. Mar. 2014.

[106]   X. Bertou (Bariloche) and T. Bretz (Aachen). *private communication*. 2015.

[107]   J. Franz. *EMV – Störungssicherer Aufbau elektronischer Schaltungen*. 4th ed. Vieweg + Teubner Verlag – Springer Fachmedien Wiesbaden GmbH, 2011. ISBN: 978-3-83480-893-6.

[108] T. Brander et al. *Trilogy of Magnetics*. 4th ed. Würth Elektronik eiSos GmbH & Co. KG, Oct. 2010. ISBN: 978-3-89929-157-5.

[109] Maxim Integrated. *MAX15059 – 76 V, 300 mW Boost Converter and Current Monitor for APD Bias Applications datasheet*. URL: https://www.maximintegrated.com/en/products/power/switching-regulators/MAX15059.html.

[110] ON Semiconductor (formerly Fairchild). *LM7805 – 3-Terminal 1 A Positive Voltage Regulator datasheet*. URL: http://www.onsemi.com/PowerSolutions/product.do?id=MC7805.

[111] J. Schumacher et al. "Dedicated power supply for silicon photomultipliers". In: *proceedings of the 34th International Cosmic Ray Conference* [PoS (ICRC2015) 605] (2015).

[112] M. Negrete. "Fiber Optic Communication Systems Benefit from Tiny, Low Noise Avalanche Photodiode Bias Supply". In: *Linear Technology – Design Note* 273 (Dec. 2001).

[113] J. Williams. "Bias Voltage and Current Sense Circuits for Avalanche Photodiodes". In: *Linear Technology – Application Note* 92 (Nov. 2002).

[114] Analog Devices. *ADT7310 – ±0.5 °C Accurate, 16 bit Digital SPI Temperature Sensor datasheet*. URL: http://www.analog.com/adt7310.

[115] Texas Instruments. *LM1086 – LM1086 1.5 A Low Dropout Positive Regulators datasheet*. URL: http://www.ti.com/product/lm1086.

[116] Analog Devices. *AD5382 – 32-Channel 14 bit 3 V / 5 V Single-Supply Voltage-Output DAC datasheet*. URL: http://www.analog.com/ad5382.

[117] Microchip Technology. *MCP4822 – Mixed Signal - System D/A Converters datasheet*. URL: http://www.microchip.com/wwwproducts/en/mcp4822.

[118] Hamamatsu Photonics. *C11204-02 – datasheet*. URL: http://www.hamamatsu.com/.

[119] Texas Instruments. *TPS62120 – 15 V, 75 mA, 96% efficiency Step-Down Converter with DCS-Control datasheet*. URL: http://www.ti.com/product/tps62120.

[120] Microchip Technology (formerly Atmel Corporation). *ATmega328 – microcontroller documentation*. URL: https://www.microchip.com/wwwproducts/en/atmega328p.

[121] Texas Instruments. *LM94021 – 1.5 °C Temperature Sensor with Multiple Gain Analog Output Options datasheet*. URL: http://www.ti.com/product/lm94021.

[122] Hamamatsu Photonics. *C11204-02 – technical document*. URL: http://www.hamamatsu.com/.

[123] T. Suomijarvi. "Surface Detector Electronics for the Pierre Auger Observatory". In: *proceedings of the 27th International Cosmic Ray Conference* Copernicus Gesellschaft 2001 (ICRC2001) 756 (Aug. 2001).

[124] Analog Devices. *AD8012 – current feedback amplifier datasheet*. URL: http://www.analog.com/ad8012.

[125] Analog Devices. *AD592 – Current Output - Precision IC Temperature Transducer datasheet*. URL: http://www.analog.com/ad592.

[126] S. Agostinelli et al. "Geant4 – a simulation toolkit". In: *Nuclear Instruments and Methods in Physics Research Section A: Accelerators, Spectrometers, Detectors and Associated Equipment* 506.3 (2003).

[127] L. Landau. "On the energy loss of fast particles by ionization". In: *J. Phys.(USSR)* 8 (1944), pp. 201–205.

[128] P. V. Vavilov. "Ionization losses of high-energy heavy particles". In: 5 (Jan. 1957), pp. 749–751.

[129] B. Gompertz. "XXIV. On the nature of the function expressive of the law of human mortality, and on a new mode of determining the value of life contingencies. In a letter to Francis Baily, Esq. F. R. S. &c". In: *Philosophical Transactions of the Royal Society of London* 115 (1825), pp. 513–583. DOI: 10.1098/rstl.1825.0026. eprint: http://rstl.royalsocietypublishing.org/content/115/513.full.pdf+html. URL: http://rstl.royalsocietypublishing.org/content/115/513.short.

[130] J. B. Birks. "Scintillations from Organic Crystals: Specific Fluorescence and Relative Response to Different Radiations". In: *Proceedings of the Physical Society. Section A* 64.10 (Apr. 1951), p. 874. URL: http://stacks.iop.org/0370-1298/64/i=10/a=303.

[131] V. Tretyak. "Semi-empirical calculation of quenching factors for ions in scintillators". In: *Astroparticle Physics* 33.1 (2010), pp. 40–53. ISSN: 0927-6505. DOI: https://doi.org/10.1016/j.astropartphys.2009.11.002. URL: http://www.sciencedirect.com/science/article/pii/S0927650509001650.

[132] E. J. Gumbel. "The Return Period of Flood Flows". In: *The Annals of Mathematical Statistics* 12.2 (1941), pp. 163–190. ISSN: 00034851. URL: http://www.jstor.org/stable/2235766.

[133] H. Salazar. "Surface detector calibration for the Auger Observatory". In: *proceedings of the 27th International Cosmic Ray Conference* Copernicus Gesellschaft 2001 (ICRC2001) 752 (Aug. 2001).

[134] J. A. Dean. *Lange's Handbook of Chemistry*. 15th ed. McGraw-Hill Professional, 1998. ISBN: 978-0-07016-384-3.

[135] L. Peralta. "Temperature dependence of plastic scintillators". In: *Nuclear Instruments and Methods in Physics Research Section A: Accelerators, Spectrometers, Detectors and Associated Equipment* 883 (2018), pp. 20–23. ISSN: 0168-9002. DOI: https://doi.org/10.1016/j.nima.2017.11.041.

[136] Z. Zong. "First results from the AugerPrime engineering array". In: *proceedings of the 35th International Cosmic Ray Conference* [PoS (ICRC2017) 449] (2017).

[137] H. Arnaldi, X. Bertou, and I. Naranjo. "ASCII prototype characterization using SiPMs (GAP2016-067)". In: *The Pierre Auger Observatory – internal GAP notes* (Nov. 2016).

[138] D. Veberič, M. Roth, and H. Dembinski. "SD reconstruction – Offline reference manual (GAP2005-035)". In: *The Pierre Auger Observatory – internal GAP notes* (2005).

[139] Analog Devices (formerly Linear Technology). *LTC3260 – Low Noise Dual Supply Inverting Charge Pump datasheet*. URL: http://www.linear.com/product/ltc3260.

[140] Future Technology Devices International Ltd. *FT232R – USB UART IC datasheet*. URL: http://www.ftdichip.com/products/ics/ft232r.htm.

[141] Kuttig Electronic GmbH. URL: http://www.kuttig.de/.

[142] HIROSE Electric Group. *U.FL-R-SMT-1(10) – U.FL Series datasheet*. URL: https://www.hirose.com/product/en/products/U.FL/U.FL-R-SMT-1(10)/.

[143]   T. Bretz (Aachen). *private communication*.

[144]   S. Menzel. *ABC of Capacitors*. 1st ed. Würth Elektronik eiSos GmbH & Co. KG, Nov. 2014. ISBN: 978-3-89929-294-7.

[145]   S. Querchfeld et al. "Integrated HV-Supply for SSD PMTs (GAP2017-014)". In: *The Pierre Auger Observatory – internal GAP notes* (Feb. 2017).

[146]   P. Muralidharan et al. "An Automatic Baseline Regulation in a Highly Integrated Receiver Chip for JUNO". In: *J. Phys.: Conf. Ser. 888 012051* (2017). DOI: 10.1088/1742-6596/888/1/012051. URL: https://doi.org/10.1088/1742-6596/888/1/012051.

[147]   T. Bretz (Aachen) and S. van Waasen (Jülich). *private communication*. 2018.

[148]   J. P. Koschinsky. "Development of Light-Collecting Cones for the IceAct Camera". Master's Thesis. RWTH Aachen University, Sept. 2017.

[149]   H. Lacker (Berlin). *private communication*. 2016.

[150]   F. Reisenhofer (Aachen). *private communication*. 2018.

[151]   H. Anderhub et al. "Design and operation of FACT – the first G-APD Cherenkov telescope". In: *Journal of Instrumentation* 8.06 (2013), P06008. URL: http://stacks.iop.org/1748-0221/8/i=06/a=P06008.

[152]   T. Hebbeker (Aachen). *private communication*.

[153]   T. Niggemann. "New Telescope Design with Silicon Photomultipliers for Fluorescence Light Detection of Extensive Air Showers". Master's Thesis. RWTH Aachen University, Jan. 2012.

[154]   G. Xiao et al. "Calibration of Photonis XP3062/FL Photomultiplier Tube". In: *proceedings of the 29th International Cosmic Ray Conference* ICRC 2005 (2005).

[155]   B. R. Dawson. "Fluorescence Detector Techniques – a paper accompanying the Auger Project Fluorescence Workshop talk by. B. R. Dawson at the University of Utah on March 4-7 1996 (GAP1996-017)". In: *The Pierre Auger Observatory – internal GAP notes* (Mar. 1996).

[156]   J. Auffenberg et al. "On improving composition measurements by combining compact Cherenkov telescopes with ground based detectors". In: *proceedings of the 35th International Cosmic Ray Conference* [PoS (ICRC2017) 401] (2017).

[157]   H. Gemmeke on behalf of the Pierre Auger Observatory. "The Auger Fluorescence Detector Electronics". In: *proceedings of the 27th International Cosmic Ray Conference* ICRC 2001 (2001).

[158]   M. Stephan. "Measurement of the Light Flux of Stars and the Night-Sky with Silicon Photomultipliers". PhD Thesis. RWTH Aachen University, Sept. 2014.

[159]   ORAFOL Fresnel Optics GmbH. *Positive Fresnel Lenses family catalog*. URL: http://www.orafol.com/12643.

[160]   M. Eichler. "Characterisation studies on the optics of the prototype fluorescence telescope FAMOUS". Master's Thesis. RWTH Aachen University, Mar. 2014.

[161]   J. Merz. "Photon detection efficiency measurement of Winston cones for the FAMOUS telescope". Bachelor's Thesis. RWTH Aachen University, July 2015.

[162] T. Niggemann et al. "The optics and detector-simulation of the air fluorescence telescope FAMOUS for the detection of cosmic rays". In: *Proc.SPIE* 8444 (2012), p. 13. DOI: 10.1117/12.925305. URL: https://doi.org/10.1117/12.925305.

[163] R. Winston, J. C. Miñano, and P. Benítez. *Nonimaging optics*. 1st ed. Elsevier Academic Press, Jan. 2005. ISBN: 978-0-12759-751-5.

[164] SCHOTT Advanced Optics. *Optical Filter Glass family catalog*. URL: https://www.schott.com/advanced_optics/english/index.html.

[165] Hamamatsu Photonics. *S12573-series silicon photomultiplier datasheet*. URL: http://www.hamamatsu.com/.

[166] Hamamatsu Photonics. *S10985-series silicon photomultiplier datasheet*. URL: http://www.hamamatsu.com/.

[167] A. Bogner. "Trigger Implementation for FAMOUS". Bachelor's Thesis. RWTH Aachen University, Oct. 2016.

[168] Texas Instruments. *LMT87 – 2.7 V-Capable,* 10 μA *Analog Output Temperature Sensor in SC70 and TO-92 datasheet*. URL: http://www.ti.com/product/lmt87.

[169] SAMTEC, Inc. *HTSS – .100inch High-Temp Shrouded Terminal Strip datasheet*. URL: https://www.samtec.com/products/htss.

[170] SAMTEC, Inc. *TEM – 0.80 mm Tiger Eye™Micro Terminal Strip datasheet*. URL: https://www.samtec.com/products/tem.

[171] SAMTEC, Inc. *SEM – 0.80 mm Tiger Eye™Micro Socket Strip datasheet*. URL: https://www.samtec.com/products/sem.

[172] Paul Sherrer Institut. *Domino Ring Sampler (DRS) version 4 datasheet*. URL: https://www.psi.ch/drs/documentation.

[173] L. Tibaldo et al. "TARGET: toward a solution for the readout electronics of the Cherenkov Telescope Array". In: *proceedings of the 34th International Cosmic Ray Conference* [PoS (ICRC2015) 932] (2015).

[174] N. L. Höflich. "Implementation and calibration of the TARGET data acquisition system for FAMOUS". Bachelor's Thesis. RWTH Aachen University, Sept. 2016.

[175] B. J. Pestka. "Commissioning of the self-trigger of the TARGET read-out board for FAMOUS". Bachelor's Thesis. RWTH Aachen University, Sept. 2016.

[176] Analog Devices. *AD9238 – Dual* 12 bit*, 20/40/65 MSPS,* 3 V *ADC datasheet*. URL: http://www.analog.com/ad9238.

[177] Xilinx. *Spartan 3-series – Multiple Domain-Optimized Platforms Spartan-3 Generation datasheet*. URL: https://www.xilinx.com/products/silicon-devices/fpga/spartan-3.html.

[178] LEMO. *Miniature 00-type connector manual*. URL: https://www.lemo.com/en/products/miniature-connector/00-connector.

[179] Texas Instruments. *TPS560200 – 17 V Input,* 500 mA *Synchronous Step-Down Regulator in SOT-23 with Advanced Eco-Mode™datasheet*. URL: http://www.ti.com/product/tps560200.

[180] Maxim Integrated. *MAX3485 – 3.3 V Powered,* $10\,\text{Mbit s}^{-1}$ *and Slew-Rate Limited, True RS-485/RS-422 Transceivers datasheet.* URL: https://www.maximintegrated.com/en/products/interface/transceivers/MAX3485.html.

[181] Analog Devices (formerly Linear Technology). *LTC6903 –* $1\,\text{kHz}$ *-* $68\,\text{MHz}$ *Serial Port Programmable Oscillator datasheet.* URL: http://www.linear.com/product/ltc6903.

[182] Texas Instruments. *DS90LV031A – 3 V Quad CMOS Differential Line Driver datasheet.* URL: http://www.ti.com/product/ds90lv031a.

[183] WIZnet. *W5500 – Hardwired TCP/IP embedded Ethernet controller datasheet.* URL: http://www.wiznet.io/product-item/w5500/.

[184] Texas Instruments. *SN74LVC1G08 – Single 2-Input Positive-AND Gate datasheet.* URL: http://www.ti.com/product/sn74lvc1g08.

[185] Texas Instruments. *SN74LVC1G123 – Single Retriggerable Monostable Multivibrator with Schmitt-Trigger Inputs datasheet.* URL: http://www.ti.com/product/sn74lvc1g123.

[186] Texas Instruments. *SN74LVC1G3157 – 1-Channel, 2-1 Analog Switch datasheet.* URL: www.ti.com/product/sn74lvc1g3157.

[187] NXP. *BFR93A – NPN* $6\,\text{GHz}$ *wideband transistor datasheet.* URL: https://www.nxp.com/pages/npn-6-ghz-wideband-transistor:BFR93A.

[188] NXP. *BFT93 – PNP* $5\,\text{GHz}$ *wideband transistor datasheet.* URL: https://www.nxp.com/pages/pnp-5-ghz-wideband-transistor:BFT93.

[189] Texas Instruments. *Code Composer Studio – Code Composer Studio™IDE.* URL: http://www.ti.com/tools-software/ccs.html.

[190] Würth Elektronik. *WCAP-AT1H Aluminum Electrolytic Capacitors.* URL: http://katalog.we-online.de/en/pbs/WCAP-AT1H.

[191] I. Hickman. *Analog Electronics.* 1st ed. Elsevier Academic Press, June 1999. ISBN: 978-0-75064-416-7.

[192] Nexperia. *PBHV9040T –* $500\,\text{V}$*,* $0.25\,\text{A}$ *PNP high-voltage low VCEsat (BISS) transistor datasheet.* URL: https://assets.nexperia.com/documents/data-sheet/PBHV9040T.pdf.

[193] Diodes Inc. *FMMT458 –* $400\,\text{V}$ *NPN High Voltage Transistor in SOT23 datasheet.* URL: https://www.diodes.com/assets/Datasheets/FMMT458.pdf.

[194] Analog Devices. *AD5668 – Octal,* 16 bit, *SPI Voltage Output denseDAC With* $5\,\text{ppm}\,^{\circ}\text{C}^{-1}$ *On-Chip Reference datasheet.* URL: http://www.analog.com/ad5668.

[195] Analog Devices. *REF196 –* $3.3\,\text{V}$ *Precision Micropower, Low Dropout, Low Voltage Reference datasheet.* URL: http://www.analog.com/ref196.

[196] Analog Devices. *ADG732 – 32-Channel,* $4\,\Omega$ $1.8\,\text{V}$ *to* $5.5\,\text{V}$*,* $\pm 2.5\,\text{V}$*, Analog Multiplexer datasheet.* URL: http://www.analog.com/adg732.

[197] Texas Instruments. *LMP8480 –* $76\,\text{V}$*, High-Side, High-Speed, Voltage Output Current Sensing Amplifier datasheet.* URL: http://www.ti.com/product/lmp8480.

[198] Analog Devices (formerly Linear Technology). *LTC6101HV – High Voltage, High-Side Current Sense Amplifier in SOT-23 datasheet.* URL: http://www.linear.com/product/ltc6101.

[199]   Department of Transportation – Federal Aviation Administration. *Advisory Circular AC 20-74: Aircraft position and anticollision light measurments*. July 1971. URL: https://www.faa.gov/documentLibrary/media/Advisory_Circular/AC_20-74.pdf.

[200]   J. Auffenberg for the IceCube-Gen2 Collaboration. "IceAct: Imaging Air Cherenkov Telescopes with SiPMs at the South Pole for IceCube-Gen2". In: *proceedings of the 35th International Cosmic Ray Conference* [PoS (ICRC2017) 1055] (2017).

[201]   R. Brun and F. Rademakers. "ROOT – An Object Oriented Data Analysis Framework". In: *Proceedings AIHENP'96 Workshop, Lausanne, Nucl. Inst. & Meth. in Phys. Res. A 389* (Sept. 1997), pp. 81–86.

Acronyms

AC alternating current. 29, 61, 136, 137, 138, 139, 152

AC/DC alternating-current-to-direct-current. 137, 138, 139, 140, 152

ADC analog-to-digital converter. 18, 27, 28, 29, 30, 44, 87, 92, 93, 99, 105, 106, 108, 109, 134, 140, 141, 146, 147, 149, 150, 151, 153

AERA Auger Engineering Radio Array. 21

AMIGA Auger Muons and Infill for the Ground Array. 23, 31

APD avalanche photodiode. 35, 40

ASCII Auger Scintillators for Composition – II. iii, 42, 76, 77, 78, 81, 82, 83, 87, 88, 89, 90, 91, 92, 93, 94, 95, 98, 101, 107, 108, 109, 161, 168, 169

ASIC application-specific integrated circuit. 126

CEN Comité Européen de Normalisation – European Committee for Standardization. 9

CERN Organisation européene pour la recherche nucléaire – Organization for Nuclear Research. 18

CFA current-feedback amplifier. 43, 44, 81, 82, 98, 105

CMS Compact Muon Solenoid. 18

CORSIKA Cosmic Ray Simulations for Kascade. 16, 84, 86

CPU central processing unit. 29, 30, 134

CTA Cherenkov Telescope Array. 126, 153

DAC digital-to-analog converter. 79, 80, 133, 140, 141, 142, 143, 144, 145, 146, 151, 152, 169, 175

DAQ data acquisition. 27, 29, 36, 42, 44, 49, 75, 87, 94, 100, 103, 109, 116, 123, 125, 126, 127, 128, 129, 131, 132, 133, 134, 135, 136, 137, 152, 153, 154, 155, 156, 158, 161

DC direct current. 29, 44, 105, 132, 136, 137, 138, 139, 152, 170

DC/DC direct-current-to-direct-current. 30, 75, 78, 102, 103, 123, 137, 139, 140, 146, 152, 169

DRS Domino Ring Sampler. 21, 126, 128, 130, 131, 133, 134, 136

EMI electromagnetic interference. 78, 101

ESR equivalent series resistance. 102, 138, 139

FACT First G-APD Cherenkov Telescope. 113, 116, 123, 125, 126, 127, 128, 129, 131, 132, 134, 136, 154, 155, 156, 158

FAMOUS First Auger Multi-pixel photon counter camera for the Observation of Ultra-high energy cosmic air Showers. iii, 42, 71, 78, 113, 114, 115, 116, 117, 118, 119, 120, 121, 123, 126, 127, 128, 129, 131, 136, 137, 138, 140, 141, 143, 144, 145, 147, 148, 151, 152, 153, 156, 157, 158, 161, 168, 173, 174, 175

FD Fluorescence Detector. 20, 21, 23, 31, 32, 113, 115, 116

FPGA field-programmable gate array. 29, 30, 101, 128, 130, 131

FWHM full width at half maximum. 62

G-APD Geiger-mode avalanche photodiode. 35, 37, 38, 40, 47, 62, 64, 75

GEANT Geometry and Tracking. 84, 85, 86

GPS global positioning system. 30

HAWC High-Altitude Water Cherenkov observatory. 17, 18, 152, 157, 158

HEAT High Elevation Auger Telescopes. 20, 21, 116

HiRes High Resolution. 21

IC integrated circuit. 101

ICRC International Cosmic Ray Conference. 23

ISO International Organization for Standardization. 9

LDF lateral distribution function. 24, 25, 31, 93, 94, 109

LDO low-dropout. 138, 140, 141, 142, 146, 148, 151

LED light emitting diode. 30, 36, 43, 44, 46, 50, 51, 61, 62, 63, 66, 67, 68, 99, 103, 130, 131, 135

LHC Large Hadron Collider. 13, 14, 15

LVDS low-voltage differential signaling. 129, 131, 133, 134

LVTTL low-voltage transistor-transistor logic. 29, 131, 133, 134

MAGIC Major Atmospheric Gamma-Ray Imaging Cherenkov. 20, 21

MIP minimal ionizing particle. 74, 75, 76, 81, 82, 83, 84, 86, 87, 88, 89, 90, 91, 92, 93, 94, 96, 99, 100, 105, 107, 108, 109

PCB printed circuit board. 61, 66, 67, 78, 83, 95, 96, 101, 121, 122, 123, 124, 125, 126, 127, 128, 131, 138, 139, 140, 144, 146, 150, 152, 154, 161, 175

PDE photon detection efficiency. 36, 38, 39, 40, 49, 50, 51, 52, 62, 63, 64, 68, 69, 70, 74, 89, 91, 96, 107

PDF probability density function. 164, 165

PMMA polymethyl methacrylate. 26, 119, 122

PMT vacuum photomultiplier tube. iii, 17, 18, 20, 21, 23, 25, 26, 27, 28, 29, 30, 31, 32, 37, 73, 74, 75, 76, 77, 78, 83, 87, 89, 102, 108, 109, 113, 114, 115, 116, 158

PSU power supply unit. 143, 147, 151, 161

QE quantum efficiency. 38

RAM random access memory. 63

RMS root mean square. 46, 47, 69, 88, 92, 103, 117, 146

SD Surface Detector. 17, 18, 20, 21, 23, 25, 30, 87, 92, 93, 94

SI système international d'unités – International System of Units. 10, 92, 141, 146, 149

SiPM silicon photomultiplier. iii, 26, 27, 28, 29, 30, 31, 32, 35, 36, 37, 38, 39, 40, 41, 42, 43, 44, 45, 46, 47, 49, 50, 51, 52, 53, 54, 55, 56, 57, 58, 59, 60, 61, 62, 63, 64, 65, 66, 67, 68, 69, 70, 71, 73, 74, 75, 76, 77, 78, 79, 80, 81, 82, 83, 85, 86, 87, 88, 89, 90, 91, 92, 93, 94, 95, 96, 97, 98, 99, 100, 101, 102, 103, 104, 106, 107, 108, 109, 110, 113, 114, 115, 116, 117, 118, 120, 121, 122, 123, 124, 125, 126, 127, 129, 133, 136, 137, 139, 140, 141, 142, 144, 145, 146, 148, 149, 150, 151, 152, 153, 157, 158, 161, 165, 167, 168, 169, 170

SMA sub-miniature version A. 29, 83, 100, 104, 129, 133

SMD surface-mounted device. 76, 101, 124

SNR signal-to-noise ratio. 28, 41, 68, 69, 70, 71, 74, 75, 76, 82, 88, 89, 98, 99, 103, 107, 109, 114, 116, 117, 122, 125

SPI serial peripheral interface. 79, 134

SPICE Simulation Program with Integrated Circuit Emphasis. 44, 62, 63, 99, 105, 139, 143, 144, 146, 147, 148

SPMT small PMT. 23, 28, 29, 30, 31

SSD Surface Scintillation Detector. iii, 23, 24, 25, 27, 28, 29, 30, 31, 32, 42, 65, 68, 71, 73, 74, 75, 76, 77, 92, 94, 95, 97, 100, 101, 102, 103, 104, 106, 108, 109, 110, 161, 168, 170, 171

UART universal asynchronous receiver-transmitter. 30, 80, 81, 95, 101, 130, 134

UB Unified Board. 28, 29, 76, 77, 81, 83, 86, 87, 88, 89, 90, 92, 94

UHECR ultra-high energy cosmic ray. iii, 12, 13, 115

USB Universal Serial Bus. 30, 76, 95, 101, 109, 148, 152

UTC Coordinated Universal Time. 155

UUB Upgraded Unified Board. 23, 27, 28, 29, 30, 32, 74, 75, 76, 92, 94, 95, 99, 100, 101, 102, 106

UV ultraviolet. 18, 19, 20, 26, 38, 42, 43, 71, 117, 118, 119, 121, 122

VEM vertical equivalent muon. 93, 94, 108, 109

VFA voltage-feedback amplifier. 43, 44

VHF very-high frequency. 21

WCD water-Cherenkov detector. 17, 18, 23, 24, 25, 28, 29, 30, 31, 77, 87, 88, 93, 94, 108, 109

WLS wavelength-shifting. 17, 18, 25, 26, 27, 32, 73, 75, 77, 86, 89, 92, 94, 107, 109

Declaration of pre-released partial results

Certain measurements, calculations, and simulations of this thesis have already been published partially in the following journal papers and proceedings. The contents of these publications rely on the results of this work and were therefore written by the author of this thesis:

- J. Schumacher, J. Auffenberg, T. Bretz, T. Hebbeker, D. Louis, and F.-P. Zantis. "Dedicated power supply for silicon photomultipliers". In: *proceedings of the 34th International Cosmic Ray Conference* PoS(ICRC2015)605 (2015) *URL:* https://pos.sissa.it/236/605/pdf.

- T. Bretz, R. Engel, T. Hebbeker, J. Kemp, L. Middendorf, C. Peters, J. Schumacher, R. Šmída, and D. Veberič. "An integrated general purpose SiPM based optical module with a high dynamic range". In *Journal of instrumentation* 13.06 P06001 (2018). *URL:* http://stacks.iop.org/1748-0221/13/i=06/a=P06001.

- T. Bretz, T. Hebbeker, J. Kemp, L. Middendorf, T. Niggemann, C. Peters, M. Schaufel, J. Schumacher, J. Auffenberg, and C. Wiebusch. "A compact and light-weight refractive telescope for the observation of extensive air showers". In *Journal of instrumentation* 13.07 P07024 (2018). *URL:* http://stacks.iop.org/1748-0221/13/i=07/a=P07024.

Some results have also been released in internal notes of the Pierre Auger Collaboration, in so-called GAP-notes. The author of this thesis exclusively wrote those parts that referred to work done in this thesis:

- J. Schumacher. "Front-end electronics for silicon photomultipliers". In: *Internal notes of the Pierre Auger Collaboration* GAP2015-009 (2015).

- T. Bretz, T. Hebbeker, J. Kemp, M. Lauscher, R. Meißner, L. Middendorf, T. Niggemann, C. Peters, and J. Schumacher. "SiPMs for SSD". In: *Internal notes of the Pierre Auger Collaboration* GAP2015-043 (2015).

Acknowledgments – Danksagungen

Ohne die Unterstützung meiner Vorgesetzten, Kollegen, Freunde und Familie wäre diese Arbeit nicht realisierbar gewesen. Daher möchte ich mich im Folgenden bei allen bedanken.

Großer Dank gebührt Professor Thomas Hebbeker, der mich nach der Bachelor- und auch Masterarbeit auch für diese Doktorarbeit in seinem Institut aufgenommen hat. Die regelmäßigen Besprechungen und Diskussionen physikalischer Themen haben dazu beigetragen mein Verständnis der Hochenergie- und Astroteilchenphysik zu vertiefen. Ebenso war Professor Hebbeker bereit meine Arbeit kritisch Probe zu lesen, wofür ich ihm auch zu danken habe.

Ebenso bedanke ich mich bei meinem langjährigen Betreuer und SiPM-Experten Junior-Professor Thomas Bretz. Die wöchentlichen Meetings und der E-Mail-Austausch auch nach den üblichen Geschäftsstunden waren der Schlüssel zum Erfolg unserer Projekte, wie FAMOUS, ASCII und SSD.

Ebenso bedanke ich mich bei den Kollegen der Pierre Auger-Kollaboration. Hier möchte ich insbesondere der Arbeitsgruppe in Aachen und auch den ehemaligen Kollegen danken, darunter Professor Martin Erdmann, Daniel Kümpel, Tim Niggemann, Rebecca Meißner, Lukas Middendorf, Christine Peters, Maurice Stephan und Julian Kemp, sowie den Kollegen von außerhalb, die bei der Datennahme und bei Messungen mit ASCII und SSD geholfen haben, wie Darko Veberic, Radomir Smida und Xavier Bertou.

Daneben war die Zusammenarbeit mit der Aachener Arbeitsgruppe der IceCube-Kollaboration unter der Leitung von Professor Christopher Wiebusch insbesondere bezüglich des FAMOUS-Teleskops sehr hilfreich. Dazu gehören u.a. auch Jan Auffenberg, Leif Rädel, Martin Rongen, Merlin Schaufel und Sebastian Schoenen.

Dank gebührt auch der gesamten FACT-Kollaboration für die Leihgabe der Datenerfassungselektronik für das FAMOUS-Teleskop, darunter Junior-Professor Thomas Bretz und Daniela Dorner.

Den Kollegen der Mechanik- und Elektronikwerkstätten der Institute IIIA und IIIB der RWTH Aachen, unter den Leitungen von Barthel Philipps, Franz-Peter Zantis und Wolfgang Feldhäuser möchte ich meinen Dank aussprechen, ebenso wie meinen Studenten Alexander Bogner, Christoph Günther, Alexander Gutsche, Nina Höflich, Robert Joppe, Jan-Paul Koschinsky, Johannes Merz und Benjamin Pestka, die ich in den Jahren meiner Promotion betreut habe.

Letztlich wäre auch als das nicht möglich gewesen ohne die Unterstützung meiner Familie und meinen Freunden, denen ich ganz besonders danken muss – auch für das Probelesen meiner Arbeit.